

# Structural Engineering Documents

9

Elsa de Sá Caetano

## Cable Vibrations in Cable-Stayed Bridges



International Association for Bridge and Structural Engineering  
Association Internationale des Ponts et Charpentes  
Internationale Vereinigung für Brückenbau und Hochbau

IABSE  
AIPC  
IVBH

@Seismicisolation

Copyright © 2007 by  
International Association for Bridge and Structural Engineering

All rights reserved. No part of this book may be reproduced in any form or by any means, electronic or mechanical, including photocopying, recording, or by any information storage and retrieval system, without permission in writing from the publisher

ISBN 978-3-85748-115-4

Publisher:  
IABSE-AIPC-IVBH  
ETH Hönggerberg  
CH-8093 Zürich, Switzerland

Phone: Int. + 41-44-633 2647  
Fax: Int. + 41-44-633 1241  
E-mail: [secretariat@iabse.org](mailto:secretariat@iabse.org)  
Web: [www.iabse.org](http://www.iabse.org)

@Seismicisolation

## Preface

The numerous episodes of cable vibration exhibited by different types of cable-stayed bridges all over the world have posed a strong demand to understand and control the involved phenomena. Intensive studies have been conducted during the last two decades, serving directly the designers' needs and at the same time framed by academic research projects funded by national science institutions and authorities interested in producing guidelines and codes for the safe design and assessment of their structures.

The present book provides a comprehensive survey on the existing and published knowledge related to cable vibrations, focusing on the governing phenomena, on the methodologies to assess their effects and on the design of control devices.

The evident need to convert research results into practice and to learn from practical experience motivated the invitation of experienced designers and consultants to present a contribution from particular cases in which they participated. I would like to deeply acknowledge the extremely interesting and enriching reports provided by Drs. Yves Bournard (VSL International), Chris Geurts (TNO), Carl Hansvold (Johs. Holt), Allan Larsen (Cowi) and Randall Poston (WDP & Associates).

I would also like to express my gratitude to the support and material provided by many researchers from all over the world, expecting that I can honour their work. In particular, I would like to refer to Professor Yozo Fujino, Dr. Hoang Nam, Professor Masaru Matsumoto and Professor Hiroshi Tanaka who carefully reviewed the manuscript and supplied important research reports. I also thank Professors Hiroki Yamaguchi and Steen Krenk, Drs. Shaohong Cheng, Olivier Flamand, Christian Cremona, and António Pinto da Costa and Mr. Craig Winters and Philippe Duflot for publications and images provided.

Finally, I want to thank IABSE for providing the opportunity and the support to publish this book, and Dr. Geoff Taplin, Chair of the Editorial Board, for his personal commitment to the success of this publication.

Porto, August 2007

Elsa de Sá Caetano  
Faculty of Engineering of the University of Porto

**Table of Contents**

	<b>Page</b>
<b>1 General</b>	1
<b>2 Organisation of the Text</b>	3
<b>3 Brief History of Cable-Stayed Bridge Construction</b>	5
<b>4 Vibration Phenomena Directly Induced by Wind and Rain</b>	13
4.1 Wind Loads on Stay Cables	13
4.1.1 Fixed cylinder immersed in smooth flow	14
4.1.2 Fixed cylinder immersed in turbulent flow	17
4.1.3 Moving cylinder immersed in turbulent flow	19
4.1.4 Linearised equations of motion	21
4.2 Buffeting	22
4.3 Vortex-shedding	23
4.3.1 Fundamental characteristics	23
4.3.2 Amplitude of oscillations	25
4.4 Galloping	29
4.4.1 Fundamentals	29
4.4.2 Prediction and control measures	32
4.5 Wake Effects	33
4.5.1 Resonant buffeting	34
4.5.2 Vortex resonance	34
4.5.3 Interference effects	35
4.5.3.1 Vortex resonance effects	36
4.5.3.2 Galloping	36
4.5.3.3 Interference galloping of free cables	37
4.5.3.4 Interference effects in stranded cables	38
4.6 Rain-wind Induced Vibrations	39
4.6.1 Identification of the phenomenon	39
4.6.2 Experimental observations	40
4.6.3 Analytical and design models	44
4.6.3.1 Analytical model from Yamaguchi	44
4.6.3.2 Analytical model of Peil and Nahrath	48
4.6.3.3 Design model of Geurts and van Staalduin	49
4.6.4 Mechanisms of instability	50
4.6.4.1 Conventional Karman vortex excitation	50
4.6.4.2 Galloping instability	51
4.6.4.3 High speed vortex excitation	51
4.6.5 Other variables to rain-wind induced oscillations	52
4.6.6 Practical cases of occurrence of rain-wind vibration and prevention measures	52
4.7 Drag Crisis	54
<b>5 Indirect Excitation</b>	55
5.1 General	55
5.2 External Excitation	55
5.2.1 Linear model	56
5.2.2 Linearity of response of current stays	58
5.2.3 Non-linear model	59

5.3	Parametric Excitation	63
5.3.1	General equations	63
5.3.2	Application to a stay cable	66
5.3.3	Practical occurrence of external/parametric excitation	67
5.4	Cable-structure Interaction	69
<b>6</b>	<b>Control of Vibrations in Cable-Stayed Bridges</b>	71
6.1	General	71
6.2	Vibration Control Systems	71
6.2.1	Aerodynamic control of vibrations	71
6.2.2	Structural control of vibrations	73
6.2.3	Mechanical control of vibrations	74
6.2.4	Active control—systems	77
6.2.4.1	Active aerodynamic appendages	77
6.2.4.2	Active mass dampers	77
6.2.4.3	Active tendon control	78
6.3	Design of an Optimal Passive Damper	78
6.3.1	General	78
6.3.2	State-of-the-art of research	79
6.3.3	Problem formulation	80
6.3.3.1	Taut cable	80
6.3.3.2	Shallow cable	85
6.3.3.3	Bending stiffness effects	90
6.3.3.4	Flexibility of the dampers or of the supports	94
6.3.3.5	Damper non-linearity	97
6.3.3.6	Combined effects of sag, bending stiffness and flexibility of damper supports	99
6.3.3.7	Combined effect of two dampers	100
6.3.4	Practical applications	103
6.3.4.1	Evaluation of maximum attainable damping ratio for a particular damper location	103
6.3.4.2	Specification of damper size to fulfil minimum damping requirements	107
<b>7</b>	<b>Case Reports</b>	109
7.1	Skarnsundet Bridge (Norway)	110
7.2	Puente Real Bridge (Badajoz)	112
7.3	Veterans Memorial and Fred Harman Bridge (Texas)	114
7.4	Erasmus Bridge (Rotterdam)	119
7.5	Kap Shui Mun Bridge (Hong Kong)	124
7.6	Oresundsbron (Denmark–Sweden)	128
7.7	Uddevallabron (Sweden)	131
7.8	Friction Damper Test	133
<b>8</b>	<b>References</b>	137
<b>Appendix A</b>		147
A.1	Objectives	147
A.2	Static Behaviour	147
A.2.1	General assumption: Elastic catenary	148

A.2.2	Elastic parabola	153
A.2.3	Numerical modelling	154
	A.2.3.1 Linear model: Truss element	154
	A.2.3.2 Linear model refinement: Equivalent modulus of elasticity	155
	A.2.3.3 Linear model refinement: Multi-link approach	156
	A.2.3.4 Non-linear model: Cable element	157
	A.2.3.5 Comparative analysis for global study of a cable-stayed bridge	157
<b>Appendix B</b>		163
B.1	Objectives	163
B.2	Linear Theory of vibrations of horizontal—cables	163
	B.2.1 Basic assumptions and equilibrium equations	163
	B.2.2 Natural frequencies and modal shapes	164
	B.2.2.1 Out-of-plane motion	164
	B.2.2.2 In-plane motion	164
B.3	Linear Theory of Vibrations of Inclined Cables	168
	B.3.1 Simplified approach	168
	B.3.2 Asymptotic approach	169
B.4	Bending Stiffness Effects	173
	B.4.1 Taut string approach	173
	B.4.2 Simplified sagged cable approach	174
<b>Appendix C</b>		177
C.1	General	177
C.2	Methods of Force Assessment	177
	C.2.1 Direct measurement of stress in tensioning jacks	177
	C.2.2 Application of ring load cells or of strain gauges in strands	177
	C.2.3 Measurement of cable elongation	178
	C.2.4 Topographic survey	179
	C.2.5 Vibration method	179
C.3	Force and Damping Assessment Based on the Vibration Method	179
	C.3.1 Vibrating chord theory	179
	C.3.2 Bending and sag effects	180
	C.3.3 Measurement of cable frequencies	181
	C.3.4 Estimation of cable damping	182
	C.3.5 Practical application	184

# 1. General

Cable-stayed bridges were established as a new category among the classical types of bridges in the second half of the twentieth century. Their relative stiffness when compared to suspension bridges, self-balancing characteristics adequate for construction in weak soil and offering an economically advantageous solution for moderate to large spans, and notable aesthetic qualities, led to an enormous increase in the construction of these structures all over the world. This expansion was naturally accompanied by significant technological developments that led to progressively larger and more slender prototypes. Cable-stayed bridges are subjected to a variety of dynamic loads like traffic, wind, pedestrians and seismic loads, which are rather complex to characterise. Considering in addition that stay cables constitute very flexible structural elements generally characterised by small damping coefficients, it is understandable that these elements are very prone to vibrations.

The former reports on cable vibrations refer to the Brotonne bridge in France, and date back to 1976 [1]. According to Stiemer *et al.* [2], the vibrations were so large that the longest cables, which were almost parallel and 1957 mm apart at the centre, hit each other. Although the source of these oscillations was not understood at that time, the problem was solved by mounting viscous dampers close to the deck anchorages. Many vibration problems have been detected ever since in bridges all over the world, which have motivated intensive research on the various phenomena. The first studies on cable vibrations date back to the 1980s and, although the full understanding of the governing mechanisms of some complex phenomena has not been achieved yet, important information concerning the various sources of vibrations and possible methodologies for prediction and control, that are of wide interest to bridge designers, can be found in the literature.

Taking these aspects into consideration, it is the purpose of this book to systematise the most recent understanding of the various phenomena of cable vibration, and to present, whenever possible, methodologies for the prediction of potential phenomena and for an efficient control of occurrences. This information will be complemented with the presentation of practical case studies by recognised bridge designers and researchers. In the Appendices, the most relevant aspects of the dynamics of stay cables are discussed.

## 2. Organisation of the Text

The current publication is divided into seven Chapters, with the following content:

- Chapters 1 and 2 introduce the problem of cable vibration in cable-stayed bridges and present the objectives and organisation of the publication.
- Chapter 3 presents a brief overview of the history of cable-stayed bridges.
- Chapter 4 describes the cable vibration phenomena that are induced by direct action of wind and/or rain, namely: buffeting, vortex-shedding, galloping, wake interference, rain–wind vibration and recently identified phenomena.
- Chapter 5 presents indirect excitation phenomena, i.e. phenomena of cable vibration that are induced in the cable by the movement of its anchorages. For convenience of study, these are separated into two groups, the so-called external excitation and the parametric excitation phenomena, which are introduced considering the study of the stay cable individually. The dynamic cable–structure interaction is also discussed in this Chapter.
- Chapter 6 is dedicated to the description of damping systems for stay cables and to the presentation of a simple methodology for the design of passive dampers.
- Chapter 7 has been developed by bridge designers recognised worldwide, reporting on specific vibration problems in particular bridges and the solutions implemented.

The text is complemented by three Appendices where theoretical and practical issues that support cable vibration studies are presented. They are:

- Description of the deformational characteristics of stay cables (Appendix A).
- Presentation of the fundamentals of cable dynamics (Appendix B).
- Reference to experimental methodologies for practical assessment of cable force and damping (Appendix C).

### 3. Brief History of Cable-Stayed Bridge Construction

The concept of supporting a bridge girder with inclined stays was introduced in the seventeenth century, with former application proposals attributed to Verantius (Italy, 1617) and Löscher (Germany, 1784) [3, 6].

Several stay applications in the form of iron chains and wire ropes were referred to in the literature throughout the nineteenth century. The lack of a full understanding of the structural behaviour of cable bridges and the technological limitations of the time have resulted in some failures and in the consideration that bridges with inclined stays were too flexible and unsafe, the consequence being the preference for suspension bridges.

During the second half of the nineteenth century, several suspension bridges were constructed. They employed additional inclined cables to stiffen the bridge structure and provide stability against wind. The famous Brooklyn bridge (*Fig. 3.1*), designed by Roebling and completed in 1883, having a total length of 1059.9 m and a main span of 486.5 m, is the major example of this hybrid type of cable bridge and represents a milestone in the history of bridge construction. Of particular note is the use, for the first time in a large construction, of steel for cable wire instead of iron, at a time when this new material (with twice the strength of iron) was only used for construction of railroads in England.

The development of modern cable-stayed bridges dates from the second half of the twentieth century, and is largely due to Dischinger, who realised that higher stiffness and stability could be achieved with high strength, pre-stressed cables [4]. Combining these properties with the calculation facilities introduced by the use of computers, systematic structural analysis became possible, leading to a rational design and permanent control of cable forces, and thereby to an efficient design for these structures.

The Strömsund bridge in Sweden, opened to traffic in 1956, is generally considered the first cable-stayed bridge of the modern era [5]. As may be seen from *Fig. 3.2*, the bridge is composed of three spans and has a total length of 332 m, and a main span of 182.6 m, the steel and concrete deck being suspended from each pylon by four pairs of diagonal stay cables.

For technical, economic and aesthetic reasons, cable-stayed bridges, that became very popular in Germany during post-war reconstruction, have gained increasing importance, and their use has quickly spread all over the world, with a multitude of innovative solutions.

It is interesting to note that the design of cable-stayed bridges underwent considerable evolution in a short period of less than 50 years. Mathivat [8], identified three so-called *generations* of cable-stayed bridges that characterise the major developments.

The bridges of the *first generation*, like the Strömsund bridge, used a limited number of stay cables, usually between two and six pairs of stays in the main span. These cables were separated by large distances, normally varying between 30 and 80 m, that required a large



Fig. 3.1: The Brooklyn bridge (United States, 1883) (Library of Congress, Washington D. C.)



Fig. 3.2: Strömsund bridge (Sweden, 1956) (Courtesy of Andreas Stedt)

bending stiffness of the deck (the usual depth varying from 3 to 4 m) [7]. Besides this, the cable tensions were so high that several ropes were necessary to form each stay. This also necessitated complicated anchorages and led to important concentrated stresses. An additional difficulty was the need for auxiliary structures to erect these bridges.

The *second generation* of cable-stayed bridges is characterised by the adoption of a partial suspension system, in which the deck is rigidly supported by the pylon and suspended by a large number of closely spaced stay cables. The use of this multiple-cable system type of suspension allowed two main achievements namely, the use of a moderate flexural stiffness

for the deck, in view of the elastic support provided by the cables and the reduction of concentrated forces applied to the deck, with the consequent use of simpler anchorages and avoidance of the need to strengthen the girder near the cable anchorages. The small spacing between deck anchorages provided additional advantages in the construction phase, allowing for a simpler, free cantilever construction. The first bridge of this generation was the Friedrich Ebert bridge, constructed in Germany in 1967. The Brotonne bridge (*Fig. 3.3*), constructed in France in 1977, with a main span of 320 m, was the first application of the multiple-cable system in a concrete cable-stayed bridge and is presently seen as the prototype of the bridges of this *second generation*.

The bridges of the *second generation* led to the transition to the so-called *third generation* of cable-stayed bridges that constitute the current trend of large cable-stayed bridges. These *third generation* bridges are characterised by the use of a large number of closely spaced stays (8–15 m, according to Leonhardt and Zellner [7]) that support the deck. A new type of structural behaviour is achieved with this form of suspension, where the deck acts as the compressive chord of a truss hung up to the towers by inclined stays. The fact that bending moments are very small makes the depth of the girder deck almost independent of the main span length, the required amount of longitudinal bending stiffness being governed by the safety against buckling and the necessity to limit local deformation under concentrated live load.

The Pasco-Kennewick bridge (*Fig. 3.4*), designed by Arvid Grant in collaboration with the consulting company Leonhardt, Andra & Partner and constructed in the USA in 1978, with a main span of 300 m and a total length of 548 m, was the first concrete cable-stayed bridge built in the United States and also the first to employ total deck suspension. The deck, composed of two triangular edge box girders connected by transverse beams, is 2.15 m deep.

Bridges of the second and third generations are considerably more slender than former cable-stayed bridges, a fact that allowed for a progressive increase in the span length, as shown in *Fig. 3.5*, relating the span length with the year of completion for some of the most representative cable-stayed bridges around the world.

With the completion of the Normandy bridge in France in 1994, a multiple-suspension bridge with a total length of 2141 m and a record main span of 856 m (*Fig. 3.6*), it was proved that cable-stayed bridges, which had initially been considered to have 150–500 m spans at the



*Fig. 3.3: The Brotonne bridge (France, 1977) (by Philip Bourret, in www.Structurae.net)*



*Fig. 3.4: The Pasco-Kennewick bridge (USA, 1978) (Courtesy of Patrick S. O'Donnell, in [www.Bridgemeister.com](http://www.Bridgemeister.com))*

most, could be successfully used, and with economic advantage, in the domain of very long spans. The Tatara bridge (*Fig. 3.7*), completed in Japan in 1999, with a main span of 890 m, is a further proof of this.

So, the question now is: How far is it possible to go?

According to Taylor [10], no element in the bridge has reached a feasibility threshold yet, and since the ratio cost/span has not shown a steep increase with the increase of span, it is still possible to expect an increase in the span range. The former proposals for cable-stayed bridges with main spans larger than 1000 m are indeed older than 20 years, and there is an ongoing project for a cable-stayed bridge in Hong Kong with a main span of 1018 m and a total length of 1596 m, the so-called Stonecutters bridge (*Fig. 3.8*).

The most significant restriction to an increase in the span length of a cable-stayed bridge is associated with the development of high compression forces introduced in the deck by the stay cables. According to Mathivat [11], this fact limits the main span length to about 1500 m. Beyond this length, it is normally assumed that the classical suspension type, with cables anchored to the ground, is the best solution.

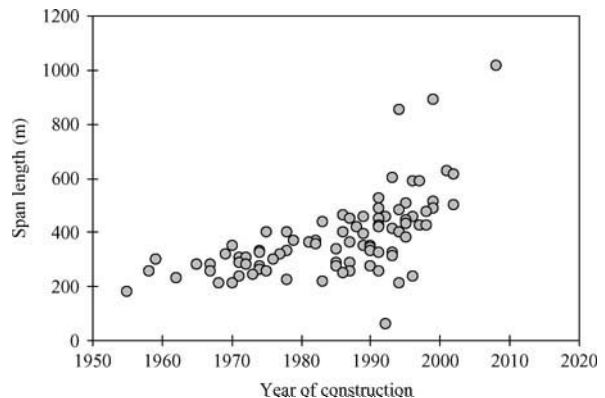


*Fig. 3.5: Evolution of span length with year of completion for cable-stayed bridges. Modified from Ref. [9]*



*Fig. 3.6: General view of the Normandy bridge (France, 1994) (Courtesy of Bouygues Construction)*

But even in those large spans the inclined stay cable suspension can play an important role. In fact, the addition of inclined stay cables to a suspension bridge in the vicinity of the pylons provides a higher global stiffness for the bridge and, consequently, better wind stability, and allows for a better control of static deformations, particularly important in the case of railway bridges. This hybrid system was used in an empirical form by Roebling [6], and it has been proposed several times for the construction of recent bridges. But no modern applications are known yet.

Another intermediate solution for wide rivers and sea crossings is based on the concept of multiple cable-stayed spans. The Millau bridge in France, and the Rion Antirion bridge in Greece, are two large projects involving different schemes of multiple cable-stayed spans [12] that have been completed in 2004.

Most of the studies already performed for very long spans are based on the use of conventional materials, steel and concrete, whose properties were significantly improved during the last decades. Also, during the last few years of investigation, the application of new, high strength, lightweight



*Fig. 3.7: General view of the Tatara bridge (Japan, 1999) (Courtesy of metropol2, 2005)*



*Fig. 3.8: Preview of Stonecutters bridge, Hong Kong (2004–2008) (Courtesy of Highways Department, Hong Kong Special Administrative Region)*

materials has progressed greatly. Several small span girder bridges have already been constructed using the so-called advanced composite materials (ACM), in the form of carbon fibres and plastics [13]. These materials, whose strength-to-density ratio is about 5–10 times the corresponding strength-to-density ratio for steels, have an enormous potential for long span cable-stayed bridge applications, since the self-weight of the deck can represent a high percentage of the bearing capacity in a very long span.

The first reported application of these new materials to cable-supported structures is a small footbridge in Scotland, the Aberfeldy Bridge (1992), across the River Tay (*Fig. 3.9*). With a total length of 113 m and a main span of 63 m, the bridge was designed by Maunsell Structural Plastics and erected without craneage by the final-year bridge engineering students of Dundee University, from super cells made of glass reinforced polymer (GRP) and parafil cables. More recently, a cable-stayed bridge with a main span of 137 m has been under design and study in San Diego, USA [14]. The bridge is composed of two asymmetric spans and one tower, and employs concrete-filled carbon/epoxy tubes as edge girders and pylon, as well as hollow transverse girders made of glass-carbon/vinylester with polypropylene-fibre reinforced concrete. Also, some of the stay cables are made of carbon/epoxy material. Pultruded carbon-fibre epoxy rods have also been used in the recent construction of a cable-stayed footbridge in France, at Laroin.



*Fig. 3.9: Aberfeldy cable-stayed bridge (Scotland, 1992) (Courtesy of Robert Cortright/Bridge Ink)*

The footbridge has only a steel/concrete span of 110 m that is suspended by 16 carbon-fibre stays, while backstays are traditional bundles of strands [15]. The use of fibre reinforced material as an outer shell to long span steel-concrete bridges constitutes another application, which can enhance the torsional stiffness of the system, improve its aerodynamic profile, increase its durability and, eventually, provide a windshield to vehicular traffic [16].

## 4. Vibration Phenomena Directly Induced by Wind and Rain

Wind is one of the most conditioning factors in the design of cable-stayed bridges, particularly of stay cables. These structural elements suffer both from direct excitation along the surface and from indirect action on the deck and towers, which result in oscillation at the supports.

The study of wind effects is normally conducted by separating the static component, associated with a mean flow velocity of air, and the dynamic component, related with vortex shedding and atmospheric turbulence. The current text presents a brief description of wind loads applied to stay cables, concentrating on the effects of the corresponding dynamic component. Particular vibrating phenomena are introduced, namely buffeting, vortex-shedding, galloping, aerodynamic interference, rain-wind induced vibration and a set of vibration phenomena that have been identified more recently, like the dry galloping and drag crisis phenomena. The mechanisms that govern these phenomena are explained according to current theories, as well as possible techniques for the suppression or attenuation of the vibrations.

### 4.1 Wind Loads on Stay Cables

When related to structural engineering problems, the wind is a flow generally characterised by three time-dependent velocity components  $U(t)$ ,  $V(t)$  and  $W(t)$ , along three mutually orthogonal directions. These components depend on a mean wind velocity  $U$ , which is horizontal and has the dominant wind direction, and on the fluctuating components  $u(t)$ ,  $v(t)$  and  $w(t)$ , according to

$$\begin{aligned} U(t) &= U + u(t) \\ V(t) &= v(t) \\ W(t) &= w(t) \end{aligned} \tag{4.1}$$

By immersing a body (a stay cable) in this flow, surface pressures are generated. If the body is fixed, the developed pressures depend on the characteristics of the flow and on the geometry of the body. If the body is free to oscillate, as happens with stay cables, the developed pressures are modified by vibration. An interaction excitation results, which is designated as aeroelastic excitation.

Although in practice these wind effects are related, they are frequently analysed separately for the sake of simplicity.

Considering the stay cable represented by a non-circular cylinder of infinite length immersed in a two-dimensional flow, the incident forces per unit length are calculated from integration of the generated surface pressures under the following conditions: (a) fixed cylinder immersed in a smooth flow; (b) fixed cylinder immersed in a turbulent flow; and (c) moving cylinder immersed in a turbulent flow. These independent conditions allow the identification and

discussion of particular features of the flow around the body, like the shape coefficients and their variation with the Reynolds number, the formation of vortices in the wake of the flow and the development of aerodynamic damping.

#### 4.1.1 Fixed cylinder immersed in smooth flow

The resultant wind loads on the cylinder are expressed in a Cartesian reference system  $(O, d, l)$ , whose axis  $d$  is obtained by a rotation of axis  $x$  from a general reference system  $(O, x, y)$  by an angle  $\beta$  counter-clockwise, in order to align with the wind velocity vector  $U$  (*Fig. 4.1(a)*).

According to the representation of *Fig. 4.1(b)*, two force components  $F_{Ds}(t)$  and  $F_{Ls}(t)$  in the along-flow and across-flow directions occur, designated as drag and lift forces, as well as a moment  $M_s(t)$  acting on the elastic centre of the body  $O$ , which are defined by

$$F_{Ds}(t) = F_D + f_{Ds}(t) \quad (4.2a)$$

$$F_{Ls}(t) = F_L + f_{Ls}(t) \quad (4.2b)$$

$$M_s(t) = M + m_s(t) \quad (4.2c)$$

$F_D$ ,  $F_L$  and  $M$  represent the mean values of wind forces, and  $f_{Ds}(t)$ ,  $f_{Ls}(t)$  and  $m_s(t)$  are nil mean fluctuations. The values of these components are determined from the balance between inertial and viscous forces around the cylinder that is quantified through the Reynolds number  $Re$ , defined as

$$Re = \frac{UB}{\nu} \quad (4.3)$$

where  $B$  is a representative dimension of the cylinder,  $U$  is the uniform wind velocity and  $\nu$  is the kinematic viscosity, whose value for the air at 20 °C is 0.150  $cm^2/s$  [17].

*Figure 4.2*, based on [17], illustrates the organisation of the flow with increasing Reynolds number for the particular case of a circular cylinder of diameter  $D$  ( $B = D$ ).

For low wind velocity  $U$ , i.e. for low values of  $Re$  ( $Re \approx 1$ ), viscosity forces are dominant, which determine the attachment of the flow to the cylinder along the perimeter (*Fig. 4.2(a)*).

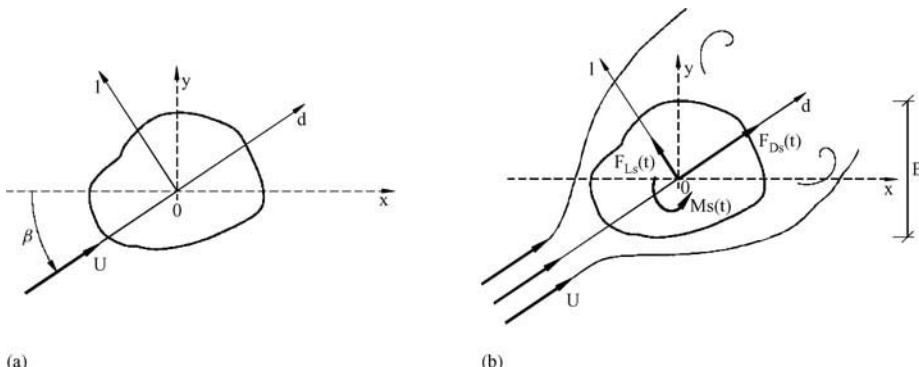


*Fig. 4.1: Fixed rigid cylinder of infinite length immersed in a smooth flow: (a) Reference Cartesian systems and wind velocity field; (b) aerodynamic forces*

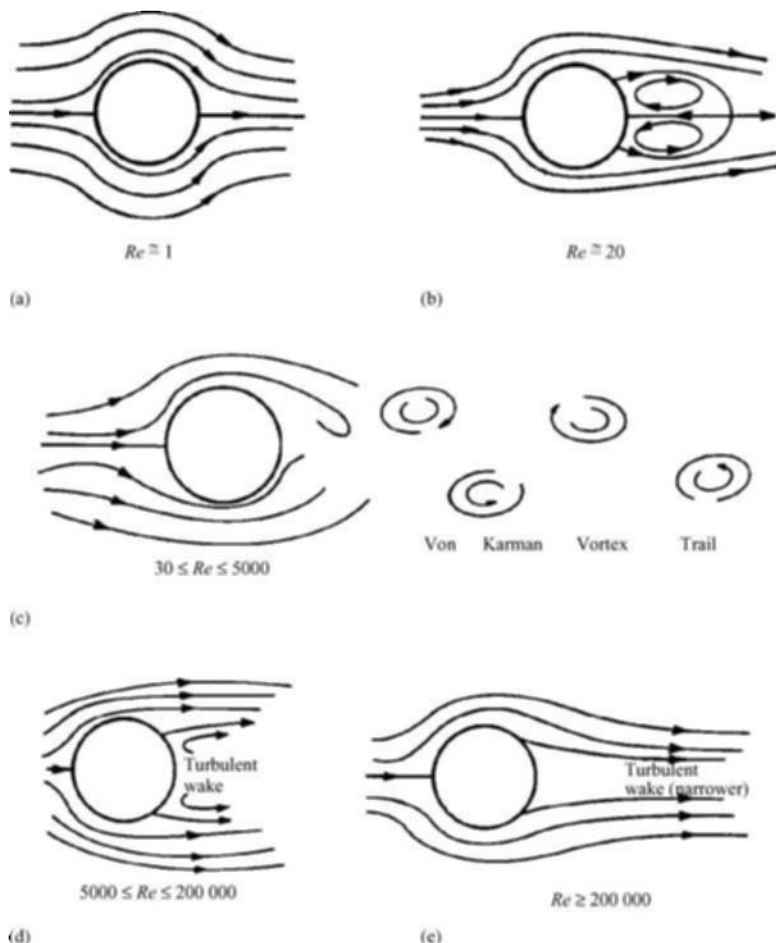


*Fig. 4.2: Flow past circular cylinder: (a) at  $Re \approx 1$ ; (b)  $Re \approx 20$ ; (c)  $30 \leq Re \leq 5000$ ; (d)  $5000 \leq Re \leq 200 000$ ; (e)  $Re \geq 200 000$  [17]\**

\*Reproduced with permission. Copyright 1996

By increasing the flow velocity, the Reynolds number increases. At  $Re \approx 20$  the flow separates, creating two symmetrical vortices near the downstream surface of the cylinder (Fig. 4.2(b)). At an increased Reynolds number of 30, the symmetrical vortices are broken and replaced by cyclic alternating vortices that form by turn at the top and bottom surfaces and are swept downstream to form a vortex trail, designated as the *Von Karman vortex trail* (Fig. 4.2(c)). Figure 4.3 presents a visualisation of the phenomenon by the emission of a dye from the cylinder immersed in a water tunnel [17].

As the Reynolds number increases into the range of  $5000 \leq Re \leq 200 000$ , the attached flow upstream of the separation point remains laminar, while transition to turbulent flow occurs in the wake (Fig. 4.2(d)), further downstream from the cylinder for the smaller  $Re$  number, and closer to the cylinder surface for the higher  $Re$ . Finally, for a very large  $Re$  number,

i.e.  $Re \geq 200\,000$ , the wake narrows, meaning that reduced forces are acting on the cable (*Fig. 4.2(e)*).

The mean wind forces  $F_D$ ,  $F_L$  and  $M$ , representing the static component of wind loads, are generally defined as

$$F_D = \frac{1}{2} \rho U^2 B C_D(\beta) \quad (4.4a)$$

$$F_L = \frac{1}{2} \rho U^2 B C_L(\beta) \quad (4.4b)$$

$$M = \frac{1}{2} \rho U^2 B^2 C_M(\beta) \quad (4.4c)$$

where  $\rho$  is the air density, with a value of  $1.2 \text{ kg/m}^3$  at  $20^\circ\text{C}$ ,  $B$  is the representative dimension of the body (*Fig. 4.1(b)*) that coincides with the outer diameter  $D$  for a circular cylinder, and  $C_D(\beta)$ ,  $C_L(\beta)$  and  $C_M(\beta)$  are shape coefficients, drag lift and moment coefficients, respectively, whose values depend on the characteristics of the cylinder surface and on the Reynolds number. *Figure 4.4* illustrates the variation of  $C_D$  with  $Re$  for a circular cylinder with a varying surface roughness, obtained from wind tunnel tests [18]. Considering the variation of stay cable diameters in the range of  $0.10\text{--}0.30 \text{ m}$  and the mean wind velocity of

interest in the range of  $5\text{--}50 \text{ m/s}$ , the Reynolds number of stay cables varies in the range of  $3 \times 10^4\text{--}10^6$ . The analysis of *Fig. 4.4* shows that three regions are defined for that range of  $Re$  values: the sub-critical region is associated with low  $Re$  numbers and relatively constant  $C_D$  values of around 1.2; the critical region, defined for  $Re$  values in the range of  $2 \times 10^5\text{--}8 \times 10^5$ , depending on the roughness of the surface, in which  $C_D$  can drop to around 0.4, corresponds to the transition from laminar to turbulent flow; and the supercritical region, for which  $C_D$  increases slightly. It is considered that for extreme wind speeds stay cables are

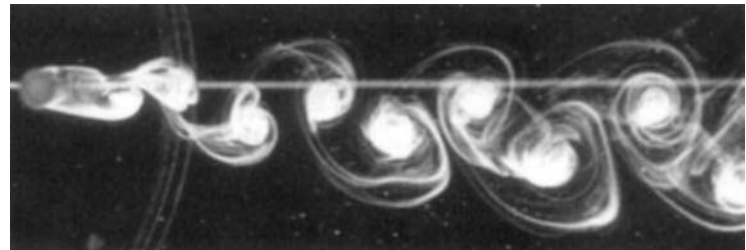


*Fig. 4.3: Vortex trail for a circular cylinder immersed in a water tank [17]\**

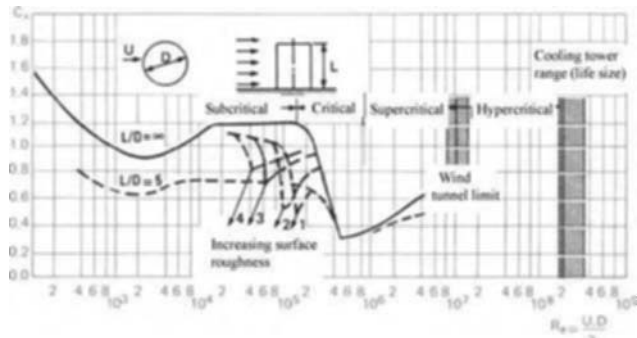


*Fig. 4.4: Variation of  $C_D$  with  $Re$  in a uniform flow for a circular cylinder [18]\**

\*Reproduced with permission. Copyrights 1996, 2002

normally in the supercritical region and a value of  $C_D$  of 0.7 is used for circular cross-sections [18].

It should be noted that non-circular cross sections can have very different drag and lift coefficients. For stranded cables, for example, average values of  $C_D$  of 1.2 are found. Considering that the wind load on the stays can be close or even more than 50% of the total transverse loads on the bridge structure [19], the choice of the cable cross section becomes a matter of utmost importance.

The fluctuating components of wind loads  $f_{Ds}(t)$ ,  $f_{Ls}(t)$  and  $m_s(t)$  in expression (4.2) are primarily associated with the vortex shedding that occurs in the wake of the cylinder and can be approximated by [20]

$$f_{Ds}(t) = \frac{1}{2} \rho U^2 B c_{Ds} \sin(4\pi f_v t) \quad (4.5a)$$

$$f_{Ls}(t) = \frac{1}{2} \rho U^2 B c_{Ls} \sin(2\pi f_v t) \quad (4.5b)$$

$$m_s(t) = \frac{1}{2} \rho U^2 B^2 c_{Ms} \sin(2\pi f_v t) \quad (4.5c)$$

where  $c_{Ds}$ ,  $c_{Ls}$  and  $c_{Ms}$  are non-dimensional wake coefficients and  $f_v$  is the shedding frequency of the vortices, defined as a function of the Strouhal number  $St$

$$f_v = \frac{U St}{B} \quad (4.6)$$

The Strouhal number  $St$  depends upon the shape of the cross section and is approximately constant with the Reynolds number for a wide range of  $Re$ , as can be observed in Fig. 4.5, that presents measurements on circular cylinders for different values of the roughness  $k/D$  [21]. For practical applications with circular cylinders, a constant value of  $St$  of 0.2 can be considered.

#### 4.1.2 Fixed cylinder immersed in turbulent flow

The fixed cylinder referred to in the previous Section is now immersed in a turbulent flow that is characterised by the same dominant direction and mean velocity  $U$ , and by the fluctuations  $u(t)$  and  $v(t)$  in the along-wind and across-wind directions, respectively (Fig. 4.6(a)).

Assuming a small turbulence ( $u/U \ll 1$ ;  $v/U \ll 1$ ), the drag and lift forces and the moment over the cylinder

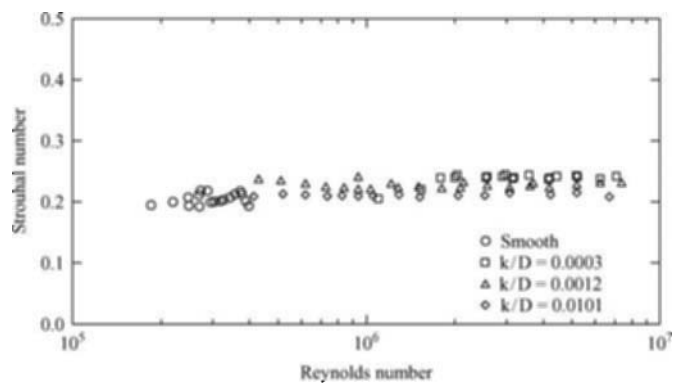


Fig. 4.5: Relation between  $St$  and  $Re$  for circular cylinder [21]

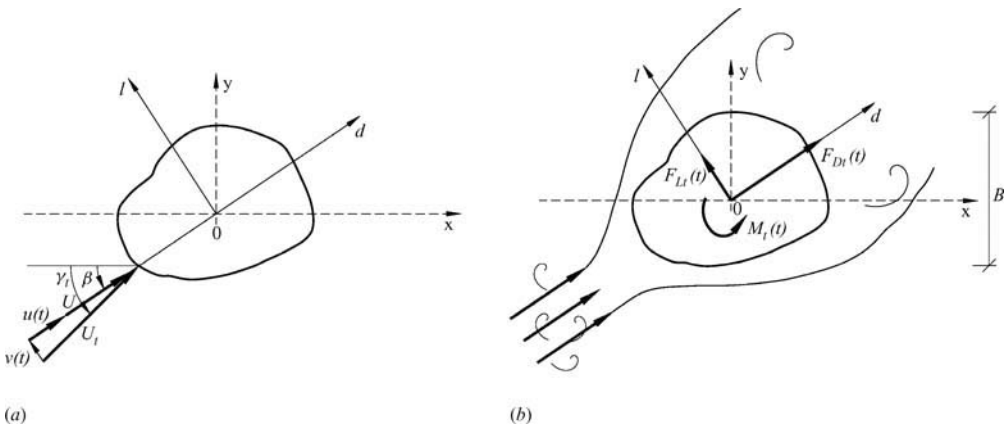


Fig. 4.6: Fixed rigid cylinder of infinite length immersed in turbulent flow: (a) Reference Cartesian systems and wind velocity field; (b) aerodynamic forces

in the turbulent flow,  $F_{Dt}(t)$ ,  $F_{Ld}(t)$  and  $M_t(t)$ , respectively, can be obtained from a linearised approximation involving the following components

$$F_{Dt}(t) = F_{Dt} + f_{Du}(t) + f_{Dv}(t) + f_{Dw}(t) \quad (4.7a)$$

$$F_{Ld}(t) = F_{Ld} + f_{Lu}(t) + f_{Lv}(t) + f_{Lw}(t) \quad (4.7b)$$

$$M_t(t) = M_t + m_u(t) + m_v(t) + m_w(t) \quad (4.7c)$$

In these expressions,  $F_{Dt}$ ,  $F_{Ld}$  and  $M_t$  represent the mean wind drag, lift and moment components of load in the turbulent flow, given as function of the corresponding shape coefficients  $C_{Dt}(\beta)$ ,  $C_{Ld}(\beta)$  and  $C_{Mt}(\beta)$  as

$$F_{Dt} = \frac{1}{2} \rho U^2 B C_{Dt}(\beta) \quad (4.8a)$$

$$F_{Ld} = \frac{1}{2} \rho U^2 B C_{Ld}(\beta) \quad (4.8b)$$

$$M_t(t) = \frac{1}{2} \rho U^2 B^2 C_{Mt}(\beta) \quad (4.8c)$$

It is relevant to note that turbulence tends to lead to a decrease of the shape coefficients. This fact can be noticed in Fig. 4.7, representing the variation of drag coefficient with the Reynolds number for different intensities of turbulence (the intensity of turbulence  $u_\sigma$  is defined as  $u_\sigma = \sqrt{\bar{u}^2}/U$ ,  $\bar{u}^2$  being the expected value of the square of the wind fluctuation  $u(t)$ ).

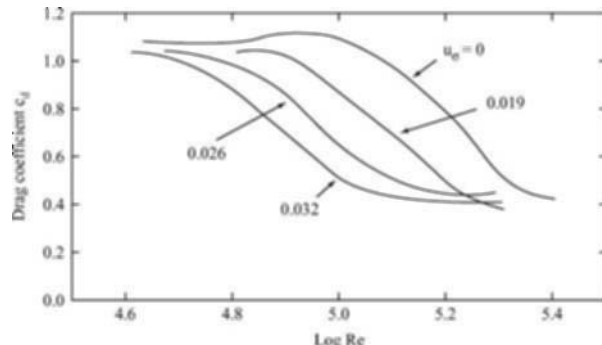


Fig. 4.7: Influence  $u_\sigma$  on the drag coefficient of a circular cylinder [22]

The terms  $f_{Du}(t)$ ,  $f_{Lu}(t)$  and  $m_u(t)$  in expression (7) represent the forces induced by the turbulence component  $u$ , while the terms  $f_{Dv}(t)$ ,  $f_{Lv}(t)$  and  $m_v(t)$  represent the forces induced by the turbulence component  $v$ . These forces are expressed as functions of the shape coefficients  $C_{Dt}(\beta)$ ,  $C_{Lt}(\beta)$  and  $C_{Mt}(\beta)$ , and of the corresponding derivatives with respect to the angle  $\gamma_t$  at  $\beta$ ,  $C'_{Dt}(\beta)$ ,  $C'_{Lt}(\beta)$  and  $C'_{Mt}(\beta)$ , respectively, according to [20]

$$f_{Du}(t) = \rho U u(t) B C_{Dt}(\beta) \quad (4.9a)$$

$$f_{Lu}(t) = \rho U u(t) B C_{Lt}(\beta) \quad (4.9b)$$

$$m_u(t) = \rho U u(t) B^2 C_{Mt}(\beta) \quad (4.9c)$$

and

$$f_{Dv}(t) = \frac{1}{2} \rho U v(t) B (C'_{Dt}(\beta) - C_{Dt}(\beta)) \quad (4.10a)$$

$$f_{Lv}(t) = \frac{1}{2} \rho U v(t) B (C_{Dt}(\beta) + C'_{Lt}(\beta)) \quad (4.10b)$$

$$m_v(t) = \frac{1}{2} \rho U v(t) B^2 C'_{Mt}(\beta) \quad (4.10c)$$

Finally the last terms of expression (4.7),  $f_{Dw}(t)$ ,  $f_{Lw}(t)$  and  $m_w(t)$ , represent the forces produced by the vortex wake. The harmonic nature of these forces in the uniform flow is disturbed by the presence of turbulence, leading to the following approximation

$$f_{Dw}(t) = \frac{1}{2} \rho U^2 B c_{Dw}(t) \quad (4.11a)$$

$$f_{Lw}(t) = \frac{1}{2} \rho U^2 B c_{Lw}(t) \quad (4.11b)$$

$$m_w(t) = \frac{1}{2} \rho U^2 B^2 c_{Mw}(t) \quad (4.11c)$$

and  $c_{Dw}(t)$ ,  $c_{Lw}(t)$  and  $c_{Mw}(t)$  are the equivalent drag, lift and moment coefficients, respectively, measured in the wake of the cylinder.

### 4.1.3 Moving cylinder immersed in turbulent flow

The cylinder referred to above is now studied when immersed in a wind field identical to the one described in the previous Section, but assuming now that due to its flexibility, two translatory and one rotation motion components,  $d(t)$ ,  $l(t)$  and  $\theta(t)$  are possible, as represented in Fig. 4.8.

Owing to the motion of the cylinder, a relative velocity vector can be defined, whose along-wind and across-wind components,  $U_r(t)$  and  $V_r(t)$ , respectively, are

$$U_r(t) = U + u(t) - \dot{d}(t) \quad (4.12a)$$

$$V_r(t) = v(t) - \dot{l}(t) \quad (4.12b)$$

The symbol  $\cdot$  in equation (4.12) represents derivative with respect to time.

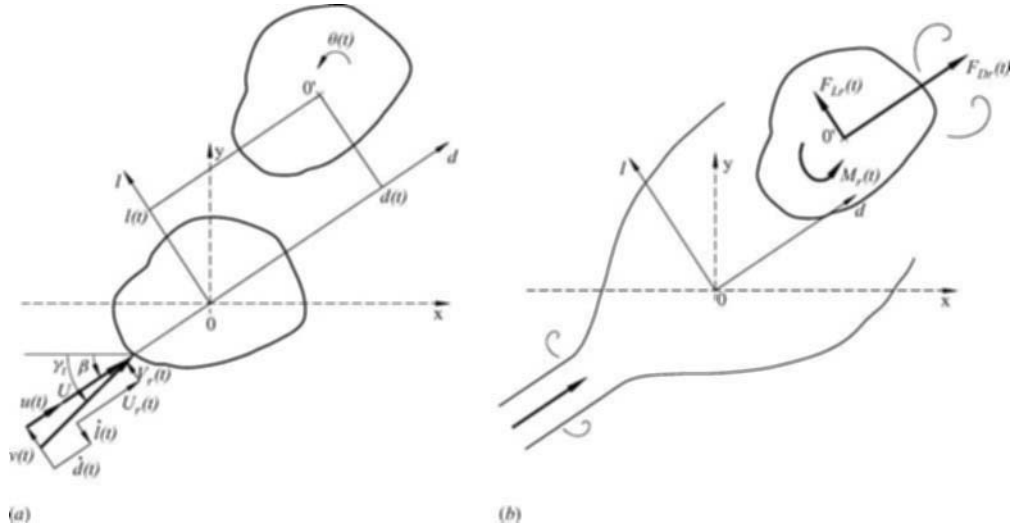


Fig. 4.8: Moving rigid cylinder of infinite length immersed in turbulent flow: (a) Reference Cartesian systems and wind velocity field; (b) aerodynamic forces

Considering small displacements and turbulence and assuming quasi-stationarity, the linearised resultant forces actuating the cylinder,  $F_{Dr}(t)$ ,  $F_{Lr}(t)$  and  $M_r(t)$  can then be approximated by [20]

$$F_{Dr}(t) = F_{Dt} + f_{Du}(t) + f_{Dv}(t) + f_{Dw}(t) + f_{Dq}(t) + f_{D\dot{q}}(t) \quad (4.13a)$$

$$F_{Lr}(t) = F_{Lt} + f_{Lu}(t) + f_{Lv}(t) + f_{Lw}(t) + f_{Lq}(t) + f_{L\dot{q}}(t) \quad (4.13b)$$

$$M_r(t) = M_t + m_u(t) + m_v(t) + m_w(t) + m_{\theta q}(t) + m_{\theta \dot{q}}(t) \quad (4.13c)$$

The first four terms in the second members of these expressions are defined above (expressions (4.8) to (4.11)), representing by order the mean wind forces and the fluctuations due to along-wind and across-wind turbulence, and to the wake effects. The last two terms in expression (4.13) are the fluctuations of the forces generated by the displacements and velocity of the cylinder, the so-called self-excited or aeroelastic forces, and are defined according to

$$f_{Dq}(t) = -\frac{1}{2} \rho U^2 \theta(t) B C'_{Dt}(\beta) \quad (4.14a)$$

$$f_{Lq}(t) = -\frac{1}{2} \rho U^2 \theta(t) B C'_{Lt}(\beta) \quad (4.14b)$$

$$m_{\theta q}(t) = -\frac{1}{2} \rho U^2 \theta(t) B^2 C'_{Mt}(\beta) \quad (4.14c)$$

$$f_{D\dot{q}}(t) = -\rho U \dot{d}(t) B C_{Dt}(\beta) - \frac{1}{2} \rho U \dot{l}(t) B (C'_{Dt}(\beta) - C_{Lt}(\beta)) \quad (4.15a)$$

$$f_{L\dot{q}}(t) = -\rho U \dot{d}(t) B C_{Lt}(\beta) - \frac{1}{2} \rho U \dot{l}(t) B (C_{Dt}(\beta) + C'_{Lt}(\beta)) \quad (4.15b)$$

$$m_{\theta \dot{q}}(t) = -\rho U \dot{d}(t) B^2 C_{Mt}(\beta) - \frac{1}{2} \rho U \dot{l}(t) B^2 C'_{Mt}(\beta) \quad (4.15c)$$

#### 4.1.4 Linearised equations of motion

The motion of the cylinder described in the above Chapters when actuated by a turbulent wind flow can now be described by the following linearised system of equations [20]

$$\underline{M} \ddot{\underline{q}}(t) + \underline{C} \dot{\underline{q}}(t) + \underline{K} \underline{q}(t) = \underline{F}_r(t) \quad (4.16)$$

where  $\ddot{\underline{q}}(t)$ ,  $\dot{\underline{q}}(t)$  and  $\underline{q}(t)$  are the acceleration, velocity and displacement vectors of the cylinder, whose components are

$$\ddot{\underline{q}}(t) = \begin{Bmatrix} \ddot{d}(t) \\ \ddot{l}(t) \\ \ddot{\theta}(t) \end{Bmatrix}; \dot{\underline{q}}(t) = \begin{Bmatrix} \dot{d}(t) \\ \dot{l}(t) \\ \dot{\theta}(t) \end{Bmatrix}; \underline{q}(t) = \begin{Bmatrix} d(t) \\ l(t) \\ \theta(t) \end{Bmatrix} \quad (4.17)$$

The matrices  $\underline{M}$ ,  $\underline{C}$  and  $\underline{K}$  in equation (4.16) represent the cylinder (cable) mass, viscous damping and stiffness per unit length with reference to  $\underline{q}(t)$ , and the vector force  $\underline{F}_r(t)$  represents the wind load, whose components (4.13) are grouped as

$$\underline{F}_r(t) = \begin{Bmatrix} F_{Dr}(t) \\ F_{Lr}(t) \\ M_r(t) \end{Bmatrix} \quad (4.18)$$

separating  $\underline{F}_r(t)$  in two components, one associated with mean, turbulent and wake effects,  $\underline{F}(t)$ , and the other with the aeroelastic effects,  $\underline{F}_a(t)$ , yields

$$\underline{F}_r(t) = \underline{F}(t) + \underline{F}_a(t) \quad (4.19)$$

with

$$\underline{F}(t) = \begin{Bmatrix} F_{Dt} + f_{Du}(t) + f_{Dv}(t) + f_{Dw}(t) \\ F_{Lt} + f_{Lu}(t) + f_{Lv}(t) + f_{Lw}(t) \\ M_t + m_u(t) + m_v(t) + m_w(t) \end{Bmatrix}; \underline{F}_a(t) = \begin{Bmatrix} f_{Dq}(t) + f_{D\dot{q}}(t) \\ f_{Lq}(t) + f_{L\dot{q}}(t) \\ m_{\theta q}(t) + f_{\theta\dot{q}}(t) \end{Bmatrix} \quad (4.20)$$

The dependence of the aeroelastic forces on the cylinder's displacements and velocities allows the expression of these force components as

$$\underline{F}_a(t) = -\underline{C}_a \dot{\underline{q}}(t) - \underline{K}_a \underline{q}(t) \quad (4.21)$$

where the matrices  $\underline{C}_a$  and  $\underline{K}_a$  can be understood as an aerodynamic viscous damping and an aeroelastic stiffness matrix, and are given, whenever small displacements and turbulence are assumed, according to expressions (4.14) and (4.15), as

$$\underline{C}_a = \frac{1}{2} \rho U B \begin{bmatrix} 2C_{Dt}(\beta) & C'_{Dt}(\beta) - C_{Lt}(\beta) & 0 \\ 2C_{Lt}(\beta) & C_{Dt}(\beta) + C'_{Lt}(\beta) & 0 \\ 2BC_{Mt}(\beta) & BC'_{Mt}(\beta) & 0 \end{bmatrix} \quad (4.22)$$

$$\underline{K}_a = \frac{1}{2} \rho U^2 B \begin{bmatrix} 0 & 0 & C'_{Dt}(\beta) \\ 0 & 0 & C'_{Lt}(\beta) \\ 0 & 0 & BC'_{Mt}(\beta) \end{bmatrix} \quad (4.23)$$

Replacing (4.19) and (4.21) in equations (4.16) yields

$$\underline{M}\ddot{\underline{q}}(t) + (\underline{C} + \underline{C}_a)\dot{\underline{q}}(t) + (\underline{K} + \underline{K}_a)\underline{q}(t) = \underline{F}_r(t) \quad (4.24)$$

Depending on the mean wind velocity and on the variation of shape coefficients, the matrices  $\underline{C}_a$  and  $\underline{K}_a$  can originate either a stable or an unstable behaviour, or even lead to a critical point of bifurcation of the response [20]. The action of wind gusts normally leads to stable systems. Instability is caused by the presence of negative terms in the aerodynamic damping matrix and can lead to galloping, for example. The presence of negative coefficients in the stiffness matrix can produce bifurcation. Given the significant stiffness of structural elements by comparison with aeroelastic stiffness coefficients, this condition is unlikely for civil engineering structures.

## 4.2 Buffeting

The action of wind gusts on a stay cable is characterised by the application of drag, lift and moment forces in the along-wind direction,  $f_{Du}(t)$ ,  $f_{Lu}(t)$  and  $m_u(t)$ , and in the across-wind direction,  $f_{Dv}(t)$ ,  $f_{Lv}(t)$  and  $m_v(t)$ , whose linearised form is given by expressions (4.9) and (4.10), respectively. These expressions show the proportionality of all force components to the mean wind speed  $U$  and to the fluctuations  $u(t)$  and  $v(t)$ , and hence to the intensity of turbulence.

As an elastic system, the amplitude of the cable response obtained by the solution of (4.16) increases with the growth of buffeting forces, and hence with the mean wind velocity. However, the growth of wind velocity leads also to an increase of the aerodynamic damping, as evidenced by the coefficients of the aerodynamic damping matrix  $\underline{C}_a$  (4.22). The importance of the aerodynamic damping can be analysed from a simplified modal analysis of a circular cable of diameter  $D$  under a smooth flow. For the  $k^{\text{th}}$  vibration mode, an aerodynamic damping coefficient  $\xi_{aer,kD}$  in the along-wind direction is approximated by

$$\xi_{aer,kD} = \frac{\rho U D C_D}{2 m \omega_k} \quad (4.25)$$

where  $m$  is the cable mass per unit length and  $\omega_k$  is the corresponding  $k^{\text{th}}$  order circular frequency. For the across-wind direction, the aerodynamic damping coefficient  $\xi_{aer,kL}$  is given by

$$\xi_{aer,kL} = \frac{\rho U D C_D}{4 m \omega_k} \quad (4.26)$$

The relation of 2:1 between the aerodynamic damping coefficients in the along-wind and across-wind direction may contribute to the fact that most vibration problems in cable-stayed bridges occur in the plane of the cables.

Practical values of  $\xi_{aer,kD}$  for two uniform wind velocities of 15 and 30 m/s have been obtained for three cables of the Vasco da Gama bridge in Portugal, including the shortest, an intermediate and the longest cables, whose characteristics are listed in *Table 4.1*. The average measured intrinsic damping of these coefficients is 0.13% [23], while the aerodynamic damping coefficient in the along-wind direction varies in the range 0.06–0.22% for a wind velocity of 15 m/s (*Table 4.1*).

The significant increase of damping at high wind velocities prevents, in most situations, the occurrence of important cable oscillations under buffeting loads.

Cable	$D$ (m)	$m$ (kg/m)	$L$ (m)	$T$ (kN)	$f_k$ (Hz)	$U = 15$ m/s	$U = 30$ m/s
						$\xi_{aer,1D}$ (%)	$\xi_{aer,1D}$ (%)
H01	0.160	42.9	34.7	2045	3.145	0.06	0.12
H15	0.200	74.8	147.5	4305.5	0.814	0.16	0.33
H24	0.250	100.1	226.0	6785.5	0.576	0.22	0.43

Table 4.1: Examples of aerodynamic damping coefficient for along-wind vibrations

## 4.3 Vortex-shedding

### 4.3.1 Fundamental characteristics

The description presented in the Section 4.1 of the effects generated by the presence of a circular cylinder in a uniform wind flow has shown that for a very low wind speed the flow detaches from the cylinder and a turbulent wake is generated, characterised by an alternate shedding of vortices at the top and bottom surfaces of the cable. These vortices induce approximately sinusoidal excitation components  $f_{Ds}(t)$ ,  $f_{Ls}(t)$  and  $m_s(t)$ , defined by expression (4.5). The actuation of the cylinder by these force components generates oscillations, which are normally characterised by very small amplitudes. However, if some cable frequency is close to frequency  $f_v$  of the shedding, as defined by expression (4.6), then a resonance effect takes place, which is known as *vortex resonance*. The increased oscillation leads the cylinder to interact strongly with the flow and control the vortex-shedding mechanism for a certain range of variation of the wind velocity; i.e. an increase of the flow velocity by a few percent will not change the shedding frequency, which coincides with the natural frequency of the cable. This aeroelastic phenomenon, illustrated in Fig. 4.9, is commonly known as *lock-in* or *synchronisation*, and produces additional across-wind loads, which are characterised by an inertial component proportional to the accelerations of the structure, and an aerodynamic damping component proportional to the velocity. In Civil Engineering applications, the inertial component associated with the ‘added mass of air’ is normally disregarded in view of its small value. The aerodynamic damping component is,

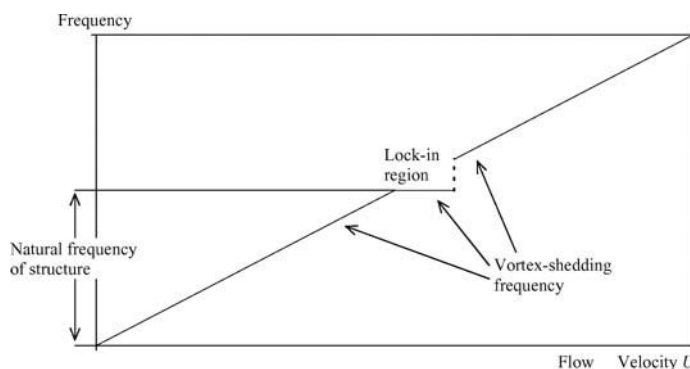


Fig. 4.9: Evolution of vortex-shedding frequency with wind velocity over elastic structure

however, of great importance, as negative aerodynamic damping coefficients produce reduced effective damping force, leading potentially to *vortex-induced* vibrations.

The *vortex-shedding* phenomenon described above is for a uniform wind flow. It is of interest to know how turbulence affects the occurrence of vibrations.

According to Dyrbye and Hansen [24], two turbulence conditions can enhance the risk of *vortex-induced* vibrations, one corresponding to locations where the air flow is smooth, and the other characterised by an increased small-scale turbulence. The first situation occurs typically for isolated structures located by the sea, for which the negative aerodynamic damping is increased. The latter condition occurs for structures located in the wake of slender nearby structures of similar size, which have increased lift coefficients. On the other hand, large-scale turbulence reduces the aerodynamic damping characterised by the logarithmic decrement  $\delta_a^T$ . This effect can be observed in Fig. 4.10, which illustrates the variation of the ratio  $\delta_a^T / \delta_a^S$  with the intensity of the turbulence,  $\delta_a^S$  being the logarithmic damping decrement in smooth flow.

The occurrence of violent *vortex-induced* vibrations depends on the intensity of large-scale turbulence, as well as on the intrinsic structural damping, which is characterised by the *Scruton number*  $S_c$ , a non-dimensional parameter defined by

$$S_c = \frac{2\delta m_e}{\rho D^2} \quad (4.27)$$

where  $\delta$  is the logarithmic decrement of the structural damping and  $m_e$  is an equivalent mass per unit length (for a uniform cylinder,  $m_e = m$ ).

High intensity large scale turbulence and/or high *Scruton numbers* reduce the risk of violent *vortex-induced* vibrations, as illustrated in Fig. 4.11. According to Dyrbye and Hansen [24], no risk of *lock-in* exists for  $S_c$  values greater than about 20. On the contrary, the risk of *lock-in* is very significant if  $S_c$  is less than 10.

Figure 4.12 illustrates the *Scruton number* values obtained by Yamada [25] for a set of cables from different types of cable-stayed bridges in Japan, assuming a logarithmic decrement of 0.01 as a representative value for oscillations in the first mode [26]. It should be noted that different definitions are employed in the literature for the *Scruton number*. Fig. 4.12 is based on the definition  $S_{c2} = \delta m_e / \rho D^2 = S_c / 2$ . According to this Figure, the  $S_c$  number is above

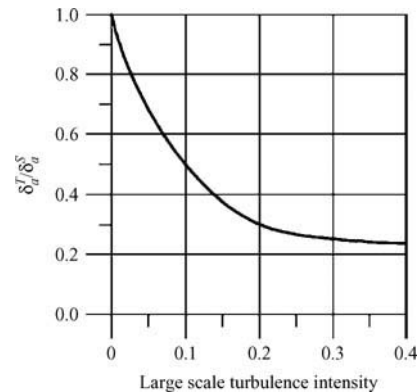


Fig. 4.10: Variation of the ratio  $\delta_a^T / \delta_a^S$  with the intensity of large scale turbulence [24]\*

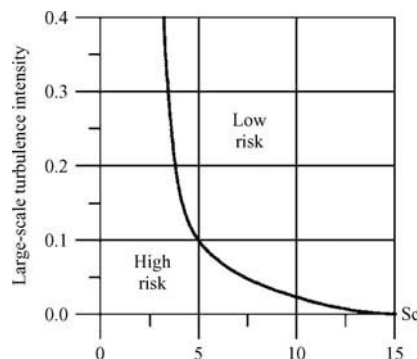


Fig. 4.11: The risk of *vortex-induced* vibrations of circular cylinders: variation with the intensity of large scale turbulence and  $S_c$  number [24]\*

\*Reproduced with permission.

Copyright 1997

20 for most of the cables and, consequently, vortex-induced vibrations of cables from cable-stayed bridges are not normally a matter of great concern. In effect, for the normal range of wind speed, *vortex-shedding* occurs at high frequencies, affecting essentially higher modes of the shortest bridge stays.

Consider as an example the stays of the Vasco da Gama bridge in Portugal, with diameters of 160–250 mm, lengths varying in the range 35–226 m, and associated first natural frequencies of 3–0.6 Hz, respectively. Assuming a constant *St* value of 0.2 and a wind velocity of 12 m/s (which could affect the deck response), the shedding frequency  $f_v$  for the shortest cable would be 15 Hz, according to equation (4.6), which is clearly distant from the natural frequencies of the first cables' modes and from the fundamental natural frequencies of the bridge, meaning that no coupling effects can be expected.

Equation (4.6), for the definition of the vortex-shedding frequency  $f_v$ , can also be used to predict the so-called critical velocity at lock-in,  $U_{cr}$ , assuming a constant *St* of 0.2

$$U_{cr} = 5 f_v D \quad (4.28)$$

So, for the shortest stay at the Vasco da Gama bridge, the critical velocity associated with the occurrence of *lock-in* in the first mode would be 2.4 m/s. This velocity is clearly too low to provide a significant energy input for the occurrence of cable oscillations.

Finally, it is still possible to estimate the amount of damping  $\xi$  required to avoid vortex-shedding vibrations, based on the practical rule of ensuring a  $S_c$  value greater than 20

$$\xi \approx \frac{\delta}{2\pi} \geq \frac{6 D^2}{\pi m} \quad (4.29)$$

The study by Tabatabai and Mehrabi [27] centred on a database formed by all the stays of 16 cable-stayed bridges has shown that a damping coefficient  $\xi$  of 0.7% would lead to Scruton numbers greater than 20 for 90% of the stay cables, and therefore also to stable cables. The application of (4.29) to the three cables of the Vasco da Gama bridge with characteristics described in *Table 4.1* leads to required damping coefficients of around 0.12%.

### 4.3.2 Amplitude of oscillations

With regard to the characterisation of the *vortex-shedding* phenomenon in terms of the definition of wind forces and evaluation of the response, no completely successful analytical method has been developed yet to represent the full range of response behaviour of a bluff body under the action of *vortex shedding*. Instead, several empirical analytical models have been developed to represent the *vortex-induced* response of bluff cylinders, whose parameters are obtained from experimental data [17]. These models are either governed by two differential equations, one to characterise the structure, and another for its wake, or by more limited

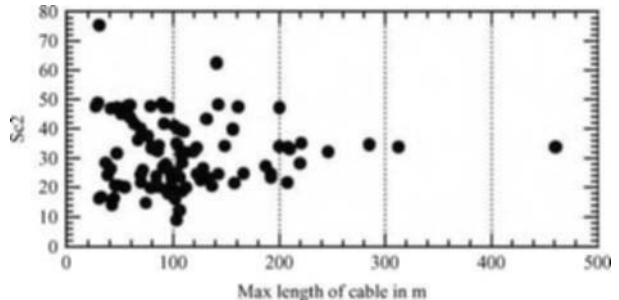


Fig. 4.12: Scruton number versus cable length for cable-stayed bridges in Japan [25]

single-degree-of-freedom models that predict the largest sustained response amplitude at *lock-in*. This is, for example, the case of the formula obtained by Griffin *et al.* [28], which gives the maximum relative amplitude of vibration  $y_0/D$  by

$$\frac{y_0}{D} = \frac{1.29}{[1 + 0.43(2\pi St^2 S_c)]^{3.35}} \quad (4.30)$$

Equation (4.30) is plotted in Fig. 4.13 for  $St$  equal to 0.2.

Considering the usual values found for the  $S_c$  numbers for cables of cable-stayed bridges (Fig. 4.12), it becomes evident that the amplitudes of vibration are generally very small. Davenport [29] states that the amplitude of *vortex-shedding* vibration rarely attains half the cable diameter.

In the case of the Vasco da Gama bridge, where the measured logarithmic decrement damping of the shortest stays is about 0.0085 (without damping devices) and the  $S_c$  number is 23.7, the maximum amplitude of vortex-induced vibration would be 0.0183  $D$  (see mark in Fig. 4.13), corresponding to a 0.003-m amplitude of oscillation. Although irrelevant for vortex-induced vibration, damping devices were installed in all stays, leading to a  $S_c$  number of 233 for the shortest stays.

A more complete model for the evaluation of the resonance amplitude at *lock-in*,  $y_0$  is the so-called *vortex resonance model*, on which the specifications of EC1 [30] are based. The *vortex resonance model* is specifically dedicated to flexible structures and has been thoroughly applied in the study of tall chimneys and stacks. This model considers in particular the fact that the vortex-shedding mechanism is not uniformly distributed along the structure; instead the cross correlation of the exciting force  $F_{y\sigma}$  decreases along the cylinder axis. Figure 4.14 represents the typical variation of the exciting force coefficient  $c_{y\sigma}$  ( $F_{y\sigma} = \frac{1}{2} \cdot c_{y\sigma} \cdot \rho \cdot U_{cr}^2 \cdot D$ ) along the cylinder for two different end conditions. The *vortex resonance model* considers a simplified distribution of vortex loading along the cylinder, which is characterised by a constant value  $c_{lat}$ , the maximum value of  $c_{y\sigma}(z)$ , and is distributed in a specific zone of the structure defined by a correlation length  $L'$  given as

$$L' = \frac{1}{c_{lat}} \int_0^h c_{y\sigma}(z) dz \quad (4.31)$$

where  $h$  represents the cylinder length and  $c_{lat}$  is obtained from measurements on model tests or from full-scale measurements.

According to Ruscheweyh [31], if the cylinder starts to vibrate in resonance with *vortex-shedding*, the correlation length  $L'$  increases with the increasing relative amplitude  $y_0/D$ . This effect can be observed in Fig. 4.15.

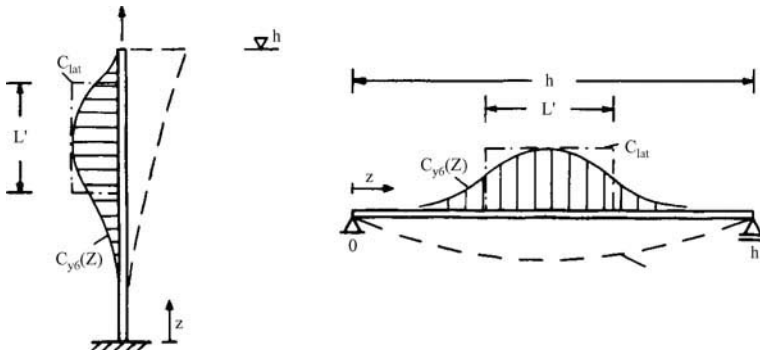


Fig. 4.14: Cross-correlation of vortex-exciting force along the cylinder axis [31]

$\frac{L_e}{D} = 6$	$\frac{y_0}{D} \leq 0.1$
$\frac{L_e}{D} = 4.8 + 12 \cdot \frac{y_0}{D}$	$0.1 \leq \frac{y_0}{D} \leq 0.6$
$\frac{L_e}{D} = 12$	$\frac{y_0}{D} \geq 0.6$

Table 4.2: Definition of an effective correlation length  $L_e$  [31]

In a simplified manner, Ruscheweyh approximated the curve of Fig. 4.15 by three linear branches (Fig. 4.16), defining an *effective correlation length*  $L_e > L'$  according to Table 4.2, also adopted by EC1.

On the other side, assuming a modal exciting force with sinusoidal character actuating along the length  $L_e$ , the maximum deflection amplitude can be obtained from the formula

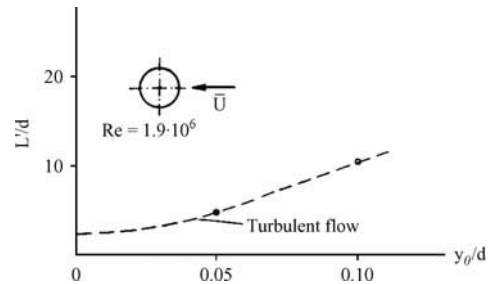
$$\frac{y_0}{D} = K_\phi K_w c_{lat} \frac{1}{S_c} \cdot \frac{1}{S^2} \quad (4.32)$$

in which  $K_\phi$  is a constant dependent on the mode shape and  $K_w$  is a correlation length factor, and are respectively defined by

$$K_\phi = \frac{\int_h |\phi(z)| dz}{4\pi \int_h \phi^2(z) dz} \quad (4.33)$$

and

$$K_w = \frac{\int_{L_e} |\phi(z)| dz}{\int_h |\phi(z)| dz} \leq 0.6 \quad (4.34)$$

Fig. 4.15: Increase of correlation length  $L'$  with increase of the relative amplitude of oscillation,  $y_0/D$  [31]

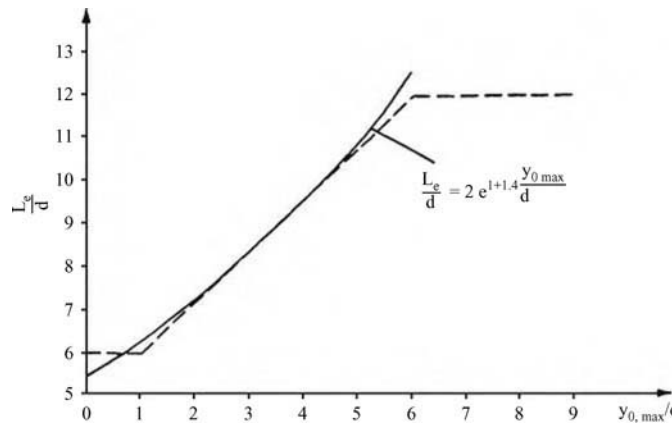


Fig. 4.16: Effective correlation length versus relative amplitude of oscillation,  $y_0/D$ . Approximation by three linear branches [31]

limited duration, which is not normally sufficient to overcome the transient phase of the response at vortex resonance, i.e. the maximum amplitude at resonance may not be attained. The correction to apply is defined in *EC1* according to *Table 4.3*, based on the difference between the mean wind velocity  $U_m$  at the centre of the effective correlation length, and the critical wind velocity  $U_{cr}$ , obtained by (4.28).

With regard to the definition of the base aerodynamic exciting force coefficient  $c_{lat,0}$  for circular cylinders, the following values are proposed by *EC1*

$$c_{lat,0} = \begin{cases} 0.7, & Re \leq 3 \times 10^5 \\ 0.2, & 5 \times 10^5 \leq Re \leq 4 \times 10^6 \\ 0.3, & Re \geq 10^7 \end{cases}$$

In each of the intervals  $3 \times 10^5 < Re < 5 \times 10^5$  and  $4 \times 10^6 < Re < 10^7$ , it is assumed that  $c_{lat,0}$  varies linearly with  $\ln(Re)$ . Figure 4.17 represents the variation of  $c_{lat,0}$  with the Reynolds number according to this proposal, as well as experimental values obtained by different authors.

$\frac{U_{cr}}{U_m} \leq 0.83$	$c_{lat} = c_{lat,0}$
$0.83 \leq \frac{U_{cr}}{U_m} \leq 1.25$	$c_{lat} = \left( 3 - 2.4 \cdot \frac{U_{cr}}{U_m} \right) \cdot c_{lat,0}$
$\frac{U_{cr}}{U_m} \geq 1.25$	$c_{lat} = 0$

Table 4.3: Aerodynamic exciting force coefficient  $c_{lat}$  versus  $U_{cr}/U_m$

The function  $\phi(z)$  in (4.33) and (4.34) represents the amplitude of the mode shape. For the particular case of a stay cable, the constant  $K_\phi$  associated with the first mode shape ( $\phi(z) = \sin(\pi z/h)$ ) is 0.101 and the constant  $K_w$  is given by

$$K_w = \cos \left[ \frac{\pi}{2} \left( 1 - \frac{L_e/D}{h/D} \right) \right] \quad (4.35)$$

As for the value of  $c_{lat}$ , a base value  $c_{lat,0}$  is obtained from measurements and a reduction correction is subsequently applied, considering that high wind speeds have a

A final comment concerning *vortex-shedding* is that the phenomenon, as described and modelled above, is essentially two-dimensional in nature. A new type of so-called *vortex-shedding* has been introduced more recently by Matsumoto *et al.* [32] in the course of wind tunnel investigations of rain-wind vibration. This complex, three-dimensional phenomenon that occurs for high wind velocities and is caused by the presence of an axial flow along the stay cable and enhanced by the presence of rain, will be described in the Section 4.6.

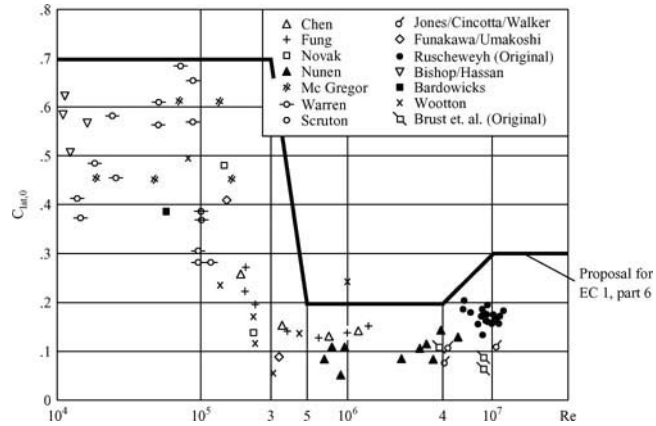


Fig. 4.17: Basic exciting force coefficient  $c_{lat,0}$  versus Reynolds number for circular cylinders [31]

## 4.4 Galloping

### 4.4.1 Fundamentals

*Galloping* is an instability phenomenon typical of slender structures with rectangular or “D” cross-sections, which is characterised, in a similar manner to *vortex-shedding*, by oscillations transverse to the wind direction, that occur at frequencies close to some natural frequency of the structure. The phenomenon is however quite different from *vortex-induced* vibration. In effect, while the latter produces small amplitudes of oscillation in restricted ranges of wind velocity, *galloping* occurs for all wind speeds above a critical value and produces high amplitude vibrations, which may be ten times or even more the typical body dimension. In the case of ice-coated power line cables, where the phenomenon was first reported, the amplitude of vibration can be one hundred times this length [22].

Consider a section of a prismatic body in a smooth oncoming flow (Fig. 4.18).

Assuming that the body is fixed and that the angle of attack of the flow velocity  $U_r$  is  $\beta$ , drag and lift forces  $F_D(\beta)$  and  $F_L(\beta)$  develop along and across the wind direction, respectively, with mean values defined by expressions (4.4a) and (4.4b).

The projection of these two force components on the direction  $y$  is then

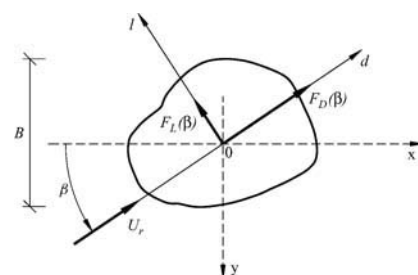


Fig. 4.18: Lift and drag forces on a fixed bluff object

$$F_y(\beta) = -F_D(\beta) \sin \beta - F_L(\beta) \cos \beta \quad (4.36)$$

Introducing (4.4a) and (4.4b) into (4.36), the following relation is obtained

$$F_y(\beta) = \frac{1}{2} \rho U^2 B C_y(\beta) \quad (4.37)$$

where

$$U = U_r \cos \beta \quad (4.38)$$

and the force coefficient along the vertical direction  $C_y(\beta)$  is

$$C_y(\beta) = -[C_L(\beta) + C_D(\beta) \tan \beta] \sec \beta \quad (4.39)$$

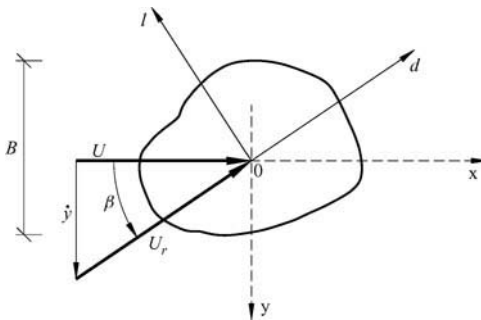


Fig. 4.19: Effective angle of attack on an oscillating bluff body

In a second situation, assume that the bluff body is vibrating in the across wind direction  $y$  in a flow with velocity  $U$  (Fig. 4.19).

The relative velocity of the flow with respect to the moving body is now obtained from the vector difference represented in Fig. 4.19, whose amplitude is

$$U_r = \sqrt{U^2 + \dot{y}^2} \quad (4.40)$$

The dynamic equation of the motion of the bluff body in the  $y$  direction is then

$$m \ddot{y} + 2\xi m\omega \dot{y} + m\omega^2 y = F_y(\beta) \quad (4.42)$$

where  $m$  is the mass of the body per unit length,  $\xi$  is the damping ratio,  $\omega$  is the natural frequency of the body and  $F_y(\beta)$  is given by (4.37).

In the case of small motions, the angle of attack can be neglected, i.e.

$$\beta \approx \frac{\dot{y}}{U} \approx 0 \quad (4.43)$$

So, an expansion of  $F_y(\beta)$  about  $\beta = 0$  followed by a linearisation leads to

$$F_y(\beta) \approx \left. \frac{dF_y}{d\beta} \right|_{\beta=0} \cdot \beta \quad (4.44)$$

Considering that

$$\frac{dF_y}{d\beta} = \frac{1}{2} \rho U^2 B \frac{dC_y}{d\beta} \quad (4.45)$$

and the derivative of the force coefficient  $C_y$  with respect to the angle of attack  $\beta$  is

$$\left. \frac{dC_y}{d\beta} \right|_{\beta=0} = - \left( \frac{dC_L}{d\beta} + C_D \right)_{\beta=0} \quad (4.46)$$

equation (4.42) can be transformed into

$$m \ddot{y} + 2\xi m\omega \dot{y} + m\omega^2 y = - \frac{1}{2} \rho U^2 B \left( \frac{dC_L}{d\beta} + C_D \right)_{\beta=0} \cdot \frac{\dot{y}}{U} \quad (4.47)$$

Equation (4.47) shows that the aerodynamic force on the bluff body is a damping force. This force modifies the overall system damping to a net value  $d$  of

$$d = 2m\omega\xi + \frac{1}{2} \rho U B \left( \frac{dC_L}{d\beta} + C_D \right)_{\beta=0} \quad (4.48)$$

The stability of the vibrating cable is guaranteed provided that the viscous damping  $d$  is positive. Given the fact that the mechanical damping is always positive, a necessary condition for instability is then

$$\left( \frac{dC_L}{d\beta} + C_D \right)_{\beta=0} < 0 \quad (4.49)$$

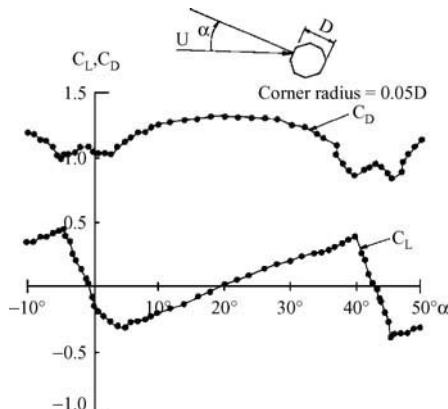


Fig. 4.20: Force coefficients on an octagonal cylinder [17]\*

\*Reproduced with permission. Copyright 1996

This is the so-called *Glauert-Den Hartog* criterion for *incipient galloping instability* [17]. An example of instability, observed on the stay cables of a cable-stayed bridge, is a bridge whose stays have an octagonal cross-section. Figure 4.20 shows the variation of the drag and lift coefficients with the angle of attack, reflecting the regions of wind approach angle  $-5^\circ < \alpha < 5^\circ$  to the faces of the octagonal section that are susceptible to instability.

The analysis of expression (4.49) shows clearly that circular cross-sections are never subjected to instability by *galloping*, as the derivative  $dC_L/d\beta$  is always null in view of the symmetry. So, except for the cases where the external shape has been altered, either by the presence of ice or of water rivulet (see Section 4.6), instability of the cables by *galloping* should not be expected in cable-stayed bridges employing

circular cross sections for these elements. The studies of Matsumoto *et al.* [32] and Saito *et al.* [33] have however shown that galloping can occur for inclined circular cables. The reason presented is the appearance of an axial flow behind the cable for certain yawing angles, which favours instability. The axial flow was identified from wind tunnel tests, and is seen in the light flag presented in Fig. 4.21. According to

*Fig. 4.22*, the axial flow velocity  $U_a$  increases with oncoming velocity  $U$  and with the yawing angle  $\beta$  of the cable. Galloping instability occurs when the axial flow velocity reaches more than 30% of the approaching velocity, for yawing angles greater than  $25^\circ$ , a situation in which the lift coefficient *versus* angle of attack representation attains a negative slope. It is shown in *Fig. 4.22* that turbulence has a stabilising effect for galloping.

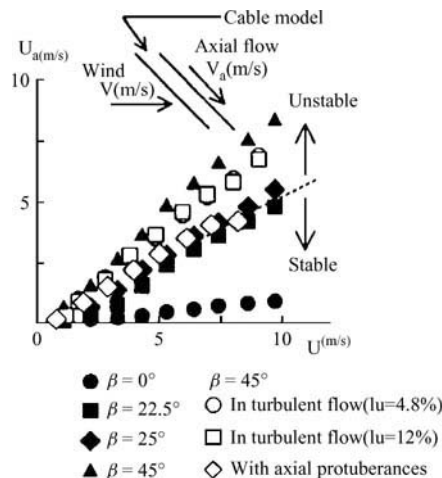


Fig. 4.21: Visualisation of axial flow by light flags [37]



Fig. 4.22: Intensity of axial flow for yawed cables [37]

In recent studies [34–36] this instability phenomenon of circular inclined cables has been identified in the laboratory, and described as *dry inclined cable galloping*.

#### 4.4.2 Prediction and control measures

On the basis of experimental testing, some researchers have developed formulae for the evaluation of onset wind velocity of divergent oscillation, as a function of the Scruton number. Honda *et al.* [38] proposed the following formula for the critical reduced velocity  $\overline{U}_{cr}$

$$\overline{U}_{cr} = \frac{U_{cr}}{fD} = 10 \cdot S_c^{\frac{2}{3}} \quad (4.50)$$

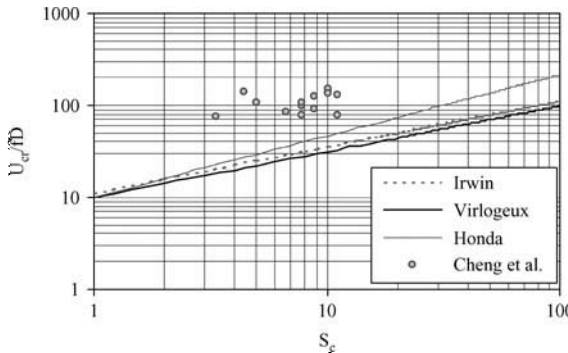


Fig. 4.23: Critical reduced wind velocity versus  $S_c$

estimates have been obtained. Figure 4.23 represents the variation of the critical wind reduced velocity with  $S_c$  according to the three formulae referred to above. Experimental values of the onset reduced wind velocity for the occurrence of instability obtained by Cheng *et al.* [34] in laboratory tests are also represented in this figure.

The most relevant aspect of Fig. 4.23 is the possibility of defining the minimum damping necessary to avoid galloping phenomena. Other strategies for avoiding galloping are based on the modification of the cross section. Figure 4.24(a) shows a stranded configuration composed by a bundle of individual strands wrapped with a spiral strand developed by Kubo *et al.* [41], while Fig. 4.24(b) shows helical plates covering the smooth surface of the cable as studied by Matsumoto *et al.* [42]. In both cases the axial flow in the wake of the cable is disturbed by the presence of an obstacle, which could be the strand or the plates.

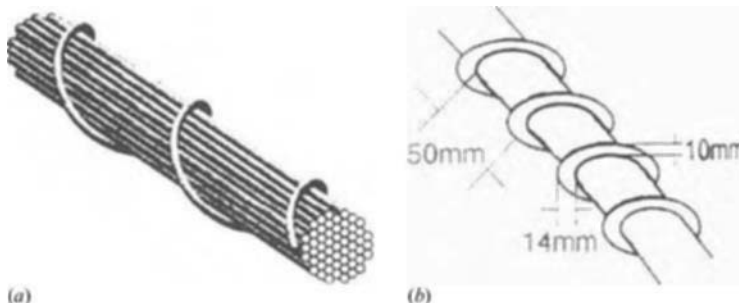


Fig. 4.24: Aerodynamic control measures against galloping: (a) Bundle of strands wrapped by spiral strand [41]; (b) Helical plates covering cable surface [42]

## 4.5 Wake Effects

*Wake effects* is the term used for all the vibration phenomena of stays that lie in the wake of other stays or structural elements, or of some construction equipment. The perturbing element affects the wind flow, creating local turbulent conditions that produce oscillations of the cable.

These oscillations may be associated with *resonant buffeting*, *vortex resonance*, *galloping* or other specific phenomena that will be described subsequently, defined as *interference effects*, which occur more easily in locations of low turbulence. In general, wake oscillations cannot be easily anticipated in the design phase, the most effective counter-measure being the addition of damping in the cable in order to balance any negative aerodynamic damping. The most common situations that produce cable vibrations due to *wake effects* are described below.

#### 4.5.1 Resonant buffeting

This phenomenon was described by Davenport [29] and can occur for bridges with two parallel planes of cables. Accordingly, the wind gusts strike the up-wind and down-wind planes of cables with a time delay of  $B/U$ ,  $B$  being the distance between the two planes of cables and  $U$  the mean wind velocity (Fig. 4.25). If this delay coincides with half the period  $T_t$  associated with the torsional deck mode, then resonant effects can be attained. The critical velocity  $U_{cr}$  for resonant buffeting is then defined by

$$U_{cr} = \frac{2B}{T_t} \quad (4.52)$$

The application of this formula to the Vasco da Gama bridge, whose first torsional period is 2.3 s and where the distance between cable planes is around 30 m, leads to a critical wind velocity of 26 m/s. But no particular vibration problems have been reported or were expected for this bridge, given that for this wind speed the aerodynamic damping of the torsional mode is positive, thereby helping to stabilise the bridge.

#### 4.5.2 Vortex resonance

This phenomenon occurs typically in cable-stayed bridges with two planes of cables, when subjected to oblique winds. In that case, the wind flow is modified in the wake of the pylons (Fig. 4.26), and vortices shed at a frequency defined by expression (4.6). Resonant effects may occur for the cables behind the pylon that have a natural frequency  $f_k$  close to the shedding frequency. The critical wind velocity  $U_{cr}$  for the occurrence of vortex resonance of a cable of frequency  $f_k$  in the wake of a pylon can therefore be evaluated from

$$U_{cr} = \frac{Hf_k}{St} \quad (4.53)$$

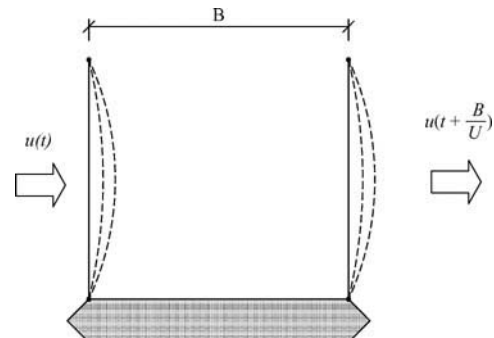


Fig. 4.25: Action of gusts on the two planes of stays

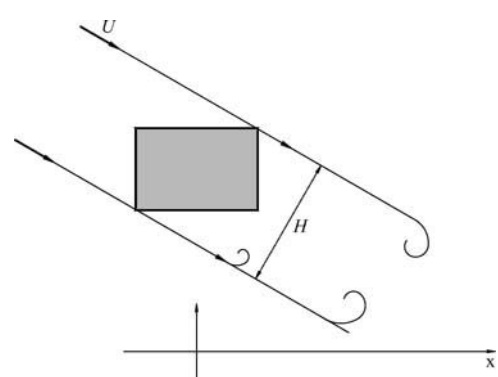


Fig. 4.26: Vortex shedding in the wake of a bridge pylon

where  $H$  is the projection of the pylon in the direction transversal to the wind and  $St$  is the Strouhal number of the pylon cross section.

According to Virlogeux [19], vortex resonance was reported in the Evripos bridge in Greece, and may have also occurred at the Normandy bridge in France, during construction, for some of the shortest cables behind a tower leg.

#### 4.5.3 Interference effects

In order to restrain the size of the cables, multiple parallel stay cables have been used in several cable-stayed bridges, particularly in Japan. These multiple cables are distant from each other by a few diameters only and are anchored at the same level in the tower and deck. *Figure 4.27* shows the twin stay cables employed in the Oresund bridge, linking Denmark and Sweden. *Figure 4.28* shows possible arrangements of cables.



*Fig. 4.27: Multiple parallel stay cables at Oresund bridge [43]*

It has been observed that, under particular conditions, the cable assembly may undergo vibrations. These oscillations are due to *vortex resonance*, to *galloping* of the cable assembly, or to so-called *interference* or *wake galloping*. The latter phenomenon is no more than a *galloping* that occurs on the downstream cable(s) induced by the turbulent wake of the upstream cable(s). The oscillation of the downstream cable(s) may induce also a perturbation of the flow around the upstream cable(s), generating oscillation of these cables, designated as *interference galloping*.

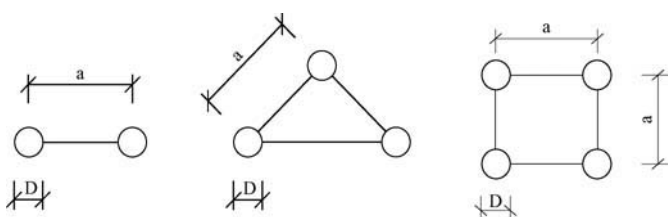


*Fig. 4.28: Possible arrangements of grouped stay cables*

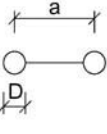
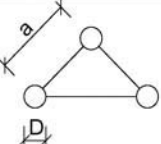
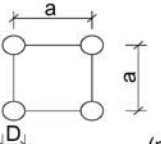
Type of association	$K_{iv}$	
	$a = D$	$a \geq 2D$
	$K_{iv} = 1.5$	$K_{iv} = 1.5$
	$K_{iv} = 4.8$	$K_{iv} = 3.0$
	$K_{iv} = 4.8$	$K_{iv} = 3.0$

Table 4.4: Interference factor  $K_{iv}$  for vortex shedding of grouped cables (EC1)

The EC1 proposes some conservative formulae for the evaluation of instability by *wake effects*. Assuming that braces or stringers connecting the twin or triple cables at certain locations along the cables establish a certain degree of coupling of the assembly, the following formulae apply to the arrangements shown in Fig. 4.28.

#### 4.5.3.1 Vortex resonance effects

The amplitude of oscillation at *vortex resonance* of the cable assembly is calculated using the vortex resonance model of a single cable, based on the procedure described in the Section 4.3.2, provided that  $1.0 \leq a/D \leq 3.0$ . However, an increased exciting force coefficient  $c_{lat(c)}$  is used, given as

$$c_{lat(c)} = K_{iv} \cdot c_{lat}, \quad 1.0 \leq a/D \leq 3.0 \quad (4.54)$$

where  $c_{lat}$  is the force coefficient defined in Table 4.3 and  $K_{iv}$  is the interference factor for vortex shedding, with values presented in Table 4.4 for the arrangements shown in Fig. 4.28.

#### 4.5.3.2 Galloping

The onset wind velocity of *galloping* of the cable assembly  $U_{cG}$  is defined as a function of the cable frequency  $f_k$ , as

$$U_{cG} = \frac{2 S_{c(c)}}{a_G} \cdot f_k \cdot D \quad (4.55)$$

where  $a_G$  is an interference factor for galloping, whose values are given in Table 4.5, and where  $S_{c(c)}$  represents the Scruton number of the assembly, defined as

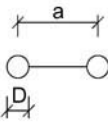
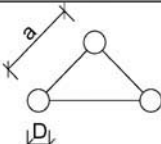
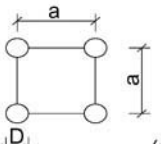
Type of association	$a_G$	
	$a \leq 1.5 D$	$a \geq 2.5 D$
 (n=2)	$a_G = 1.5$	$a_G = 3$
 (n=3)	$a_G = 6$	$a_G = 3$
 (n=4)	$a_G = 1$	$a_G = 2$

Table 4.5: Constant  $a_G$  for the estimation of the critical velocity of galloping in associations of cables (EC1)

$$S_{c(c)} = \frac{2 \delta \sum_{i=1}^n m_i}{\rho D^2} \quad (4.56)$$

In this expression  $m_i$  represents the distributed mass of cable  $i$  of the assembly of  $n$  cables. The critical galloping velocity should satisfy the relation

$$U_{cG} > 1.25 U \quad (4.57)$$

where  $U$  is the mean wind velocity calculated at the point of maximum amplitude of oscillation.

#### 4.5.3.3 Interference galloping of free cables

*Interference galloping* may occur when two or more cables are arranged close together without being connected to each other. The EC1 proposes the estimation of the critical wind velocity  $U_{cIG}$  by the following formula

$$U_{cIG} = 3.5 \cdot f_k \cdot D \cdot \sqrt{\frac{\frac{a}{D} \cdot S_c}{a_{IG}}} \quad (4.58)$$

where  $a_{IG}$  is a combined stability parameter with a value of 3.0, if not otherwise specified and  $S_c$  is defined by expression (4.27). This formula is valid if  $a/D < 3$  and the angle of wind attack is in the range of the critical wind direction  $\beta_k$ , as defined in Fig. 4.29. As in the previous case of instability of the cable assembly by *galloping*, the critical velocity should satisfy a relation of the type of (4.57).

Referring to practical cases of occurrence of *interference galloping*, Matsumoto *et al.* [44], Miyata [45] and Tanaka [35] have defined the main aspects of the phenomenon: it generally produces elliptical vibrations in the first mode of less than  $3 D$ , it occurs when the wind direction is about  $0^\circ$  to  $45^\circ$  from the transverse direction of the bridge axis, and it is conditioned by the spacing between the cables. Accordingly, instability can be found for close spacings [ $D \leq x \leq 4D$  and  $-2D \leq y \leq 2D$  (Fig. 4.30)], or for widely spaced cables. For the first case, it starts at a critical reduced wind velocity  $(U/fD)_{cr}$  of around 40, that corresponds to mean wind velocities  $U_{cr}$  of 5–20 m/s. By increasing the cable spacings, interference effects diminish, until another range of instability is reached, for  $8D \leq y \leq 20D$ , where the interference effects occur only for the downstream cable. This range of instability is not however of interest for stays of cable-stayed bridges. The phenomenon of *interference galloping* was observed in several cable-stayed bridges in Japan, such as the Hitsuishijima, Iwakurojima, Yobuko and Shima Maruyama bridges [46]. For the particular case of the Yobuko bridge, amplitudes of oscillation of  $2.5 D$  were reported. Figures 4.31 and 4.32 summarise amplitudes and ranges of cable spacing associated with interference galloping, based on field observations and wind tunnel tests, respectively.

$$D \leq x \leq 4D - 2D \leq y \leq 2D$$

Kubo *et al.* [47] and Kubo [48] proposed the following measures to prevent interference effects: adopt a close spacing between cables in the range 1.2–1.3  $D$ , which show no galloping at reduced wind velocity  $\bar{U} = U/fD$  of 200 (an increase of that spacing to more than  $5 D$  would produce equivalent effects, although not so convenient for practical reasons); connect parallel cables by spacers or stringers at lengths defined by a deflection of the connecting points no greater than  $0.2 D$ . Another alternative has been suggested by Yoshimura *et al.* [49, 50], consisting in the use of a pair or three cables stranded helically.

#### 4.5.3.4 Interference effects in stranded cables

The composition of stay cables by bundles of individually protected strands clamped

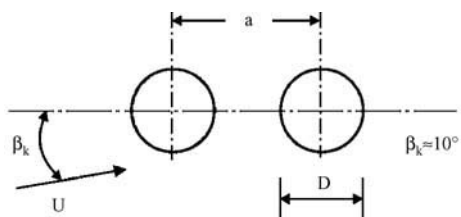


Fig. 4.29: Critical wind direction range for interference galloping

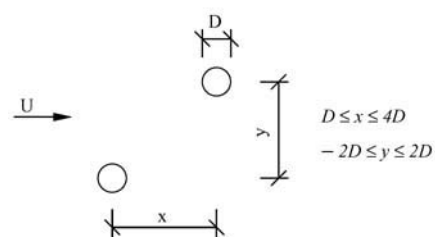


Fig. 4.30: Critical cable spacings for interference galloping

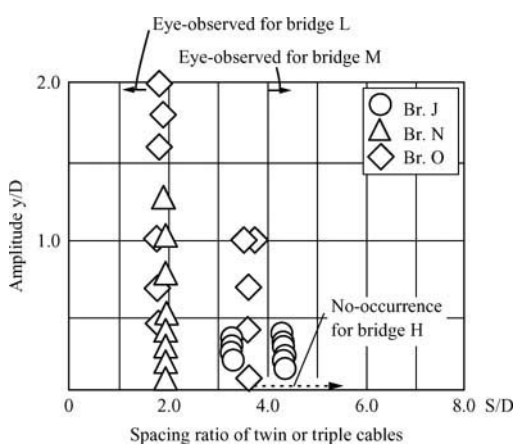


Fig. 4.31: Amplitude versus spacing of twin or triple cables associated with instability by wake galloping: observations on prototypes [44]

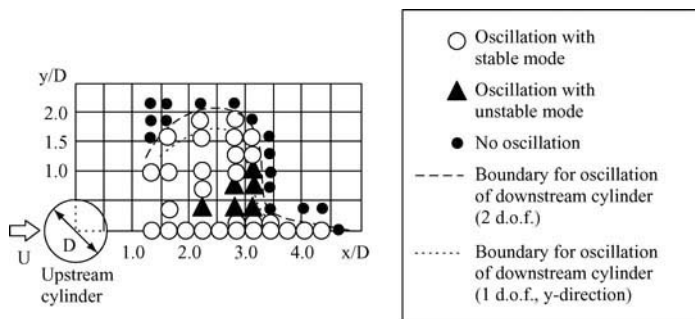


Fig. 4.32: Amplitude versus spacing of twin circular cylinders associated with instability by wake galloping: results from wind tunnel tests [44]

with collars at distances of 30 to 50 m corresponds to a technology introduced in 1988, for the purpose of improving the protection against corrosion and ensuring the tension and replacement of strands. Although newly constructed bridges normally encase the strands in HDPE pipes, many bridges constructed in the late 1980s and early 1990s employ the technology described first and suffer from diverse vibration problems. The most frequent vibrations are associated with interference phenomena similar in type to those previously described, and occur due to the aerodynamic interaction between strands, which knock against each other, generating global vibration of the cable and producing a loud and disagreeable rattling noise. Virlogeux [19] defines these movements as *breathing of strands*. Apparently the vibrations are started by wind and attain significant amplitudes of around 1–2  $D$ . This *breathing* of the cables produces damage of the bracings and so it may be necessary to encase the bundles in pipes. There is however the risk of ‘slapping’ of the pipes against the bundles, as the latter are not normally packed inside the former. This problem has been reported at the Glebe Island bridge in Australia [18].

## 4.6 Rain-wind Induced Vibrations

### 4.6.1 Identification of the phenomenon

Although *rain-wind induced vibration* of power lines, designated as *rain vibration*, had been reported in the literature 10 years earlier [51, 52], it was only in 1986 that Hikami identified the phenomenon of cable vibration in cable-stayed bridges, induced by the combined action of wind and rain, during the construction of the Meiko-Nishi bridge [53, 54]. The general characteristics identified by these authors were soon associated with several past and many subsequent occurrences of vibrations in cable-stayed bridges. It is presently considered that rain-wind induced oscillations cause about 95% of the reported vibration problems in cable-stayed bridges [55].

Despite the intense research developed both through wind tunnel tests and through observation of prototypes, the mechanisms of rain-wind induced vibrations are yet to be fully understood. Some main aspects of this complex phenomenon can however be outlined [35]: first, it is under the combined action of rain and wind, at specific angles of attack and intensity of rainfall, that rivulets form at the upper and lower surfaces of the cable (Fig. 4.33). The formation of these rivulets as the result of the balance of gravitational, aerodynamic and surface capillarity

forces, leads to a loss of symmetry of the cable cross-section, and therefore to a variation of aerodynamic forces on the cable. Eventually a decrease in the drag coefficient and a negative slope of the lift coefficient associated with a small variation of the angle of attack may lead to a negative aerodynamic damping, resulting in a galloping instability of the Den Hartog type (see Section 4.4.1). Once the cable starts oscillating, the rivulets tend to oscillate circumferentially with the same frequency. A coupling of this oscillation with the flexural oscillation of the cable may lead to aerodynamic instability, which is likely to intensify the vibrations.

Considering these aspects, it is necessary to understand the conditions for the formation of the rivulets and for the occurrence of instability. It is also the objective of the designer to predict the occurrence of rain-wind vibrations and employ adequate counter-measures. The following Sections describe the main findings and the existent models for predicting instability and estimating the amplitude of oscillation.

#### 4.6.2 Experimental observations

The events that prompted the research in *rain-wind vibration* were the strong vibrations exhibited by several cables of the Meiko-Nishi bridge during construction, under the combined action of rain and wind, at a relatively low wind velocity of 14 m/s. According to Hikami [53], peak to peak amplitudes of 0.55 m were observed under rainfall, which could not be classified as *vortex-induced oscillations*, or *wake galloping*. A five month observation program of the bridge prototype was then developed in which all the 24 cables of one cable plane connected to one of the towers were instrumented (Fig. 4.34), allowing the measurement of transverse oscillations in the vertical plane. Wind speed and direction were also measured simultaneously and damping factors were identified from the set of observations. The following observations were made:

- The logarithmic decrement of the cables varied between 0.007 and 0.028, depending on the vibration mode, cable length (65–200 m) and position.
- The occurrence of cable vibration was always accompanied by rain. This can be observed in Fig. 4.35, which represents the variation in wind speed, direction and maximum amplitude of vibration in a 10-h record for three of the vibrating cables.
- The occurrence of cable vibration was limited to the cables that geometrically declined in the direction of the wind.

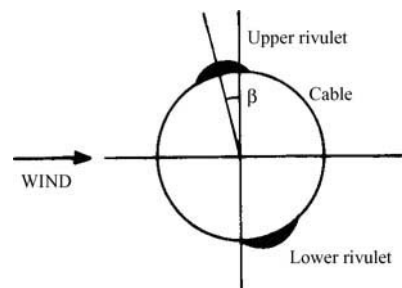


Fig. 4.33: Formation of water rivulet at upper and lower surface of cable under rain and wind

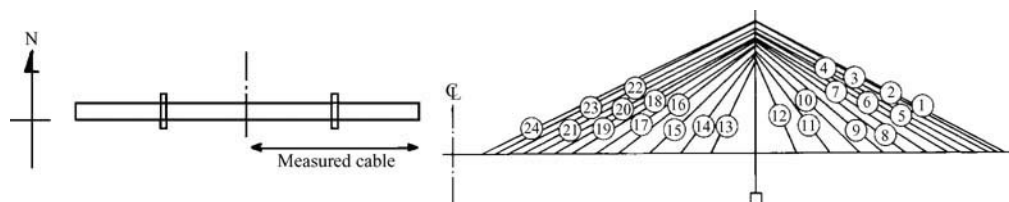


Fig. 4.34: Instrumentation of cables at the Meiko-Nishi bridge [54]

- All the observed cable motions occurred in the vertical plane for wind speeds in the range 5–15 m/s. These vibrations were composed mostly of a single mode, although some associations of two modes were found, always characterised by natural frequencies in the range of 1–3 Hz.
- During vibration of a cable, a water rivulet was formed at the lower cable surface, which oscillated circumferentially.

Additional wind tunnel tests under similar rain conditions were performed by Hikami and Shiraishi [54], to understand the generating mechanism of *rain-wind induced vibration* better, investigating in particular, the formation and role of the water rivulet along the cable. The tests were performed on a 2.6-m segment of a prototype polyethylene pipe which was mounted at an inclination angle  $\alpha$  to the horizontal plane of  $45^\circ$  and an angle to the wind direction  $\beta$  of  $\pm 45^\circ$ , according to the scheme presented in Fig. 4.36, so as to reproduce the prototype motion as much as possible. The rain condition was achieved by spraying water.

In addition to the confirmation of the set of observations previously reported from full scale measurements on the bridge, the wind tunnel tests showed the formation of another water rivulet along the upper windward surface of the cable at an angle  $\beta$  of  $45^\circ$ , that is, for a cable geometrically declining in the wind

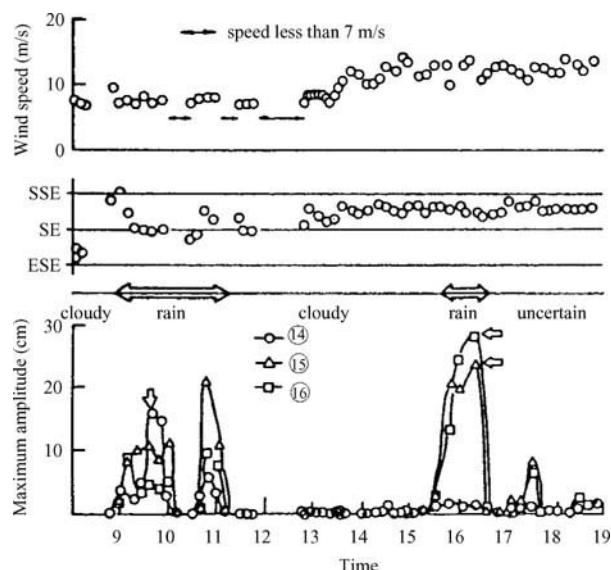


Fig. 4.35: Ten hour record of vibration amplitudes and weather conditions at the Meiko Nishi bridge [54]



Fig. 4.36: Example of the wind tunnel test of a stay cable [56]. Scheme of setup

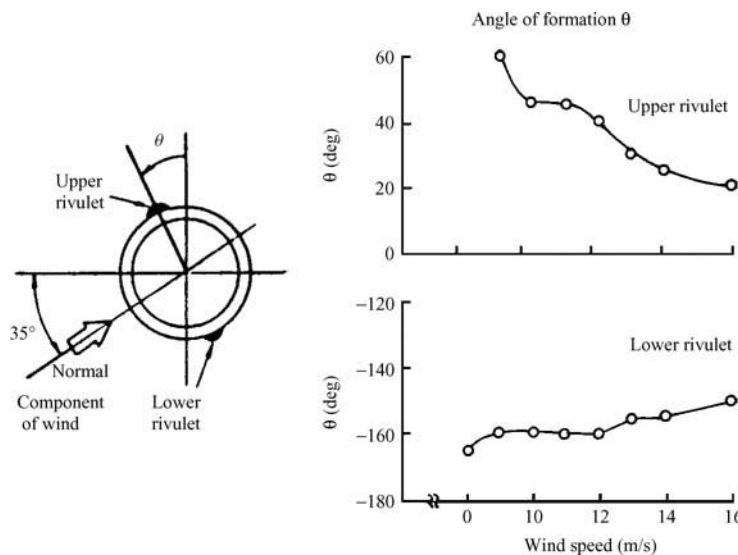


Fig. 4.37: Variation of the angle of formation of the water rivulet with wind speed for  $\alpha = 45^\circ$ ,  $\beta = 45^\circ$  [54]

direction. In effect, for a small wind velocity, a raindrop falling on the windward surface of the cable slides down the surface. For a wind velocity greater than a certain value (9 m/s in this case), a drag force of flow acting on the raindrop overcomes the gravity and friction forces, so that the raindrop climbs up the surface and becomes part of the rivulet. As the wind velocity increases, the angle  $\theta$  of formation of the upper rivulet represented in Fig. 4.37 decreases, i.e. the rivulet moves up. Moreover, when the cable vibrates, both the upper and lower rivulets oscillate circumferentially at the same frequency of the cable oscillation. A maximum angular oscillation of about  $20^\circ$  has been measured for the upper rivulet, according to the representation of Fig. 4.38. It can also be observed from this figure that the increase in the wind velocity produces a gradual shift of the bottom boundary of the rivulet. When this shift reached up to  $40^\circ$ , at a wind velocity of 14 m/s, the rivulet was disorganized and the vibration ceased.

By measuring the drag force associated with the upper and lower rivulet formed separately at different wind speeds (Fig. 4.39), Hikami and Shiraishi showed that the lower rivulet has a stabilising role, as its formation produces aerodynamic forces in opposition to the cable motion, i.e. damping forces. On the contrary, the upper rivulet generates exciting forces and is responsible for the unstable behaviour of the cable. Hikami and Shiraishi explained this type of behaviour based on the analogy to the phenomenon of instability of an iced overhead conductor as ‘torsional’ galloping.

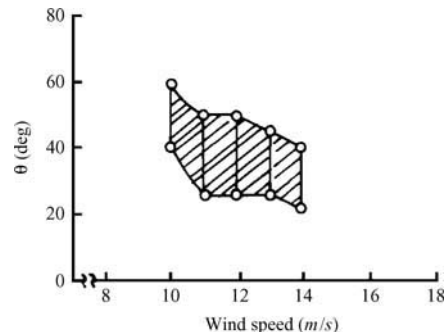


Fig. 4.38: Variation of the upper rivulet circumferential oscillation region with wind speed [54]

Although the observations from Hikami and Shiraishi [54] were essential to clarify the role of the circumferential oscillation of the rivulets at the cable frequencies, subsequent studies have led to the identification of slightly different mechanisms of oscillation. Verwiebe [57] in particular observed that, contrary to what was expected, almost vertical cables or bars could suffer from rain-wind induced vibrations. He identified three different mechanisms of rain-wind excitation. The first mechanism occurs when the wind is in the direction of the cable ( $\beta = 90^\circ$ ). The wind speed must be great enough to separate the windward rivulet into two symmetric rivulets in the lateral areas of the cable, as represented in Fig. 4.40. The oscillation of these rivulets with the oscillation of the cable promotes a rhythmic change of aerodynamic forces on the cable, thereby intensifying the oscillations, which are maximum when the angle  $\alpha$  of the cable to the horizontal is around  $30^\circ$ , for a wind velocity of  $25 \text{ m/s}$ .

The second and third mechanisms of rain-wind oscillation occur during predominant cross-wind vibration, if the lateral wind force coefficient changes harmonically at the natural frequency of the cable. This change can be caused by the oscillation of one or both rivulets. The mechanism represented in Fig. 4.41 occurs for cables that have the direction of the wind ( $\beta = 90^\circ$ ), whose cross-wind vibration stimulates the anti-symmetrical oscillation of the two rivulets. For an angle  $\alpha$  of the cable to the horizontal of  $30^\circ$  the required wind velocity for instability is  $18 \text{ m/s}$ .

The mechanism of oscillation illustrated in Fig. 4.42 occurs when cables are inclined orthogonally to the wind direction ( $\beta = 0^\circ$ ), or for yaw angles  $\beta$  of  $-45^\circ \dots +45^\circ$ , implying the oscillation of only the underside rivulet, for smaller wind velocities (e.g.  $\beta = 0^\circ$ ;  $\alpha = 30^\circ$ ;  $U = 19 \text{ m/s}$ ), or the oscillation of upper and underside rivulets, for higher wind velocities. As it is essentially the lift coefficient that changes with vibration when only one rivulet oscillates, the motion of the cable can be described as elliptical, with a slight inclination to the cable plane of around  $10^\circ\text{--}40^\circ$ , a fact that is consistent with the observation at the Farø bridges (Fig. 4.43). On

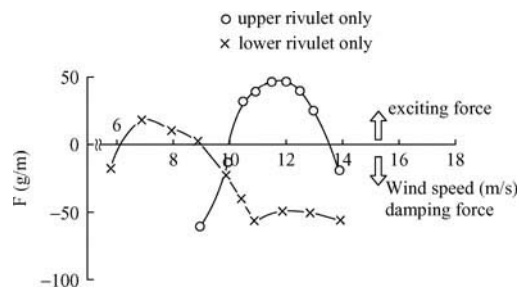


Fig. 4.39: Unsteady aerodynamic force with rivulet formed separately [54]

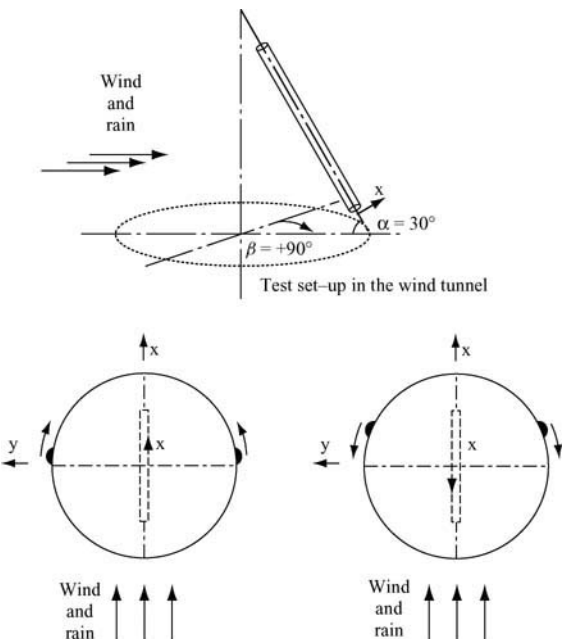


Fig. 4.40: Rain-wind exciting mechanism for along-wind vibrations [57]

the contrary, for higher wind velocities, the motion of the two rivulets leads to a continuously changing elliptic motion.

### 4.6.3 Analytical and design models

Although the growth mechanism of oscillations motivated by rain and wind is clearly restricted to a wind velocity range in such a way that a too small wind velocity may not be sufficient to induce oscillation of the rivulets, or a too high velocity may disrupt their formation, it seems that the characteristics of the vibrations are close to the phenomenon of galloping. In fact, rain-wind vibrations are generally vibrations of high amplitudes almost independent of frequency, and their occurrence seems to be triggered by the oscillation of rivulets. Also it is understood that the phenomenon occurs for very slightly damped cables.

Owing to the complexity of the phenomenon, few models have been developed for the simulation of rain-wind excitation. The simple model of Yamaguchi [59] presented here helps understand the mechanism of instability. A more complex model recently developed by Peil and Nahrath [60] is also described, which provides an interesting qualitative interpretation of stability. Finally a more simplified model by Geurts and van Staalduin [61] is presented, which may be used for an estimation of the damping necessary to avoid vibrations.

#### 4.6.3.1 Analytical model from Yamaguchi

Considering that the upper rivulet is the origin of rain vibration, Yamaguchi based his studies on the analytical model described in Fig. 4.44, formed by a cable cross section with diameter  $D$ , and an upper cylinder simulating the

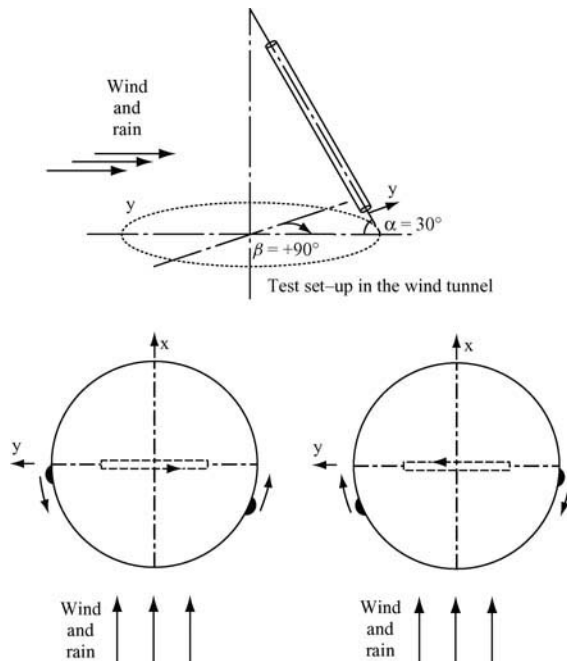


Fig. 4.41: Rain-wind exciting mechanism for across-wind vibrations involving oscillation of two rivulets [57]

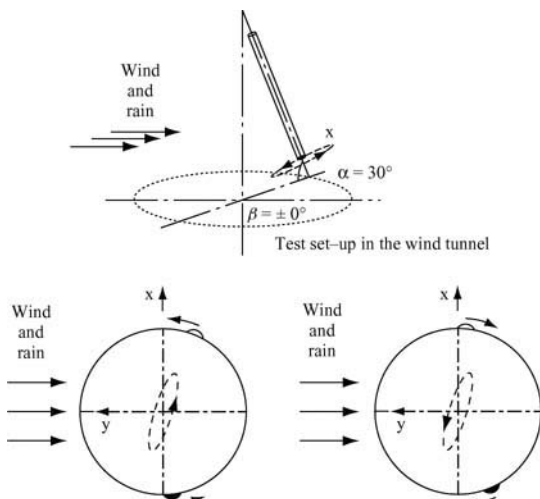


Fig. 4.42: Rain-wind exciting mechanism for across-wind vibrations involving oscillation of one rivulet [57]

water rivulet, with diameter  $d$ , located at an angle  $\beta$  to the vertical axis (with respect to the wind direction).

Given the reported circumferential oscillation of the rivulet during cable vibration, a two-degree-of-freedom galloping model [62] was adopted, with allowance for degrees of motion for both the rotation  $\theta$  and the vertical motion  $y$ , according to the representation in Fig. 4.45.

Designating by  $F_y$  and  $M$  the vertical component and moment per unit length of the unsteady aerodynamic force, respectively, the dynamic equilibrium equations are

$$m \ddot{y} + k y = F_y \quad (4.59a)$$

$$I \ddot{\theta} = M \quad (4.59b)$$

where  $m$  is the cable mass per unit length,  $k$  is the generalised stiffness of the normal mode under consideration, and  $I$  is the polar moment of inertia per unit length of the rivulet about the cable axis. It should be noted that both the mass of the rivulet and the damping force on the cable are neglected for simplification.

The unsteady aerodynamic forces  $F_y$  and  $M$  are now evaluated introducing a quasi-steady assumption that allows the quantification of a relative wind velocity  $U_{rel}$  and relative angle of attack  $\alpha^*$  based on the velocity of vertical translation  $\dot{y}$  and on the angular velocity of the rotation of the rivulet  $\dot{\theta}$ , as represented in Fig. 4.45.

According to the geometric construction presented in this figure,  $U_{rel}$  and  $\alpha^*$  are

$$U_{rel} = \frac{U + R\dot{\theta} \cos(\beta + \theta)}{\cos \alpha^*} \quad (4.60a)$$

$$\alpha^* = \tan^{-1} \frac{\dot{y} + R\dot{\theta} \sin(\beta + \theta)}{U + R\dot{\theta} \cos(\beta + \theta)} \quad (4.60b)$$

In these equations,  $U$  represents the mean wind velocity and  $R$  represents  $(d + D)/2$ .

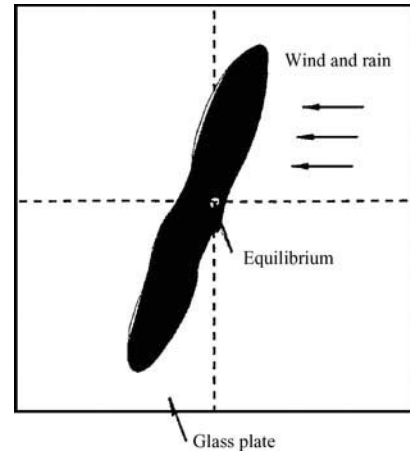


Fig. 4.43: Registration of cable motion at Farø bridges [57, 58]

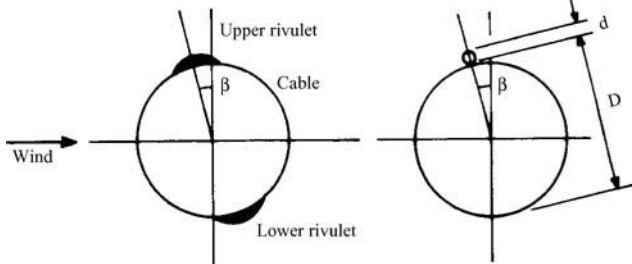


Fig. 4.44: Model of cable with rivulet

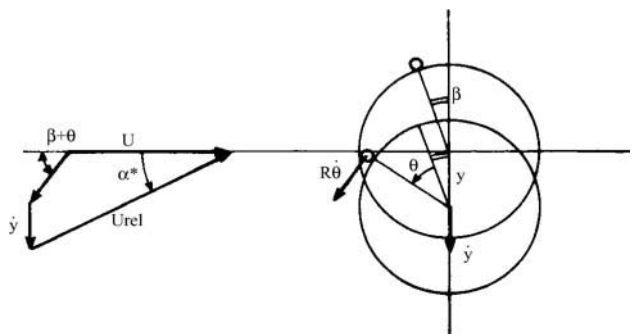


Fig. 4.45: Relative flow for translation of cable with rotation of the rivulet [59]

Considering that a bluff body in a quasi-steady flow characterised by average wind velocity and angle of attack  $U_{rel}$  and  $\alpha^*$ , respectively, generates a drag force  $F_D$ , lift force  $F_L$  and a moment  $M$  as represented in Fig. 4.46, given according to expressions (4.4), it results that

$$F_D = \frac{1}{2} \rho U_{rel}^2 (d + D) \cdot C_D(\alpha) \quad (4.61a)$$

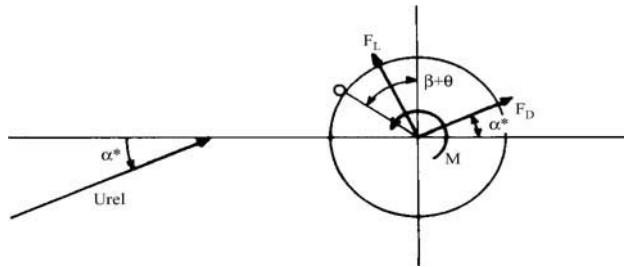


Fig. 4.46: Action of quasi-steady wind force [59]

$$F_L = \frac{1}{2} \rho U_{rel}^2 (d + D) \cdot C_L(\alpha) \quad (4.61b)$$

$$M = \frac{1}{2} \rho U_{rel}^2 (d + D) \cdot C_M(\alpha) \quad (4.61c)$$

The force components  $F_y$  and  $M$  are then

$$F_y = -\frac{1}{2} \rho U_{rel}^2 (d + D) \cdot [C_D(\alpha) \sin \alpha^* + C_L(\alpha) \cos \alpha^*] \quad (4.62a)$$

$$M = \frac{1}{2} \rho U_{rel}^2 (d + D) \cdot C_M(\alpha) \quad (4.62b)$$

Assuming that the maximum velocities of the cable and rivulet are much less than the mean wind velocity  $U$ , the following relations hold:

$$U_{rel} \approx U; \alpha = -\theta + \alpha^* \approx -\theta + \frac{\dot{y}}{U} + \frac{R \sin \beta \dot{\theta}}{U} \quad (4.63)$$

For small angles of attack  $\alpha$  the expansion of the aerodynamic coefficients and trigonometric functions in (4.62) about  $\alpha = \theta = 0$  followed by a linearisation and substitution into (4.59) yields the following equations of motion

$$\underline{M} \begin{Bmatrix} \ddot{y} \\ \ddot{\theta} \end{Bmatrix} + \underline{C} \begin{Bmatrix} \dot{y} \\ \dot{\theta} \end{Bmatrix} + \underline{K} \begin{Bmatrix} y \\ \theta \end{Bmatrix} = \begin{Bmatrix} 0 \\ 0 \end{Bmatrix} \quad (4.64)$$

with

$$\underline{M} = \begin{bmatrix} 1 & 0 \\ 0 & 1 \end{bmatrix}; \underline{K} = \begin{bmatrix} \omega_y^2 & -\frac{1}{m} \cdot \frac{1}{2} \rho (d + D) U^2 \frac{dC_L}{d\alpha} \\ 0 & \frac{1}{I} \cdot \frac{1}{2} \rho (d + D)^2 U^2 \frac{dC_M}{d\alpha} \end{bmatrix} \quad (4.65)$$

$$\underline{C} = \frac{1}{2} \rho (d + D) U \begin{bmatrix} \frac{1}{m} \left\{ C_D + \frac{dC_L}{d\alpha} \right\} & \frac{(d + D) \sin \beta}{2m} \left\{ C_D + \frac{dC_L}{d\alpha} \right\} \\ -\frac{(d + D)}{I} \frac{dC_M}{d\alpha} & -\frac{(d + D)^2 \sin \beta}{2I} \frac{dC_M}{d\alpha} \end{bmatrix} \quad (4.66)$$

The quantity  $\omega_y$  in (4.65) represents the natural frequency of the vertical translation of the cable. Figure 4.47 illustrates the variation of  $C_L$ ,  $C_D$  and  $C_M$  with the angle of attack  $\alpha$  obtained from wind tunnel tests for a  $d/D$  ratio of 0.1.

On the basis of the equations defined above, Yamaguchi performed a complex eigenvalue analysis, assuming that the rivulet was located at an angle  $\beta$  of  $10^\circ$  (with regard to the vertical) and the ratio  $d/D$  was 0.1. Figures 4.48–4.50 illustrate the main results of this analysis which can be summarised in the following points:

- The natural frequency of circumferential motion is proportional to the wind velocity, while the natural frequency of vertical motion is independent of this quantity (Fig. 4.48).
- The modal aerodynamic damping exhibits a strong variation with wind speed (Fig. 4.49). In particular, for a wind speed around  $10 \text{ m/s}$ , the logarithmic decrement  $\delta$  attains significant negative values, indicating the generation of self-exciting forces. These results are qualitatively consistent with the estimates of damping obtained previously by Hikami [53], also represented in Fig. 4.49. It can be observed from this figure that a conventional single-degree-of-freedom galloping analysis would provide positive damping in the full range of wind speeds and is not consequently sufficient to explain the mechanism of rain-wind induced vibration.
- The amplitude of rotation is strongly coupled with vertical motion at a wind speed close to  $10 \text{ m/s}$  (Fig. 4.50). Considering that the oscillation of the rivulet motivated by the aerodynamic stiffness can only occur when  $dC_M/d\alpha$  is positive, as given by (4.65), then it is evident from (4.66) that this coupled motion of the rivulet generates the negative aerodynamic damping that causes instability.

The study of Yamaguchi therefore seems conclusive in terms of the indispensability of circumferential oscillation of the upper rivulet to the generation of rain vibration in a stay cable. And this result was indeed confirmed by other authors who performed wind tunnel tests on prototype segments of cables, such as Flamand [63], [64] and Verwiebe [57]. Flamand, in particular, developed wind tunnel tests using false fixed rivulets glued on to the cable surface at the position in which the formation of the real rivulet is observed, and he concluded that instability did not occur. These results are not however in agreement with other reported wind tunnel observations, namely by Matsumoto *et al.* [44], who also installed false rivulets near the separation

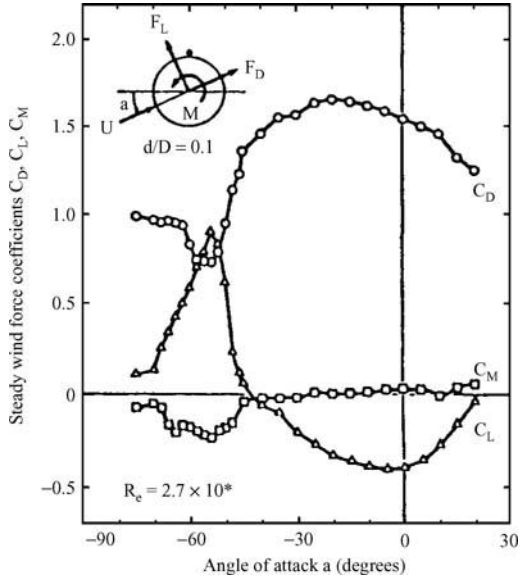


Fig. 4.47: Steady wind force coefficients of Figure 8-section at various angles of wind attack for a  $d/D$  ratio of 0.1 [59]

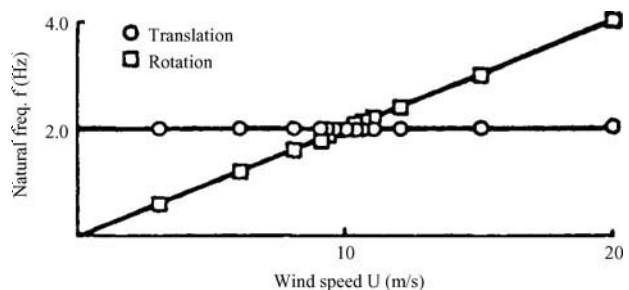


Fig. 4.48: Change of natural frequency with wind speed [59]

points on an inclined cylinder and concluded that the resulting modified cross-section was already unstable, the presence of rain acting as an amplifier of that instability. Therefore, the *rain-wind induced vibration* would be no more than a particular case of the most general *inclined cable aerodynamic instability* phenomenon.

#### 4.6.3.2 Analytical model of Peil and Nahrath

The model developed by Peil and Nahrath [60] is a two-mass oscillator with three degrees of freedom ( $z$ ,  $y$  and  $\varphi$ ). According to the schematic representation of Fig. 4.51, the oscillation of a cable of diameter  $D$  and mass per unit length  $m_s$  is considered in the along-wind ( $z$ ) and across-wind ( $y$ ) directions. Since large amplitudes of oscillation are expected, non-linear behaviour of the cable is considered, by addition of non-linear springs in both directions. Viscous dampers are also added along the two translational directions to simulate the cable damping. The rivulet, simulated by a mass  $m_R$ , moves tangentially to the cable surface, the corresponding position being characterised by an angle of rotation  $\varphi$ , as represented in Fig. 4.51. A viscous damper is added to simulate the friction between the rivulet and the cable surface.

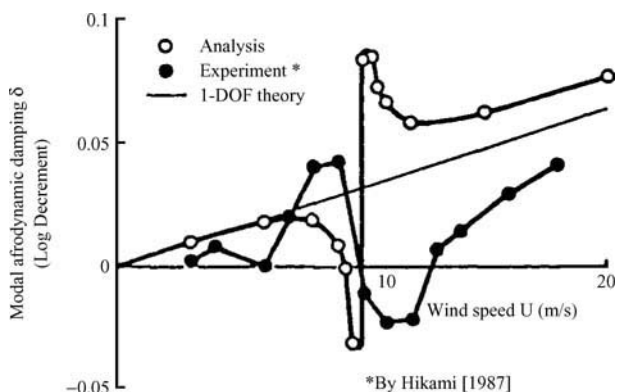


Fig. 4.49: Change of modal aerodynamic damping with wind speed [59]  
\*By Hikami [1987]

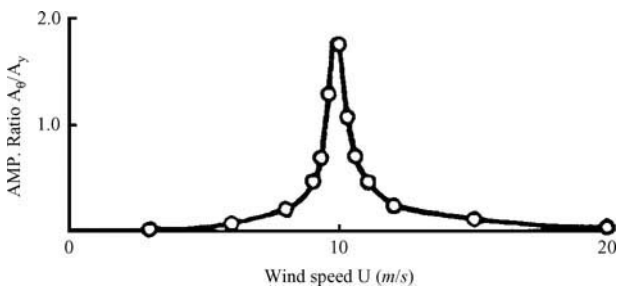


Fig. 4.50: Coupled torsional amplitude versus wind speed [59]

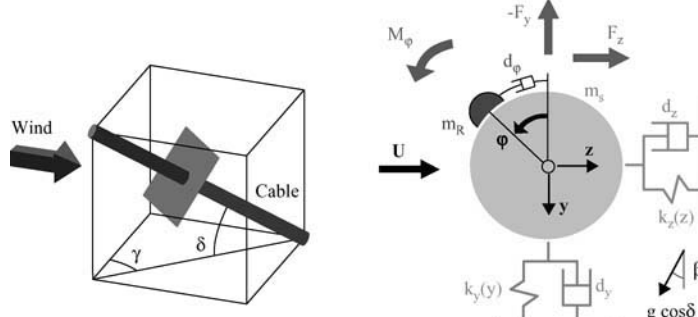


Fig. 4.51: Three-degree-of-freedom model for rain-wind induced vibration [60]

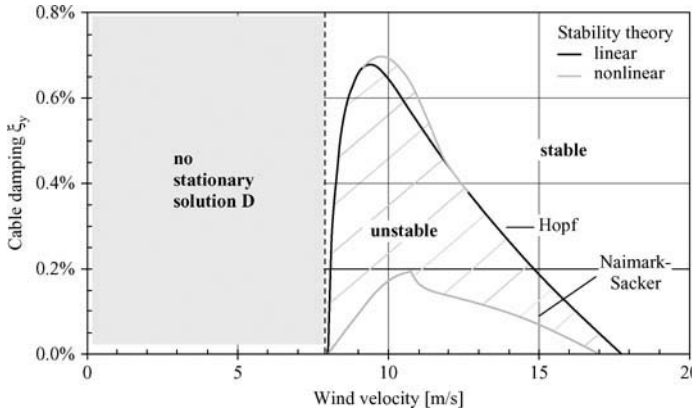


Fig. 4.52: Stability diagram [60]

Using a quasi-steady approach, the coupled non-linear equations of motion are established. Given the numerous input parameters involved in the description of the model, an adequate calibration based on experimental testing must be performed. It is however interesting to note that qualitatively this model describes the various features observed on site occurrences of vibrations. Figure 4.52, representing the stability regions as a function of the cable damping, illustrates some of these features. It is observed that no stationary solution exists for the differential equations of motion for small wind velocities, i.e. the rivulet cannot be formed. Also the critical velocity is independent of cable damping. On the contrary, at high wind velocities a stable solution exists, meaning that even though the rivulet is formed, no vibrations are induced. A cross-hatched region in Fig. 4.52 represents the region of instability where vibrations occur, which is characterised by a progressively smaller wind velocity range as the cable damping increases. It can be observed also that, for a cable damping higher than a critical value of around 0.7%, no rain-wind excitation occurs. This result is consistent with practical experience [27].

#### 4.6.3.3 Design model of Geurts and van Staalanduin

In the sequence of the occurrence of rain-wind induced vibrations at the Erasmus bridge in Rotterdam, an extensive research was carried out that led to the development of a model for the estimation of the effects of rain-wind induced vibrations [65]. The model is based on a modified galloping mechanism whose parameters, namely the lift coefficient and derivatives with respect to the angle of wind attack, were adjusted based on the amplitudes and frequencies of vibration measured on the bridge prototype. The model was useful in the numerical simulation of the bridge behaviour for selecting and tuning the final measures (hydraulic dampers installed at the cable ends) to prevent further vibrations on the bridge.

In a more recent paper, and based on the same model, Geurts and van Staalanduin [61] have developed formulae for a rough estimation at the design stage of the critical wind speed  $U_{cr}$  associated with the occurrence of rain-wind vibration and of the maximum amplitude of vibration  $y_0$  given by

$$U_{cr} = \frac{8m\pi f_e}{-\rho \left( \frac{dC_y(\alpha)}{d\alpha} + C_D \right) \cdot D} \quad (4.67)$$

and

$$\left( \omega_e \cdot \frac{y_0}{U} \right)^2 = \frac{8}{\frac{d^3 C_y}{d\alpha^3}} \left( -\frac{dC_y}{d\alpha} - \frac{2\xi m \omega_e}{\frac{1}{2} \rho U D} \right) \quad (4.68)$$

where  $f_e$  is the natural frequency of the cable in Hz,  $\omega_e$  is the corresponding value in rad/s,  $U$  is the wind velocity,  $C_y$  is the coefficient for loading in the vertical direction and  $\alpha$  is the relative angle of attack.

According to Geurts and van Staalanduin, these formulae do not attempt to describe the exact generating mechanism of rain-wind induced vibration, but consider instead the main features that were extracted from wind tunnel observations. Particular care should be taken in the choice of the derivatives of the lift coefficient, which are in fact the key values of equations (4.67) and (4.68), and should be obtained from wind tunnel tests on a model of the cable to be used for a worst case scenario. Geurts and van Staalanduin adopted values of  $-0.8$  and  $54$  for the quantities  $dC_y/d\alpha$  and  $d^3 C_y/d^3 C_y d\alpha^3$  respectively, based on a wind tunnel test of a smooth cable model with an artificial upper rivulet.

The application of equation (4.68) to a particular cable of a cable-stayed bridge leads to a series of curves of variation of the maximum amplitude of oscillation with wind speed for different possible damping ratios, as depicted in Fig. 4.53. Fixing acceptable limits for  $y_0$ , the necessary damping ratio can be estimated from this figure.

#### 4.6.4 Mechanisms of instability

Although the studies referred to previously consider that the essential phenomenon under the occurrence of rain-wind induced oscillation is galloping, it is possible that various phenomena are present simultaneously, which combine to define particular characteristics like high amplitude oscillations at velocity restricted ranges. Based on the results of numerous wind tunnel tests performed under different conditions and models ([32, 42, 44]; [37]), the team of Professor Matsumoto in particular, classified the generating mechanisms of this instability into three main types: *conventional Karman vortex excitation*, *galloping instability* and *high speed vortex excitation*.

##### 4.6.4.1 Conventional Karman vortex excitation

The *conventional Karman vortex excitation* phenomenon has already been discussed in the Section 4.3, as occurring for relatively small values of the reduced velocity  $U_r = U/fD$

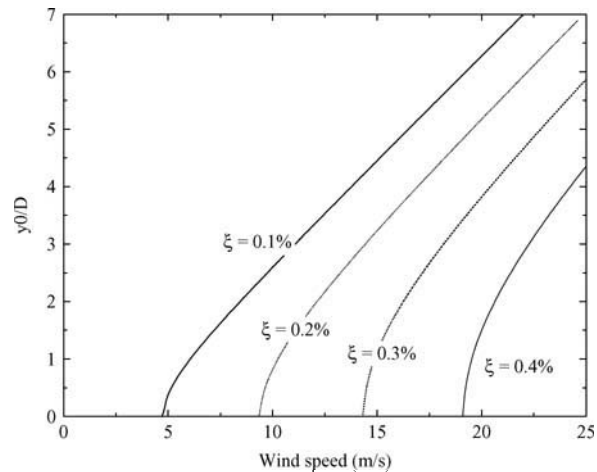


Fig. 4.53: Estimation of maximum amplitude of vibration as a function of the wind speed and damping ratio  $\xi$  for a stay cable with a smooth cable coating

( $U$  – wind velocity;  $f$  – vibration frequency;  $D$  – Cable diameter) around 5, and being characterised by relatively small amplitudes, which do not normally exceed 0.3  $D$ .

#### 4.6.4.2 Galloping instability

Galloping instability is caused not only by the coupled circumferential oscillation of the water rivulet with the cable vibration as described by Hikami [53] and Yamaguchi [59], but also by an axial flow generated in the wake of the inclined cable, as described in the Section 4.4. As mentioned in that Section, the axial flow is likely to induce galloping when the corresponding velocity reaches more than 30% of the approaching wind velocity, for yawing angles greater than 25°. The presence of an artificial rivulet produces an extension of the instability regions as shown in Fig. 4.54, which summarises the response characteristics of a yawed cable in smooth flow with and without the artificial rivulet. It is, however, possible that the rivulet may have a stabilising role. In fact, by increasing the velocity of the flow, the rivulet moves leeward to a region where the lift coefficient's slope is positive, thus ‘erasing’ the galloping instability. Matsumoto calls this phenomenon *velocity restricted galloping*.

#### 4.6.4.3 High speed vortex excitation

The third cause of aerodynamic instability of an inclined cable, as described by Matsumoto, the *high speed vortex excitation*, is directly associated with the formation of the axial flow in the wake of the cable. According to Matsumoto [37], the conventional two-dimensional Karman vortex interacts with the axial flow, generating an amplified vortex, once after every three Karman vortex as illustrated in Fig. 4.55. Figure 4.56 presents a visualisation of this phenomenon using the liquid paraffin method.

Though the characteristics of this *axial vortex* have not been entirely identified yet, the frequency of the shedding seems to be about one-third the conventional Karman frequency, depending on factors such as the yawing of the cable, the location of the upper rivulet and the frequency of cable vibration. The occurrence of this type of instability is greatly affected by

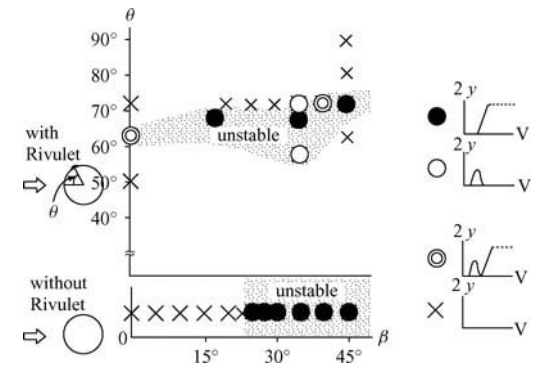


Fig. 4.54: Response characteristics of yawed cable with and without rivulet in smooth flow [37]

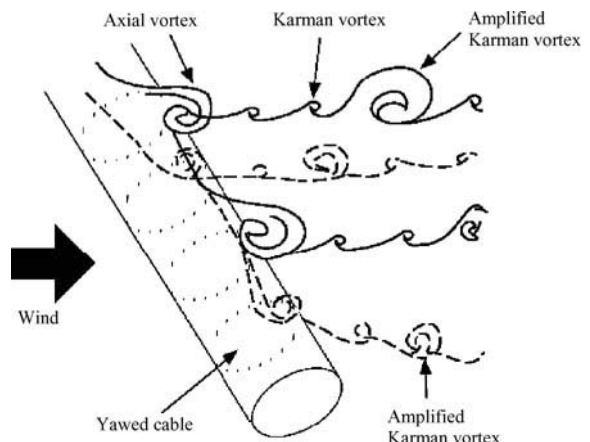


Fig. 4.55: Illustration of the axial vortex and Karman vortex around the yawed inclined cable [37]

the intensity of turbulence and is associated with reduced velocities that are integer times of about 20. These facts are consistent with the observations at the Higashi Kobe bridge [33], where, despite the use of protuberated cables preventing the formation of water rivulets, the cables became unstable with small amplitude oscillations at a high wind velocity of 40 m/s, corresponding to reduced velocities of 161, 241 and 468 for the fundamental vibrating modes [37].

#### 4.6.5 Other variables to rain-wind induced oscillations

The results presented above suggest that the phenomenon of rain-wind induced vibration may include different excitation mechanisms acting simultaneously. The complexity of the phenomenon is evident and can still be enhanced when considering other variables to the problem, like the adhesion property of the cable coating material, or the intensity of the rainfall.

The former has been thoroughly investigated by Flamand [64]. Noting that cable instability usually occurred with standard polyethylene smooth casing of the cable, Flamand studied the influence of the characteristics of several materials and surface types in the formation of the rivulet, realising for example that a stable, smooth surface became unstable when covered by a coating of soot resulting from fuel-oil combustion (which is like atmospheric pollution).

With regard to the latter, reference should be made to the studies of Ohshima and Nanjo [66] and more recently of Main and Jones [67]. The first authors developed wind tunnel tests based on a prototype cable model of the Ajigawa cable-stayed bridge in Japan, subject to different rates of rainfall, concluding that the higher this rate is, the lower is the onset wind velocity for the occurrence of cable vibrations. These results seem consistent with the observations on the Fred Hartman and East Huntington cable-stayed bridges by Main and Jones.

#### 4.6.6 Practical cases of occurrence of rain-wind vibration and prevention measures

With regard to the occurrence of rain-wind induced vibration in cable-stayed bridges, it is important to note that, since the identification of the phenomenon in 1986 until now, many unanticipated vibration problems in prototypes have been reported all over the world. As far as is known by the author, the first report of cable oscillations dates back to 1979 and concerns the Brotonne bridge [1]. It is thought now that these vibrations were caused by rain and wind. The experience of the phenomenon has also been reported for the Farø bridge in Denmark [58], [143] the Ben-Ahin and Wandre bridges in Belgium [68], and more recently, for the

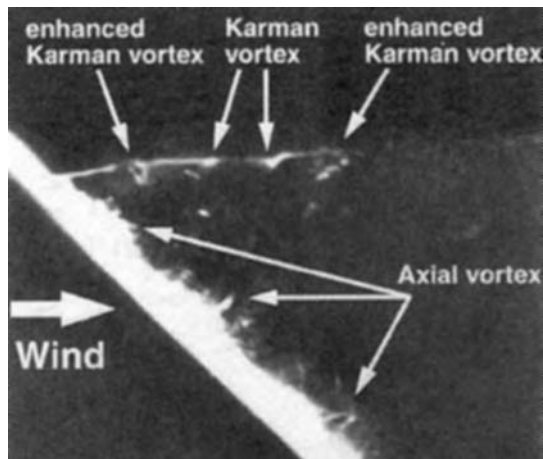


*Fig. 4.56: Visualised axial vortex and intermittently enhanced Karman vortex for the yawed cable ( $\beta = 45^\circ$ ) in smooth flow (by liquid paraffin method [37])*

Second Severn bridge in UK [19] and the Erasmus bridge in the Netherlands [65]. In Japan, besides the Meiko-Nishi bridge (West Meiko), the Aratsu [69], the Higashi Kobe [37], the Tempozan [37] and the Central Meiko bridges [70] have also experienced rain-wind vibration. In the US, rain vibration occurred at the Weirton-Steubenville bridge, in West Virginia [71], and at the Fred Hartman and East Huntington bridges, located in Texas and West Virginia, respectively [67]. And in Australia, rain vibration amplitudes of several meters have been observed at the Glebe Island bridge.

Based upon the experience gathered from the observation of rain vibration in prototypes of cable-stayed bridges and on wind tunnel tests, the main conditions and characteristics associated with the occurrence of the phenomenon can be summarised as follows [35, 37, 56, 67, 72]:

- The wind speed varies in the range of 5–20  $m/s$ , the majority of reported cases lying in the interval 8–12  $m/s$ , corresponding to reduced wind velocities  $U_{cr}$  ( $U_{cr} = U/fD$ ) of 20–90;
- The wind direction varies in the range of 20° to 60° to the longitudinal axis of the bridge;
- The cables are inclined to the horizontal at angles of 20°–45°. Some cases have however been reported for almost vertical hangers of arch bridges;
- There is rain fall, heavy, light or a drizzle, although in most cases, moderate rain is reported;
- The cable surface is smooth, as in polyethylene or painted, metal-cased cables;
- The cable diameter is in the range of 80–200  $mm$ ;
- Typical vibration frequencies are in the range of 0.3–3  $Hz$ ;
- Typical amplitudes of vibration are about twice the cable diameter. However, amplitudes of  $7D$  have been observed;
- The structural damping of the cables is very low (logarithmic damping decrement less than 0.01);
- The cable is located behind the bridge pylon and declines in the direction of the wind;
- The cable-stayed bridge is located in an area where the intensity of turbulence is expected to be low, such as in a seaside area;
- The vibration orbit varies according to the intensity of the rainfall: during light rain and drizzle, vibration occurs essentially in the vertical plane, while during heavy rainfall the orbit may exhibit significant two-dimensionality.

With respect to possible measures against rain-wind vibrations, two strategies can be followed, one based on the application of aerodynamic measures to the cable cross-section, and the other based on the increment of damping through the addition of special devices.

As for the implementation of aerodynamic measures, and given that it seems conclusive that the motion of rivulets enhances oscillations, the adoption of non-smooth surfaces has proved to be an adequate strategy. In fact, protuberances (*Fig. 4.57(a)*), helical wire whirling (*Fig. 4.57(b)*), or a dimpled surface (*Fig. 4.57(c)*), have been proved to disrupt the formation of rivulets. It is essential nevertheless to ensure that the increase in drag coefficient is not significant. This problem was particularly evident in the Tatara bridge in Japan, given the length of the stay cables (longest cable of 460  $m$ ), and was successfully solved with the dimpled surface represented in *Fig. 4.57(c)*.

With respect to the addition of damping devices, and in the absence of other studies, the indication proposed by the PTI guide [40] to ensure that the Scruton number  $S_{c0}$  (calculated as

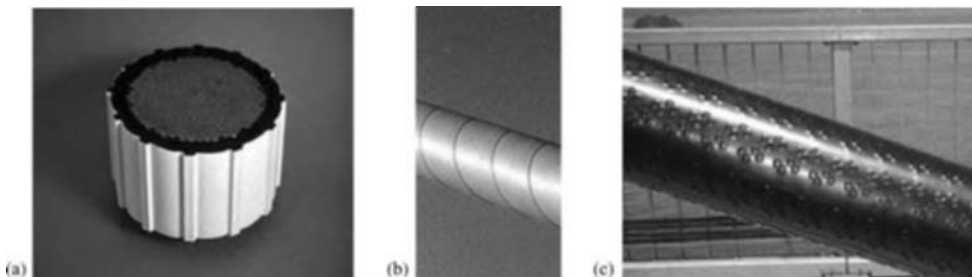


*Fig. 4.57: Examples of non-smooth surfaces of cable coating to prevent rain-wind induced vibration: (a) Protuberated, Higashi-Kobe bridge; (b) Helical wire whirling, Vasco da Gama bridge; (c) Dimpled, Tatara bridge (Courtesy of H. Yamada)*

$S_{c0} = m\xi/\rho D^2$ ) is greater than 10 for avoiding rain-wind induced vibrations, can be employed as a practical rule. The studies of Tabatabai and Mehrabi [27], centred on a database of all the stay cables of 16 cable-stayed bridges constructed in the United States, have shown that an intrinsic damping  $\xi$  of 0.7% would ensure a  $S_{c0}$  greater than 10 for 90% of the stay cables of the database. Given that the current stay cable intrinsic damping ratios lie in the range of 0.05–0.5%, the necessity to design dampers for the majority of cables seems evident.

It should be noted however that a detailed study of the bridge stay cables may lead to less damping requirements, as shown by Geurts and van Staalanduin [61] with the application of the design model described in the Section 4.6.3 to the estimation of damping requirements at the Erasmus Bridge in Rotterdam, and at another bridge constructed in Kampen, the Netherlands. For the longest cables of the two bridges, with lengths of 295 and 158 m, respectively, the two authors suggest minimum damping coefficients of 0.5% and 0.4%.

## 4.7 Drag Crisis

A recent concern of several researchers is that many wind-induced vibrations have occurred in the critical Reynolds number range [35, 73, 74]. In fact, as observed in the Section 4.1.1, the critical range of Reynolds number is  $2 \times 10^5$ – $8 \times 10^5$  for smooth circular cylinders, meaning that for a circular stay cable with a diameter of 0.20 m this range would occur for mean wind velocities of 20–60 m/s. So, assuming vibration of the cable in that particular range of Reynolds numbers, a small increase of the mean wind velocity might create a sudden decrease of the drag force, and hence of the lift force over the cable, the result being a reduced motion. This approximation to the equilibrium position would cause an increase of the relative velocity of the flow and so a slight increase of the drag force and of cable vibration, with the consequence of reducing the relative wind velocity of the flow. An oscillation of the cable could then be created merely by a slight fluctuation of wind flow.

The so-called *drag crisis* has not been truly identified on a cable-stayed bridge, although it is currently understood as the source of a large oscillation observed from 1959 to 1961 at the 1619 m span transmission line across the Severn River in UK [35]. It is thought that a Reynolds number in the critical range can enhance the generation of rain-wind induced vibrations [73]. The phenomenon is however quite complex, and depends on the attitude of the circular cylinder to the flow as demonstrated by Larose *et al.* [74], and requires further investigation.

## 5. Indirect Excitation

### 5.1 General

The vibration of the deck and towers caused by wind, traffic and earthquakes, produces an *indirect excitation* of the cables through the motion of their anchorages (Fig. 5.1). In certain circumstances, the induced cable vibrations attain very high amplitudes. Two phenomena can be identified under these circumstances, described here as *external* and *parametric* excitation. The *external excitation* corresponds to an amplification of motion applied at some anchorage perpendicular to the cable chord, while the *parametric excitation* corresponds to oscillations in the direction of the chord. The phenomena of *external* and *parametric excitation* have been observed in several bridges in the past (some examples are the Brottonne bridge in France, the Ben-Ahin and Wandre bridges in Belgium, and the Annacis bridge in Canada). The literature on the topic of *indirect excitation* concentrates essentially on studies on the *parametric excitation* phenomenon, which is considered more important. The usual approach to the study of *parametric excitation* consists of an evaluation of the cable resonance condition from the dynamic equilibrium equations of a single cable under harmonic motion of the supports. A modified Mathieu-Hill type equation is obtained [75–78], which is characterised by a set of secondary resonances, i.e. the response to a harmonic of frequency  $\omega$  is not increased exclusively at resonance (when the natural frequency of the cable system coincides with  $\omega$ ), but also at specific ratios between the exciting frequency and the system natural frequency: 1/2, 1/3, 2 and 3. It is possible then to define instability regions, i.e. intervals of frequency oscillation of the supports where high amplitudes of vibration occur and to characterise both the threshold amplitude for the occurrence of instability, and the maximum amplitude of oscillation inside the instability regions.

The various phenomena of cable vibration have been most frequently studied by considering the stay cables isolated from the bridge structure. It is important however to understand the type of interaction that these elements exert with the deck/towers system when integrated in the bridge structure, as well as the interaction between the various stay cables on a bridge.

From an engineering point of view, the goal is to quantify the amplification of the deck/tower motion and define the amount of damping necessary to prevent the cable system from undergoing large vibrations. This Chapter analyses the problem of harmonic oscillation of the supports considering the *external* and *parametric excitations* separately, and presenting formulae for predicting the occurrence of instability and for the estimation of maximum amplitudes of vibration. The issue of cable-structure interaction is also discussed.

### 5.2 External Excitation

The horizontal cable represented in Fig. 5.2 is subjected to a harmonic oscillation  $z_B(t)$  of the anchorage B, given by

$$z_B(t) = z_B \cdot \sin \omega t \quad (5.1)$$

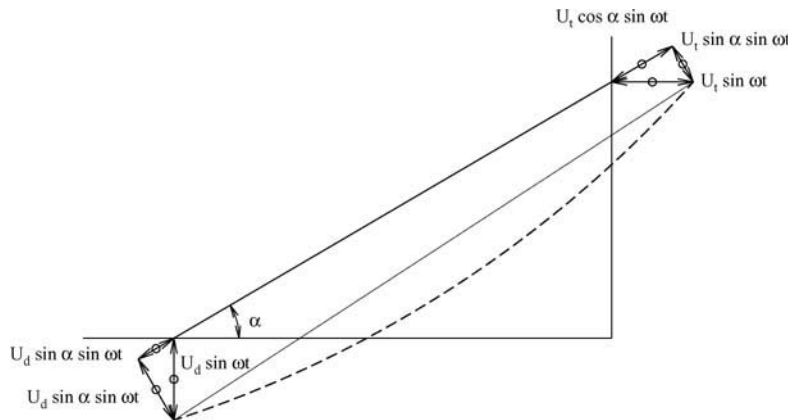


Fig. 5.1: Stay cable subjected to harmonic motion at the anchorages

Accordingly, the position  $z(x, t)$  of a generic point is given by the sum

$$z(x, t) = z_g(x) + z_0(x, t) + w(x, t) \quad (5.2)$$

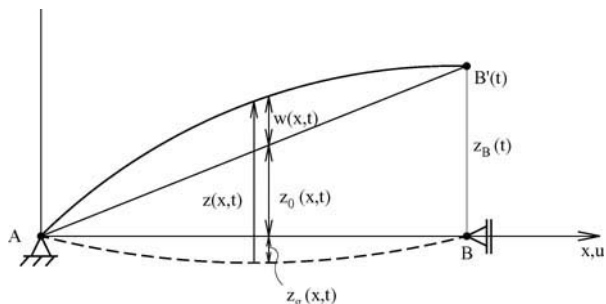


Fig. 5.2: Stay cable subjected to transverse motion at one anchorage

### 5.2.1 Linear model

Assuming that the cable is a taut string and neglecting the additional component of tension  $\tau$  by comparison with the initial tension in the cable  $T$ , the dynamic equilibrium equation of the cable in the vertical direction (see Appendix B) is

$$T \frac{\partial^2 z}{\partial x^2} = m \frac{\partial^2 z}{\partial t^2} - mg \quad (5.4)$$

The substitution of (5.2) and (5.3) into (5.4) yields

$$T \frac{\partial^2 w}{\partial x^2} = m \frac{\partial^2 w}{\partial t^2} + m \cdot \frac{x}{\ell} \cdot \frac{\partial^2 z_B}{\partial t^2} \quad (5.5)$$

Equation (5.5) can be solved by decomposition of  $w(x, t)$  in a Fourier series, whose coefficients  $\alpha_k(t)$  represent the contribution of the  $k$ th mode shape, with an assumed sinusoidal configuration

$$w(x, t) = \sum_{k=1}^n \alpha_k(t) \cdot \sin\left(\frac{k \pi x}{\ell}\right) \quad (5.6)$$

Considering that the anchorage motion is the sinusoid of amplitude  $z_B$  and frequency  $\omega$  given by equation (5.1) and introducing a viscous damping term characterised by a damping coefficient  $\xi_k$ , the following equation of motion is obtained

$$\ddot{\alpha}_k(t) + 2\xi_k \omega_k \dot{\alpha}_k(t) + \omega_k^2 \cdot \alpha_k(t) = \frac{2}{k \pi} (-1)^k \omega^2 z_B \cdot \sin(\omega t) \quad (5.7)$$

where  $\omega_k$  represents the circular frequency associated with the  $k$ th mode of vibration, given according to the taut string theory (see Appendix B) as

$$\omega_k = \frac{k \pi}{\ell} \sqrt{\frac{T}{m}} \quad (5.8)$$

The solution  $\alpha_k(t)$  of equation (5.7) is the response of a damped single-degree-of-freedom oscillator to a sinusoidal excitation [79]

$$\alpha_k(t) = \frac{\frac{2}{k \pi} (-1)^k \beta_k^2 z_B}{\sqrt{(1 - \beta_k^2)^2 + (2\xi_k \beta_k)^2}} \cdot \sin(\omega t - \theta_k) \quad (5.9)$$

with  $\beta_k = \omega / \omega_k$  and  $\theta_k = \tan^{-1} \frac{2\xi_k \beta_k}{1 - \beta_k^2}$ . The vibration of a generic point along the cable is then given by

$$\bar{z}(x, t) = z_B \cdot \frac{x}{\ell} \cdot \sin(\omega t) + \sum_{k=0}^n \left[ \frac{\frac{2}{k \pi} (-1)^k \beta_k^2 z_B}{\sqrt{(1 - \beta_k^2)^2 + (2\xi_k \beta_k)^2}} \cdot \sin(\omega t - \theta_k) \cdot \sin \frac{k \pi x}{\ell} \right] \quad (5.10)$$

Equation (5.10) evidences that the contribution of a mode of  $k$ th order depends both on the ratio  $\beta_k$  between the excitation frequency  $\omega$  and the cable frequency  $\omega_k$ , and on the damping coefficient  $\xi_k$ . This contribution is maximum whenever  $\beta_k$  is close to unity, that is, when the excitation frequency is in resonance with one of the natural frequencies of the cable and, in particular, when  $k \geq 1$ . This is the so-called *primary resonance*, the maximum amplitude of oscillation in the first mode being

$$(\alpha_1)_{\max} = \frac{z_B}{\pi \xi_1} \quad (5.11)$$

Considering the small amount of damping associated with stay cables, which, in the absence of other mechanical devices and aerodynamic influence varies in the range 0.1–0.5% for the majority of the stays, it is evident from (5.11) that the amplification of the support oscillation may be enormous. The validity of the linear approach presented above to evaluate the amplitude of cable vibration should then be questioned.

### 5.2.2 Linearity of response of current stays

In order to have a measure of the degree of non-linearity in the stay cable vibration associated with *external excitation*, the response of a medium size stay cable to harmonic oscillation at the support is evaluated numerically, based on a geometric non-linear formulation.

The characteristics of the stay cable presented in *Fig. 5.3* correspond approximately to one of the stay cables of the Ben-Ahin cable-stayed bridge (Belgium, 1987) and were obtained from refs [77, 80]. According to *Fig. 5.3*, the 110.5 m long stay cable was analysed in a horizontal layout and divided into a total of thirty truss elements. These elements were subjected both to dead weight and to an initial strain that led to the installed tension  $T$  of 4902.7 kN. Fixing the vertical displacement at anchorage  $B$ , and considering the stiffness matrix derived in the deformed position, the linear eigenvalue problem was solved, which led to the first natural frequencies of in-plane vibration presented in *Table 5.1*.

In a second step, the response to a vertical harmonic displacement at anchorage  $B$  was evaluated numerically, considering different amplitudes and an excitation frequency of 1.25 Hz (situation of *primary resonance*). In this analysis, a Rayleigh damping matrix proportional to the mass matrix was used with an assumed damping coefficient of 1% for the first mode of vibration (this coefficient can be considered an average value of the damping coefficient in a stay cable after mechanical devices are added).

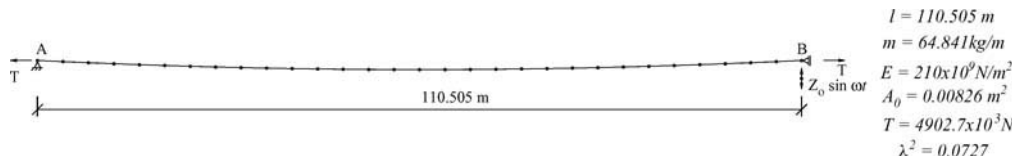


*Fig. 5.3: Stay cable of Ben-Ahin cable-stayed bridge. Discretisation for FEM analysis. Main characteristics*

Order	1st	2nd	3rd	4th	5th
Frequency (Hz)	1.25	2.49	3.75	5.01	6.29

*Table 5.1: First natural frequencies of vibration for in-plane motion of stay cable*

*Figure 5.4* summarises the limit cycle response and the increment of tension calculated for several amplitudes of support oscillation in the range 0.005 m–0.2 m, considering two different damping coefficients, 0.5% and 1%, for the first vibration mode. Superimposed in graph (a) of the figure are straight lines that represent the maximum response calculated on the basis of the linear model described above, given by equation (5.11). A bold curve in that graph describes the results obtained under an analytical non-linear formulation that will be explained subsequently.

*Figure 5.4(a)* clearly evidences a deviation of the numerically calculated response from the linear model. For a support oscillation of 0.05 m of amplitude, for example, the numerical response is actually 30% of the linear response for  $\xi = 0.5\%$  and 59% for  $\xi = 1\%$ . It can

be also observed that for large amplitudes of deck vibration, the increment of cable tension attains significant values and should not be neglected (Fig. 5.4(b)).

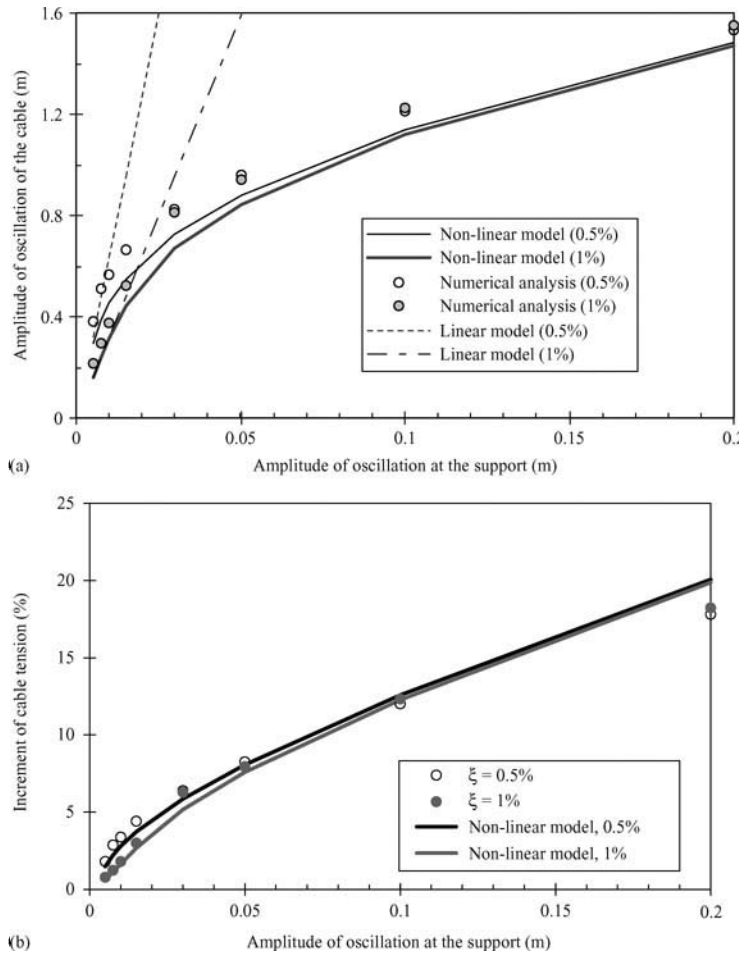


Fig. 5.4: Variation of the amplitude of oscillation/increment of cable tension with the amplitude of harmonic oscillation at the anchorage at primary resonance, considering  $\xi = 0.5\%$  and  $\xi = 1\%$ : Linear model, numerical response, and non-linear model

### 5.2.3 Non-linear model

A non-linear correction for the maximum resonant amplitude of oscillation in a stay cable was obtained by Caetano [81] adapting the non-linear differential equations developed by Pinto da Costa *et al.* [77] for an inclined cable subjected to vertical harmonic motion of one support. Accordingly, the transverse displacement  $w(x, t)$  is approximated by a function containing

the contribution of the first linear free-oscillation mode of the taut cable

$$w(x, t) = z_B \cdot \frac{x}{\ell} \cdot \sin(\omega t) + \alpha_1(t) \sin \frac{\pi x}{\ell} \quad (5.12)$$

The equation in  $\alpha_1(t)$  reduces to

$$\begin{aligned} \ddot{\alpha}_1(t) + 2\xi_1 \omega_1 \dot{\alpha}_1(t) + \omega_1^2 \cdot \left[ 1 + \frac{1}{2} \left( \frac{2}{\pi} \right)^4 \cdot \lambda^2 - \frac{\lambda z_B}{2\sqrt{X_0 \ell}} \sin(\omega t) \right] \alpha_1(t) \\ - \frac{3\omega_1^2}{\pi\sqrt{X_0 \ell}} \cdot \lambda \cdot \alpha_1^2(t) + \frac{\pi^2}{4} \cdot \frac{\omega_1^2}{X_0 \ell} \alpha_1^3(t) = 2 \frac{\omega_1^2}{\pi} \cdot z_B \cdot \left[ 1 - \left( \frac{\lambda}{\pi} \right)^2 \right] \cdot \sin(\omega t) \end{aligned} \quad (5.13)$$

where  $X_0$  is the elastic elongation of the cable,  $X_0 = T\ell/(EA_0)$ , and  $\omega_1$  is the linear circular frequency associated with the first vibration mode of a taut string, given by

$$\omega_1 = \frac{\pi}{\ell} \sqrt{\frac{T}{m}}.$$

Considering the application to taut cables, for which  $\lambda^2$  is very small (say  $\lambda^2 \leq 0.5$ ), the periodic component term in  $\alpha_1(t)$ , named the *parametric term*, has generally a lower order of magnitude than the other terms and is consequently neglected. In this case, the differential equation in  $\alpha_1(t)$

$$\begin{aligned} \ddot{\alpha}_1(t) + 2\xi_1 \omega_1 \dot{\alpha}_1(t) + \omega_1^2 \cdot \left[ 1 + \frac{1}{2} \left( \frac{2}{\pi} \right)^4 \cdot \lambda^2 \right] \alpha_1(t) - \frac{3\omega_1^2}{\pi\sqrt{X_0 \ell}} \cdot \lambda \cdot \alpha_1^2(t) \\ + \frac{\pi^2}{4} \cdot \frac{\omega_1^2}{X_0 \ell} \alpha_1^3(t) = 2 \frac{\omega_1^2}{\pi} \cdot z_B \cdot \left[ 1 - \left( \frac{\lambda}{\pi} \right)^2 \right] \cdot \sin(\omega t) \end{aligned} \quad (5.14)$$

can be understood as the governing equation of a system with quadratic and cubic nonlinearities subjected to a harmonic excitation.

An important characteristic of non-linear systems is the existence of *secondary resonances*. A system with quadratic non-linearities only (taut string) possesses a so-called *subharmonic resonance* of order 1/2 and a *superharmonic resonance* of order 2, in addition to the primary resonance, of order 1. A system with cubic non-linearities only (inextensible cable) possesses a *subharmonic resonance* of order 1/3 and a *superharmonic resonance* of order 3. In any of the cases, the existence of *secondary resonances* means that, if the system is subjected to a harmonic excitation characterised by a frequency  $\omega$  that is in the vicinity of the fundamental frequency  $\omega_1$ , then in addition to the steady-state response in the frequency  $\omega_1$ , a component in a *subharmonic/superharmonic* frequency ( $\frac{1}{2}\omega_1, \frac{1}{3}\omega_1, 2\omega_1, 3\omega_1$ ) occurs. This component either vanishes with time, or converges to a finite value, according to the initial conditions.

Both *subharmonic* and *superharmonic resonances* of order 1/3, 1/2, 2 and 3, respectively, exist in the current system, given that quadratic and cubic non-linearities are present. Additionally, other so-called *combination resonances* may exist, if the system is excited by a combination of harmonics with particular values [76].

Focusing on the *primary resonance*, which dominates the steady-state response, Nayfeh and Mook [76] developed a solution for equation (5.14) in a vicinity of the resonance  $\omega_1$ , given by

$$\alpha_1(t) = a \sin(\omega_1 t - \gamma) + \frac{3\lambda}{2\pi\sqrt{X_0\ell}} a^2 \cdot \left[ 1 - \frac{1}{3} \sin(2\omega_1 t - 2\gamma) \right] \quad (5.15)$$

In this expression the amplitude of vibration  $a$  (that governs the total response) and the phase of the response  $\gamma$  are given by

$$a = \frac{z_B}{\pi\xi_1} \cdot \frac{1 - (\frac{\lambda}{\pi})^2}{\left[1 + \frac{1}{2}(\frac{2}{\pi})^4\lambda^2\right]^{1/2}} \cdot \sin \gamma \quad (5.16)$$

and by the solution of

$$\sin^2 \gamma \cdot \tan \gamma = \frac{32}{3} \cdot X_0 \ell \cdot \frac{\left[1 + \frac{1}{2}(\frac{2}{\pi})^4\lambda^2\right]^4}{\left[1 - (\frac{\lambda}{\pi})^2\right]^2 \cdot \left[1 - 32\frac{\lambda^2}{\pi^4}\right]} \cdot \frac{\xi_1^3}{z_B^2} \quad (5.17)$$

Designating by  $C$  the quantity  $C = \left[1 - (\frac{\lambda}{\pi})^2\right] / \left[1 + \frac{1}{2}(\frac{2}{\pi})^4\lambda^2\right]^{1/2}$ , the maximum value of the amplitude of the steady-state response  $a$  in the frequency  $\omega_1$  reduces to

$$a = \frac{z_B}{\pi\xi_1} \cdot C \cdot \sin \gamma \quad (5.18)$$

Given that  $C \approx 1$ , this is no more than the linear amplitude of the response weighted by a function  $\sin \gamma$  that reflects the non-linear character of the system and whose value is obtained by numerical solution of equation (5.17). *Figure 5.5* illustrates the variation of  $\sin \gamma$  with the amplitude of support oscillation at *primary resonance* for different damping coefficients, for

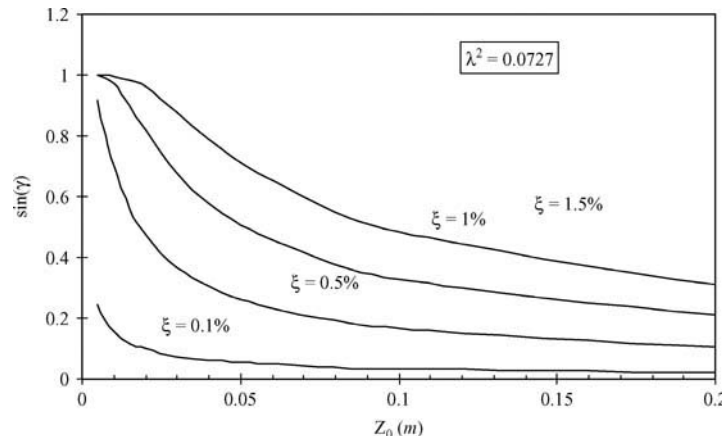


*Fig. 5.5: Variation of  $\sin \gamma$  with the amplitude of support oscillation for different damping coefficients and  $\lambda^2 = 0.0727$*

the cable described in *Fig. 5.3*. It is clear from that figure that for small damping coefficients, significant non-linearities in the response occur at very small amplitudes of oscillation.

Another aspect evidenced by equation (5.15) is the appearance of a drift in the steady-state response that grows with the amplitude of oscillation.

The maximum amplitude of oscillation was calculated for the stay cable described above, using equations (5.15) to (5.17) and is plotted in bold solid line in *Fig. 5.4* for the two values of the damping coefficient considered, 0.5% and 1%. The analysis of this Figure shows a small deviation between the numerical and theoretical model, the latter producing, however, a smaller response than the former. Another characteristic evidenced both by the numerical and analytical responses, is the relatively slight dependence of the amplitude of vibration on the damping coefficient for large amplitudes of vibration. This can be observed in *Fig. 5.4(a)*, considering the two damping coefficients of 0.5% and 1%, and is framed by the shaded area of *Fig. 5.6* both for this cable ( $\lambda^2 = 0.0727$ ) and for the longest cable of the Vasco da Gama bridge ( $\lambda^2 = 0.4321$ ), for damping coefficients in the range 0.1–1.5%.

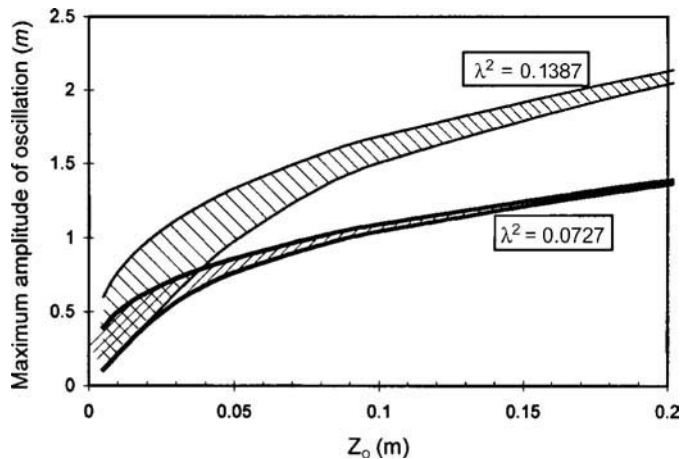


*Fig. 5.6: Variation of maximum steady-state amplitude of oscillation at primary resonance with amplitude of support oscillation for damping coefficients within the range 0.1–1.5%*

Finally, based on a second order definition of the elastic strain  $\varepsilon$  of the cable and considering only motion in the plane, the dynamic increment of tension  $\tau$  in the cable can be obtained from

$$\tau(t) = \frac{EA_0}{\ell} \cdot \left[ 2 \frac{\ell}{\pi} \cdot \frac{mg}{T} \alpha_1(t) + \frac{1}{2} \cdot \frac{z_B^2}{\ell} \sin^2 \omega_1 t + \frac{\pi^2}{4\ell} \cdot \alpha_1^2(t) \right] \quad (5.19)$$

Considering that for the primary resonance  $\alpha_1(t)$  is approximately given by a sinusoid of frequency  $\omega_1$  and amplitude  $a$  (see equation (5.15)), the maximum increment of cable tension can be approximated by

$$\tau_{\max} \approx \frac{EA_0}{\ell} \left[ 2 \frac{\ell}{\pi} \cdot \frac{mg}{T} \cdot a + \frac{z_B^2}{2\ell} + \frac{\pi^2}{4\ell} \cdot a^2 \right] \quad (5.20)$$

The variation of the increment of cable tension with the amplitude of oscillation was calculated for the stay cable analysed above, using equation (5.20). *Figure 5.4(b)* shows the good agreement between the non-linear estimates and the numerical response for the two damping coefficients of 0.5 and 1% considered in the analysis.

## 5.3 Parametric Excitation

### 5.3.1 General equations

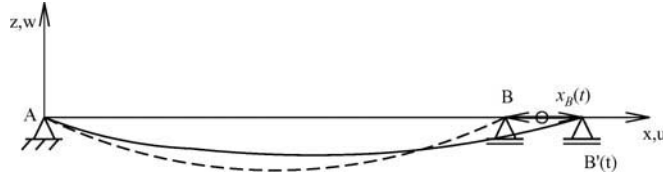


Fig. 5.7: Horizontal cable subjected to longitudinal harmonic motion at one anchorage

The horizontal cable represented in Fig. 5.7 is now subjected to a harmonic oscillation at anchorage  $B$  along the longitudinal axis  $x_B(t)$  given by

$$x_B(t) = x_B \sin 2\omega t \quad (5.21)$$

As in the previous case, the vertical vibration  $w(x, t)$  of the stay cable is determined by separation of variables, considering the contribution of the first mode according to

$$w(x, t) = \alpha_1(t) \cdot \sin \frac{\pi x}{\ell} \quad (5.22)$$

The coefficient  $\alpha_1(t)$  is given by the solution of

$$\begin{aligned} \ddot{\alpha}_1(t) + 2\xi_1\omega_1\dot{\alpha}_1(t) + \omega_1^2 \cdot \left(1 + \frac{\lambda^2}{\pi^2} + \frac{x_B}{X_0} \sin 2\omega t\right) \cdot \alpha_1(t) \\ + 2 \frac{\omega_1^2}{\pi \sqrt{X_0 \ell}} \cdot \lambda \cdot \left(1 + \frac{\pi^2}{16}\right) \cdot \alpha_1^2(t) + \frac{\pi^2}{4} \cdot \frac{\omega_1^2}{X_0 \ell} \cdot \alpha_1^3(t) = \frac{\omega_1^2 \cdot \ell}{2\pi \sqrt{X_0 \ell}} \cdot \lambda \cdot x_B \sin 2\omega t \end{aligned} \quad (5.23)$$

Equation (5.23) is a so-called *modified Mathieu equation*, which has the following general form

$$\ddot{u} + (\delta^2 + 2\varepsilon \sin 2\bar{t}) \cdot u = \varepsilon f(u, \dot{u}) \quad (5.24)$$

with  $\varepsilon \ll 1$ . This is the equation of a system characterised by small non-linearities subjected to a small excitation. Particular solutions of (5.24) have been obtained in the past [76] using perturbation methods. A case of interest is the *Duffing equation* with *small damping*, for which the function  $f$  in (5.24) is  $f = -\alpha u^3 - 2\mu \dot{u}$ , resulting in

$$\ddot{u} + 2\varepsilon \mu \dot{u} + (\delta^2 + 2\varepsilon \sin 2\bar{t}) u + \varepsilon \alpha u^3 = 0 \quad (5.25)$$

This type of equation represents for example the governing equation of motion of a weightless taut string, and can be obtained directly from (5.23), after a convenient normalisation, neglecting the contribution of both the quadratic term and the second member, which are of the same order of magnitude

$$\begin{aligned} \bar{t} &= \omega t; u(\bar{t}) = \frac{\alpha_1(\bar{t})}{K}; K = \frac{4}{\pi} \cdot \sqrt{\frac{X_0 \ell}{3}} \\ \delta &= \omega_1 / \omega; \varepsilon = \delta^2 \cdot \frac{x_B}{2X_0}; \alpha = \frac{4}{3} \cdot \frac{\delta^2}{\varepsilon}; \mu = \xi_1 \cdot \frac{\delta}{\varepsilon} \end{aligned} \quad (5.26)$$

It is known [75, 76] that the solutions of (5.25) may be bounded or unbounded, according to the combination of parameters  $\delta$  and  $\varepsilon$ . Neglecting the cubic term, a set of so-called transition curves divide the  $\varepsilon - \delta$  plane into regions that correspond either to unstable or to stable motions, as represented in Fig. 5.8, and designated as a Strutt diagram (hatched regions are unstable).

These curves emanate from  $\delta^2 = n^2$  ( $n = 1, 2, \dots$ ) for each instability region of order  $n$ th, and are defined for the first two instability regions by [76, 78]

$$\delta^2 = 1 - 2\mu^2\varepsilon^2 \pm (1 - 4\mu^2 + 4\mu^2\varepsilon^2)^{\frac{1}{2}}, \delta^2 \approx 1 \quad (5.27a)$$

$$\delta^2 = 4 + \frac{\varepsilon^2}{\delta^2} \pm \frac{\varepsilon^2}{\delta^2} \cdot \left(1 - 4\mu^2 + \frac{4\mu^2\delta^4}{\varepsilon^2}\right)^{\frac{1}{2}}, \delta^2 \approx 4 \quad (5.27b)$$

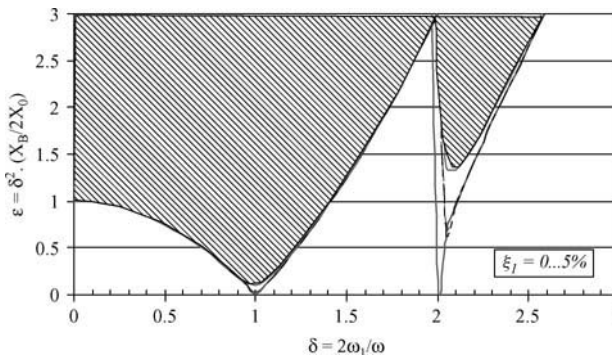


Fig. 5.8: Transition curves for different values of the damping coefficient  $\xi_1$ : 0 (in bold), 0.5 and 5%

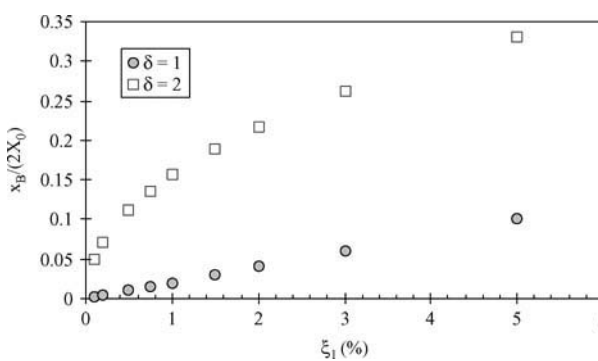


Fig. 5.9: Threshold amplitudes of support oscillation for instability in the first ( $\delta^2 = 1$ ) and second ( $\delta^2 = 4$ ) resonances

Figure 5.9 represents the threshold non-dimensional amplitudes  $x_B/2X_0$  for the first two parametric resonances as a function of the damping coefficient. This figure can be employed for the estimation of required damping coefficient in order to avoid parametric resonance.

Different values of the damping coefficient frame different instability regions, as shown in Fig. 5.8. The effect of the linear viscous damping term is a lift of the unstable regions from the  $\delta$ -axis. This means that higher amplitude of support oscillations are required to attain instability, for a given excitation frequency ratio  $\delta$ . This effect is more pronounced for the second order resonance ( $\delta^2 \approx 4$ ).

Considering the *first parametric resonance*  $\delta^2 \approx 1$ , the threshold amplitude for the occurrence of instability is, according to equation (5.27a), given by

$$\frac{x_B}{2X_0} = 2\xi_1 \quad (5.28)$$

The threshold amplitudes of oscillation associated with the second resonance ( $\delta^2 = 4$ ) are higher than those associated with *primary resonance* and can be obtained solving (5.27b) for

$$\frac{2}{\delta} = 1 + 4\xi_1^2 \pm 2\xi_1 \sqrt{1 + 4\xi_1^2} \quad (5.29)$$

Once parametric excitation occurs, the oscillation builds up. So the evaluation of amplitudes of oscillation in the instability regions requires the accounting of the cubic term of equation (5.25) in the solution of the dynamic equilibrium equation. The presence of this term does not affect the definition of the transition regions, according to Nayfeh and Mook [76] and Clement and Cremona [78]. Therefore, the threshold values defined above for the beginning of instability hold. In fact, the effect of adding this cubic term is that the amplitude of oscillation will not grow unlimitedly inside an instability region, but will converge instead to a finite-amplitude value. Tagata [75], Pinto da Costa *et al.* [77] and Clement and Cremona [78], employing the method of harmonic balance, and Nayfeh and Mook [76], using the method of multiple scales, obtained an approximation of the steady-state response in the vicinity of the first resonance ( $\delta \approx 1$ ), which can be expressed as

$$\alpha_1(t) = a \sin \left( \omega t - \frac{1}{2} \psi \right) \quad (5.30)$$

where

$$a = \frac{4}{\pi} \cdot \sqrt{\frac{X_0 \ell}{3}} \cdot \frac{1}{\delta} \cdot \left\{ 1 - \delta^2 \pm \left[ \delta^4 \cdot \left( \frac{x_B}{2X_0} \right)^2 - 4 \delta^2 \xi_1^2 \right]^{\frac{1}{2}} \right\}^{\frac{1}{2}} \quad (5.31)$$

and

$$\tan \psi = - \frac{2\xi_1 \delta^2}{2(1-\delta) - \delta^4 a^2} \quad (5.32)$$

Equation (5.31) is plotted in Fig. 5.10 for the cable studied in the previous Section (Fig. 5.3), considering two values of the relative support motion  $x_B/(2X_0)$ , of 0.05 and 0.3, and a damping coefficient of 1%. The non-linearity of the differential equation induces, as can be observed from this Figure, a bending of the frequency-response curves into the right (the cable behaves as a hardening spring), which leads to multi-valued responses and, consequently, to a so-called *jump* phenomenon. The evolution of the amplitude of the response is represented by the arrows in Fig. 5.10, where it can be observed that in a vicinity of the first parametric resonance ( $\delta \approx 1$ ) the trivial solution is not stable.

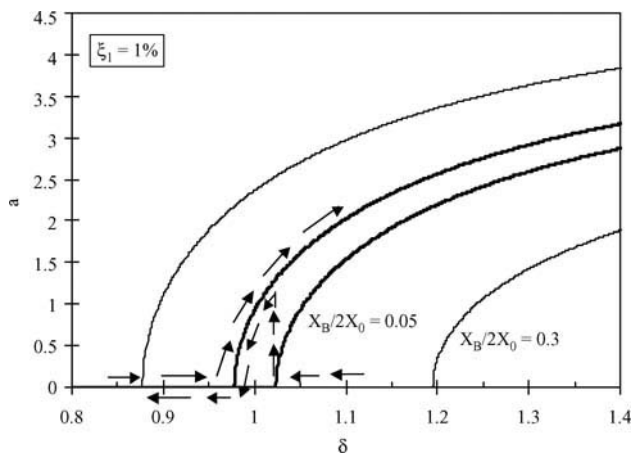


Fig. 5.10: Frequency-response functions for a stay cable subjected to two different amplitudes of support motion:  $x_B/(2X_0) = 0.05$ , and  $x_B/(2X_0) = 0.3$

As for the increment of cable tension, the following expression can be obtained

$$\tau(t) = \frac{EA_0}{\ell} \cdot \left[ x_B \sin 2\omega t + \frac{\sqrt{2}\ell}{\pi} \cdot \frac{mg}{T} \cdot \alpha_1(t) + \frac{\pi^2}{8\ell} \cdot \alpha_1^2(t) \right] \quad (5.33)$$

with  $\alpha_1(t)$  given by equation (5.30). In addition to the excitation term, this expression encloses, as in the case of *external excitation*, a non-negligible term in the double frequency.

For the vicinity of the second parametric resonance ( $\delta \approx 2$ ), the steady-state amplitude of oscillation can be approximated by [78]

$$a \approx \frac{4}{\pi} \cdot \sqrt{\frac{X_0\ell}{3}} \cdot \left[ \frac{2\delta^2 \cdot \left( \frac{x_B}{2X_0} \right)^2 + 4 - \delta^2}{3\delta^2 - 8} \right]^{\frac{1}{2}} \quad (5.34)$$

### 5.3.2 Application to a stay cable

Using the finite element model described by Fig. 5.3 for the stay cable of the Ben-Ahin bridge and a nonlinear geometric formulation, the amplitude of steady-state response was calculated for a longitudinal harmonic motion at the anchorage at twice the linear natural frequency of the cable. Different amplitudes of support motion and a damping coefficient of 1% were considered. Both the analytical (equation (5.31)) and the numerically calculated amplitude of the steady-state oscillation are represented in Fig. 5.11(a). The agreement between the two estimates of steady-state response is very good. Also, it can be observed, by comparison with the *external excitation* response represented in Fig. 5.4, that *parametric excitation* induces amplitudes of vibration that almost double the amplitude of oscillations induced by *external excitation* for identical amplitudes of oscillation. However, in contrast to external excitations, parametric excitation occurs

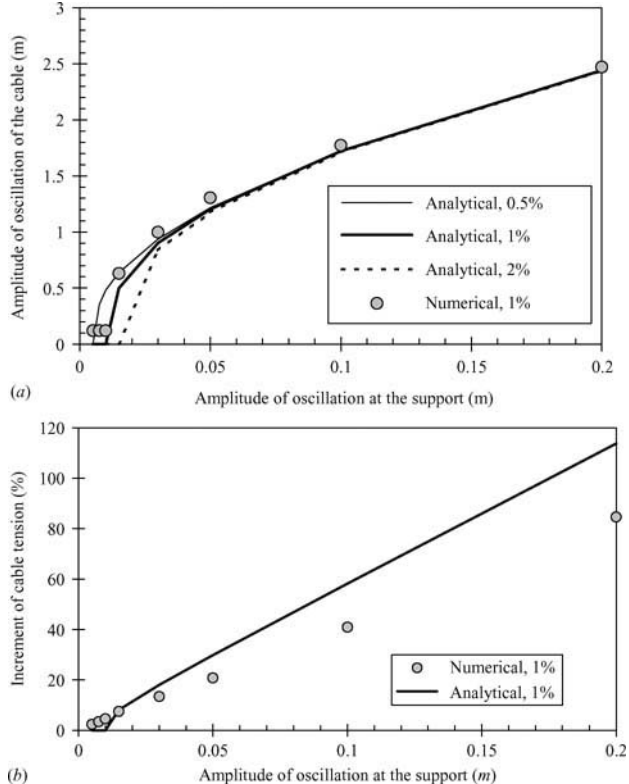


Fig. 5.11: Numerical versus analytical amplitude of the steady-state response at the principal parametric resonance: (a) amplitude of cable oscillation; (b) maximum increment of cable tension

only for longitudinal oscillations greater than  $0.006\text{ m}$  or  $0.012\text{ m}$ , for damping coefficients of 0.5 and 1%, respectively.

The variation of the maximum value of  $\tau(t)$  given by (5.33) with the amplitude of support oscillation is represented in *Fig. 5.11(b)*, assuming that the quantity  $\psi$  in equation (5.30) is very small.

The comparison between analytical and numerical response shows a rather good agreement, the theoretical response leading in general to greater values of the increment of cable tension for high amplitudes of support oscillation.

An important aspect to consider is that damping is important only to prevent parametric excitation. Once the oscillations set up, the amplitude is almost independent of the corresponding value.

### 5.3.3 Practical occurrence of external/parametric excitation

With regard to the practical occurrence of vibrations in cable-stayed bridges, induced by *parametric/external excitation*, some authors consider that, given the relatively large amplitudes of deck vibration required for the onset of oscillations, the phenomenon happens to be rare. The threshold amplitude of oscillation in the direction of the chord  $x_B$  has been calculated for some cable stays based on the characteristics reported in the literature and on three possible damping coefficients: 0.2%, 0.5% and 1%. *Table 5.2* summarises the obtained values of  $x_B$ , as well as the amplitudes of steady-state oscillation  $a$  for a sinusoid support excitation of  $2\text{ cm}$  amplitude at twice the cable frequency ( $\delta = 1$ ). Knowing that various centimetres of deck oscillation can be measured during strong events of wind excitation, parametric excitation does not seem unfeasible for small damping coefficients, especially those smaller than 0.5%. But another requirement should be added, which concerns the persistence of oscillation for a certain period. In fact, numerical simulations have shown the presence of a transient for a period that depends both on the amplitude of support oscillation and on the damping coefficient of the stay cable, that can last for more than 3 minutes.

Referring to reported cases concerning parametric oscillation events, although it has not always been possible to identify with certainty the real causes of instability observed in some bridges because several causes may be present together in many circumstances, the following examples can be cited: In the Ben-Ahin and Wandre bridges in Belgium, amplitudes of vibration of  $0.50\text{ m}$  and  $0.30\text{ m}$ , respectively, were observed, accompanied by a slight vibration of the deck. Although attributed to the combined action of rain and wind, it is also thought that the motion of the cable supports (deck) may have enhanced these vibrations [68, 82]. Other cases where support motion or, more precisely, an interaction between cable and deck/towers vibration were observed, are the Annacis bridge in Canada [2], the Farø bridges in Denmark [58], the Helgeland bridge in Norway [83], the Erasmus bridge in the Netherlands [65], and the Burlington and the Second Severn Crossing bridges in US and UK, respectively [19]. On the Guazú bridge in Argentina, a stay cable broke due to corrosion and fatigue. It was proved that part of the problem was the high cable vibration resulting from the large motion of the bridge deck at certain wind speeds and directions [144]. Recent observations of large oscillations at the Guadiana bridge in Portugal have been investigated [84]. In this case it was observed that even though very large cable oscillations were attained, showing a strong parametric interaction with deck oscillation, the levels of measured deck oscillation were much lower than the threshold values calculated, based on the formulae referred to above.

Cable	$L$ (m)	$f_1$ (Hz)	$X_0$ (m)	$x_B = 2$ cm					
				$x_B$ (mm)			a (m)		
				$\xi_1 = 0.2\%$	$\xi_1 = 0.5\%$	$\xi_1 = 1.0\%$	$\xi_1 = 0.2\%$	$\xi_1 = 0.5\%$	$\xi_1 = 1.0\%$
V. Gama									
HC01	34.7	3.145	0.0783	0.6	1.6	3.1	0.43	0.43	0.43
HC24	226.0	0.576	0.7181	5.7	14.4	28.7	1.08	0.92	
HC15	147.5	0.814	0.3946	3.2	7.9	15.8	0.89	0.86	0.70
Guadiana									
Central 1	168.5	0.763	0.5407	4.3	10.8	21.6	0.94	0.88	
Central 16	49.5	3.239	0.2055	1.6	4.1	8.2	0.52	0.51	0.49
Normandy	440.9	0.257	1.0389	8.3	20.8	41.6	1.47		
Ikuchi*	246.2	0.446	0.5025	4.0	10.0	20.1	1.14	1.07	

Table 5.2: Threshold amplitude of oscillation for parametric excitation in the first instability region,  $\delta = 1$ . Amplitude of cable vibration for  $x_B = 2$  cm

## 5.4 Cable-structure Interaction

The dynamic interaction between the stay cables and the deck/towers has been proved on several occasions in the past, in situations where the vibration of the deck produced oscillation of some cables or vice-versa. Various situations reported in the literature are referred to in the previous Section. Using as reference the traditional separate modelling of the dynamics of the global bridge and of stay cables, a research centred on the experimental testing of a physical model by Caetano [85] has shown that dynamic cable-structure interaction may have both a favourable and an unfavourable role in the overall bridge behaviour, depending on the input level of vibration, on the damping coefficients and on the relation between cable and bridge natural frequencies.

In order to illustrate the main characteristics of the phenomenon, a simplified study of a cable-bridge system is presented. The system consists of a horizontal taut cable (with the characteristics of the Ben-Ahin stay cable) connected to a mass-spring system according to the representation of Fig. 5.12. The mass-spring system is given by an association of a mass  $M_1$  of 15 000 ton with a stiffness  $K_1$  of 3.70 GN/m. These characteristics have been defined in order to obtain a frequency of the spring/mass system corresponding to twice the fundamental frequency of the cable.

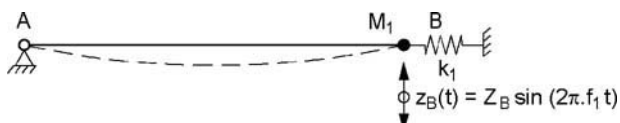


Fig. 5.12: Simplified system for the study of cable-structure interaction

The idea is that the steady-state increment of cable tension for *external excitation* at fundamental resonance given by (5.19) is characterised essentially by a component in the resonance frequency and by a component in the second harmonic, which depends on the square of the amplitude of cable oscillation. For large amplitudes of support oscillations, the latter component may be significant. If, additionally, the cable is connected to a system whose frequency is in resonance with this second harmonic, then an amplification of the tension will occur and will induce *parametric excitation*, magnifying the amplitudes of oscillation of the stay cable. On the contrary, for small amplitudes of oscillation, the *parametric excitation* term will be very small. A phase delay in the term  $\alpha_1(t)$  defined both for *external* (expression (5.15)) and *parametric* (expression (5.30)) excitations, may inclusively reduce the amplitudes of oscillation. The two contradictory effects are evident in the representations of Figs 5.13(a) and 5.13(b), which show the variation of the maximum steady-state amplitude of vibration and increment of cable tension, respectively, with the amplitude of support excitation at fundamental resonance, calculated either neglecting the effect of cable-structure interaction (cable horizontally fixed at supports), or considering that interaction (system of Fig. 5.12).

In practice it can be said that whenever the bridge exhibits global frequencies that are close to the cable frequencies or to twice those frequencies, it is expected that cable-structure interaction is more significant and therefore the dynamic analysis of the bridge should include a simultaneous description of the bridge and cable mass. But it is also important to stress that the information provided by such a model is essentially of a qualitative nature, given the uncertainties associated with the prototype characteristics, namely the exact tension in the stay cables and the very localised frequency character of the resonance phenomena associated with

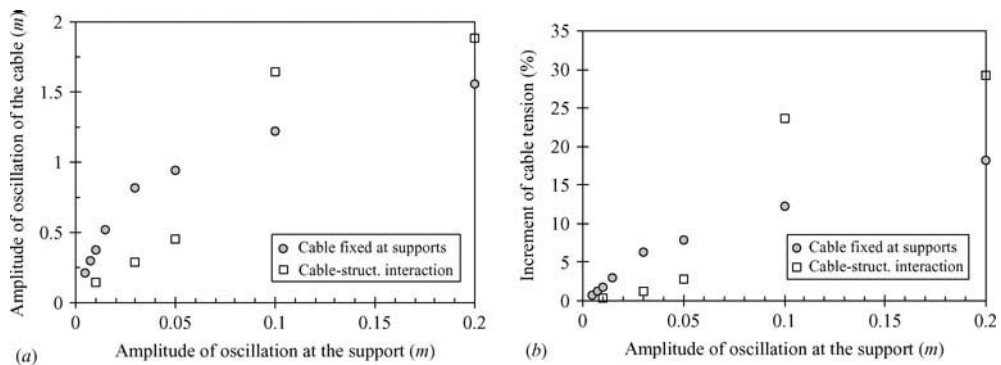


Fig. 5.13: Variation of the: (a) amplitude of oscillation and; (b) increment of cable tension with the amplitude of vertical support excitation

small structural damping. This explains why oscillations of parametric type are frequently observed only for one of the two “identical” stay cables anchored at opposite sides of the deck.

# 6. Control of Vibrations in Cable-Stayed Bridges

## 6.1 General

Once the mechanisms that generate cable vibration have been identified, appropriate countermeasures to reduce or suppress large oscillations should be taken. These countermeasures can be implemented at the source, in such a way that the generation of vibrations is limited, or at the structure, through the installation of control systems that have the effect of limiting the response, either by de-tuning the cables or by increasing their damping. In general, these measures can be classified into three types, namely *aerodynamic*, *structural* and *mechanical*, and belong to a category of so-called *passive techniques of control*. Although extensively used around the world with proven effectiveness in structural performance, these techniques have inherent limitations [86]. In recent years, however, some attempts have been made to implement *active* and *semiactive control* techniques, using some technological transfer from the area of Control Engineering to Structural Engineering. *Active* and *semiactive* control are, in effect, extensions of *passive control techniques* where the structural motion is controlled or modified by an actuator commanded by a control system through external supply of energy. These systems may actually combine the three types of measures described above with *passive control* devices. Practical applications of these devices are however at the research stage and will not be considered in the current publication.

The following Sections present a brief description of possible systems for control of vibration, focusing in particular on the installation and design of dampers and tuned-mass dampers in cables, the most commonly used approaches.

## 6.2 Vibration Control Systems

The occurrence of cable vibrations can be prevented or limited by specific operation conditions and maintenance procedures. For the case of indirect vibrations, i.e. vibrations generated by oscillation of the anchorages, possible implementation measures include limiting the number, speed and mass of crossing vehicles and maintenance of the road surface. Deeper interventions may attempt to modify the shape (*aerodynamic control*), the mass and stiffness (*structural control*), or the damping (*mechanical control*). For indirect oscillations, these measures can be introduced both at the deck and towers, while direct oscillations require the introduction of control systems on the cables.

### 6.2.1 Aerodynamic control of vibrations

The *aerodynamic control* of vibrations is performed by modifying the cross sectional configuration. For the bridge deck, some appendages are attached, as represented in Fig. 6.1

(round fairings, triangular fairings, splitter plates and flaps) to prevent the occurrence of vortices and achieve the streamlining effect.

For the bridge towers, either deflectors can be installed, or the corner edges can be cut (*Fig. 6.2*).

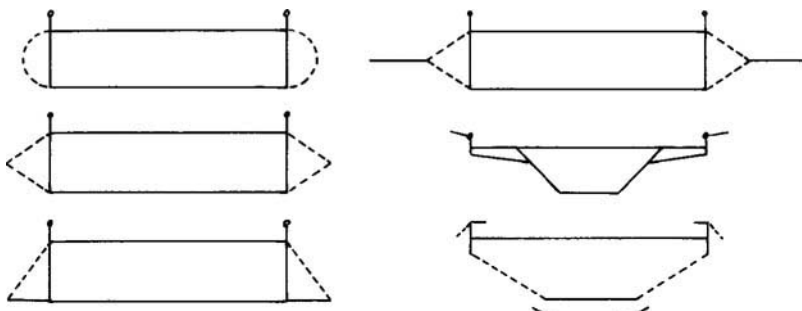


*Fig. 6.1: Examples of aerodynamic appendages for a bridge deck*

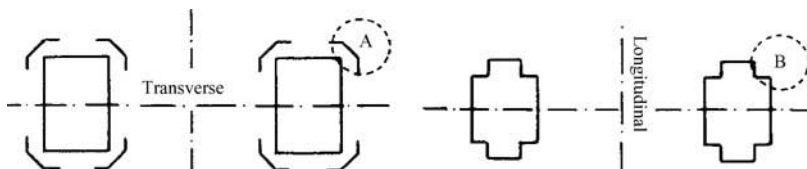


*Fig. 6.2: Examples of aerodynamic control of vibration for bridge towers: A: deflectors; B: corner edge cuts*

Although modification of the shape of cables is limited, recent studies [33, 64, 87] have proved that, by roughening the polyethylene surface of the cable sheath, the formation of water rivulets is prevented and, consequently, rain-wind induced vibration of the cables is suppressed. Examples of applications of this concept have been presented in *Fig. 4.57*. The main drawback of this procedure is the risk of increasing the drag force for the design wind speed in comparison with the drag force on the normal smooth cable. This aspect is particularly relevant for long span cable-stayed bridges, as the wind load on the cable system is a significant part of the overall wind load. It is however possible to control the drag forces, if a convenient roughness arrangement is chosen. This was proved by Miyata *et al.* [88] who performed a series of wind tunnel tests on cable models with different densities and arrangements of dot surface roughness, arriving at the final dimpled surface presented in *Fig. 4.57(c)* for the cables of the Tatara bridge.

Finally, another form of *aerodynamic control of vibrations* consists in adopting a specific cable arrangement. For PC cable-stayed bridges, a closely spaced arrangement significantly changes the flow around the cables. This solution was effective in preventing wake-induced vibration at the Ikara Island bridge in Japan [89].

### 6.2.2 Structural control of vibrations

*Structural control of vibrations* by interconnecting ropes has been used very frequently, either temporarily, before the installation of damping devices on the cables, or as a permanent measure. The use of cross-cables was first proposed (although never implemented) by Leonhardt for the Messina Straits Crossing [90], with the aim of achieving a stiffer system by reducing the cable sag. Later, cross-cables were used in several cable-stayed bridges, with the purpose of suppressing cable vibrations, or preventing cable-structure interaction. Examples of bridges where this system was installed according to the schemes presented in *Fig. 6.3*, are the Farø bridge in Denmark [58], the Helgeland bridge [83] in Norway, and the Yobuko bridge [91] in Japan.



Fig. 6.3: Scheme of cross-cable systems installed at: (a) Farø; (b) Helgeland; (c) Yobuko bridges

In terms of structural behaviour, the addition of cross-ropes to the stay cable system creates intermediate supports at those elements and, consequently, increases their natural frequencies for vertical vibrations. With a proper design of these ropes, the fundamental frequency of the stay cables is shifted to relatively high values, thus reducing the possibility of internal resonance with global bridge modes at the fundamental mode shapes. Another effect of the installation of cross-cables is an increase of the damping. A study by Yamaguchi [91] showed that this increase is higher for soft secondary cables than for taut ties. However, the initial tension on these cables should have a sufficiently high value, so that under extreme effects the cross-cables are not detensioned, producing



Fig. 6.4: Cross-cables at the Normandy bridge (Courtesy of Paul Kozlowski, in [www.Structurae.net](http://www.Structurae.net))

shocks and causing damage to the tie devices, as reported by Virlogeux [19] in the Farø bridge and some of the Honshu-Shikoku bridges. In the case of the Normandy bridge, given the closeness of the main vertical global bridge frequency ( $\approx 0.22$  Hz) to the longer cables' frequencies, the designers decided to use taut cross-cables made of ropes with a short pitch length (Fig. 6.4), which led to an increase of those cables' frequencies to around 0.66 Hz, and provided a high internal damping and a satisfactory resistance to fatigue [19, 92].

### 6.2.3 Mechanical control of vibrations

The *mechanical control of vibrations* is achieved by installing damping devices at certain locations along the bridge structure. The Forth Road bridge, completed in 1964 in Scotland was the first, according to Narita and Yokoyama [46], to have a damper installed in the tower, which consisted of a 16 t concrete block connected by rope wire at the tower top (150 m) that dissipated energy by Coulomb friction effect when moving on the ground. This type of damper was subsequently used during construction in several other bridge towers in Japan, such as the Kammon bridge, the Innoshima bridge and the Kita-Bisanseeto bridge. Oil dampers have been used in more recent applications, providing better results. Alternative devices for installation either at the bridge towers or inside the bridge deck are the *Tuned Mass Dampers* (TMD) and *Tuned Liquid Dampers* (TLD).

*Tuned mass dampers* are associations of sprung masses (typically 1% to 2% of the overall structure mass) and dashpot systems which, when properly tuned and attached at convenient locations along the bridge structure, reduce its dynamic response near resonance. The effectiveness of these systems, that were initially used in the aircraft and automobile industry, was first proved by Den Hartog [93]. Later applications to Civil Engineering structures include the road decks of the Kessock bridge, in Scotland [94], the Chao Phya bridge in Bangkok [95], and the Normandy Bridge, during construction [96], and the towers of the Aratsu-Ohashi bridge, Japan [69], the Yokohama Bay bridge [97], the Chao Phya bridge and the Meiko-Nishi bridge, during construction [98]. Figure 6.5 presents a photograph and scheme of the TMD installed at the Normandy bridge deck during construction. A response reduction of 35% was observed for the bridge under wind excitation using this device. Figure 6.6 presents the scheme and location of a set of TMDs installed at the Yokohama Bay bridge.

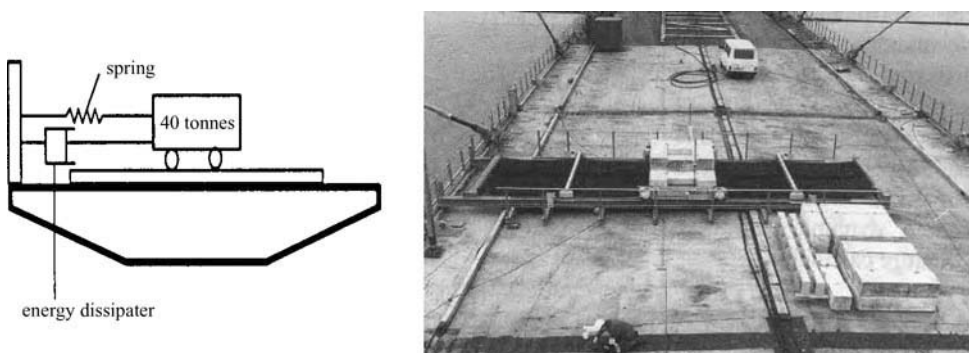
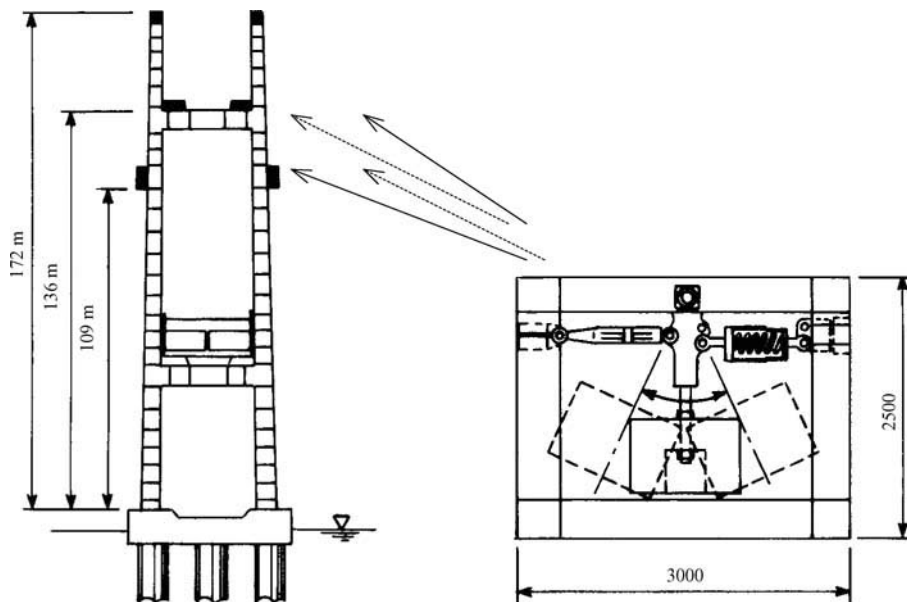


Fig. 6.5: TMD of the Normandy bridge, scheme and photograph [96]



*Fig. 6.6: Location and scheme of TMDs installed at the towers of the Yokohama Bay bridge [97]*

Tuned mass dampers can also be installed in stay cables. Although a significant increase of damping can be achieved for the tuned vibration mode [27], the efficiency of these devices is limited whenever more than one vibration mode is induced.



*Fig. 6.7: Hydraulic dampers at: (a) Iroise (Courtesy of O. Flamand) and (b) Aratsu bridge [101]*

*Tuned liquid dampers* use the motion of liquid inside a container as energy dissipator. Although several applications of these devices are known (mainly for tall buildings and towers), the physical phenomenon of the liquid sloshing motion that reduces the structural response is not fully understood, particularly for large amplitude excitation [99], and the numerical modelling has not yet been completely assessed.

The installation of hydraulic or viscous dampers close to the stay cables' anchorages is a classic and efficient solution for suppressing cable vibrations. The damping capacity of external dampers is defined according to a specified requirement. In general, it is considered that viscous dampers have low maintenance costs, but show a dependence of damping characteristics with temperature and frequency, while hydraulic dampers have high maintenance costs and a complex adjustment [100]. Another reported inconvenience associated with these mechanical devices is the lowering of the aesthetical quality of the bridge.

The first known application of external dampers in cable-stayed bridges is in the Brotonne bridge, where two oil dampers were attached at an angle close to the lower cable anchorage of each stay cable. This system was used in several other bridges around the world. *Figure 6.7* presents photographs of the devices employed at the Iroise (France) and Aratsu (Japan) bridges.

A recent innovation consists in the use of the so-called internal dampers, which are devices composed by a ring made of neoprene, high damping rubber, or other viscous products placed inside the cable pipe (the deviator guide). The scheme of a ring damper mounted at the lower end anchorage is shown in *Fig. 6.8*.

According to Fuzier *et al.* [92] the internal ring dampers need virtually no maintenance and can provide sufficient damping for cables of 350 m length. *Figure 6.9* shows an internal damper installed at one stay of Vasco da Gama bridge, which combines a high damping rubber ring with a viscous damper composed by a chamber where oil is placed. Logarithmic decrements of 3.8–5.8% were attained for the cables of this bridge.

It is necessary to emphasise the difference between an internal damper and the neoprene rings placed around the cable close to its anchorages with the purpose of reducing bending

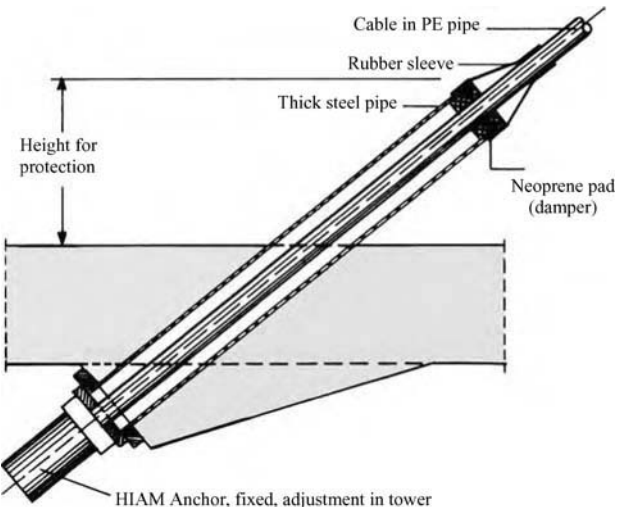


*Fig. 6.8: Scheme of ring damper*



*Fig. 6.9: Internal damper installed on a stay cable of Vasco da Gama bridge*

stresses. These are normally made of elastomer and provide an elastic support, and a variable increase of damping, that depends on the degree of pre-compression in the ring. Ignoring the component of damping increase, Main and Jones [102] have shown that the addition of these devices leads to an effective reduced distance of the damper to the end of the cable and consequently reduces the maximum attainable damping ratio in each mode and increases the optimal value of external damper constant.

Finally it is relevant to refer to the possibility of increasing cable damping by using an adequate grout filler. The study of Tabatabai and Mehrabi [27] on scaled 1:7 physical models of a representative stay cable showed that latex filler provided an increase of 60% of damping with respect to conventional cement grout. However, given the extremely low damping associated with the latter (the measured damping on the scaled model was around 0.05%), these authors concluded that this treatment is not effective in avoiding cable vibrations.

### 6.2.4 Active control—systems

The basic scheme of an *active control system* includes the following components: (i) sensors located on the structure for measurement of external excitations and/or structural responses; (ii) devices to process the measured information and compute the necessary control forces, according to a specified control algorithm (closed loop, open-loop, or open-closed loop); and (iii) actuators, usually driven by external sources. Basically, the control system can follow two strategies, according to the chosen control algorithm, the first corresponding to a modification of the structural stiffness and damping so that the structure can respond favourably to the external excitations (closed-loop), and the second, consisting in the reduction or elimination of the external forces (open-loop).

The main control mechanisms studied for application in the specific domain of bridges are: (i) *active aerodynamic appendages*; (ii) *active mass dampers*, and (iii) *tendon control*.

#### 6.2.4.1 Active aerodynamic appendages

The idea of applying *active aerodynamic appendages* in ultra-long-span bridges was first introduced by Ostenfeld and Larsen [103], inspired by principles used in the stabilisation of surfaces in the aircraft industry. Two concepts were suggested, as represented in Fig. 6.10. The first (Fig. 6.10(a)), consists in actively changing the geometry of the side of a streamlined box bridge deck, modifying the flow pattern around the girder to reduce wind-induced excitation. The second (Fig. 6.10(b)) consists in the addition of control surfaces attached beneath the edges of the deck by aerodynamically shaped pylons at a convenient distance. The rotation of the surfaces by means of hydraulic actuators produces aerodynamic forces that stabilise the structure, increasing the critical wind speed. Recent studies [104] showed that a great advantage of this technique of control over the structural methods is the fact that the source of stabilising forces, the wind, is actually the same as the source of the aerodynamic forces that causes instability. However, the practical implementation is very complex, requiring the design of two or three parallel control systems, to ensure that the failure of a controller does not cause the collapse of the bridge.

#### 6.2.4.2 Active mass dampers

In contrast to *TMDs*, which are designed to reduce the response in only one mode of vibration, usually the fundamental one, *Active Tuned Mass Dampers (ATMDs)* can be effective over a wide frequency range. These devices have been studied in recent years with the purpose of

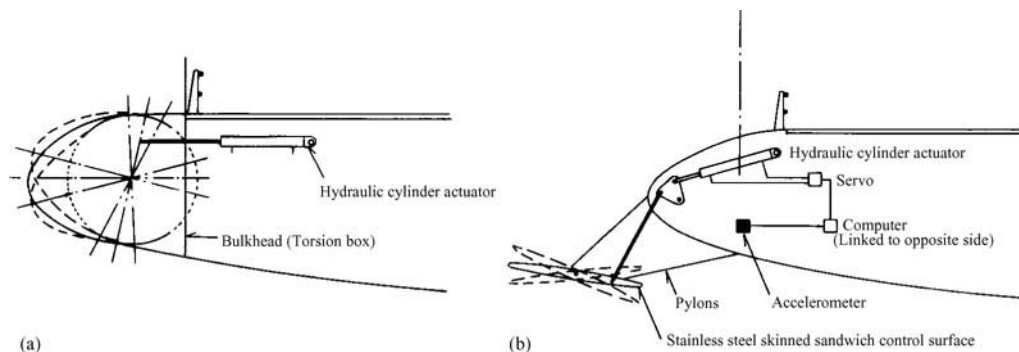


*Fig. 6.10: Suggestions for implementation of active control surface systems in streamlined bridge girders [103]*

application to tall buildings [105]. Wind tunnel tests [106] have shown in particular that the efficiency of a *TMD* can be achieved with an *ATMD* of 60% mass using simple control algorithms. However, these devices are still at the experimental phase of research.

#### 6.2.4.3 Active tendon control

Finally, *active tendon control* has been considered by several authors as a possible alternative technique to control cable vibrations, particularly for long span cable-stayed bridges, in which the application of passive dampers near the cable anchorage is less effective. Studies in *active tendon control* have been developed in two directions: the modal control, which uses the axial motion of the cable-support [107, 108], and the wave-control approach that applies transversal control forces in the cable span support [109]. Given the number of cables on a typical cable-stayed bridge and the need for individual control of each cable using external power sources, either technique of active control may encounter many practical implementation difficulties. Very recent research is focusing on the so-called *semiactive damping* devices. Unlike active devices, which can induce unfavourable forces in the structure if not appropriately tuned, *semiactive dampers* can only exert dissipative forces [110].

## 6.3 Design of an Optimal Passive Damper

### 6.3.1 General

It has been explained that increasing cable damping is one of the most efficient techniques to avoid vibrations in cable-stayed bridges. Not only are local stay vibrations less prone to occur, but stay cables may also act as tuned mass dampers in the control of deck vibrations induced by wind and traffic.

As a rule of thumb, and given that in a great majority of cases, cable vibrations are due to the combined action of rain and wind, the damping ratio  $\xi$  of a stay cable should be defined in order to guarantee that the Scruton number  $S_{c0}$  ( $S_{c0} = m\xi/\rho D^2$ ) is greater than 10 [40]. In practical terms, this means that, for the majority of stay cables, a damping ratio of 0.7% is sufficient to avoid vibration problems [27].

A thorough study of the stay cable can however be developed, in which a maximum amplitude of oscillation is specified for a particular wind or load condition, which leads to lower required damping ratios.

Given that undamped stay cables exhibit in general damping ratios in the range 0.05% to 0.5% [27], mechanical devices should be installed to achieve the required damping level.

The current Section focuses on the design of a passive damper (internal or external), mounted close to the cable anchorage, presenting the available methodology to derive the damping characteristics of such devices.

### 6.3.2 State-of-the-art of research

The problem of defining the optimal characteristics of a damper installed at a point close to the anchorage of a cable was studied by Kovács [111], who proposed a practical optimal damping estimation method and empirically defined the maximum attainable modal damping. Yoneda and Maeda [112] developed empirical equations to define the optimum damper size and corresponding modal damping. Uno *et al.* [113] extended this work, introducing non-dimensionalised damping coefficient, but it was Pacheco *et al.* [114] who introduced a universal curve for estimation of modal damping of stay cables, taking into consideration the following parameters: damping ratio, mode number, damper size, cable length, mass and fundamental frequency. This universal curve can be applied to taut cables ( $\lambda^2 < 1$ ) where the distance of damper to anchorage is within a few percent of cable length (e.g. 1%–10%). Two different approaches can be followed:

1. Choice of damper size or location, for the required amount of damping of a particular mode;
2. Estimation of additional modal damping at other vibration modes, once a particular size and location of damper are selected.

Although a universal curve is extremely useful for design applications, the corresponding graph is achieved on the basis of a complex eigenvalue analysis that requires the use of several hundred terms, say 200–300, for each point of the graph. In this context, it is relevant to refer to the studies of Krenk [115], who derived an analytical formula for this universal curve, as the asymptotic result of a complex mode analysis.

Considering that current applications of cable-stayed bridge construction have resulted in longer cables, with Irvine parameters  $\lambda^2 \geq 1$ , and where sag effects can be significant, leading to a decrease of damper effectiveness, Crémona [116] extended the universal curve introduced by Pacheco *et al.* to inclined cables, with a sag/span ratio no greater than 1:8, and with an Irvine parameter no greater than  $4\pi^2$  (first transition region), covering therefore all stays from cable-stayed bridges. Krenk and Nielsen [117] derived an extended asymptotic solution for shallow cables, giving evidence of the reduction of efficiency of the damper as a function of the Irvine parameter.

From the analysis of a US cable-stayed bridge database, Tabatabai and Mehrabi [118] noticed that 95% of the stay cables have Irvine parameters no greater than one, and also that the reduction of damping coefficient associated with curvature effects affects essentially the first vibration mode. These authors have however pointed the dependence of modal damping on the cable bending stiffness, and derived a design formula expressing that dependence, from the numerical analysis developed over the cable database.

Hoang and Fujino [119] provided a deeper insight into the effects of bending stiffness on the performance of viscous dampers installed in taut cables. These authors [120, 121] as well as Krenk and Hogsberg [122] explored the effect on the performance of dampers induced by other

factors, such as the damper flexibility or the flexibility of the support and the non-linearity of behaviour.

### 6.3.3 Problem formulation

#### 6.3.3.1 Taut cable

The dynamic equilibrium equation (B.1) that describes the lateral vibrations of the stay cable of uniform cross section presented in Appendix B is now modified for the stay cable with an attached viscous damper represented in Fig. 6.11, assuming in the first instance a taut cable, and neglecting both the static deformation and the dynamic component of tension

$$H \frac{\partial^2 w}{\partial x^2} = m \cdot \frac{\partial^2 w}{\partial t^2} + c \frac{\partial w}{\partial t} \cdot \delta(x - x_c) \quad (6.1)$$

In this equation  $H$  represents the static cable tension,  $m$  is the mass per unit length,  $c$  is the viscous damper constant,  $\delta$  is the Dirac function,  $x_c$  is the distance of the damper to the cable anchorage,  $w$  is the transverse displacement from the static configuration,  $x$  is the coordinate along the chord, and  $t$  represents time.

As shown by Kovács [111] and illustrated in Fig. 6.12, the effect of adding a viscous damper depends on the constant  $c$  of the damper. Neglecting the intrinsic cable damping, it can be inferred that for  $c = 0$ , the first vibration mode is undamped (Fig. 6.12(b)), and the dynamic amplification curve associated with the cable tends to infinity at the fundamental frequency  $\omega_{01}$ . When  $c = \infty$ , i.e. when a very large damper is installed, the force generated is so large, that it blocks the cable at the damper, therefore acting as if there was a support at that location (Fig. 6.12(c)). The consequence is a slight modification of the fundamental cable frequency to  $\omega_{01}/(1 - x_c/L)$ , but once more the mode of vibration is undamped and the corresponding dynamic amplification curve tends to infinity at the frequency  $\omega_{01}/(1 - x_c/L)$ . The optimal damper is characterised by a constant  $c_{opt}$  that provides the amplification curve represented by the solid bold line in Fig. 6.12(d), whose maximum value is approximated by  $L/x_c$ , and occurs at the frequency at which the two previously referred to amplification curves intersect,  $\Omega \approx \omega_{01}(1 + x_c/2L)$ . The modal damping associated with this system is the maximum and is given by

$$\xi_{max} \approx \frac{1}{2} \cdot \frac{x_c}{L} \quad (6.2)$$

Kovács estimated the optimum damper size  $c_{opt}$  as

$$\frac{c_{opt}}{mL\omega_{01}} \approx \frac{1}{2\pi \left(\frac{x_c}{L}\right)} \quad (6.3)$$

It is important to note that the ratio  $x_c/L$  is normally no greater than 0.015, meaning that the maximum damping added by a viscous damper attached close to the anchorage does not

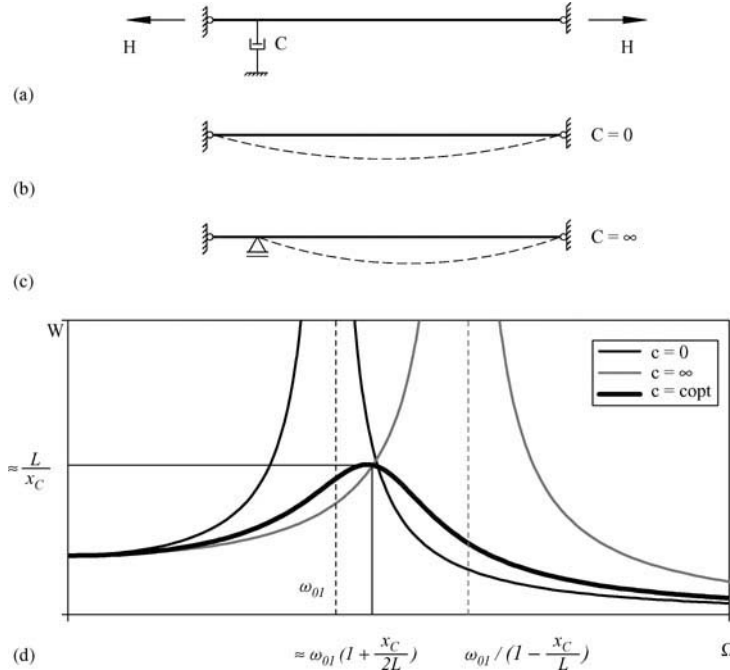


Fig. 6.12: Limiting amplification behaviour characteristics of cable with attached viscous damper: (a) general representation; (b)  $c = 0$ ; (c)  $c = \infty$ ; (d) dynamic amplification curves for  $c = 0$ ,  $c = \infty$  and  $c = c_{opt}$

normally exceed 0.75%. Pacheco *et al.* [114] have shown that the formulae presented here can be extended for higher order modes, ie., the damping ratio  $\xi_{n,\max}$  and constant  $c_{opt,n}$  associated with the  $n^{th}$  order mode are given by

$$\xi_{n,\max} \approx \frac{1}{2} \cdot \frac{x_c}{L} \quad (6.4)$$

and

$$\frac{c_{opt,n}}{mL\omega_{01}} \approx \frac{1}{2\pi n \left( \frac{x_c}{L} \right)} \quad (6.5)$$

In order to define a damping coefficient as a function of the constant  $c$ , Pacheco *et al.* [114] presented a solution to equation (6.1), based on the approximation of the lateral displacement  $w(x, t)$  as a function of the undamped vibration modes  $\phi_{0n}(x)$  of a taut cable

$$w(x, t) = \sum_{n=1}^k b_n(t) \cdot \phi_{0n}(x) \quad (6.6)$$

where

$$\phi_{0n}(x) = \sin \left( \frac{\pi n x}{L} \right) \quad (6.7)$$

Substituting (6.6) for (6.1), applying the following non-dimensionalisation to modal coordinates  $b_n(t)$  and to time  $t$

$$\bar{b} = \frac{1}{L} \cdot [b_1(t) \dots b_k(t)]^T \quad (6.8)$$

$$\tau = \omega_{01} t \quad (6.9)$$

with

$$\omega_{0n} = \frac{\pi n}{L} \cdot \sqrt{\frac{H}{m}} \quad (6.10)$$

and applying the Galerkin method based on the modes  $\phi_{0n}(x)$  as weighting functions, the following system of equations is obtained

$$\underline{M} \bar{b}'' + \underline{C} \bar{b}' + \underline{K} \bar{b} = \underline{0} \quad (6.11)$$

where

$$M_{np} = \delta_{np} \quad (6.12)$$

$$C_{np} = 2 \left( \frac{c}{mL\omega_{01}} \right) \cdot \sin \left( \frac{\pi nx_c}{L} \right) \cdot \sin \left( \frac{\pi px_c}{L} \right) \quad (6.13)$$

$$K_{np} = n^2 \delta_{np} \quad (6.14)$$

and the quantity  $(\cdot)'$  means  $\frac{\partial(\cdot)}{\partial\tau}$ .

The analysis of the terms of the damping matrix  $\underline{C}$  shows that the system is non-proportionally damped. Therefore a state-space formulation should be applied in order to extract complex eigenvalues  $\nu_n$  and from those equivalent damping ratios  $\xi_n$

$$\nu_n = \omega_n \cdot (-\xi_n + \sqrt{-1} \cdot \sqrt{1 - \xi_n^2}) \quad (6.15)$$

Pacheco *et al.* [114] have shown that, assuming small values of  $x_c/L$ , and choosing appropriately the coordinate axes, a curve is obtained (Fig. 6.13), which represents the modal damping of any taut cable for the first few modes of vibration. This universal curve is characterised by a maximum that corresponds to the maximum attainable damping ratio  $\xi_{n,\max}$  of vibration mode of order  $n$ , achieved by the attachment of a damper with optimum constant  $c_{opt,n}$ . These quantities are given by

$$\xi_{n,\max} = 0.52 \cdot \frac{x_c}{L} \quad (6.16)$$

$$c_{opt,n} = 0.10 \cdot \frac{mL\omega_{01}}{n \frac{x_c}{L}} \quad (6.17)$$

and are in close agreement with the solution of Kovács, and also with the results provided by Yoneda and Maeda [112], and by Uno *et al.* [113], as can be observed from Table 6.1.

The interest in the use of the universal curve is that, not only can an optimum viscous damper be designed for a particular vibration mode of a cable whose damping coefficient has been specified, but the achieved damping coefficient for other vibration modes can also be estimated.

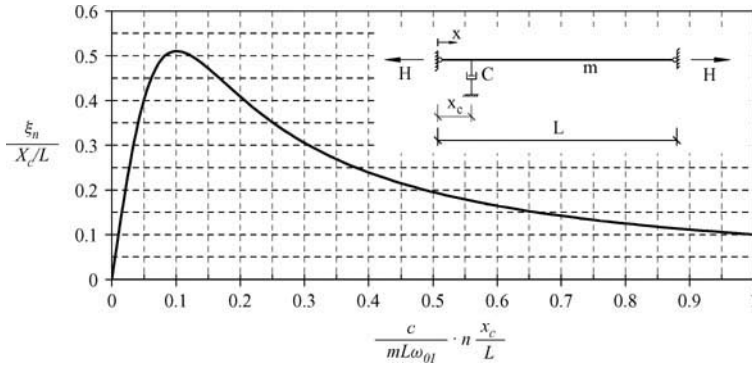


Fig. 6.13: Universal curve relating modal damping ratio  $\xi_n$  with damper size  $c$ , location of damper  $x_c$  and cable parameters,  $m$ ,  $L$  and  $\omega_{01}$

Authors	$c_{\text{opt},n}$	$\xi_{n,\text{max}}$
Pacheco <i>et al.</i> [114]	$0.10 \cdot mL\omega_{01}/(nx_c/L)$	$0.52 \cdot x_c/L$
Uno <i>et al.</i> [113]	$6.25/(2\pi) \cdot (mL\omega_{01}x_c/L)/[n \sin^2(\pi x_c/L)]$	$3.3/(2\pi) \cdot x_c/L$
Yoneda and Maeda [112]	$6.25/(2\pi) \cdot (mL\omega_{01}nx_c/L)/[\sin^2(\pi nx_c/L)]$	$6.25/(2\pi) \cdot x_c/L \cdot [0.45 + x_c/L]$
Kovács [111]	$1/(2\pi) \cdot mL\omega_{01}/(nx_c/L)$	$0.5 \cdot x_c/L$

Table 6.1: Optimal damping constant and maximum damping coefficient for a viscous damper

The only difficulty in the use of this universal curve is the definition of its points, which, in virtue of the non-proportionality introduced by the damper, requires the solution of a complex eigenvalue problem using a significant number of terms (200–300, according to Pacheco *et al.* [114]).

In this respect, it is interesting to refer to the analytical formulation introduced by Krenk [115], based on the use of complex eigenfunctions to solve equation (6.1) instead of the real undamped eigenfunctions (6.7). As a result, a transcendental equation for the complex eigenvalues  $v_n$  is obtained, which can be expressed as

$$\tan(\beta L) = \frac{i\eta \sin^2(\beta x_c)}{1 + i\eta \cos(\beta x_c) \cdot \sin(\beta x_c)} \quad (6.18)$$

where  $\beta$  is a parameter designated as wave number, relating with the complex frequency  $v$  by

$$\beta = v \sqrt{\frac{m}{H}} \quad (6.19)$$

and  $\eta$  is a non-dimensional damping parameter, defined as

$$\eta = \frac{\pi c}{mL\omega_0} \quad (6.20)$$

Equation (6.18) can be solved numerically using the following iterative scheme for a new estimate of the  $n^{th}$  order wave number at iteration of order  $j+1$ ,  $\beta_n^{j+1}$

$$\beta_n^{j+1} \cdot L = n\pi + \arctan \left( \frac{i\eta \sin^2(\beta_n^j x_c)}{1 + i\eta \cos(\beta_n^j x_c) \cdot \sin(\beta_n^j x_c)} \right), j = 0, 1, \dots \quad (6.21)$$

and using for the first estimate  $\beta_n^0$  the undamped wavenumber,  $\beta_n^0 = n\pi/L$ .

Krenk [115] also developed an asymptotic solution to this equation, which can be expressed in the form

$$\frac{\xi_n}{x_c/L} = \frac{\eta n \pi x_c/L}{1 + (\eta n \pi x_c/L)^2} \quad (6.22)$$

The expression provides a good approximation of the universal curve for the first few modes of vibration, as long as the ratio  $x_c/L$  is small. This effect is illustrated in Fig. 6.14 for the ratios 0.02 and 0.05.

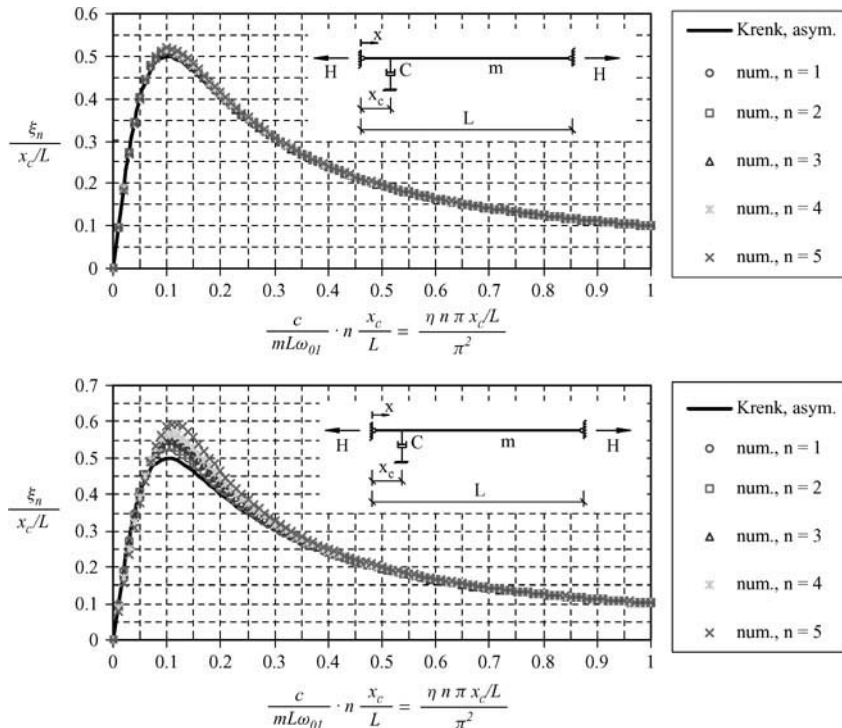


Fig. 6.14: Universal curve, asymptotic and numeric solution for taut cable Krenk [115]

### 6.3.3.2 Shallow cable

Although the universal curve presented above is valid for a wide range of applications, it has been noticed by Pacheco *et al.* [114] that, by comparison with a taut cable, the addition of a viscous damper to a long, sagging cable can lead to a reduction of the achieved optimal damping. This effect was investigated by Crémona [116], who extended the concept of universal curve to sagging cables, based on the formulation of Irvine (see Appendix B), where the effect of the inclination of the cable chord is ignored, and the static profile is assumed as parabolic. The starting point is equation (B.2) for the lateral vibrations of a horizontal sagging cable, which, by addition of a viscous damper (Fig. 6.15), is modified to

$$H \frac{\partial^2 w}{\partial x^2} + h_\tau \frac{d^2 z}{dx^2} = m \cdot \frac{\partial^2 w}{\partial t^2} + c \cdot \delta(x - x_c) \cdot \frac{\partial w}{\partial t} \quad (6.23)$$

This equation is solved based on the decomposition of  $w(x, t)$  according to (6.6), where the functions  $\phi_{0n}(x)$  are now the vibration modes of the sagging cable  $\phi_n(x)$ , which are defined in Appendix B by equations (B.8) and (B.11). These functions coincide with the corresponding functions for taut cables for anti-symmetric (even) modes of vibration.

Substituting (6.6) for (6.23), and defining the quantities  $\gamma_n$  and  $\varphi_n$  as

$$\gamma_n = \frac{1}{L} \cdot \int_0^L [\phi_n(x)]^2 dx \quad (6.24)$$

and

$$\varphi_n = \frac{1}{L} \int_0^L \phi_n(x) dx \quad (6.25)$$

with the vibration mode  $\phi_n(x)$  normalised to mid-span, i.e.  $\phi_n(L/2) = 1$ , the following system of equations is obtained

$$\underline{M} \ddot{\underline{b}} + \underline{C} \dot{\underline{b}} + \underline{K} \underline{b} = 0 \quad (6.26)$$

where

$$\underline{b} = [b_1(t) \dots b_k(t)]^T \quad (6.27)$$

$$M_{np} = \delta_{np} \quad (6.28)$$

$$C_{np} = \frac{c}{m L \gamma_n} \cdot \phi_n(x_c) \cdot \phi_p(x_c) \quad (6.29)$$

$$K_{np} = \omega_n^2 \delta_{np} \quad (6.30)$$

and the quantity  $(\dot{b})$  means  $\frac{\partial b}{\partial t}$ . Note that non-dimensionalisation to time is not considered now, as the successive cable frequencies are not pure harmonics.

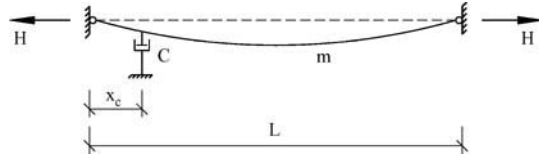


Fig. 6.15: Sagging cable equipped with viscous damper

Once more a non-proportional damping matrix is obtained, requiring the solution of a complex eigenvalue problem.

Crémona verified the existence of a universal curve relating modal damping with damper size and position, and the characteristics of the vibration mode. This curve uses for coordinates the following quantities

$$\text{Abscissa: } a_n = \frac{c}{mL\omega_{01}} \cdot k_n \cdot \frac{x_c}{L} \quad (6.31)$$

$$\text{Ordinate: } \theta_n = \frac{\xi_n}{x_c/L} \cdot G(n) \quad (6.32)$$

The quantity  $k_n$  in expression (6.31) depends on the Irvine parameter  $\lambda^2$ , defined by expression (A.12) in Appendix A, and expresses the ratio between the angular frequency  $\omega_n$  of vibration mode  $n$  and the fundamental frequency of the taut cable  $\omega_{01}$ , defined by (6.10)

$$k_n = \frac{\omega_n}{\omega_{01}} \quad (6.33)$$

The quantity  $G(n)$  is a parameter that depends on the characteristics of the  $n^{th}$  vibration mode, and is defined as

$$G(n) = \begin{cases} \frac{2\gamma_n}{\left(\frac{\sin(\frac{\pi k_n}{2})}{\cos(\frac{\pi k_n}{2}) - 1}\right)^2}, & \text{odd } n \text{ (symmetric mode shapes)} \\ 1, & \text{even } n \text{ (anti-symmetric mode shapes)} \end{cases} \quad (6.34)$$

It is thus clear that the damping characteristics of anti-symmetric modes of shallow cables are identical to those of taut cables. On the contrary, the damping characteristics of symmetric modes depend on the value of the Irvine parameter  $\lambda^2$ . The definition of the universal ordinate  $\theta_n$  by (6.32) and the representation of the variation of  $G(n)$  with  $\lambda^2$  in Fig. 6.16 for the first two symmetric modes ( $n = 1$  and  $n = 3$ ) show that, compared with a taut cable, a sagging cable experiences a reduction of modal damping. This reduction affects essentially the first symmetric mode. The representation in Fig. 6.17 of the variation of  $\gamma(n)$  with  $\lambda^2$  for successive symmetric modes shows that, for higher order modes,  $\gamma(n)$  tends to 0.5 and, consequently,  $G(n)$  approaches unity.

For a very long stay cable, the reduction of modal damping of the fundamental mode can be significant. Considering as an example the longest cable of the Normandy bridge, for which an Irvine parameter  $\lambda^2$  of 3.085 was obtained (see Appendix A), a 30% reduction occurs in the achieved modal damping for the first mode of vibration, by comparison with the taut cable solution (Fig. 6.16, where  $G(1) = 1.43$ ).

It is now relevant to describe the numerical and asymptotic solution to the shallow cable introduced by Krenk and Nielsen [117], as an extension to the taut cable case presented above.

Figure 6.18 introduces the problem, which consists of a shallow cable supported on elastic springs of stiffness  $K_1$  and  $K_2$  at either end, with an attached viscous damper at a distance  $x_c$  from one end. The dynamic equilibrium of this cable is described by equation (6.23), which

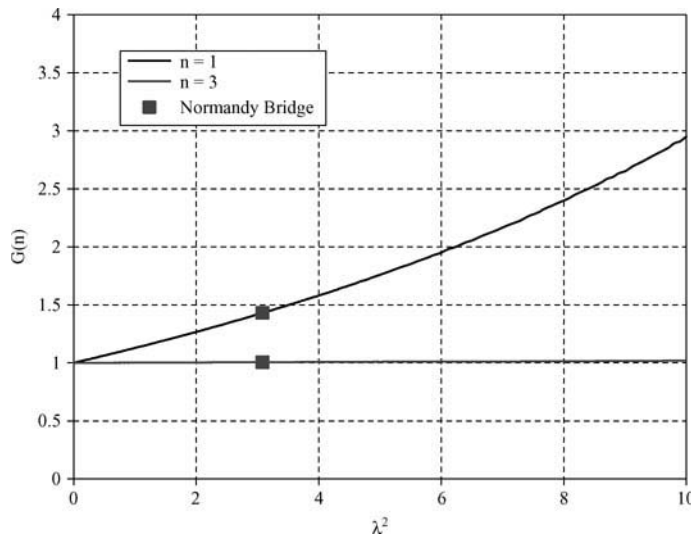


Fig. 6.16: Variation of  $G(n)$  with  $\lambda^2$  for the first two symmetric modes of a shallow cable

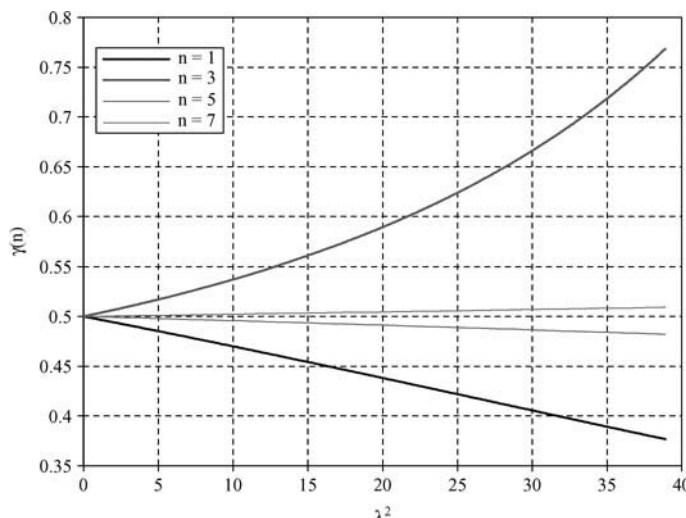


Fig. 6.17: Variation of  $\gamma(n)$  with  $\lambda^2$  for symmetric modes of vibration ( $n = 1, 3, 5, 7$ )

is solved based on complex eigenfunctions, leading to the transcendental equation

$$\begin{aligned} \sin\left(\frac{1}{2}\beta L\right) \cdot \left\{ \sin\left(\frac{1}{2}\beta L\right) - \cos\left(\frac{1}{2}\beta L\right) \cdot \left[ \frac{\beta L}{2} - \frac{4}{\lambda^2} \left( \frac{\beta L}{2} \right)^3 \right] \right\} = \\ = -2i\eta \sin\left(\frac{1}{2}\beta x_c\right) \cdot \sin\left(\frac{1}{2}\beta(L - x_c)\right) \cdot \left\{ \sin\left(\frac{1}{2}\beta L\right) - \cos\left(\frac{1}{2}\beta x_c\right) \right. \\ \left. \cdot \cos\left(\frac{1}{2}\beta(L - x_c)\right) \cdot \left[ \frac{\beta L}{2} - \frac{4}{\lambda^2} \left( \frac{\beta L}{2} \right)^3 \right] \right\} \end{aligned} \quad (6.35)$$

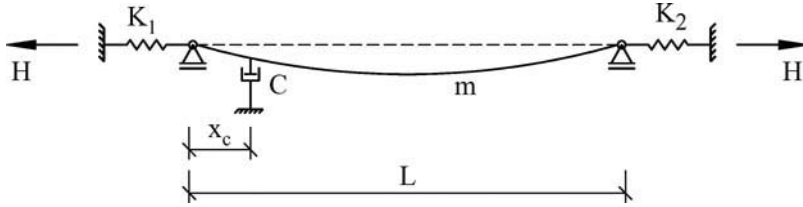


Fig. 6.18: Shallow cable on elastic supports equipped with viscous damper

where  $\beta$  is the wavenumber defined by (6.19),  $\eta$  is the non-dimensional damping parameter defined by (6.20), and the Irvine parameter  $\lambda^2$  combines the elastic stiffness and tension of the cable through

$$\frac{1}{\lambda^2} = \frac{H^3}{(mgL)^2} \cdot \left( \frac{L_e}{EA_0 L} + \frac{1}{K_1 L} + \frac{1}{K_2 L} \right) \quad (6.36)$$

The quantity  $L_e$  in equation (6.36) is defined in Appendix A by expression (A.13).

Equation (6.35) can be solved numerically, considering two sets of branches, one for nearly anti-symmetric solutions, and the other for nearly symmetric solutions.

The anti-symmetric solution can be obtained by an iterative scheme similar to the one described by (6.21) for taut cables, where the  $n^{th}$  order wave number at iteration of order  $j+1$ ,  $\beta_n^{j+1}$ , is given as a function of the previous iteration  $\beta_n^j$  by

$$\beta_n^{j+1} \cdot L = n\pi + \frac{4i\eta \sin^2\left(\frac{1}{2}\beta_n^j x_c\right) \cdot F(\beta_n^j, x_c, L, \lambda^2)}{\sin\left(\frac{1}{2}\beta_n^j L\right) - \cos\left(\frac{1}{2}\beta_n^j L\right) \cdot \left[ \frac{\beta_n^j L}{2} - \frac{4}{\lambda^2} \left( \frac{\beta_n^j L}{2} \right)^3 \right] + i\eta \sin(\beta_n^j x_c) \cdot F(\beta_n^j, x_c, L, \lambda^2)} \quad (6.37)$$

with

$$F(\beta_n^j, x_c, L, \lambda^2) = \sin\left(\frac{1}{2}\beta_n^j L\right) - \cos\left(\frac{1}{2}\beta_n^j x_c\right) \cdot \cos\left(\frac{1}{2}\beta_n^j (L - x_c)\right) \cdot \left[ \frac{\beta_n^j L}{2} - \frac{4}{\lambda^2} \left( \frac{\beta_n^j L}{2} \right)^3 \right] \quad (6.38)$$

and using once more for first estimate  $\beta_n^0 = n\pi/L$ , ( $n = 2, 4, \dots$ ). Figure 6.19 illustrates the variation of modal damping coefficient, expressed through the ordinate  $\frac{\xi_n}{x_c/L}$ , with the abscissa  $\frac{c}{mL\omega_{01}} \cdot n \frac{x_c}{L} = \frac{\eta n \pi x_c / L}{\pi^2}$ , for the first anti-symmetric mode shape ( $n = 2$ ), considering values of the Irvine parameter of  $\lambda^2 = 0.01, 1$  and  $100$ , and a ratio  $x_c/L$  of  $0.02$ . It is clear from the figure that the numerical solution defined by Krenk for nearly anti-symmetric mode shapes defines a curve that approximates the universal curve deduced for taut cables, and the asymptotic solution previously developed by Krenk. This confirms the conclusion of Crémona

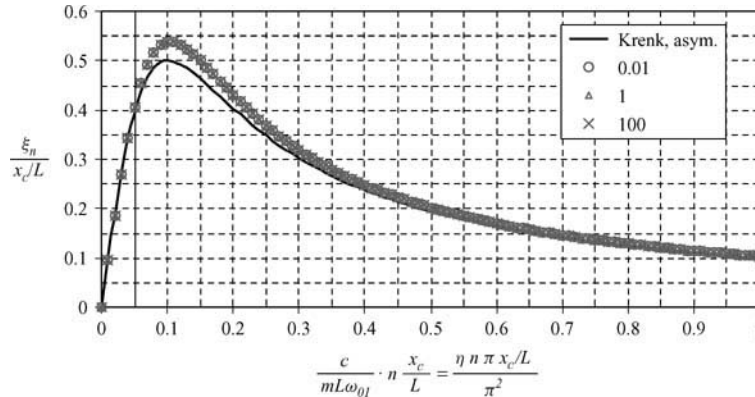


Fig. 6.19: Universal curve, asymptotic and numeric solution for first anti-symmetric mode of a shallow cable, according to Krenk and Nielsen [117]:  $\lambda^2 = 0.01$ ; 1 and 100, and  $x_c/L = 0.02$

[116] that for anti-symmetric mode shapes the damping is practically independent of the elastic properties and sag of the cable.

This fact is however not valid for symmetric modes, as was emphasised by Crémona as well. A clear evidence of this comes from the analysis of the variation of symmetric mode shape configuration with  $\lambda^2$  (see Appendix B). For  $\lambda^2$  above the first cross-over  $\lambda^2 = 4\pi^2$ , the first symmetric mode shape exhibits two nodes in the vicinity of each support. The effect of the application of a viscous damper in the vicinity of these nodes is therefore almost nil.

The numerical solution of equation (6.35) is now obtained for nearly symmetric mode shapes. The rearrangement of this equation leads to the following iterative scheme for the  $n^{th}$  order wave number at iteration of order  $j+1$ ,  $\beta_n^{j+1}$

$$\begin{aligned} \beta_n^{j+1} \cdot L &= 2 \cdot a \tan \left( \left[ \frac{\beta_n^j L}{2} - \frac{4}{\lambda^2} \left( \frac{\beta_n^j L}{2} \right)^3 \right] \right. \\ &\quad \times \left. \left( 1 + \frac{2i\eta \cdot [F(\beta_n^j, x_c, L)]^2 \cdot \left[ \frac{\beta_n^j L}{2} - \frac{4}{\lambda^2} \left( \frac{\beta_n^j L}{2} \right)^3 \right]}{1 + 2i\eta \cdot F(\beta_n^j, x_c, L) \cdot \left\{ 1 - F(\beta_n^j, x_c, L) \cdot \left[ \frac{\beta_n^j L}{2} - \frac{4}{\lambda^2} \left( \frac{\beta_n^j L}{2} \right)^3 \right] \right\}} \right) \right) \end{aligned} \quad (6.39)$$

with

$$F(\beta_n^j, x_c, L) = \frac{\sin(\frac{1}{2}\beta_n^j x_c) \cdot \sin(\frac{1}{2}\beta_n^j (L - x_c))}{\sin(\frac{1}{2}\beta_n^j L)} \quad (6.40)$$

Figure 6.20 represents the variation of the resulting damping ratio with the normalised abscissa  $a_n$ , defined by expression (6.31), for the first symmetric mode shape, considering three different values of the Irvine parameter  $\lambda^2$ : 0.01, 1 and 100, and  $x_c/L = 0.02$ . It has been confirmed that the modal damping ratio of a sagging cable reduces with sag, attaining almost null values in the vicinity of the cross-over  $\lambda^2 = 4\pi^2$ .

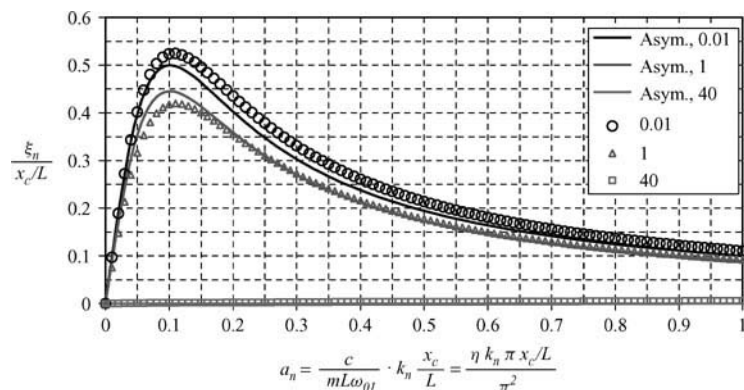


Fig. 6.20: Effect of sag in modal damping ratio of cable, for first symmetric mode:  $\lambda^2 = 0.01$ , 1 and 40 and  $x_c/L = 0.02$

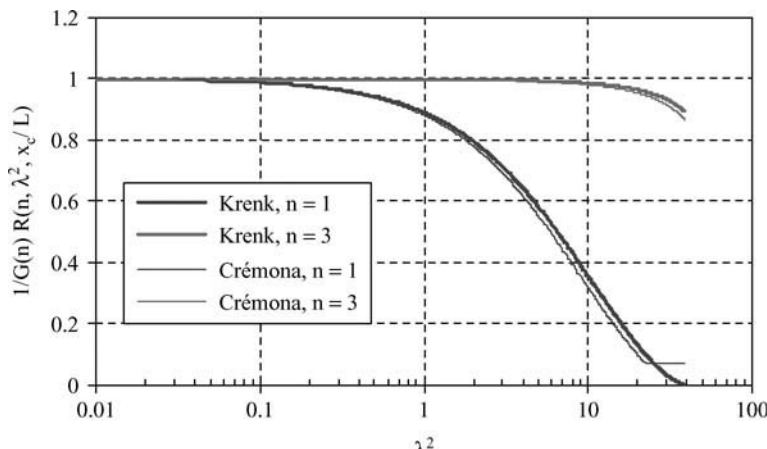


Fig. 6.21: Variation of  $I/G(n)$  and  $R(n, \lambda^2, x_c/L)$  with  $\lambda^2$ , for  $x_c/L = 0.02$

Krenk and Nielsen [117] deduced an asymptotic relation for the modal damping ratio of nearly symmetric mode vibrations, which provides a good approximation for cables with Irvine parameter below the critical values of  $\lambda_*^2 = 41.95$ , for  $n = 1$ , and  $\lambda_*^2 = 167.8$ , for  $n = 3$

$$\frac{\xi_n}{x_c/L} = \frac{\eta_n}{1 + (\eta_n)^2} \cdot \frac{\left[ \tan\left(\frac{k_n \pi}{2}\right) - \left( \frac{k_n \pi}{2} \cdot \frac{x_c}{L} \right) \right]^2}{\tan^2\left(\frac{k_n \pi}{2}\right) + \frac{12}{\lambda^2} \cdot \left( \frac{k_n \pi}{2} \right)^2} \quad (6.41)$$

with

$$\eta_n = \eta k_n \pi \frac{x_c}{L} \quad (6.42)$$

This relation is plotted in Fig. 6.20, in correspondence with the numerical solution, for the first symmetric mode of a cable with  $x_c/L = 0.02$ , showing a good agreement.

Assuming that the universal curve is well represented by the asymptotic solution (6.22) obtained for the taut cable, then the quantity  $R(n, \lambda^2, x_c/L)$  in the second member of (6.41), defined by

$$R(n, \lambda^2, x_c/L) = \frac{\left[ \tan\left(\frac{k_n \pi}{2}\right) - \left(\frac{k_n \pi}{2} \cdot \frac{x_c}{L}\right) \right]^2}{\tan^2\left(\frac{k_n \pi}{2}\right) + \frac{12}{\lambda^2} \cdot \left(\frac{k_n \pi}{2}\right)^2} \quad (6.43)$$

expresses the reduction of modal damping ratio of a shallow cable with respect to the taut cable solution. Using the definition (6.32) for the ordinate  $\theta_n$ , then the solutions obtained by Crémona and Krenk and Nielsen for the shallow cable can be compared by analysis of the closeness between  $1/G(n)$  and  $R(n, \lambda^2, x_c/L)$ , respectively. Figure 6.21 represents the variation of the two functions with  $\lambda^2$  for the first two symmetric modes ( $n = 1$  and  $n = 3$ ) and for  $x_c/L = 0.02$ , showing a very good approximation.

### 6.3.3.3 Bending stiffness effects

Sag extensibility and bending stiffness are the parameters that, according to Tabatabai and Mehrabi [27], most affect the modal damping of a cable. These authors have developed a numerical formulation to calculate vibration frequencies and damping ratios of sagging cables with non-negligible bending stiffness equipped with a viscous damper (Fig. 6.22). For such cables the differential dynamic equilibrium equation is

$$H \frac{\partial^2 w}{\partial x^2} + h_\tau \frac{d^2 z}{dx^2} - EI \frac{\partial^4 w}{\partial x^4} = m \frac{\partial^2 w}{\partial t^2} + c \frac{\partial w}{\partial t} \cdot \delta(x - x_c) \quad (6.44)$$

where  $h_\tau$  relates to the dynamic component of cable force generated by the vibrations according to the definition (B.4) presented in Appendix B.

The developed formulation is based on the expression of the solution of (6.44) by separation of variables, followed by a discretisation, resulting in a complex eigenvalue problem. The application of this general formulation to the stays of a database formed by more than 1400 cables from 16 cable-stayed bridges in US allowed the development of a simplified relationship between modal damping of the first vibration mode  $\xi_1$  and the characteristics of the cable and damper, expressed in non-dimensional form by

$$\begin{cases} \xi_1 = \frac{a\xi^b}{\eta^e(\xi^b+d)} \cdot \ln(\eta) & 2 \leq \eta \leq \eta_e \\ \xi_1 = \xi_1(\eta=2) \cdot \frac{\eta}{2} & 0 < \eta < 2 \end{cases} \quad (6.45)$$

where  $\xi$  is the non-dimensional bending stiffness parameter defined in Appendix B by  $\xi = \sqrt{HL^2/EI}$ ,  $\eta$  is the non-dimensional damping for the attached damper, defined by  $\eta = c/\sqrt{Hm} = \pi c/(mL\omega_{01})$ ,  $\eta_e$  is the optimum damping parameter, and the coefficients  $a, b, d$  and  $e$ , derived from a series of regression analyses, are defined in Table 6.2 for locations of the damper  $x_c/L = 0.02, 0.04$  and  $0.06$ .

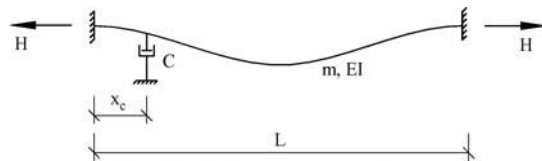


Fig. 6.22: Shallow cable with non-negligible bending stiffness equipped with viscous damper

$x_c/L$	a	b	d	e
0.02	0.259	2.080	5613	-0.129
0.04	1.276	1.795	841	0.081
0.06	3.278	1.700	259	0.305

Table 6.2: Coefficients of equation (6.45) [27]

The formula (6.45) has been derived for stay cables with Irvine parameter  $\lambda^2$  no greater than 1 for which, according to Tabatabai and Mehrabi, the sag effect is almost nil (note however that a reduction of the efficiency of the damper of around 13% was found, by comparison to the taut cable solution, for  $\lambda^2 = 1$ , using the formulation of Crémona and Krenk and Nielsen). The analysis of the stay cable database showed that  $\lambda^2$  varied between 0 and 2.84, 95% of the cables exhibiting  $\lambda^2$  inferior to 1, meaning that the simplified formula (6.45) is valid for application to a wide range of stay cables. As for the bending stiffness parameter, Tabatabai and Mehrabi stated a range of variation of  $\zeta$  as 10–600. According to these authors, bending stiffness effects are small whenever  $\zeta \geq 100$ , which occurs for 82% of the cables of the database. Finally, the damping parameter  $\eta$  varies approximately in the range 0–60. For locations  $x_c/L = 0.02, 0.04$  and  $0.06$ , the optimum damping parameter  $\eta_e$  has been derived as 20, 8 and 6, respectively (while the equivalent parameter deduced for taut cables by Pacheco *et al.* [114] is given by 15.74, 7.85 and 5.24).

Figure 6.23 represents the variation of the quantity  $\frac{\xi_1}{x_c/L}$  with  $\zeta$ , based on formula (6.45), using the parameters defined in Table 6.2, for the three damper locations referred to, and considering for  $\eta$  the optimum values of 20, 8 and 6. It can be noticed that the maximum attainable damping ratio is around 8% higher than that obtained using the taut cable formulation. It can also be concluded that bending effects are more relevant for dampers that are located closer to the cable anchorage and that they can be neglected whenever  $\zeta \geq 200$ . High bending stiffness of the cable (small  $\zeta$  value) has the effect of locking the damper and, consequently, of limiting its efficiency.

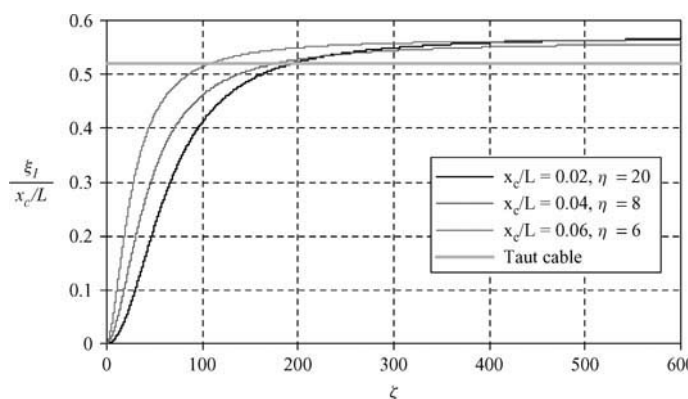


Fig. 6.23: Variation of maximum  $\frac{\xi_1}{x_c/L}$  with  $\zeta$ , for  $\lambda^2 = 0.01$

Despite the evident interest in formula (6.45), some limitations are observed, namely that only the damping of the first cable vibration mode is addressed and that an optimal damper size is not explicitly obtained for a combination of the parameters  $\lambda^2$ ,  $x_c/L$  and  $\zeta$  that leads to a maximum modal damping of the cable. A recent formulation by Hoang and Fujino [119] addresses the two problems for the taut cable with an attached transverse damper of a general type. In that case, the dynamic equilibrium governing the equation is

$$H \frac{\partial^2 w}{\partial x^2} - EI \frac{\partial^4 w}{\partial x^4} = m \frac{\partial^2 w}{\partial t^2} + f_c(x_c, t) \cdot \delta(x - x_c) \quad (6.46)$$

where  $f_c(x_c, t)$  represents the concentrated damping force at the attached damper. The solution of (6.46) by separation of variables yields a transcendental equation of complex eigenvalues, from which imaginary part the modal damping of the cable is determined, based on iterative numerical methods. Hoang and Fujino provide also an asymptotic solution for the modal damping of the cable that is valid for a particular range of bending stiffnesses, i.e. whenever the parameter  $\zeta \geq 100$  and that, for the particular case of a linear viscous damper, assumes the form

$$\frac{\xi_n}{x_c/L} \approx (1 - q^2) \cdot \frac{\eta_n}{1 + (1 - q - rq^2/2)^2 \cdot \eta_n^2} \quad (6.47)$$

For the taut cable  $\eta_n$  reduces to

$$\eta_n = \pi n \eta \frac{x_c}{L} \quad (6.48)$$

and

$$q = \frac{1 - e^{-r}}{r}, \text{ with } r = \zeta \cdot \frac{x_c}{L} \quad (6.49)$$

The maximum modal damping ratio for a particular combination of  $x_c/L$ ,  $\zeta$  and  $\eta_n$  is then

$$\frac{(\xi_n)_{\max}}{x_c/L} \approx \frac{(1 - q)^2}{2 \cdot (1 - q - rq^2/2)} \quad (6.50)$$

and the optimal damping is given by

$$(\eta_n)_{opt} = \frac{1}{1 - q - rq^2/2} \quad (6.51)$$

Considering that for the flexible taut cable a maximum damping ratio of  $0.5x_c/L$  is attained, it can be observed by analysis of (6.50) that bending stiffness induces a reduction of the maximum damping factor. The ratio  $R_{EI}(q, r)$  to the flexible taut cable is defined by

$$R_{EI}(q, r) \approx \frac{(1 - q)^2}{1 - q - rq^2/2} \quad (6.52)$$

This factor is represented in Fig. 6.24 for  $x_c/L = 0.01, 0.02, 0.04$  and  $0.06$ . It can be observed that the highest reduction of attainable damping results for dampers that are closer to the anchorage and also that the increase in bending stiffness (decrease of  $\zeta$ ) results in a decrease of the damper efficiency. This same fact can be appreciated in Fig. 6.25, representing the variation of modal damping with the damper properties, expressed by  $\eta_n$  for different levels of bending stiffness  $\zeta$ . Finally it is observed in Fig. 6.25 that the higher the bending stiffness, the higher the optimal damping force.

### 6.3.3.4 Flexibility of the dampers or of the supports

Dampers can be installed externally to the cable (*Fig. 6.7*) or else inside the protective guide (*Fig. 6.9*). It is of interest to investigate the influence of the corresponding performance that is associated either to the flexibility of these devices or of the corresponding supports.

#### *Flexibility of the dampers*

This problem was investigated by Krenk and Hognesberg [122] for the taut flexible cable with attached viscous damper. *Figure 6.26* illustrates the idealised model, which considers the parallel association of a spring of stiffness constant  $k$  with viscous damper constant  $c$ .

The dynamic equilibrium equation is then

$$H \frac{\partial^2 w}{\partial x^2} = m \frac{\partial^2 w}{\partial t^2} + f(x_c, t) \cdot \delta(x - x_c) \quad (6.53)$$

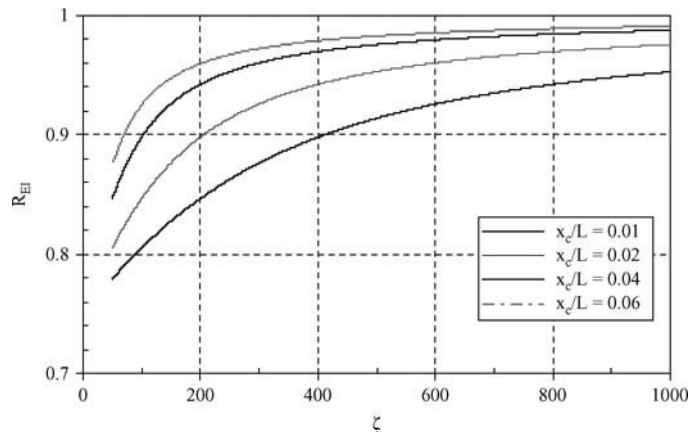


*Fig. 6.24: Variation of  $R_{EI}$  with  $\zeta$  induced by bending stiffness for taut cable*

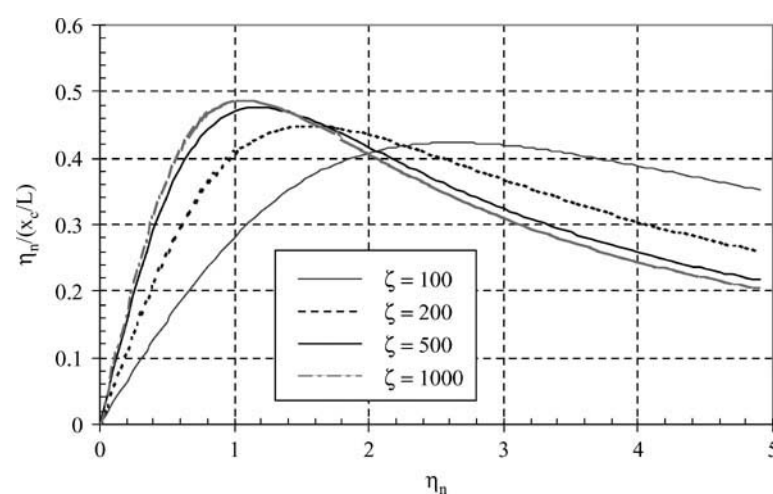


*Fig. 6.25: Variation of modal damping with  $\eta_n$  for various values of  $\zeta$  on a taut cable*

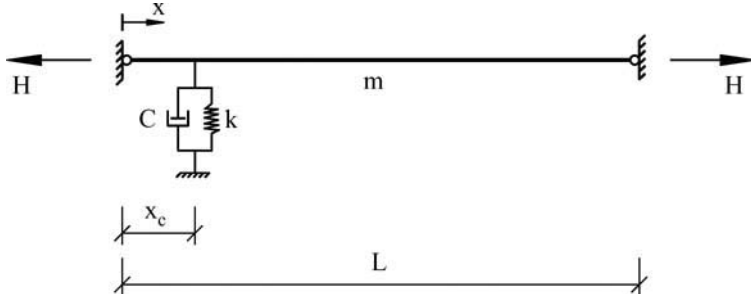


Fig. 6.26: Cable with parallel association of viscous damper and spring

where

$$f(x_c, t) = c \frac{\partial w}{\partial t}(x_c, t) + kw(x_c, t) \quad (6.54)$$

The asymptotic solution proposed by Krenk and Hogsberg corresponds to the free vibration of the cable without the spring, with an attached damper at a reduced distance from the anchorage  $x_c^*$  defined by

$$x_c^* = \frac{x_c}{1 + x_c \cdot \frac{k}{H}} \quad (6.55)$$

The maximum cable modal damping  $(\xi_n)_{\max}$  and the optimal damper coefficient  $c_{opt}$  are then obtained from

$$(\xi_n)_{\max} = \frac{1}{2} \cdot \frac{x_c^*}{L} \quad (6.56)$$

$$c_{opt} \approx \frac{H}{x_c^* \cdot \omega_n^0} \quad (6.57)$$

On the basis of the reduced distance to the anchorage  $x_c^*$  defined by (6.55) and on the resulting maximum modal damping given by (6.56), it can be concluded that the consequence of damper flexibility is a reduction of efficiency. The ratio of maximum modal damping with respect to the rigid situation  $R_k$  is defined by

$$R_k = \frac{1}{1 + \frac{x_c}{L} \cdot \frac{kL}{H}} \quad (6.58)$$

The minimum stiffness  $k$  of the damper can therefore be estimated which leads to a reduction of the damper efficiency no greater than a certain value, say 5%, and is given for that case by  $k \approx 0.053H/x_c$ .

#### *Flexibility of damper supports*

Fujino and Hoang [120] investigated the effect of the flexibility of the damper support. This is due for example to the flexibility of the anchor tube where the damper is accommodated, in the case of the so-called internal dampers. The model idealised for such a situation is

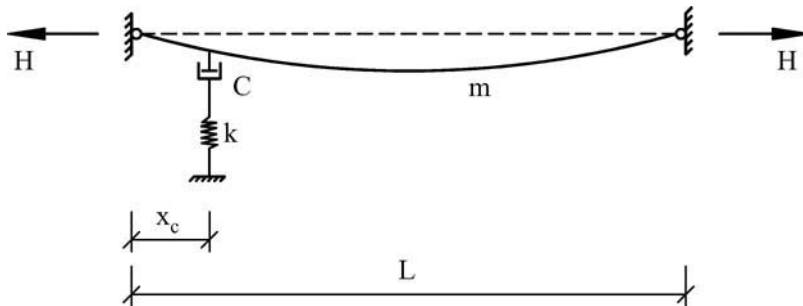


Fig. 6.27: Sagging cable with tandem association of viscous damper and spring

represented in Fig. 6.27, corresponding to a sagging flexible cable with an attached damper associated in tandem with a spring, whose constant  $k$  represents the stiffness of the anchor tube. This system is characterised by the dynamic equilibrium equation (6.23) for which the damping force member is replaced by  $f(x_c, t)$ , defined as

$$f(x_c, t) = c \cdot \left( \frac{\partial w}{\partial t}(x_c, t) - k \frac{\partial w_k}{\partial t}(t) \right) \quad (6.59)$$

The quantity  $w_k(t)$  represents the displacement of the anchor tube at the damper location.

The asymptotic solution of the resulting differential equation is based on the formulation of Krenk and Nielsen [117] and leads to the following expression for the attained modal damping

$$\frac{\xi_{kn}}{x_c/L} = \frac{\eta_n \eta_k^2}{\eta_k^2 + (1 + \eta_n \eta_k)^2} \cdot R(n, \lambda^2, \frac{x_c}{L}) \quad (6.60)$$

where  $\eta_n$  is defined by expression (6.42) and is

$$\eta_n = \frac{k x_c}{H \eta_n} \quad (6.61)$$

A comparison with expression (6.41) for a sagging cable with a damper on rigid support provides a coefficient  $R_{kt}(k, x_c, H)$  that expresses the reduction of the attained modal damping associated with support flexibility

$$R_{kt}(k, x_c, H) = \frac{(\xi_{kn})_{\max}}{(\xi_n)_{\max}} = \frac{\bar{\eta}_k}{1 + \bar{\eta}_k} \quad (6.62)$$

with

$$\bar{\eta}_k = \frac{k x_c}{H} \quad (6.63)$$

The variation of  $R_{kt}$  with  $\bar{\eta}_k$  is represented in Fig. 6.28. It is observed that the reduction in modal damping associated with damper support flexibility is independent of the cable mode. Moreover, a minimum value of  $\bar{\eta}_k$  can be determined, which guarantees a reduction of damper performance no greater than a certain value. If 5% reduction is considered,  $\bar{\eta}_k$  should have a minimum value of 19.

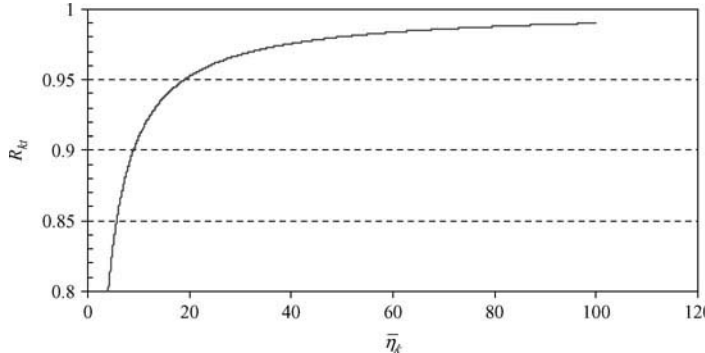


Fig. 6.28: Variation of the modal damping reduction  $R_{kt}$  with  $\bar{\eta}_k$

### 6.3.3.5 Damper non-linearity

The efficiency of non-linear dampers has been studied by Main and Jones [123] and by Krenk and Hogsberg [122]. These authors investigated in particular the case of non-linear viscous damping, for which, at a characteristic level of vibration, an equivalent viscous constant  $c_{eq}$  is calculated as a result of the linearisation of the damping force  $f_c(t)$

$$f_c(t) = c \left( \frac{\partial w}{\partial t} \right)^\alpha \cong c_{eq} \frac{\partial w}{\partial t} \quad (6.64)$$

Following the formulation of Krenk and Hogsberg, the modal damping of the cable  $\xi_n$  is obtained from

$$\frac{\xi_n}{x_c/L} = \frac{\eta_n^*}{1 + (\eta_n^*)^2} \quad (6.65)$$

where  $\eta_n^*$  is defined as

$$\eta_n^* = \frac{c \cdot (\omega_n^0 w_c)^\alpha}{H} \cdot \frac{x_c}{w_c} \cdot g(\alpha) \quad (6.66)$$

$w_c$  represents the displacement of the damper located at the distance  $x_c$  from the anchorage and  $g(\alpha)$  is derived based on the Gamma function  $\Gamma(\alpha)$  as

$$g(\alpha) = \frac{2\Gamma(\frac{1}{2}\alpha + 1)}{\sqrt{\pi}\Gamma(\frac{1}{2}\alpha + \frac{3}{2})} \quad (6.67)$$

The optimal damping  $c_{opt}$  is also derived for the specified amplitude of vibration  $w_c$  as

$$c_{opt} = \frac{H}{g(\alpha)(\omega_n^0 w_c)^\alpha} \cdot \frac{w_c}{x_c} \quad (6.68)$$

Expression (6.68) shows the dependence of the optimal damper and hence of the maximum attainable modal damping on the amplitude of oscillation for each vibration mode. According to the value of the damper exponent  $\alpha$ , an increasing ( $\alpha < 1$ ) or decreasing ( $\alpha > 1$ ) variation of the modal damping with amplitude results, meaning that the damper non-linearity results

in a stiffening or softening effect, respectively. Practical values of  $\alpha$  for fluid viscous dampers are in the range  $0.2 \leq \alpha \leq 1.8$  [123].

The dependency of the efficiency of the non-linear damper on the vibration mode is an inconvenience that can be overcome with the choice of another type of damper. Fujino and Hoang [120] obtained the modal damping  $\xi_R$  associated with a high damping rubber (HDR) damper, for which the damper force  $f_c(t)$  is characterised as

$$f_c(t) = K \cdot (1 + i\varphi) \cdot w_c(t) \quad (6.69)$$

In this expression,  $K$  is the spring constant of the damper and  $\varphi$  is the loss factor of the material.

For a damper located at a distance  $x_R$  from the anchorage (Fig. 6.29), and defining a non-dimensional spring factor  $\eta_R$  as

$$\eta_R = \frac{x_R K}{H} \quad (6.70)$$

the modal damping  $\xi_R$  results from

$$\frac{\xi_R}{x_c/L} = \frac{\varphi \eta_R}{(1 + \eta_R)^2 + (\varphi \eta_R)^2} \quad (6.71)$$

It can therefore be concluded that the maximum attainable damping and consequently the optimal damping are independent of the vibration mode. Figure 6.29 shows the variation of modal damping with  $\eta_R$ , considering a cable force of 10 000 kN, a spring constant of 2800 kN/m and a loss factor of 0.25.

The optimal damper parameter  $(\eta_R)_{opt}$  can be calculated which provides a maximum modal damping as a function of the loss factor of the material, and is given by

$$(\eta_R)_{opt} = \frac{1}{\sqrt{1 + \varphi^2}} \quad (6.72)$$

The maximum modal damping is then

$$\frac{(\xi_R)_{max}}{x_c/L} = \frac{\varphi}{2 + 2\sqrt{1 + \varphi^2}} \quad (6.73)$$

Figure 6.30 represents the variation of  $(\xi_R)_{max}$  with  $\varphi$ , considering the range  $0.2 \leq \varphi \leq 1.8$ . It can be concluded that the maximum attainable modal damping for a HDR damper is of the order of  $0.3x_c/L$ . This value is identical for all vibration modes. However, it is 44% lower than the maximum modal damping attained for one particular vibration mode when a linear viscous damper is employed.

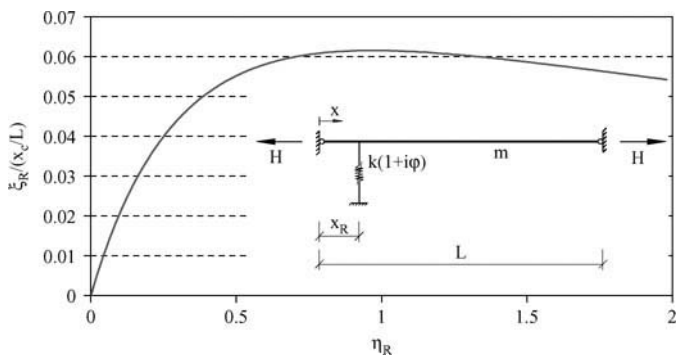


Fig. 6.29: Variation of modal damping  $\xi_R$  with  $\eta_R$  for a HDR damper

rubber (HDR) damper, for which the damper force  $f_c(t)$  is

characterised as

$$f_c(t) = K \cdot (1 + i\varphi) \cdot w_c(t) \quad (6.69)$$

In this expression,  $K$  is the spring constant of the damper and  $\varphi$  is the loss factor of the material.

For a damper located at a distance  $x_R$  from the anchorage (Fig. 6.29), and defining a non-dimensional spring factor  $\eta_R$  as

$$\eta_R = \frac{x_R K}{H} \quad (6.70)$$

the modal damping  $\xi_R$  results from

$$\frac{\xi_R}{x_c/L} = \frac{\varphi \eta_R}{(1 + \eta_R)^2 + (\varphi \eta_R)^2} \quad (6.71)$$

It can therefore be concluded that the maximum attainable damping and consequently the optimal damping are independent of the vibration mode. Figure 6.29 shows the variation of modal damping with  $\eta_R$ , considering a cable force of 10 000 kN, a spring constant of 2800 kN/m and a loss factor of 0.25.

The optimal damper parameter  $(\eta_R)_{opt}$  can be calculated which provides a maximum modal damping as a function of the loss factor of the material, and is given by

$$(\eta_R)_{opt} = \frac{1}{\sqrt{1 + \varphi^2}} \quad (6.72)$$

The maximum modal damping is then

$$\frac{(\xi_R)_{max}}{x_c/L} = \frac{\varphi}{2 + 2\sqrt{1 + \varphi^2}} \quad (6.73)$$

Figure 6.30 represents the variation of  $(\xi_R)_{max}$  with  $\varphi$ , considering the range  $0.2 \leq \varphi \leq 1.8$ . It can be concluded that the maximum attainable modal damping for a HDR damper is of the order of  $0.3x_c/L$ . This value is identical for all vibration modes. However, it is 44% lower than the maximum modal damping attained for one particular vibration mode when a linear viscous damper is employed.

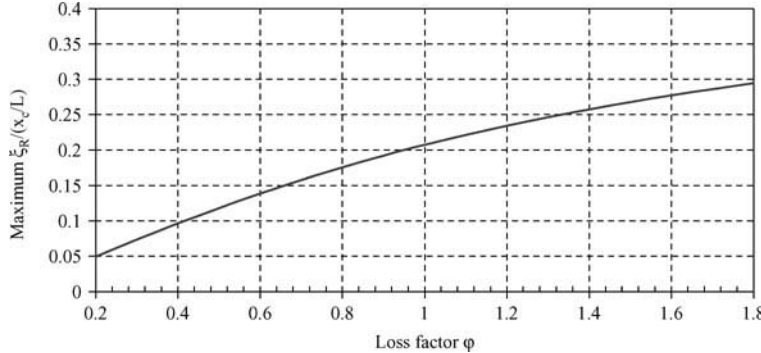


Fig. 6.30: Variation of maximum cable modal damping ( $\xi_R$ )<sub>max</sub> with  $\varphi$

### 6.3.3.6 Combined effects of sag, bending stiffness and flexibility of damper supports

In the context of the design of a damper for control of cable vibrations, it is of interest to combine the effects of sag, bending stiffness and flexibility of the support in order to obtain a global estimate of the reduction of efficiency and of the increase of the optimal damping coefficient with respect to the taut cable approach. The simplified formulae derived by Fujino and Hoang [120] for viscous and high-damping rubber dampers installed in sagging cables with flexible supports are then of increased interest. For a viscous damper, these authors propose the following expression for the attained modal damping ratio

$$\frac{\xi_n}{x_c/L} = R_n \cdot R_{EI} \cdot R_{kEI} \cdot \frac{\eta_n \cdot \eta_{kEI}}{1 + (\eta_n \cdot \eta_{kEI})^2} \quad (6.74)$$

where  $\eta_n$  and  $R_n$  are the non-dimensional damping parameter and the reduction factor due to sag effect, defined by (6.42) and (6.43), respectively,  $R_{EI}$  is the reduction factor calculated according to expression (6.52) considering exclusively the bending effects,  $\eta_{kEI}$  is a non-dimensional damping parameter related to the stiffness  $k$  of the support and to the bending stiffness of the damper by

$$\eta_{kEI} = \eta_{EI} + \frac{1}{\bar{\eta}_k} \quad (6.75)$$

with  $\eta_{EI} = 1 - q - 1/2 \cdot rq^2$  (see expression (6.49)) and  $\bar{\eta}_k$  defined by (6.63), and  $R_{kEI}$  is the reduction factor associated with the support stiffness, given by

$$R_{kEI} = \frac{\bar{\eta}_k \cdot \eta_{EI}}{1 + \bar{\eta}_k \cdot \eta_{EI}} \quad (6.76)$$

The maximum modal damping ratio is then obtained by

$$\frac{\xi_n^{\max}}{x_c/L} = 0.5 \cdot R_n \cdot R_{EI} \cdot R_{kEI} \quad (6.77)$$

and occurs for a non-dimensional optimal damping parameter  $\eta_n^{opt}$  defined as

$$\eta_n^{opt} = \frac{1}{\eta_{kEI} \cdot k_n} \quad (6.78)$$

It should be pointed out that formulae (6.77) and (6.78) have been derived based on the assumption that the viscous damper is linear. The non-linearity of the damper is probably one of the most important reasons for the reduction of their efficiency. Therefore, even though small curvature, bending and support stiffness effects are associated with a typical medium size cable, the damper effectiveness can be actually of the order of 50–70% of that assumed in theory, as noted by Sun *et al.* [124].

Considering now a high-damping rubber damper with a damper force–displacement relationship defined by (6.69) as a function of the damper spring constant  $K$  and of the loss factor of the material  $\varphi$ , the modal damping ratio derived by Fujino and Hoang [120] is obtained from

$$\frac{\xi_n}{x_c/L} = R_n \cdot R_{EI} \cdot R_{kEI} \cdot \frac{\varphi \cdot \eta_R \cdot \eta_{kEI}}{(1 + \eta_{kEI} \cdot \eta_R)^2 + (\varphi \cdot \eta_{kEI} \cdot \eta_R)^2} \quad (6.79)$$

where the non-dimensional spring constant  $\eta_R$  is defined by (6.70). Introducing the parameters  $\eta_\varphi$  and  $R_\varphi$  as

$$\eta_\varphi = \sqrt{1 + \varphi^2} \quad (6.80)$$

$$R_\varphi = \frac{\varphi}{1 + \sqrt{1 + \varphi^2}} \quad (6.81)$$

the following expression results for the maximum modal damping ratio

$$\frac{\xi_n^{\max}}{x_c/L} = 0.5 \cdot R_n \cdot R_{EI} \cdot R_{kEI} \cdot R_\varphi \quad (6.82)$$

which occurs for an optimal non-dimensional spring constant defined by

$$\eta_R^{opt} = \frac{1}{\eta_{kEI} \cdot \eta_\varphi} \quad (6.83)$$

Considering the variation of  $\varphi$  in the range 0.2–1.8,  $R_\varphi$  will have values varying from 0.3 to 0.5. This means that, compared with a linear viscous damper, the high-damping rubber damper provides a very small increase of modal damping. The added damping is however equal for all vibration modes, while for a viscous damper an optimal damping is obtained for a particular vibration mode, and the added damping for the higher order modes can be of the order of about 40% of that value. Under these circumstances, the combination of two dampers, one viscous and another high-damping rubber, can provide an effective control system. This solution is of significance for very long stay cables where the installation of a single damper does not provide the necessary damping and was employed for the Tatara bridge in Japan, with maximum cable lengths of more than 500 m [120].

#### 6.3.3.7 Combined effect of two dampers

The installation of a single damper may not provide sufficient damping to a stay cable. It is therefore of interest to investigate possible combinations of dampers that result in an increased damping ratio. From a study of different combinations of dampers located close to the cable anchorages, Hoang and Fujino [121] concluded that the combination of two dampers close to the same anchorage does not provide an increased damping with respect to the effect of the damper located at the longest distance from the anchorage. On the contrary, the installation of a damper close to each anchorage of a cable leads to an increased damping

effect that is asymptotically the sum of the individual contributions from the single dampers. On the basis of the research of Hoang and Fujino, this effect is discussed in the current text considering the following combinations of dampers/locations: (i) identical linear viscous dampers at equal distance from each anchorage; (ii) different constant linear viscous dampers at different distances from each anchorage; (iii) combination of linear viscous and HDR dampers at different distances from each anchorage.

#### *Identical linear viscous dampers at equal distance from each anchorage*

For a taut cable with installed linear viscous dampers at distances  $x_c$  from each anchorage (Fig. 6.31), the asymptotic approximation of the universal curve is defined as

$$\frac{\xi_n}{x_c/L} = \frac{2\eta_n}{1 + (\eta_n)^2} \quad (6.84)$$

The achieved modal damping is therefore twice the modal damping attained by the single damper (expression (6.22)).

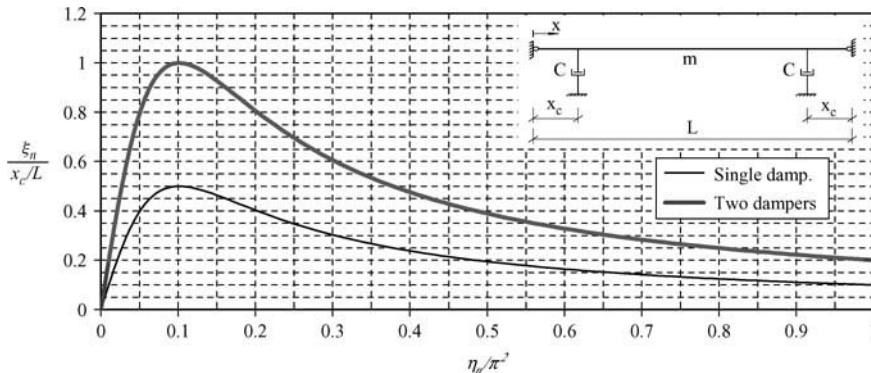


Fig. 6.31: Modal damping associated with combination of linear viscous dampers

#### *Different constant linear viscous dampers at different distances from each anchorage*

Considering two different linear viscous dampers with constants  $c_1$  and  $c_2$  equipping a taut cable at distances from the anchorages of  $x_{c1}$  and  $x_{c2}$ , respectively (Fig. 6.32), the asymptotic expression of modal damping is obtained as

$$\xi_n = \frac{\eta_{1n}}{1 + \eta_{1n}^2} \cdot \frac{x_{c1}}{L} + \frac{\eta_{2n}}{1 + \eta_{2n}^2} \cdot \frac{x_{c2}}{L} \quad (6.85)$$

where the non-dimensional damping constants  $\eta_{1n}$  and  $\eta_{2n}$  are defined by (6.42) for the damping constants  $c_1$  and  $c_2$ , respectively. Equation (6.85) and the representation of Fig. 6.32 show the increased modal damping of the cable is a weighted measure of the modal damping obtained for single installation of each damper, based on the relative distance of each damper to the corresponding anchorage.

The maximum modal damping ratio is then achieved when each damper is separately tuned to optimal condition. The optimal non-dimensional damping parameters are  $\eta_{1n}^{opt} = \eta_{2n}^{opt} = 1$

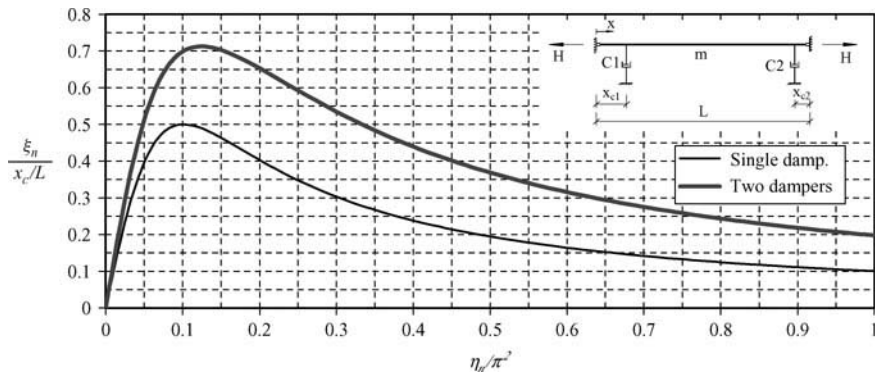


Fig. 6.32: Modal damping associated with combination of linear viscous dampers installed at different anchorage distances

and

$$\xi_n^{\max} = \frac{x_{c1} + x_{c2}}{2L} \quad (6.86)$$

*Combination of linear viscous and HDR dampers at different distances from each anchorage*

An asymptotic expression for the modal damping ratio of the cable equipped with a linear viscous and a HDR damper at distances  $x_c$  and  $x_R$  from the anchorages (Fig. 6.33) has been derived by Hoang and Fujino [121], which is defined as a function of the non-dimensional damping ratios  $\eta_n$  and  $\eta_R$  of the viscous and the HDR damping, defined respectively by (6.42) and (6.70), and of the material loss factor  $\varphi$ , according to

$$\xi_n = \frac{\eta_n}{1 + \eta_n^2} \cdot \frac{x_c}{L} + \frac{\varphi \eta_R}{(1 + \eta_R)^2 + \varphi^2 \eta_R^2} \cdot \frac{x'_R}{L} \quad (6.87)$$

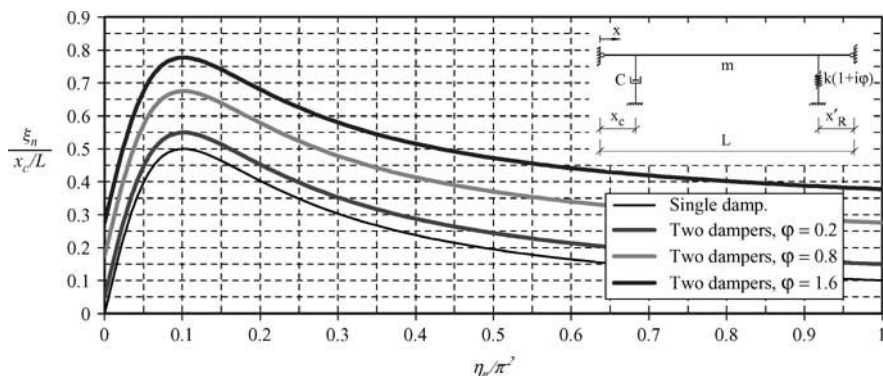
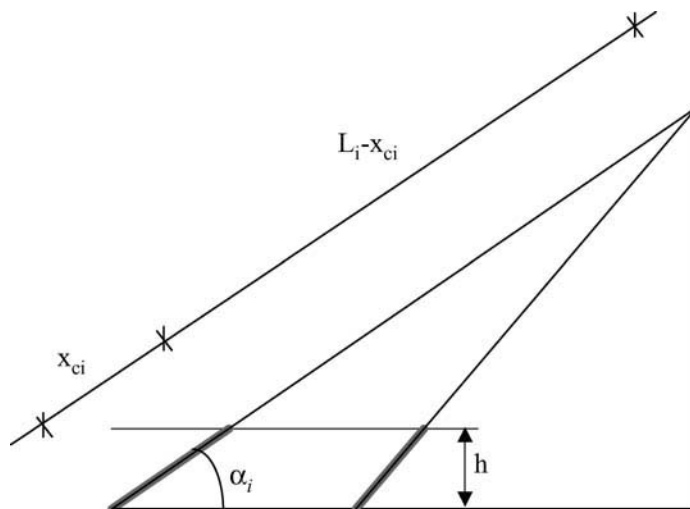


Fig. 6.33: Modal damping associated with combination of linear viscous and HDR dampers

The achieved modal damping is again the sum of the modal damping ratios obtained under individual installation of each damper and is represented in *Fig. 6.33* considering the optimal value  $\eta_R$  defined by (6.72) and different values of the loss factor  $\varphi$ .



*Fig. 6.34: Definition of damper location according to length of deviator guide*

### 6.3.4 Practical applications

The formulae presented above can be applied to the design of dampers for a set of stay cables with characteristics that cover most of the practical cases found. This serves to illustrate the sensitivity of the achieved damping ratio to sag-extensibility and bending stiffness.

The analysed cases are divided into two series of problems, namely: (i) evaluation of maximum attainable damping ratio for a particular damper location; and (ii) specification of damper size to fulfil minimum damping requirements.

#### 6.3.4.1 Evaluation of maximum attainable damping ratio for a particular damper location

The damper sizes for the stay cables with properties listed in *Table 6.3* are evaluated, assuming that maximum damping is required for the first vibration mode. Chosen as examples are three cables of Vasco da Gama bridge (the largest, shortest and mid-length), the largest cables of Normandy and Ikuchi bridges, and two cables studied previously by Tabatabai and Mehrabi [27], and by [112].

One of the key issues in the design of the damper is the specification of location along the cable, characterised by  $x_c/L$ . It is known that the maximum benefit is obtained from the most distant damper from the cable anchorage. However, aesthetic and technical restrictions limit this distance. Considering, for example, that the damper is inserted in a deviation guide with height  $h$ , then for each cable of chord length  $L_i$ , the maximum allowable distance to the

Cable	L (m)	H (kN)	mass (kg/m)	EA (kN)	$\xi$	$\lambda^2$	f <sub>01</sub> (Hz)	x <sub>c</sub> /L
V. Gama								
HC01	34.7	2045	42.9	906 750	24	0.023	3.145	0.0600
HC24	226.0	6786	100.1	21 352 50	117	0.344	0.576	0.0400
HC15	147.5	4306	74.8	16 087 50	95	0.241	0.814	0.0400
Normandy	440.9	6851	133.0	29 070 00	182	3.085	0.257	0.0100
Ikuchi	246.2	3502	72.5	17 160 00	161	1.254	0.446	0.0100
Tabatabai and Mehrabi [27]	93.0	5017	114.1	16 150 00	119	0.139	1.127	0.0200
Yoneda and Maeda [112]	215.1	3690	98.6	171 000	380	0.147	0.450	0.0235

Table 6.3: Properties of stay cables used in the design of viscous damper

anchorage  $x_{ci}$  is given by

$$x_{ci} = \frac{h}{\sin(\alpha_i)} \quad (6.88)$$

where  $\alpha_i$  is the angle of the cable chord with the horizontal (Fig. 6.34). So for the three cables of the Vasco da Gama bridge, a height of around 3 m was considered, and approximate ratios  $x_c/L$  were defined (for cable HC01, a ratio of 0.06 was used instead of 0.1, as the analysis of bending effects was of interest, and the coefficients available to employ the simplified formula (6.45) do not cover that ratio). The ratios adopted for the other cables were taken from literature.

Once the location of the damper  $x_c/L$  has been fixed, and using the universal curve from Pacheco *et al.* [114] (UCP), based on the taut cable approach, or the asymptotic solutions developed by Krenk [115] and by Krenk and Nielsen [117] for taut (AKT) or shallow cables (AKS), it can be stated that the maximum damping ratio is given by the peak of the universal/asymptotic curve, with abscissa 0.1. Figure 6.35 describes the procedure, based on the UCP formulation, according to the following steps:

1. Abscissa associated with optimal damper equal to 0.1. This allows the evaluation of the damper size  $c_{opt}$  as

$$c_{opt} = \frac{0.1 \cdot mL\omega_{01}}{x_c/L} \quad (6.89)$$

The obtained  $c_{opt}$  values based on the universal curve are listed in Table 6.4.

2. The ordinate associated with abscissa 0.1 is equal to 0.52. So the damping coefficient of the first mode is obtained as

$$\xi_{1,opt} = 0.52 \cdot \frac{x_c}{L} \quad (6.90)$$

3. Once the damper size is fixed, the abscissa for the second mode is defined as 0.2.

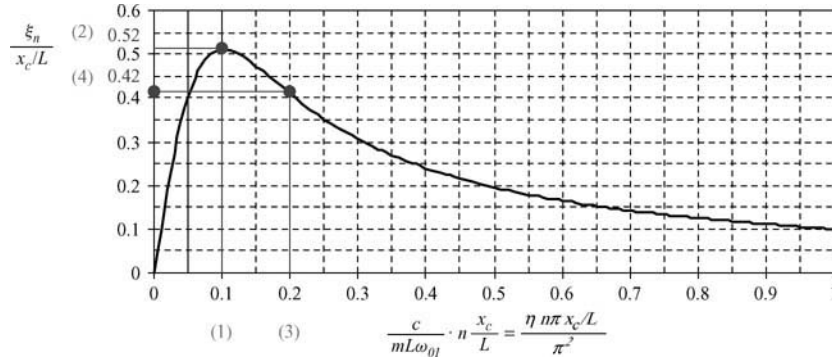


Fig. 6.35: Procedure for estimation of maximum damping ratio and size of damper, using the universal curve deduced for taut cables [114]

4. The corresponding ordinate of 0.42 is taken from the universal curve, allowing the definition of the second mode damping ratio,  $\xi_2$

$$\xi_2 = 0.42 \cdot \frac{x_c}{L} \quad (6.91)$$

The damping ratios obtained from the application of (6.90) and (6.91) to the set of cables under analysis are listed in *Table 6.4*. If the *AKT* formulation is employed, based on the relationship (6.22) to analytically express the universal curve, the ordinates in correspondence with abscissas 0.1 and 0.2 are 0.50 and 0.403, respectively. The results obtained, listed in *Table 6.4* are naturally very similar to those based on the *UCP* formulation.

The consideration of sag-extensibility effects, through the use of the *AKS* formulation, based on the relationship (6.41), leads to the damping ratio values represented in *Table 6.4*.

It can be concluded from the analysis of *Table 6.4* that sag-extensibility effects are almost nil for cables with small  $\lambda^2$ , but can be significant for cables with Irvine parameter larger than 1. In effect, the analysis of the reduction function  $R(n, \lambda^2, x_c/L)$ , defined by (6.43) and represented in *Figure 6.31* for  $x_c/L = 0.02$ , shows that the maximum reduction of damping is attained for the smallest  $x_c/L$ . It shows also that for  $x_c/L = 0.01$ , a 5% reduction in the modal damping ratio is achieved, with respect to the taut cable solution, with  $\lambda^2 = 0.42$ , and a 10% reduction results if  $\lambda^2 = 0.88$ .

Finally, the inclusion of bending effects is considered, using the simplified formula (6.45) developed by Tabatabai and Mehrabi [27] (*BTM*), which accounts only for low sag-extensibility effects ( $\lambda^2 < 1$ ). Accordingly, the maximum damping is obtained for  $\eta_e = 20, 8$  or 6, for  $x_c/L = 0.02, 0.04$  or 0.06, respectively. This provides the optimum damper size as

$$c_{opt, EI} = \frac{mL\omega_{01}}{\pi} \cdot \eta_e \quad (6.92)$$

The optimum size of damper  $c_{opt, EI}$ , listed in *Table 6.4*, is very similar to the one obtained with the previous formulations when  $x_c/L$  is 0.04 or 0.06, but is clearly higher than  $c_{opt}$  for  $x_c/L$  of the order of 0.02. The maximum damping ratio for the first mode, also listed

<b>Cable</b>	<b>L (m)</b>	$\lambda^2$	$\xi$	$c_{opt}$ (KN.s/m)	<b>UCP</b>		<b>AKT</b>		<b>AKS</b>	<b>BTM</b>		<b>BHF</b>		<b>CSB</b>
					$\xi_{1,opt}$ (%)	$\xi_2$ (%)	$\xi_{1,opt}$ (%)	$\xi_2$ (%)	$\xi_{1,opt}$ (%)	$c_{opt,EI}$ (KN.s/m)	$\xi_{1,opt}$ (%)	$c_{opt,EI}$ (KN.s/m)	$\xi_{1,opt}$ (%)	$R_n, R_{EI}$ (%)
V. Gama														
HC01	34.7	0.023	24	49	3.12	2.52	3.00	2.42	2.99	56	1.57			
HC24	226.0	0.344	117	205	2.08	1.68	2.00	1.61	1.92	209	1.92	304	1.82	87
HC15	147.5	0.241	95	141	2.08	1.68	2.00	1.61	1.95	144	1.81	232	1.79	87
Normandy	440.9	3.085	182	948	0.52	0.42	0.50	0.40	0.43			2769	0.42	60
Ikuchi	246.2	1.254	161	501	0.52	0.42	0.50	0.40	0.43			1663	0.42	72
Tabatabai and Mchrabi [27]	93.0	0.139	119	376	1.04	0.84	1.00	0.81	0.98	478	0.90	854	0.86	85
Yoneda and Maeda [112]	215.1	0.147	380	255	1.22	0.99	1.18	0.95	1.16	381	1.16	311	1.11	93

Table 6.4: Optimal damper size  $c_{opt}$  and modal damping ratios achieved with mechanical viscous damper

in *Table 6.4*, depends on the non-dimensional bending stiffness parameter  $\zeta$ , as shown in *Fig. 6.33*.

Bending stiffness effects are also evaluated based on the formulae derived by Hoang and Fujino [119] for taut cables (BHF), which are valid for  $\zeta \geq 100$ . Based on expressions (6.50) and (6.51), the maximum modal damping ratio of the first mode and the optimal damping constant have been calculated and are given in *Table 6.4*. There are some differences between them and the results obtained by Tabatabai and Mehrabi, which are particularly significant for the optimal damping estimates. It should be noted however that the bending stiffness parameter  $\zeta$  has been defined with rather low values, reflecting a relatively large stiffness (estimated as 70% of the stiffness of the equivalent full section of the cable), leading, therefore, to higher than expected reduction of the damper performance. Moreover it is precisely for the lower values of  $\zeta$  that a more significant variation of modal damping with damper properties occurs (*Fig. 6.35*).

Finally the last column of *Table 6.4* represents the product  $R_n \cdot R_{EI}$  that expresses the reduction of the maximum attained damping, considering the simultaneous effects of sag and bending (CSB) according to formula (6.77), and neglecting the flexibility of the damper support ( $R_{kEI} = 1$ ). Although bending effects may be calculated by excess, it can be concluded that a considerable reduction of damper efficiency can occur for very long sagging cables (60–70% of efficiency with respect to taut cable approach), while for medium sized cables, an efficiency of 80–90% can be achieved, if the viscous damper is linear.

#### 6.3.4.2 Specification of damper size to fulfil minimum damping requirements

It was seen in the Section 4.6 that one possible form of avoiding rain-wind induced vibration is to ensure a minimum damping ratio of the stay cables, taken from the specification of a minimum Scruton number  $S_{c0} = m\xi/\rho D^2$  of 10. The application of this criterion leads to the specification of a minimum damping requirement  $\xi_{\min}$  for each stay cable

$$\xi_{\min} = \frac{\rho D^2}{m} \cdot 10 \quad (6.93)$$

which should be satisfied, for example, by all cable modes in the range 0.3–3 Hz.

If intrinsic damping is neglected, it becomes necessary to design a damper that provides the required modal damping for the first few modes of the cable.

Considering as an example the longest stay cable HC024 of the Vasco da Gama bridge, with its properties listed in *Table 6.3*, the application of the above criterion leads to a minimum required modal damping ratio of 0.81% for the first five modes of vibration, with natural frequencies of 0.576, 1.152, 1.728, 2.304 and 2.88 Hz.

Given that for this cable both sag-extensibility and bending stiffness effects are reduced, the asymptotic formulation of Krenk for taut cables (AKT) is used, and the abscissas  $\eta n \pi x_c/L$  ( $n = 1, \dots, 5$ ) of formula (6.22) are found, which guarantee that

$$\frac{\xi_n}{x_c/L} = \frac{\eta n \pi x_c/L}{1 + (\eta n \pi x_c/L)^2} \geq \frac{0.0081}{0.04} = 0.205 \quad (6.94)$$

Solving (6.94) for  $n = 5$ , results in  $5\eta\pi x_c/L = 4.7267$  (Fig. 6.36). So the damper size is given by

$$c = \frac{mL\omega_{01}\eta}{\pi} = 196kN \cdot s/m \quad (6.95)$$

It is now necessary to verify that the damping ratio associated with the first *four* modes is higher than 0.81%. For that purpose, the abscissas associated with each mode are taken:  $0.09578\pi^2$ ,  $0.1916\pi^2$ ,  $0.2873\pi^2$  and  $0.3831\pi^2$ , and the corresponding ordinates calculated using (6.22): 0.499, 0.413, 0.383 and 0.247 (Fig. 6.36). These lead to damping ratios of 2.0, 1.65, 1.53 and 0.99%, respectively.

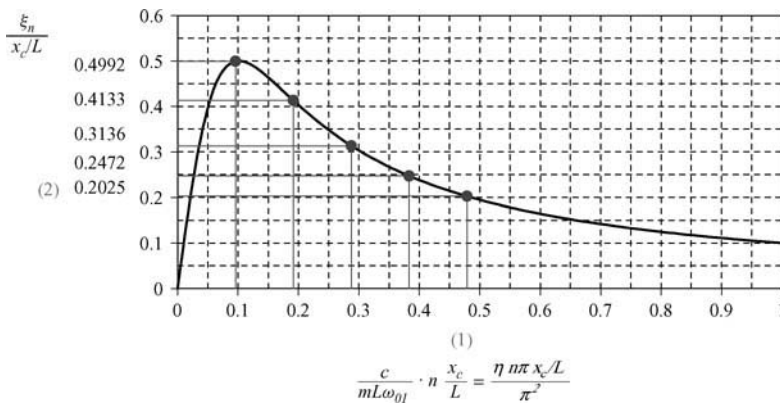


Fig. 6.36: Procedure for estimation of damper size and damping ratio, using the AKT formulation

## 7. Case Reports

The complex phenomena associated with cable vibrations and control have been individually described and analysed so far. On the basis of the contributions from designers, consultants, researchers and manufacturers, this chapter describes a number of practical situations of cable vibration design studies/occurrences which impelled the investigation and evaluation of control design/retrofit measures. Various situations have been covered in terms of occurrences and extension of measures undertaken. The contributors to this chapter, are fully acknowledged for sharing their experiences and providing extremely valuable information.

Cable-stayed bridges constructed in the 1980s and the early 1990s were not investigated for possible cable vibrations. Therefore no special measures were undertaken at the design stage to prevent oscillations, especially the installation of dampers. In the late 1980s and early 1990s, the new technique of individual protection of the strands motivated in several cases the release of the bundle of strands from protective pipes and, consequently, new problems of vibration occurred, related to galloping and interference galloping between strands of the same bundle, eventually increased by particular resonance conditions [84]. Yet, many bridges constructed in this period have not exhibited noticeable vibrations, especially those with medium or low span, as the intrinsic damping of a cable clearly increases with the decrease of its length. At the same time, some of these and other more recent bridges have suffered from vibrations on very few occasions, caused by particular wind and resonance conditions. Such was the case of the Skarnsundet bridge, described in this chapter. The limited number of occurrences and the evidence of no damage have motivated a non-retrofit. Other bridges were not expected to experience certain weather conditions like rain, as was the case of the Puente real bridge, located in Badajoz, Spain, where rain-wind vibration occurred. In this case, additional resonance effects were observed that motivated the installation of dampers close to the anchorages.

Large unexpected rain-wind vibrations were also observed in two different bridges located in Texas, USA. The need to understand these vibrations and develop retrofit measures led to extensive monitoring of the two bridges and to the test of damper prototypes before a definite retrofit measure was chosen, based on the installation of dampers at all stay cables. Many recently constructed bridges have dampers installed in cables from the beginning, as a consequence of the demands posed by more or less extensive studies on cable vibration phenomena conducted at the design stage, as in the case of the Öresund and Erasmus bridges, described here. The installation of cable dampers is not however a guarantee of protection against vibrations. The strong instabilities associated with rain/wind vibration and the deposition of snow under moderate wind (also not fully understood by the current state-of-art) that were observed on these bridges, causing damage to those devices and producing large vibrations, have necessitated a higher damping capacity than the original dampers provided for them.

One possible cause of the inadequacy of dampers to control vibrations might be that the efficiency was only a fraction of that estimated at the design stage.

The understanding of phenomena like curvature, bending effects, flexibility of damper support and non-linearity of damper fluid that cause a decrease in the efficiency of such devices, are very recent, as shown in Chapter 6. Another aspect is that damper technology is also improving and, besides the traditional and less aesthetical hydraulic and viscous dampers, a new generation of dampers of visco-elastic, hydraulic, friction or high damping type are being installed between the cable and the protective pipe, and have been proved to introduce the necessary damping. Examples of successful applications are the Vasco da Gama bridge [125], which incorporates a combination of visco-elastic and hydraulic dampers inside the deviator guides, or the Uddevalla bridge, described here, which is located in a harsh environment and incorporates friction dampers in all cables.

Considering the importance of damping devices and recent technological developments relating to the evaluation of the performance of a damper, some results of a full-scale controlled test on a 215 m long stay cable are shown. This test is actually part of a study of the efficiency of mechanical damping systems on very large cable-stayed bridges, developed by the Tongji University at Shanghai [124]. It is significant that a set of seven dampers of different types were tested, which did not activate or at least add the full amount of theoretical damping for very small amplitudes of oscillation. Moreover, based on the results of these tests, Sun and co-authors indicate a global efficiency factor of 50% with respect to the theory for most damping systems associated with non-linearities and flexibility of the supports and dampers.

## 7.1 Skarnsundet Bridge (Norway)

### General aspects

- **Name and location:** Skarnsundet bridge, located in Norway, Nord Trøndelag County
- **Owner:** Norwegian Public Roads Administration
- **Year of completion:** 1991
- **Date of retrofit:** No retrofit has been carried out
- **Spans:** Cable-stayed part of bridge:  $3 \times 27 + 109 + 530 + 109 + 3 \times 27 = 910 \text{ m}$
- **Structural system:** Continuous concrete box girder supported by 208 cables (fan type)
- **Cable type and length:** Locked coil cables. Length: 77–278 m. Diameter: 0.052–0.082 m
- **Damping system:** none

### Description of bridge

The Skarnsundet bridge (*Fig. 7.1*) is a cable-stayed bridge with a total length of 1010 m and a main span of 530 m, which was a world record at the time of construction in 1991. It is formed by a very slender continuous box girder 2.15 m thick and 13 m wide that is supported at both towers and also by a total of 208 cables arranged in semi-fan design. The concrete A-shaped pylons are 152 m high.

Aerodynamic stability was tested in wind tunnels at the design stage. Full scale measurements confirmed findings from those tests.



Fig. 7.1: Skarnsundet bridge in Norway

### Description of vibration events

A single occurrence of cable vibration was reported on 25 January, 1995. Two of the longer cables vibrated with an amplitude of approximately 0.70 to 0.80 m (visual observations). The bridge was exposed to a low turbulent wind of speed approximately equal to 13 m/s. The angle of attack was approximately 60° with the bridge axis. The cables were vibrating for a few hours. No further reports on cable vibration are available.

### Inspection details and damage occurrence

**Visual:** No damage has been observed on the bridge.

**Measurements:** The bridge was instrumented with accelerometers placed close to the vibrating cables.

### Analysis of occurrences

A vertical deck frequency equal to exactly two times the fundamental cable frequency was found. It is thus believed that cable vibrations were caused by parametric excitations.

### Retrofit proposal and implemented control measures

None.

**Bibliography:** An internal report (in Norwegian) has been made

## 7.2 Puente Real Bridge (Badajoz)

### General aspects:

- **Name and location:** Puente Real, Badajoz, Extremadura, Spain
- **Owner:** Badajoz City Hall
- **Year of completion:** 1994
- **Date of retrofit:** 1996
- **Spans:** Main span: 136 m; side span: 88 m + 32 m
- **Structural system:** Continuous pre-stressed deck with central suspension by a total of 28 stay cables arranged in semi-fan design, A-shaped pylon with 81.2 m height, continuity with access viaduct
- **Cable type and length:** Bundled strands protected by PE-tube with cement injection, diameters of 0.180, 0.200 and 0.225 m. CTT stronghold anchorage system
- **Damping system:** none

### Description of bridge:

The Puente Real bridge over the Guadiana River at Badajoz (*Fig. 7.2*), Spain, is an asymmetric cable-stayed road bridge with a main span of 136 m, side and transition spans of 88 and 36 m that are continuous with an approach viaduct formed by six spans of 32 m. The deck has a total width of 23 m and is formed by a central pre-stressed concrete box girder 11.4 m wide with side cantilevers of 5.8 m, which is suspended by a total of 28 stay cables arranged in a semi-fan design along the longitudinal axis of the bridge. These cables are anchored at the top of a composite pylon of 81.2 m height.



*Fig. 7.2: Puente Real bridge in Badajoz*

### Description of vibration events:

Strong cable vibrations were observed in the winter of 1995 that led to the loosening of anti-vandalism pipes. Reports of user discomfort due to visual observation of vibrations and to noise from lower cable connections motivated the relevant public authority Junta de Extremadura, Direccion General de Infraestructuras, to order a technical review.

### Inspection details and damage occurrence:

**Visual:** Cable inspection by Fomento de Construcciones y Contratas (FCC) detected damage on the fixing arrangement of the neoprene rings of the lower anchorages. Video recordings of severe events have been obtained.

**Calculations:** Bending frequencies of deck lie at 0.53 Hz and above. In-plane longitudinal frequency was 0.75 Hz. Fundamental cable frequencies were in the range of 0.9–2.1 Hz.

### Analysis of occurrences

The analysis of the video recording resulted in the identification of two different vibration mechanisms: rain and wind induced galloping, and ‘parametric double resonance’.

The first mechanism is associated with first mode vibrations occurring under combined action of rain and wind and affecting a group of cables inclined in one direction. The amplitudes of vibration attained maximum estimated values of 0.40 m. The second mechanism has been identified from an episode in which only one cable vibrated with an estimated amplitude of 0.010–0.020 m, in a high frequency of about 8 Hz. It is thought this vibration was a consequence of dynamic interaction with deck vibration.

### Retrofit proposal and implemented control measures

Besides the inspection and repairing of neoprene supports at the anchorages and eventually of cables, in case of damage due to direct impacts with steel parts, it has been proposed to install friction dampers at all cables in the vicinity of the lower anchorages.

### Bridge behaviour after retrofit

No vibrations have been observed since.

### Bibliography

- [1] BFB, Büro für Baudynamik, Cable Vibrations, Report no. 1, Feb. 1996
- [2] BFB, Büro für Baudynamik, Cable Vibrations, Report no. 2, Dec. 1996

## 7.3 Veterans Memorial and Fred Hartman Bridge (Texas)

### General aspects:

- **Name and location:** Veterans Memorial bridge (VM), in Port Arthur, Texas; Fred Hartman bridge (FH) in Harris County, Texas
- **Owner:** Texas Department of Transportation (TxDOT)
- **Year of completion:** 1991/1995
- **Date of retrofit:** 2004
- **Spans:** VM- main span 195 m; FH- Main span 381m
- **Structural system:** VM: concrete box deck, concrete pylons; FH: steel twin girder deck and floor beam system, steel pylons
- **Cable type and length:** Grouted stays with smooth surface cover and lengths of 6–100 m for the VM and of 59–197 m for the FH bridge
- **Damping system:** Retrofit with viscous dampers from Taylor Devices

### Description of bridges:

The Veterans Memorial bridge in Port Arthur (*Fig. 7.3*) has a total length of about 380 m and a main span of 195 m. It has a concrete box deck with a width of 17 m and is suspended by 112 stay cables arranged in harp from H-shaped pylons.

The Fred Hartman bridge (*Fig. 7.4*) is about 4 km long and crosses the Houston Ship Channel in LaPorte. The bridge consists of twin decks, each approximately 24 m wide. The main cable-stay unit is 754 m long and consists of five spans. The main span length is 381 m. The cable-stay unit superstructure consists of steel girders, transverse floor beams, and a composite concrete deck. The 192 stay-cables project in a fanned configuration from each side of four diamond shaped concrete towers and attach to the outside edges of the bridge decks.



*Fig. 7.3: The Veterans Memorial bridge in Port Arthur, Texas*

### Description of vibration events:

Since 1997, rain vibration has been observed at the two cable-stay bridges in Texas. During rain-induced vibrations, some stays have reached peak amplitudes of oscillation of more than 5–10 times the stay diameter. This has generally been found to occur in one of the first three modes of vibration.

The weather events that trigger the rain vibrations generally have very distinctive characteristics. The intensity of the rain is typically light to moderate, as is the wind. If the rain is too hard or if the wind has too high a velocity, the stay vibrations do not occur because the water is simply blown off. However, the precise conditions that trigger the vibrations are not fully understood.

Rain-induced vibrations of stay cables appear to be independent, at least to a degree, of bridge length and overall superstructure stiffness. The Veterans Memorial bridge has a span about half the span of the Fred Hartman bridge. Both bridges have experienced rain vibrations of stay cables despite having significant differences in superstructure flexibility, albeit the stay vibrations at the Fred Hartman bridge have been more severe. It is believed that the overall flexibility of the steel superstructure and its vibrational characteristics are such that the superstructure “pumps” energy back into the stays in the case of the Fred Hartman bridge.



Fig. 7.4: The Fred Hartman bridge in Harris County, Texas

### Inspection details and damage occurrence:

**Visual:** Approximately 100 welds connecting the steel stay transition pipes to the superstructure are known to have cracked or failed, presumably from large amplitude, low cycle fatigue caused by the vibrating cables.

**Measurements:** The large amplitude vibrations, transition pipe weld failures, and concerns regarding the durability of the stay-cable strands and corrosion protection grout prompted

TxDOT to initiate an evaluation and repair of the bridge. A monitoring program was implemented to evaluate the conditions under which the vibrations occur and to assess non-destructively if significant damage of the stay cables had occurred. This damage assessment was conducted using vibration monitoring techniques to determine effective stay tensions. Using these techniques, assumptions must be made about stiffness, which may not be uniform along the stay, depending on the degree of cracking and damage to the grout at various locations. At best, this method can assess whether there has been a significant reduction in stay tension associated with the gross loss of the pre-stressing steel. The method is not sensitive enough to detect loss of individual wires or even a single prestressing strand that makes up a stay cable. Detection of individual wire breaks within the grouted confines of the stay pipe is possible with the recent advances in acoustic monitoring. An acoustic monitoring system has been installed on the Fred Hartman Bridge, and is proposed for the Veterans Memorial bridge.

### **Retrofit proposal and implemented control measures:**

Various methods were studied to mitigate stay vibrations. In one form or another, all involved increasing damping in the stays.

#### *Cable Restrainers, restraint system for Fred Hartman bridge*

Adding restrainers to the stay cables in effect provides additional mass and damping to individual stay cables tending to respond to excitation mechanisms by tying the cable to others. However, the restrainers also change the natural dynamics of the cables by restraining motion of some points and forcing the cable to respond in shorter, higher-frequency segments. This second effect provides a way to address the issue of unknown excitation mechanisms. Based on videotape of rain vibrations, higher frequency excitation mechanisms ( $>2\text{ Hz}$ ) are concluded to be infrequent or acting with much smaller amplitude because the higher-frequency stays show a pattern of failure resistance. Consequently, the goal of the restrainer design was to have in-plane stay cable substructure frequencies above a target value of about  $2\text{ Hz}$ .

A cable restraint system configuration using three lines of restrainer cables was developed. Analyses were performed on various three-line restrainer configurations. These analyses generally met the design requirement of increasing the stay cable and stay cable substructure frequencies to a value greater than the target value of  $2\text{ Hz}$ . The configuration implemented is shown schematically in Fig. 7.5 along with the principal mode shape of the stay-restrainer system. Using this configuration, most substructure modes were

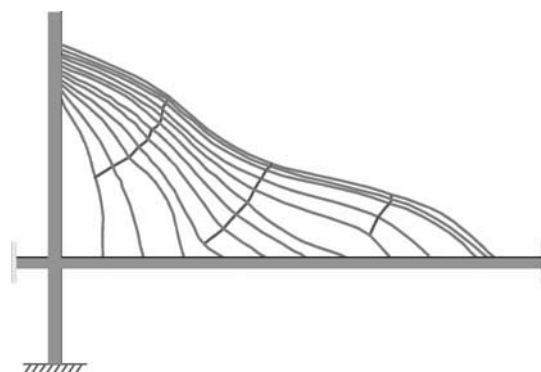


*Fig. 7.5: Cross-tie configuration and principal mode shape of stay-restrainer system*

greater than the  $2\text{ Hz}$  minimum selected as the design criterion for the restraint system.

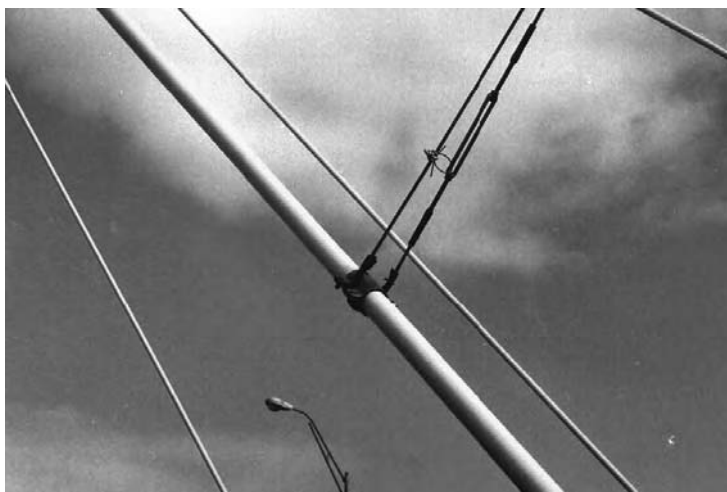


*Fig. 7.6: Detail of temporary restrainer connection to cable*

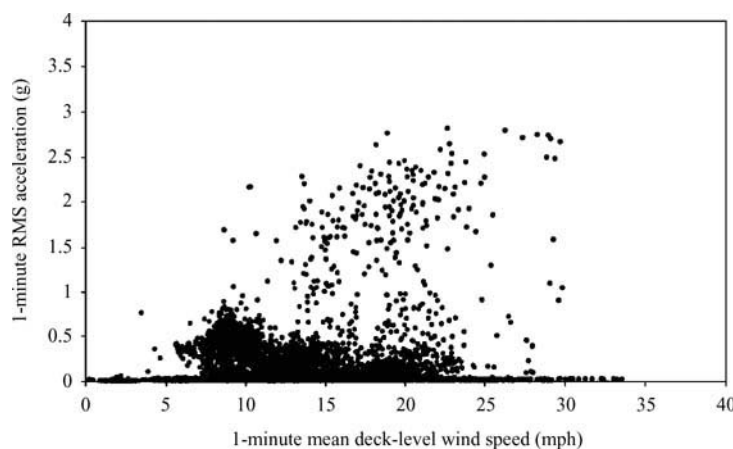


*Fig. 7.7: Stay AS23: In-plane acceleration versus wind speed prior to cable restrainer system Figure*

Figure 7.6 shows a detail of the restrainer connections to main cables, which includes a “safety tether” so that should the restrainer fall due to fatigue or fracture, it won’t fall down to the deck but instead will slide along the stay.

Figures 7.7 and 7.8 illustrate the significant decrease in measured stay accelerations of a stay on the Fred Hartman bridge before and after the cross-ties were installed. Although this method has been proven to be effective, it is temporary and a permanent active system was ultimately developed.

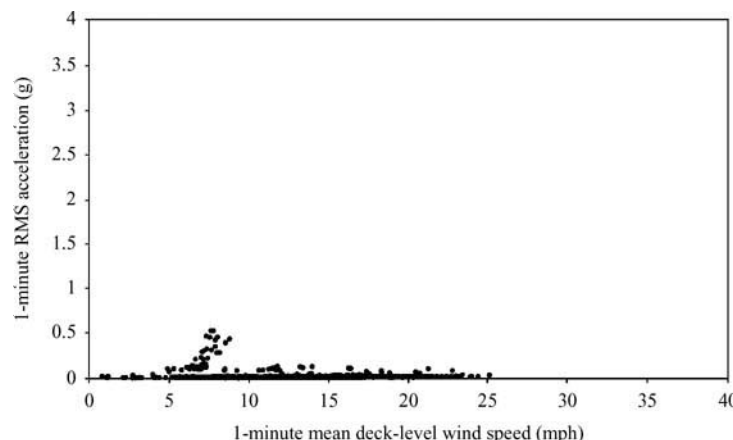


Fig. 7.8: Stay AS23: In-plane acceleration versus wind speed with cable restrainer system installed

### Viscous Dampers

Retrofit viscous dampers were the principal vibration control measure investigated for the permanent mitigation of rain vibration of the stay cables. To evaluate the potential use of retrofit dampers, prototype dampers were developed for both the Fred Hartman and Veterans Memorial bridges.

The damper mechanism for the two bridges was designed using the optimum damping constant obtained based on the procedure developed by Pacheco *et al.* [114], the cable natural frequency and the expected motions at the attachment to determine the required stroke and velocity characteristics. The prototype dampers were attached into the bridge deck by means of an inclined, double-angle strut. Figure 7.9 shows a prototype damper that was evaluated for the Fred Hartman bridge.

### Bridge behaviour after retrofit

Figure 7.9 shows the significant decrease in measured accelerations of a stay with the viscous damper installed (compare to Fig. 7.7). Because of the positive results from the prototype damper over more than a two-year period, the permanent vibration mitigation solution chosen for both bridges was dampers. Figure 7.10 shows the type of damper system selected for the final design for both of the Texas bridges. Note that the final design allowed for the collar to rotate freely around the stay, which ensured that the damper force always passed through the centroid of the stay cross-section.

### Acknowledgements

The contents of this paper reflect the views of the contributor who is responsible for the facts and accuracy of the data presented. The contents do not necessarily reflect the views or

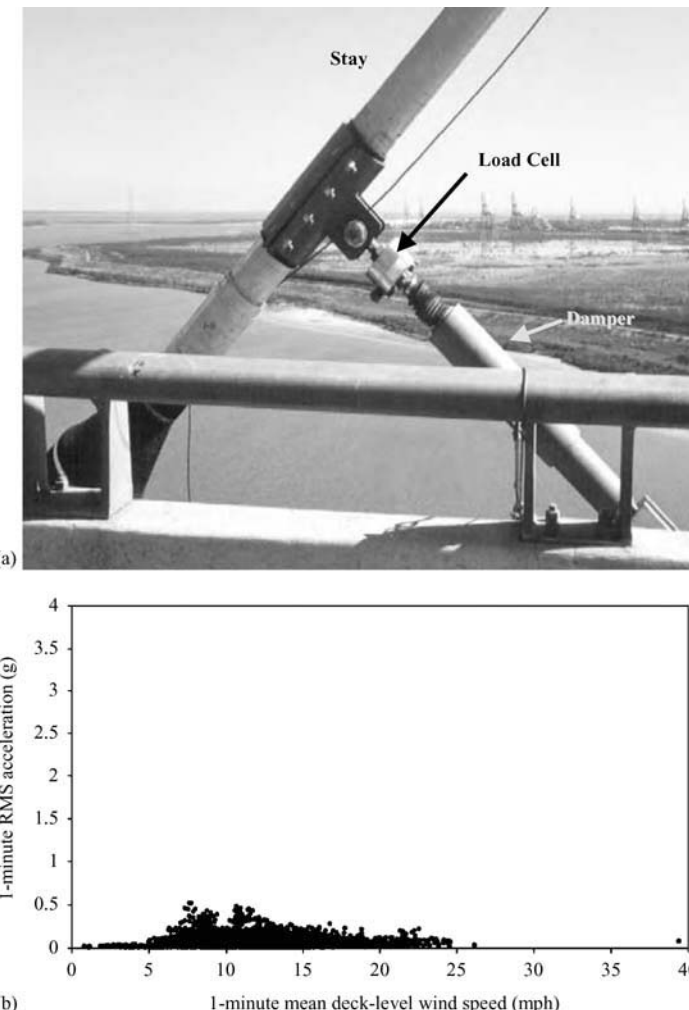


*Fig. 7.9: (a) Viscous damper at the Fred Hartman bridge (b) Stay AS23: In-plane acceleration versus wind speed, with damper*

policies of TxDOT. The author acknowledges the contributions of Dr. Nick Jones of Johns Hopkins University, Baltimore Maryland, for the vibration data collected as part of the overall research program funded by TxDOT.

## 7.4 Erasmus Bridge (Rotterdam)

### General aspects

- **Name and location:** Erasmus bridge, Rotterdam, The Netherlands
- **Owner:** City of Rotterdam

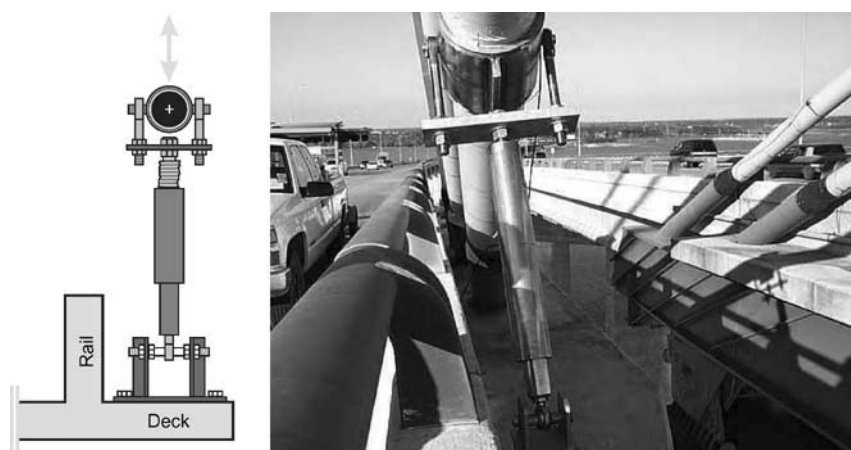


*Fig. 7.10: Final damper system installed on both Texas bridges*



*Fig. 7.11: Erasmus bridge in Rotterdam*

- **Year of completion:** 1996
- **Date of retrofit:** 1997
- **Spans:**  $51.7 + 284 + 73.6\text{ m}$
- **Structural system:** Asymmetric cable stayed bridge. Steel deck suspended in the central span by two planes of 16 cables from a single pylon 139 m high and backstayed by a pair of stay cables.
- **Cable type and length:** Stranded cables in HDPE cover, length varying in the range of 85–300 m, diameters varying in the range of 0.160–0.225 m
- **Damping system:** Hydraulic dampers

Natural frequency (Hz)	Characteristic of deck mode
0.45	1st bending
0.67	2nd bending
0.67	2nd torsion
0.84	1st combined bending and torsion
0.96	3rd bending

Table 7.1: Some calculated natural frequencies of bridge deck

Cable no.	Natural frequency (Hz) (1st; 2nd; 3rd)	$\xi(\%)$ (original damper)
13	0.44; 0.79; 1.21	—
15	0.37; 0.74; 1.11	0.33
16 (longest)	0.38; 0.76; 1.14	0.30

Table 7.2: Measured natural frequencies and critical damping ratios of some cables

## Description of bridge

The Erasmus bridge is an important landmark in the skyline of Rotterdam. The bridge connects the northern and southern parts of Rotterdam over the river Maas and has a steel deck supported by two box girders 2.25 m thick and 1.25 m wide with a main span of 284 m, guided to a single pylon 139 m high by two rows of 16 frontal cables. At the back of the pylon, two backstays, each consisting of four individual, coupled stay cables, stabilise the structure. Every cable consists of 30–48 individual galvanised and polyethylene-coated strands, inside a HDPE cover, with some tolerance between cable and cover. To prevent vortex vibrations, two small dampers have been mounted on every cable between the bridge deck and the steel cover, close to the cable anchoring. Dynamic characteristics of the bridge deck were numerically evaluated at the design stage and verified experimentally. Some of the most relevant calculated natural frequencies are summarised in *Table 7.1*.

Characteristics of the original cables and dampers on the bridge were determined experimentally on site, after occurrence of rain-wind-induced vibrations. Critical damping ratios of the largest two cables (cable numbers 15 and 16) were estimated to be about 0.15% without these dampers, and 0.3% with the two dampers. According to experience at other bridges, this value is not sufficient to avoid rain-wind induced vibrations. Some natural frequencies and damping values of the cables are given in *Table 7.2*.

## Description of vibration events

Large amplitude vibration of the cables and deck were observed under windy and rainy weather conditions on 4 November, 1996. The mean wind direction was nearly south, resulting in a yaw angle  $\beta$  of 25°, directed towards the decreasing cable height (*Fig. 7.12*). The mean wind

speed at average height of the cables was in the order of 14 m/s. From videotapes of the rain-wind-induced vibrations of the Erasmus bridge, it was observed that cables 9–13 vibrated predominantly in the second and higher modes of vibration, at 0.8–1.2 Hz. The first mode of vibration was not excited. An overview is given in *Table 7.3*. The maximum observed amplitudes were in the order of 3 times the diameter of the cable, about 0.7 m (*Fig. 7.13*). The bridge deck vibrated in a torsion-sway mode with maximum vertical amplitude of about 0.025 m.

### Inspection details and damage occurrence

**Visual:** No damage

**Measurements:** Analysis of videotapes allowed the identification of the pattern of cable vibration and the involved frequencies. The characteristics of installed cable dampers were determined experimentally.

### Analysis of occurrences

On the basis of the observations on the Erasmus bridge, and from the information available in literature, a model has been devised, which was implemented in the Finite element code DIANA. In this model, cable movements have been described by a modified galloping equation. The observations of cable response based on the videotapes induced a problem in the modelling of the loading of the cables, as normally the galloping mechanism is dominant in the first natural frequency of the system. Therefore a frequency-selectivity was incorporated in the numerical simulations, which was tuned to the observations for one cable. Using this model, only the vibration mode with frequency located within the range of the filter function was excited.

It was found that modelling the mean wind field was sufficiently accurate to simulate the loading on the cables. A more detailed analysis, taking into account the time and spatial variation of the wind field, caused by turbulence, gave only minor improvements of the results, with a large increase of calculation time.

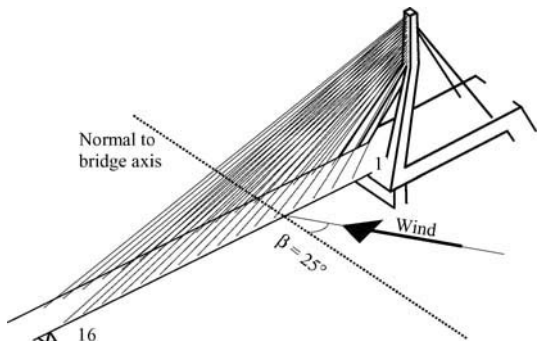


Fig. 7.12: Direction of wind during rain-wind vibration event

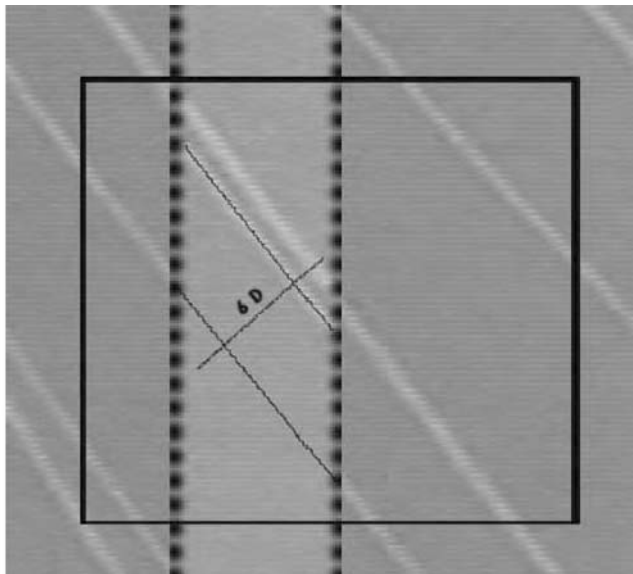


Fig. 7.13: Video frame showing the maximum peak-to-peak amplitude of cable vibration

Cable no.	Frequency (Hz)	Amplitude
9	0.83	—
	1.25	1.5–2D (0.33–0.44 m)
10	0.83	—
11	0.83	—
	0.90	—
12	0.70	3D (0.67 m)
	0.83	—
	0.83	2.5D (0.55 m)

Table 7.3: Observed vibration amplitudes, based on video-tapes

(A detailed description of the analysis made is given in SEI journal 2/98, ref [65].)

### Retrofit proposal and implemented control measures

As a temporary measure, the bridge stay cables were connected to the bridge deck using polypropylene ropes. Immediately after the installation of these ropes, cable vibrations stopped. Later, ropes were replaced by ribbons and the cables were interconnected at three heights (Fig. 7.14). It was observed that due to mild stiffness of the ribbons, cable frequencies did not suffer a significant variation. However, the damping was raised to about 0.6%, which was considered large enough to suppress vibrations. In fact, no further episodes of cable vibration were detected after installation of the ropes.

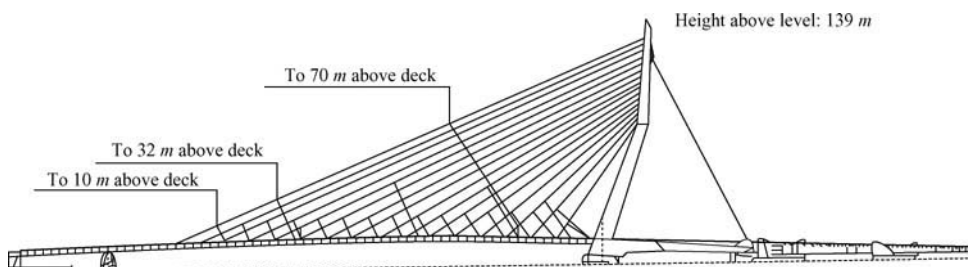


Fig. 7.14: Bridge elevation, showing temporary restraint of cables

As for permanent control of vibrations, three types of permanent measures were considered: changing the surface roughness of the cable duct, cross-connecting the cables and adding damping. For a bridge that is already built, the first two measures are difficult to include. Therefore, special studies were performed to estimate the required amount of damping per cable.

The effects of additional dampers were studied. Increasing the damping constant of discrete dampers may cause a decrease in the effective damping of the cable for higher frequencies.

This result was supported by on-site measurements on prototypes, and was calculated by a complex modal analysis of the cable with discrete dampers. If the dampers are too stiff, they will act as a support, and decrease the damping of the cables. Also, if the dampers are mounted too close to the anchorage, they will not be effective.

Using two dampers of  $25 \text{ kNs/m}$  each, the damping ratio of the cable was in the order of 0.8% at the observed exciting frequency of  $0.8 \text{ Hz}$ , which was sufficient to achieve the required damping of cables 2–13. These new dampers were placed at a larger distance from the anchoring of the cables, compared to the positions of the original dampers. Cables 1 and 14–16 have been supplied with dampers with a damping constant of two times  $30 \text{ kNs/m}$ .

During on-site measurements on prototypes of new dampers, it was found that non-linear damping behaviour of the dampers, e.g. caused by dry friction, reduces the effectiveness and results in a lower damping. Therefore, the dampers were modified and their non-linear property was included in the calculations to successfully increase the correlation between calculations and measurements.

## Bridge behaviour after retrofit

Continuous monitoring of the displacements of the bridge deck since 1997 showed no vibrations during wind-rain events. Problems occurred only when the annual dance parade crossed the bridge.

## Bibliography

- [1] C.P.W. Geurts, T. Vrouwenvelder, P. van Staalduin, J. Reusink. *Structural Engineering International* 2/98, pp. 129–135, also presented as poster at COWI Symposium on bridge aerodynamics, May 1998.
- [2] C.P.W. Geurts, P.C. van Staalduin. 1999. 10th International Conference on Wind Engineering, Copenhagen, June 1999: In: *Wind Engineering into the 21st Century*. Volume 2, pp. 885–893, 1999, Balkema.
- [3] C.P.W. Geurts In: ‘Winderregte Schwingungen von Tragwerken’, WTG Berichte Nr. 6: 6. Dreiländertagung D-A-CH ’99, WTG, November 1999, Berlin, 1999, pp. 121–134.
- [4] Third European-African Conference on Wind Engineering Excursion to the city of Rotterdam 4 July, 2001, 3–6.
- [5] Persoon, A.J., Noorlander, K. 1999. 10th International Conference on Wind Engineering, Copenhagen, June 1999: In *Wind Engineering into the 21st Century*, Vol. 2, pp. 1019–1026. Balkema.

## 7.5 Kap Shui Mun Bridge (Hong Kong)

### General aspects

- **Name and location:** Kap Shui Mun bridge, Hong Kong
- **Owner:** Hong Kong Department of Highways
- **Year of completion:** 1997
- **Spans:**  $80 + 80 + 430 + 80 + 80 \text{ m}$



*Fig. 7.15: Kap Shui Mun bridge in Hong Kong*

- **Structural system:** Cable-stayed double-deck 35.2 m wide, partial support at H-shaped towers 150 m high
- **Cable type and length:** Double-plane fan arrangement, total of 176 cables, length varying in range from 64 to 225 m. Cables are bundles of 51–102 parallel wire strands inside HDPE cover
- **Damping system:** None

### Description of bridge

The Kap Shui Mun bridge (*Fig. 7.15*) is part of the Lantau Link and spans the main marine channel Kap Shui Mun between the islands of Ma Wan and Lantau, in Hong Kong. The bridge has a total length of 750 m and is formed by a central span of 430 m and two lateral spans of 80 m on each side (*Fig. 7.16*). It has a double-deck that is used for road and railway traffic. The central 387 m of the 35.2 m wide deck is of steel/concrete type, while the rest is pre-stressed concrete. The towers are H-shaped and rise to a height of 150 m. The deck is supported by the towers and by a total of 176 stay cables, which are arranged like a fan in two planes. Each cable is a bundle of 51–102 parallel wire strands, with lengths varying in the range of 64–225 m. Bundles of strands are encased in a HDPE cover, which is formed by two half shells.

### Description of vibration events

During severe meteorological conditions, high amplitude vibrations of cables occur.

### Inspection details and damage occurrence

Vibrations of the stay cables with large amplitudes have been observed. These vibrations may cause damage on the stay cable.

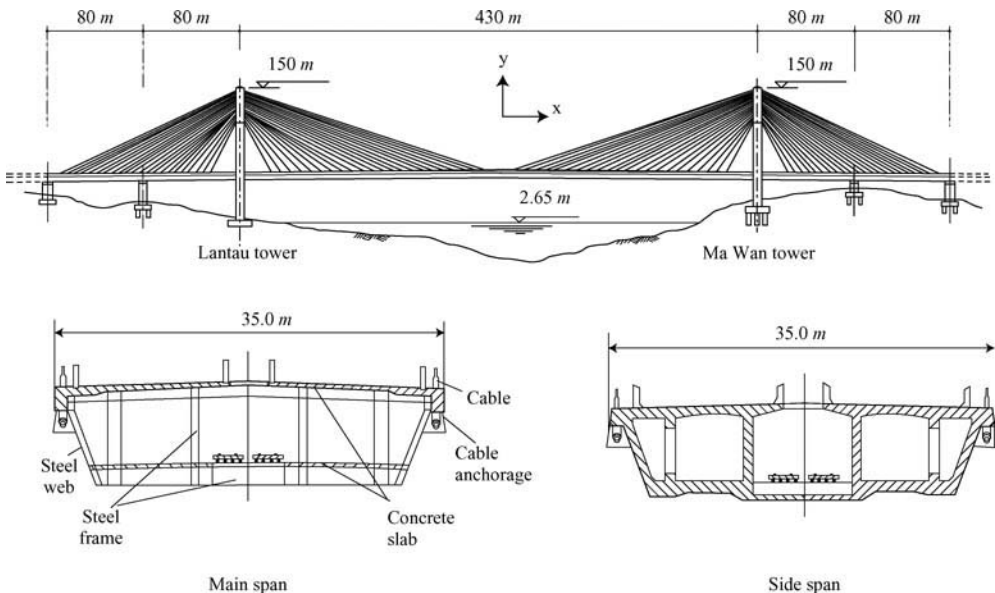


Fig. 7.16: Lateral view and cross sections of Kap Shui Mun bridge

## Measurements

One of the second largest cables (length of  $L = 214\text{ m}$ ) from the central span was instrumented with two accelerometers and excited with a rope by four workers, in order to attain resonance in the first and second modes. The free vibration response was measured and used to assess structural damping (referred to critical damping), estimated in the order of  $\xi_s = 0.10\%$ .

## Analysis of occurrences

During part of the tests, wind speed was estimated to be in the range of 4–10 m/s and some rainfall occurred, with creation of water rivulets on the bottom position of the stay sheath. Rain/wind vibrations are one of the possible explanations for large oscillations.

## Retrofit proposal and implemented control measures

To prevent any damage to the stay cables, the Highways authorities have decided to test the effectiveness of dampers installed close to the deck anchorages.

*Figure 7.17* shows the installation of the friction damper from VSL at the end of the guide pipe, at a distance  $x_c$  to the anchorage plates of about 6.4 m ( $x_c/L = 0.03$ ). VSL proposes the following formula for the final damping  $\xi$  of the cable (referred to critical damping):  $\xi = \frac{\alpha\beta}{2} \cdot \frac{x_c}{L} + \xi_s$ , where  $\alpha$  is a second order loss coefficient, defined as 95% and  $\beta$  is the anchorage flexibility loss coefficient, considered as 89%. A damping ratio  $\xi$  of 1.35% is therefore expected, and measurement of the free decay response after installation of the damper showed a value of 1.55%.



Fig. 7.17: Installation of VSL friction damper. Application of clamper force to generate friction

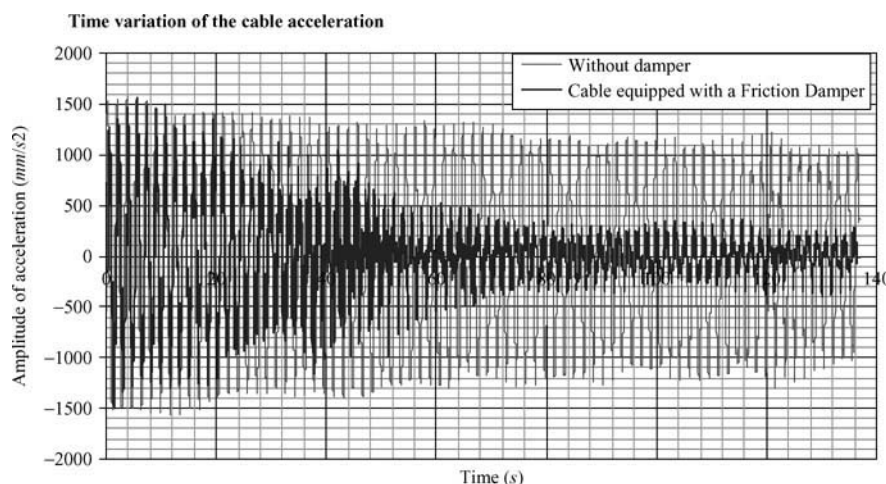


Fig. 7.18: Time variation of the acceleration of the cable with and without friction damper

Since the friction damper is non-linear, it is necessary to evaluate the variation of damping with the amplitude of oscillation. The threshold amplitude for activation of the damper can be selected and for the current case a value in the order of 0.020 m was selected. Then the friction force can be determined in order to select the amplitude at which the added damping ratio by the friction damper is maximal. Figure 7.18 shows the time variation of the acceleration of the cable equipped with a friction damper, and without the damper. Figure 7.19 shows the variation of measured and theoretical damping ratio with the amplitude of oscillation at mid span. The drop in the logarithmic decrement for a vibration amplitude of 0.070 m is probably a consequence of a train-crossing added response to the free vibration resultant from manual excitation.

### Bridge behaviour after retrofit

The VSL damper has matched and even exceeded the theoretical performances when all losses are considered. The amount of damping provided should be sufficient to cope with high amplitude vibrations.

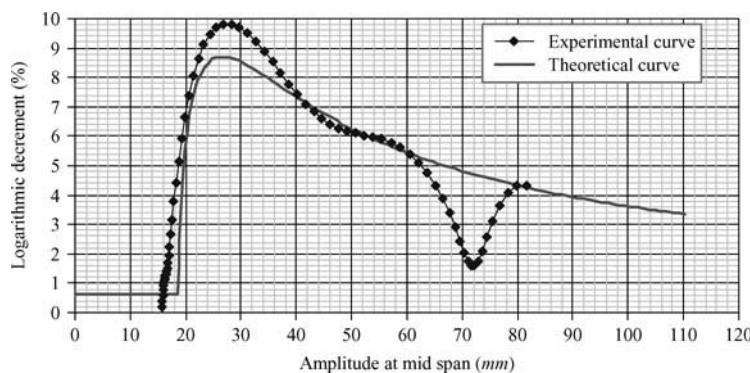


Fig. 7.19: Damping curve associated with installed friction damper, theoretical and measured

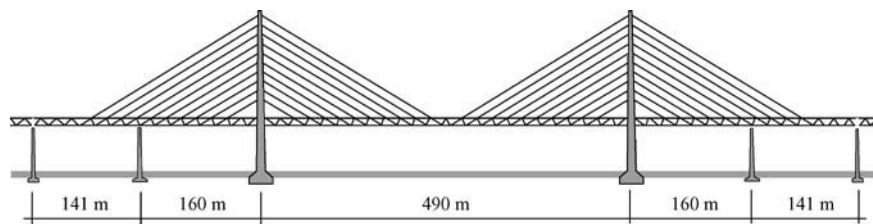


Fig. 7.20: Öresund cable-stayed bridge [43]

## Bibliography

- [1] Annan, Rachid *Friction Damper Test: Report of Test Achieved with Hong Kong Highways Authorities on Kap Shui Mun Bridge* VSL International, 2006.

## 7.6 Oresundsbron (Denmark–Sweden)

### General aspects

- **Name and location:** Oresund bridge, Copenhagen, Denmark—Malmö, Sweden
- **Owner:** Sund og Belt
- **Year of completion:** 2000
- **Date of retrofit:** 2003
- **Spans:**  $141 + 160 + 490 + 160 + 141 \text{ m}$
- **Structural system:** Truss girder
- **Cable type and length:** Twin stays made of parallel strands inside HDPE cover, harp arrangement, maximum length of 500 m, diameter of 0.250 m
- **Damping system:** Hydraulic dampers, helical fillets in HDPE cover

## Description of bridge

The Öresund cable-stayed bridge (*Fig. 7.20*) is the central part of the 7.8 km link between Denmark and Sweden. It is a two-level structure that carries simultaneously a railway running inside a steel truss, and a motorway on an upper slab (*Fig. 7.21*). The bridge has a central span of 490 m and two lateral spans of 141 and 160 m. The cable system consists of a total of 160 stay cables arranged like a harp in two vertical cable planes. The cables are formed by groups of two closely spaced parallel strand cables (*Fig. 7.22*) encased in black HDPE tubes of 0.250 m diameter (each cable is a bundle of 68–73 strands).

Design studies related to cables included the investigation of the effects from buffeting, vortex shedding, cable-structure interaction, rain/wind induced vibrations and wake galloping. Maximum design amplitude vibrations were defined as  $L/3000$ ,  $L$  representing the cable length, and 0.060 m for a 20 m/s mean wind (10 min) at a height of 100 m. In order to protect the cables against rain/wind excitation, the HDPE cover was produced with 0.002 m thick helical ribs. The possibility of wake galloping resulting from the association of the cables in pairs was investigated in a wind tunnel and the distance between stays, necessary to avoid instability, was determined as 0.670 m. In order to improve stability, connectors were added between cables at 100 m intervals.

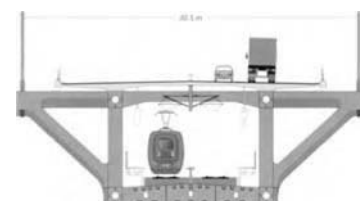


*Fig. 7.21: The Öresund bridge cross section [126]*

## Description of vibration events

Large amplitude vibrations were reported by bridge workers during the final stages of completion of the bridge, in 2000. As a consequence, it was decided to install hydraulic dampers at the lower anchorages of the longest cables. These were based on an oil-filled hose inserted between the stay cable and the guide tube, 3.8 m above the anchorage. Large stay cable vibrations were not observed for  $1\frac{1}{2}$  years, until the permanent monitoring system detected a large amplitude incident in December 2001, followed by more incidents in the early spring of 2002. Visual inspection of the dampers revealed severe damage, indicating the damper design was inadequate for the bridge.



*Fig. 7.22: The Öresund bridge [43]*

In the period between the summer of 2002 and 2004 several episodes of cable vibration were noticed in cables using two different types of dampers. In particular, an episode of

vibration occurred on 24 February, 2004 that lasted for about 1 h and was associated with snow accumulation on the cables and wind speeds close to 14 m/s. This condition resulted in an amplitude of vibration of 3 m for a cable with a damper of the former type (that was found broken after the storm), while another cable equipped with a new type of damper (formed by three hydraulic pistons mounted in radial fashion between the stay and the guide tube 4.6 m above the anchorage) reached a maximum amplitude of vibration of about 0.5 m.

## Inspection details and damage occurrence

**Measurements:** Accelerometers mounted on stay cables were used for assessment of the stay cable vibrations, supplemented by visual inspections.

## Analysis of occurrences

Correlation between weather conditions and large amplitude vibrations indicated that the major source of vibrations was related to rain/wind action or galloping caused by aggregation of snow or ice on the stays.

The analysis carried out was aimed at identifying the cause of the cable vibrations. Moreover the monitoring of stay cables equipped with different types of dampers allowed the assessment of the amount of damping necessary to mitigate vibrations.

## Retrofit proposal and implemented control measures

Two types of hydraulic dampers were introduced as retrofit measures. The first set of dampers comprising an oil-filled torus inserted between the stay cable and anchor tube proved to be insufficient to mitigate the ice/wind induced stay vibrations. A new design, comprising three commercial dashpot dampers replacing the oil-filled torus dampers, has until now (one winter season track record) provided sufficient damping (a damping ratio of 0.7% of critical damping was measured with the latter damper system).

## Bridge behaviour after retrofit

Stay cables have not experienced large amplitude vibrations since fitting the dashpot dampers.

## Bibliography

- [1] Gimsing, N. & Nissen, J. 1998. The Pylons on the Øresund Bridge. *Structural Engineering International*, Vol. 8, No. 4, Nov.: 263–264. IABSE.
- [2] Hauge, L. & Petersen, A. 1999. *Detailed Design of the Cable-stayed Bridge for the Øresund Link*. Proceedings of the IABSE Conference, Malmö.
- [3] Larsen, A., Larfrenière, A. 2005. *Application of a limit cycle oscillator model to bridge cable galloping*. Proc. Sixth International Symposium on Cable Dynamics, Charleston SC. September 19–22.
- [4] Øresund Konsortiet 1998. *The Øresund Fixed Link: Design and Construction*.
- [5] Sørensen, L. & Thorsen, N. 1999. *The Øresund Bridge, Erection of the Cable-stayed Main Span*. Proceedings of the IABSE Conference, Malmö.

## 7.7 Uddevallabron (Sweden)

### General aspects

- **Name and location:** Uddevalla bridge, located in Sweden close to the town of Uddevalla
- **Owner:** Swedish National Road Administration Western Region
- **Year of completion:** 2000
- **Date of retrofit:** No retrofit has been carried out
- **Spans:** Cable-stayed part of bridge:  $179 + 414 + 179 = 772 \text{ m}$
- **Structural system:** Continuous composite cross section made up of an open steel grid and prefabricated concrete slab elements. Supported by a total of 120 stay cables.
- **Cable type and length:** VSL Stay Cable System 200 SSI. Number of strands: 22–77. Cable length varying from 61–211 m. Bundles of strands encased in HDPE stay pipe.
- **Damping system:** The bridge was equipped with the following damping systems from the beginning:
  - a) The external HDPE pipe was equipped with small ribs on the outside ( $0.002 \times 0.002 \text{ m}$ );
  - b) A specially designed friction damper was installed between the stay cable and the support pipe extending from the lower anchorage at the bridge deck (Fig. 7.23).

### Description of bridge

The Udevalla bridge (Fig. 7.24) is a high-level bridge with a total length of 1712 m between abutments. The central part is formed by three cable-stayed spans of 179, 414 and 179 m, which are continuous with the approach viaducts on each side. The bridge cross section (cable-stayed part) is formed by an open steel grid in composite action with prefabricated concrete slab elements. It is supported both by the towers and by a total of 120 stay cables. These are arranged in semi-fan fashion and form slightly inclined cable planes. The stay cables are bundles of 22–77 strands encased in HDPE pipes, with lengths varying from 61–211 m. The towers are diamond shaped and made of concrete, reaching a height of 140 m. In order to avoid cable vibrations, some measures were taken, which consisted of: selection of a HDPE with external helical ribs for protection against rain-wind vibrations; installation of friction dampers close to the deck anchorage of all cables; and design of cable system allowing future installation of transverse stiffening ropes, if deemed necessary.

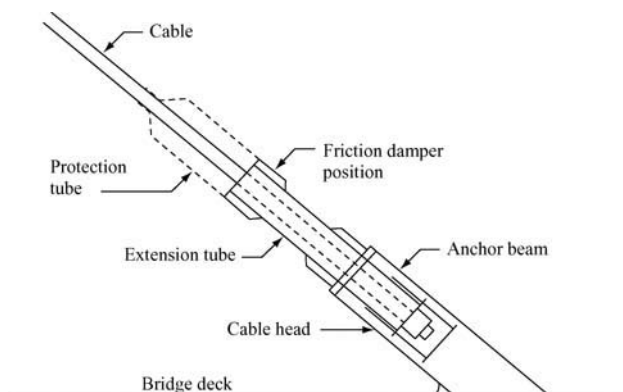


Fig. 7.23: Principal design of lower cable anchorage and friction damper position



Fig. 7.24: *Uddevalla bridge, general view*

### Description of vibration events

No events of cable vibration have been reported.

### Inspection details and damage occurrence

**Visual:** After two years of service, one third of the dampers were controlled in order to check their condition. The visual control of the sliding plates that form the damper demonstrated that the cables have been submitted to small movements. The friction components were in good condition.

**Measurements:** The bridge was instrumented and monitored from August 2002 to January 2006. No cable vibrations of noticeable magnitude have been recorded during this period.

### Bibliography

- [1] Kovacs, I., Strømmen, E. & Hjorth-Hansen, E. 1999. Damping devices against cable oscillations on Sunningesund bridge. Proceedings of Third International Symposium on Cable Dynamics, Trondheim, 16–18 August;
- [2] Hjorth-Hansen, E., Strømmen, E., Myrvoll, F., Hansvold, C. & Ronnebrant R. 2001. Performance of a friction damping device for the cables on the Udevalla cable-stayed bridge. Proceedings of the Fourth International Symposium on Cable Dynamics, Montreal, 28–30 May.
- [3] Bournand, Y. & Crigler, J. 2005. The VSL friction damper for cable-stayed bridges. Some results from maintenance and testing of long cables. Proceedings of the Sixth International Symposium on Cable Dynamics, Charleston, USA, 19–22 September.



*Fig. 7.25: View of vandalism pipes covering dampers. Lifting of vandalism pipe for inspection of damper*

## 7.8 Friction Damper Test

**Damper test:** VSL Friction damper

### General aspects

- **Location:** China
- **Cable manufacturer:** Jiangsu Fasten Nippon Steel
- **Cable type and length:** Parallel wire strand with diameter of 0.113 m and length of 215.6 m.
- **Damping system:** Friction damper with varying composite friction material and friction force. The damper is formed by a steel collar rigidly fixed to the cable and moving together with the cable; two spring blade half-rings fixed to the bridge structure around the cable; and four soft friction components that are pressed against hard friction partners held by the spring rings. The damper works in any direction of motion and allows longitudinal movement of the cable. It is adjusted to function only when vibrations attain a certain level, thereby reducing maintenance costs.

### Description of test

The test has been developed on a stay cable with a length of 215.6 m and a diameter of 0.113 m, mounted horizontally at the Jiangsu Fasten Nippon Steel factory (Fig. 7.26), and tensioned to a force of 3950 kN. The friction damper from VSL was one of the seven mechanical damping systems that were tested by the Tongji University of Shanghai [124].

The performance of the VSL damper was measured at two different locations, at distances from the anchorage of 3.5 m (1.6% of cable length) and 5 m (2.3% of cable length). In both cases the damper (Fig. 7.27) was tested with different composite friction materials. Resonant excitation was achieved by two men pulling the cable by hand at the frequencies associated with the first three cable modes. The measurement of the free vibration response after resonance excitation allowed the identification of damping ratios as functions of the amplitude of cable oscillation.



Fig. 7.26: Test cable at Jiangsu Fasten Nippon Steel factory



Fig. 7.27: VSL friction damper and accelerometer. Damper support is prevented from longitudinal and transversal movement

Figure 7.28 shows the damping curve obtained for the first vibration mode based on the measurements performed at quarter the cable length. It can be observed that a maximum logarithmic damping of 8% ( $\xi = 1.3\%$ ) was measured for a distance to the cable support corresponding to 2.3% of the cable length, and that  $\xi = 0.95\%$  for a distance to the cable support corresponding to 1.6% of the cable length. This means that the initial cable damping,

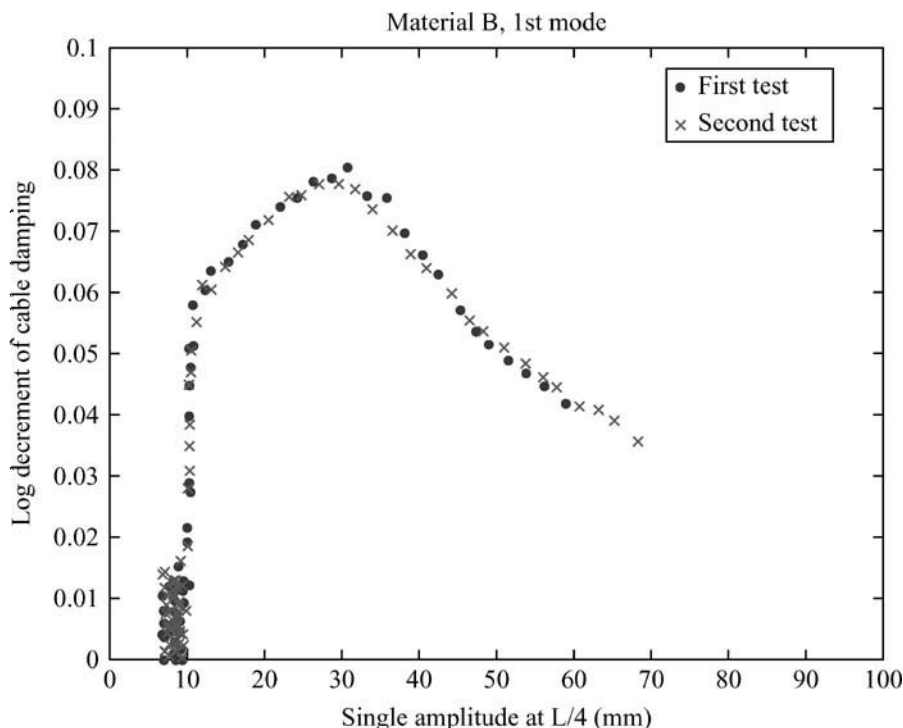


Fig. 7.28: Damping curve of friction damper at mode 1 for  $x_c/L = 0.023$

measured as  $\xi_1 = 0.08\%$ , increased 1.22% and 0.87%, respectively, thereby providing more than 100% the theoretical value.

Figure 7.28 shows also that the damper is not always active. It was actually tuned to activate at minimum amplitude vibrations of 0.014 m (0.010 m at the measurement point, at quarter the cable length), and maximum damping has been reached at an amplitude of vibration of 0.042 m (0.030 m at quarter the cable length). Finally it is observed that a minimum logarithmic damping of 3% ( $\xi = 0.5\%$ ) is always obtained and that the reduction of the friction force does not significantly affect the damper efficiency.

## Bibliography

- [1] Bournand, Y. 2004. Friction damper: Main results of the tests achieved by Tongji University, Shanghai, VSL Technical Report.
- [2] Bournand, Y. & Crigler, J. 2005. The VSL friction damper for cable-stayed bridges. Some results from maintenance and testing on long cables. Proceedings of the Sixth International Symposium on Cable Dynamics, Charleston, USA, 19–22 September.
- [3] Sun, L., Shi, C., Zhou, H. & Zhou, Y. 2005. Vibration mitigation of long stay cable using dampers and cross-ties. Proceedings of the Sixth International Symposium on Cable Dynamics, Charleston, USA, 19–22 September.

## 8. References

- [1] Wianecki, J.: "Cables Wind Excited Vibrations of Cable-Stayed Bridges" in Proceedings of the 5th International Conference of Wind Engineering, Colorado, 1979, 1381–1393
- [2] Stiemer, S.F., Taylor, P. and Vincent, D.H.C.: "Full Scale Dynamic Testing of the Annacis Bridge"; IABSE Periodica, Vol. 1, 1–16, 1988
- [3] Podolny, W. and Scalzi, J.: "Construction and Design of Cable-Stayed Bridges"; John Wiley & Sons, New York, 1976
- [4] Leonhardt, F. and Zellner, W.: "Cable-Stayed Bridges", 1980, IABSE Surveys, S-13/80
- [5] Gimsing, N.J.: "Cable Supported Bridges: Concept and Design"; Wiley Interscience, Chichester, 1983
- [6] Troitsky, M.S.: "Cable-Stayed Bridges: Theory and Design", 2nd Edition; BSP Professional Books, UK, 1988
- [7] Leonhardt, F. and Zellner, W.: Past, Present and Future of Cable-Stayed Bridges, in Ito, M., Fujino, Y., Myiata, T. and Narita, N. (eds), "Cable-Stayed Bridges: Recent Developments and their Future"; Elsevier, 1991, 1–33
- [8] Mathivat, J.: "The Cantilever Construction of Prestressed Concrete Bridges"; John Wiley and Sons Ltd, UK, 1983
- [9] Karoumi, R.: "Response of Cable-Stayed Bridges Subjected to Moving Vehicles"; Licentiate Thesis, Structural Engineering, Royal Institute of Technology, Sweden, 1996
- [10] Taylor, P.R.: Precast and Composite Concrete Cable-Stayed Bridges, in Ito, M., Fujino, Y., Myiata, T. and Narita, N. (eds), "Cable-Stayed Bridges: Recent Developments and their Future"; Elsevier, 1991, 107–124
- [11] Mathivat, J.: "Les ponts à câbles. Des Origines à la Conquête des Grandes Portées" in Proceedings of the IABSE/FIP International Conference on Cables-Stayed and Suspension Bridges; Deauville, 12–15 October, Vol. 1, 3–32, 1994
- [12] Virlogeux, M.: "Bridges with Multiple Cable-Stayed Spans" in Proceedings of the IABSE Conference on Cable-Stayed Bridges-Past, Present and Future; Malmö, Sweden, 1999, 332–343
- [13] Khalifa, M.A.: "Dynamic Vibration of Cable-Stayed Bridges Using Carbon Fiber Composite Cables", in Proceedings of the 1st Conference on Advanced Composite Materials in Bridges and Structures; CSCE, 1992, 465–477
- [14] Seible, F., Karbhari, V. and Burgueno, R.: "Kings Stormwater and I-5 Gilman Bridges, USA"; Structural Engineering International, No. 4, 250–253, 1999
- [15] Geffroy, R.: "The Laroin Footbridge with Carbon Composite Stay Cables", in "Footbridge 2002"; Paris, 2002
- [16] Richmond, B. and Sham, R.S.H.: "Present and Future Developments in Cable-supported Bridge Technology using New Materials", in Proceedings of the IABSE/FIP International Conference on Cable-Stayed and Suspension Bridges, Deauville, 12–15 October, Vol. 1, 79–90 1994
- [17] Simiu, E. and Scanlan, R.: "Wind Effects on Structures: Fundamentals and Applications to Design", 3rd Edition; John Wiley & Sons, USA, 1996, ISBN 0-471-12157-6

- [18] SETRA: “Cable Stays”; Recommendations of French Interministerial Commission on Prestressing, France, 2002
- [19] Virlogeux, M.: Cable Vibrations in Cable-Stayed Bridges, in Larsen, A. and Esdahl, S. (eds), “Bridge Aerodynamics”; Balkema, 1998, 213–233
- [20] Solari, G.: Gust-Excited Vibrations, in Sockel, H. (ed), “Wind-Excited Vibrations of Structures”, CISM Courses and Lectures No. 335; International Centre for Mechanical Sciences, Springer-Verlag, 1994, 195–291
- [21] Shi, W., Wang, C., Coles, D. and Roshko, A.: “Experiments on Flow Past Circular Cylinders at Large Reynolds Numbers”; Journal of Wind Engineering and Industrial Aerodynamics, Vol. 49, 348–351, 1993
- [22] Sockel, H.: Fundamentals of Wind Engineering, in Sockel, H. (ed), “Wind-Excited Vibrations of Structures”, CISM Courses and Lectures No. 335; International Centre for Mechanical Sciences, Springer-Verlag, 1994, 85–161
- [23] Cremona, C. and Foucriat, J.-C. (eds): “Comportement au Vent des Ponts”; Presses de l’École Nationale des Ponts et Chaussées AFGC, 2002
- [24] Dyrbye, C. and Hansen, S.: “Wind Loads on Structures”; John Wiley & Sons, Chichester, 1999. Copyright John Wiley & Sons Limited. Reproduced with Permission.
- [25] Yamada, H.: “Control of Wind-Induced Cable Vibrations from a Viewpoint of the Wind Resistant Design of Cable-Stayed Bridges” in Proceedings of the International Seminar on Cable Dynamics, Tokyo JAWE, 13 October 1997, 129–138
- [26] Yamaguchi, H. and Fujino, Y.: Larsen, A. and Esdahl, S. (eds), “Bridge Aerodynamics”; Balkema; 1998, 235–253
- [27] Tabatabai, H. and Mehrabi, A.: “Evaluation of Various Damping Treatments for Stay Cables”, in Proceedings of IMAC XVIII, San Antonio, Texas, 2000, 836–841
- [28] Griffin, O., Skop, R. and Ramberg, S.: “The Resonant Vortex-Excited Vibrations of Structures and Cable Systems” in Offshore Technology Conference, Paper OTC-2319, Houston, 1975
- [29] Davenport, A.: “A Simple Representation of the Dynamics of a Massive Stay Cable in Wind” in Proceedings of the IABSE/FIP International Conference on Cables-Stayed and Suspension Bridges, Deauville, 12–15 October, Vol. 2, 427–438, 1994
- [30] CEN: Eurocode 1: Actions on structures—Part 1–4: General actions—Wind actions, prEN1991-1-4.6, 2002
- [31] Ruscheweyh, H.: Vortex Excited Vibrations, in Sockel, H. (ed), “Wind Excited Vibrations of Structures”, CISM Courses and Lectures No. 335; Springer-Verlag, 1994, 51–84
- [32] Matsumoto, M., Shiraishi, H. and Shirato, H.: “Rain-Wind Induced Vibration of Cables of Cable-Stayed Bridges”; Journal of Wind Engineering and Industrial Aerodynamics, Vol. 44, 2011–2022, 1992
- [33] Saito, T., Matsumoto, M. and Kitazawa, M.: “Rain-Wind Excitation of Cables on Cable-Stayed Higashi-Kobe Bridge and Cable Vibration Control” in Proceedings of IABSE/FIP International Conference on Cables-Stayed and Suspension Bridges, Deauville, 12–15 October, Vol. 2, 507–514, 1994
- [34] Cheng, S., Tanaka, H., Irwin, P. and Jakobsen, J.: “Aerodynamic Instability of Inclined Cables”, in Fifth International Symposium on Cable Dynamics, Santa Margherita Ligure, Italy, 2003, 69–76

- [35] Tanaka, H.: "Aerodynamics of Cables", in Fifth International Symposium on Cable Dynamics, Santa Margherita Ligure, Italy, 11–25, 2003
- [36] Cheng, S.: "Aerodynamic Behaviour of an Inclined Circular Cable"; Journal of Wind and Structures, Vol. 6, No. 3, 197–208, 2003
- [37] Matsumoto, M.: Observed Behaviour of Prototype Cable Vibration and its Generating Mechanism, in Larsen, A. and Esdahl, S. (eds), "Bridge Aerodynamics"; Balkema, 1998
- [38] Honda, A., Yamanaka, T., Fujiwara T. and Saito, T.: "Wind Tunnel Test on Rain-Induced Vibration of the Stay-Cable" in Proceedings of the International Symposium on Cable Dynamics, Liège, Belgium, 1995
- [39] Irwin, P.: "Wind Vibrations of Cables on Cable-Stayed Bridges" in Proceedings of the ASCE Structures Congress, Vol. 1, 383–387, 1997
- [40] PTI Guide Specification: "Recommendations for Stay Cable Design, Testing and Installation"; PTI, USA, 2000
- [41] Kubo, Y., Kimura, K., Tanaka, H., Isobe, T., Fujita, M., Higashi, H. and Kato, K.: "Aerodynamic Responses of Inclined Cables in Section Model Test and Full Model Test" in Fifth International Symposium on Cable Dynamics, Santa Margherita Ligure, Italy, 383–390, 2003
- [42] Matsumoto, M., Ishizki, H., Kitazawa, M., Aoki, J. and Fujii, D.: "Cable Aerodynamics and its Stabilization" in Proceedings of the Internation Symposium on Cable Dynamics, Liège, Belgium, 1995
- [43] Gimsing, N. and Nissen, J.: "The Pylons on the Øresund Bridge"; Structural Engineering International, Vol. 8, No. 4, 263–264, 1998
- [44] Matsumoto, M., Yokoyama, K., Miyata, T., Fujino, Y. and Yamaguchi, H.: "Wind-Induced Cable Vibration of Cable-Stayed Bridges in Japan" in Proceedings of Canada-Japan Workshop on Bridge Aerodynamics, Ottawa, Canada, 1989
- [45] Miyata, T.: Design Considerations for Wind Effects on Long-Span Cable-Stayd Bridges, in Ito, M., Fujino, Y., Myiata, T. and Narita N. (eds), "Cable-Stayed Bridges: Recent Developments and their Future"; Elsevier, 1991, 235–256
- [46] Narita, N. and Yokoyama, K.: A Sumarized Account of Damping Capacity and Measures Against Wind Action in Cable-Stayed Bridges in Japan, Ito, M., Fujino, Y., Myiata, T. and Narita N. (eds), "Cable-Stayed Bridges: Recent Developments and their Future"; Elsevier, 257–278, 1991
- [47] Kubo, Y., Kato, K., Maeda, H., Oikawa, K. and Takeda, T.: "New Concept on Mechanism and Suppression of Wake Galloping of Cable-Stayed Bridges" in Proceedings of the IABSE/FIP International Conference on Cables-Stayed and Suspension Bridges, Deauville, 12–15 October, Vol. 2, 491–498, 1994
- [48] Kubo, Y.: "Aeroelastic Instability and its Improvement of Bundle Cable for Cable-Stayed Bridge", in Proceedings of the International Seminar on Cable Dynamics; JAWE, Tokyo, 13 October 1997, 49–56
- [49] Yoshimura, T., Savage, M.G., Tanaka, H. and Wakasa, T.: "A Device for Suppressing Wake Galloping of Stay Cables for Cable-Stayed Bridges"; Journal of Wind Engineering and Industrial Aerodynamics, Vol. 49, 497–506, 1993
- [50] Yoshimura, T., Savage, M.G., Tanaka, H. and Urano, D.: "Wind-Induced Oscillations of Groups of Bridge Stay-Cables"; Journal of Wind Engineering and Industrial Aerodynamics, Vol. 54/55, 251–262, 1995

- [51] Hardy, C., Watts, J.A., Brunelle, J. and Clutier, L.J.: "Research on the Dynamics of Bundled Conductors at the Hydro-Quebec Institute of Research"; Canadian Electrical Association Transactions, Engineering and Operating Division, Vol. 14, Part 4, 1975
- [52] Hardy, C. and Bourdon, P.: "The Influence of Spacer Dynamic Properties in the Control of Bundle Conductor Motion" in IEEE PES Summer Meeting, Vancouver, British Columbia, Canada, July 1979
- [53] Hikami, Y.: "Rain Vibrations of Cables of a Cable-Stayed Bridge". Journal of Wind Engineering (Japan), Vol. 27, 17–28, 1986 (In Japanese)
- [54] Hikami, Y. and Shiraishi, N.: "Rain-Wind Induced Vibrations of Cables in Cable-Stayed Bridges"; Journal of Wind Engineering and Industrial Aerodynamics, Vol. 29, 409–418, 1988
- [55] Wagner, P. and Fuzier, J-P.: "Health Monitoring of Structures with Cables-Which Solutions. Dissemination of the Results of the IMAC European Project" in Fifth International Symposium on Cable Dynamics, "Tutorial on Health Monitoring of Structures with Cables", Santa Margherita Ligure, Italy, 2003
- [56] Yamada, Y., Shiraishi, N., Toki, K., Matsumoto, M., Matsuhashi, K., Kitazawa, M. and Ishizaki, H.: Earthquake Resistant and Wind-Resistant Design of the Higashi-Kobe Bridge, in Ito, M., Fujino, Y., Miyata, T. and Narita N. (eds), "Cable-Stayed Bridges: Recent Developments and their Future"; Elsevier; 1991, 397–416
- [57] Verwiebe, C.: Rain-Wind-Induced Vibrations of Cables and Bars, in Larsen, A. and Esdahl, S. (eds), "Bridge Aerodynamics"; Balkema, 1998, 255–263
- [58] Langsoe, H. and Larsen, O.: Generating Mechanism for Cable Stay Oscillations at the Farø Bridges, in Kanok-Nukulchai W. (ed), "Cable-Stayed Bridges: Experience and Practice, Vol. 1"; AIT, 1987, 1023–1033
- [59] Yamaguchi, H.: "Analytical Study on Growth Mechanism of Rain Vibration of Cables"; Journal of Wind Engineering and Industrial Aerodynamics, Vol. 33, 73–80, 1990
- [60] Peil, U. and Nahrath, N.: "Modeling of Rain-wind Induced Vibrations"; Wind and Structures, Vol. 6, No. 1, 41–52, 2003
- [61] Geurts, C. and van Staalanden, P.: Estimation of the Effects of Rain-Wind Induced Vibration in the Design Stage of Inclined Cables. In Larsen, A., Larose, G. and Livesey, F. (eds), "Wind Engineering into the 21st Century"; Proceedings of the Tenth International Conference on Wind Engineering, Vol. 2, Balkema, Copenhagen, 21–24 June 1999, 885–892
- [62] Blevins, R. and Iwan, W.: "The Galloping Response of a Two-Degree-of-Freedom System"; Journal of Applied Mechanics, Paper no. 75-APMW-9, Transactions of ASME, 1113–1118, 1974
- [63] Flamand, O.: "Rain-Wind Induced Vibration of Cables", in Proceedings of Structural Dynamics—EURODYN'93; Rotterdam, Balkema, 1019–1025, 1993
- [64] Flamand, O.: "Rain-Wind Induced Vibration of Cables", in Proceedings of the IABSE/FIP International Conference on Cables-Stayed and Suspension Bridges, Deauville, 12–15 October, Vol. 2, 523–531, 1994
- [65] Geurts, C., Vrouwenvelder, T., Staalanden, P. and Reusink, J.: "Numerical Modelling of Rain-Wind-Induced Vibration: Erasmus Bridge, Rotterdam"; Structural Engineering International, Vol. 2, 129–135, 1998

- [66] Ohshima, K. and Nanjo, M.: "Aerodynamic Stability of the Cables of a Cable-Stayed Bridge Subject to Rain (A Case Study of the Ajigawa Bridge)" in Proceedings of the US-Japan Seminar on Natural Resources, Tsukuba, Japan, 1987
- [67] Main, J. and Jones, N.: "Full-Scale Measurements of Stay Cable Vibration" in Proceedings of the 10th International Conference on Wind Engineering, 21–24 June, Copenhagen, 1999
- [68] Cremer, J., Counasse, C., de Ville de Goyet, V., Lotaire, A. and Dumortier, A.: "The Stays, their Dynamic Behaviour, their Equipments-Bridges at Ben-Ahin, Wandre and upon Alzette" in Proceedings of the International Symposium on Cable Dynamics, Liège, Belgium, 19–21 October 1995, 489–496
- [69] Yoshimura, T., Inoue, A., Kaji, K. and Savage, M.G.: "A Study of the Aerodynamic Stability of the Aratsu Bridge" in Canada-Japan Workshop on Bridge Aerodynamics, Ottawa, 25–27 September 1989, 41–50
- [70] Ito, M.: "The Cable-Stayed Meiko Grand Bridges, Nagoya"; Structural Engineering International, Vol. 8, No. 3, 168–171, 1998
- [71] Thiele, K.: "Full-Scale Investigations of Cable Vibrations on Cable-Stayed Bridges and Development of a Cable Damper Using Viscoelastic Material"; Master Science Thesis, The University of Western Ontario, Canada, 1996
- [72] Sarkar, P., Jones, N. and Scanlan, R.: "Identification of Aeroelastic Parameters of Flexible Bridges"; Journal of Engineering Mechanics, Vol. 120, No. 8, 1718–1743, 1994
- [73] Larose, G. and Zan, S.: "The Aerodynamic Forces on the Stay Cables of Cable-stayed Bridges in the Critical Reynolds Number Range" in Proceedings of the 4th International Symposium on Cable Dynamics, Montréal, Canada, 77–84, May 27–30 2001
- [74] Larose, G., Jakobsen, J. and Savage, M.: "Wind-Tunnel Experiments on an Inclined and Yawed Stay Cable Model in the Critical Reynolds Number Range" in Fifth International Symposium on Cable Dynamics, Santa Margherita Ligure, Italy, 279–286, 2003
- [75] Tagata, G.: "Harmonically Forced, Finite Amplitude Vibration of a String"; Journal of Sound and Vibration, Vol. 51, No. 4, 483–492, 1977
- [76] Nayfeh, A. and Mook, D.: "Nonlinear Oscillations"; John Wiley & Sons, USA, 1979
- [77] Pinto da Costa, A., Martins, J., Branco, F. and Lilien, J.: "Oscillations of Bridge Stay Cables Induced by Periodic Motions of Deck and/or Towers"; Journal of Engineering Mechanics, Vol. 122, No. 7, 613–622, 1996
- [78] Clement, H. and Cremona, C.: "Étude Mathématique du Phénomène d'Excitation Paramétrique Appliqué aux Haubans de Pont" in Études et recherches des Laboratoires des Ponts et Chaussées, OA18, LCPC, Paris, 1996
- [79] Clough, R. and Penzien, J.: "Dynamics of Structures", 7th Edition; McGraw-Hill International Editions, Singapore, 1986, ISBN 0-07-Y85098-4
- [80] Lilien, J.L. and Pinto da Costa, A.: "Vibration Amplitudes caused by Parametric Excitation of Cable Stayed Structures"; Journal of Sound and Vibration, Vol. 174, No. 1, 69–90, 1994
- [81] Caetano, E.: "Indirect Excitation of Stays on Cable-Stayed Bridges" in Proceedings of the 4th International Symposium on Cable Dynamics, Montréal, Canada, May 27–30 2001, 129–136

- [82] Dumortier, A.: "Étude Dynamique du Comportement des Haubans de Pont"; Licentiate Thesis, University of Liège, Belgium, 1990
- [83] Jakobsen, K.A., Jordet, E., Rambjor, S.K. and Jakobsen, A.A.: "Full Scale Measurements of the Behaviour of the Helgeland Bridge- A Cable-Stayed Bridge Located in a Harsh Environment" in Proceedings of the International Symposium on Cable Dynamics, Liège, Belgium, 19–21 October 1995, 473–480
- [84] Caetano, E. and Cunha, A.: "Identification of Parametric Excitation at the International Guadiana Bridge" in Fifth International Symposium on Cable Dynamics, Santa Margherita Ligure, Italy, 2003, 525–532
- [85] Caetano, E.: "Dynamics of Cable-Stayed Bridges: Experimental Assessment of Cable-Structure Interaction"; Ph.D. Thesis, University of Porto, Portugal, 2000
- [86] Soong, T.T.: "State-of-the-art Review: Active Structural Control in Civil Engineering"; Engineering Structures, Vol. 19, 74–84, 1988
- [87] Miyata, T., Yamada, H. and Hojo, T.: "Aerodynamic Response of PE Stay Cables with Pattern Indented Surface" in Proceedings of the IABSE/FIP International Conference on Cables-Stayed and Suspension Bridges, Deauville, 12–15 October, Vol. 2, 515–522, 1994
- [88] Miyata, T., Yamada, H., Hojo, T. and Yamazaki, S.: "On Aerodynamically Stable PE-Stay-Cables with Decreased Drag Force by Introduction of Newly Developed Lumped Surface Roughness" in Proceedings of the International Symposium on Cable Dynamics", Liège, Belgium, 19–21 October 1995, 481–488
- [89] Fujino, Y. and Kimura, K.: "Cables and Cable Vibration in Cable-Supported Bridges" in International Seminar on Cable Dynamics, Tokyo, 13 October 1997, 1–11
- [90] Leonhardt, F.: "Cable-Stayed Bridges", Keynote Lecture. FIP Congress 1986, New Delhi 16 February; The Institution of Structural Engineers, 1986
- [91] Yamaguchi, H.: "Control of Cable Vibrations with Secondary Cables", in Proceedings International Symposium on Cable Dynamics, 19–21 October 1995, Liège, Belgium, 445–452
- [92] Fuzier, J.P., Stubler, J., Ladret, P. and Bignon, F.: "The Øresund Stay Cables: Design for Fatigue Resistance and Easy Maintenance", Tutorial on Health Monitoring of Structures with Cables; Santa Margherita Ligure, Italy, September 2003
- [93] Den Hartog, J.P.: "Mechanical Vibrations", 4th Edition; McGraw-Hill, New York, 1956
- [94] Wallace, A.A.C.: "Wind Influence on Kessock Bridge"; Engineering Structures, Vol. 7, 18–22, 1985
- [95] Malhotra, P. and Wieland, M.: Tuned Mass Damper for Suppressing Wind Effects in a Cable-Stayed Bridge, in Kanok-Nukulchai W. (ed), "Cable-Stayed Bridges: Experience and Practice, Vol. 1"; AIT, 557–568, 1987
- [96] Conti, E., Grillaud, G., Jacob, J. and Cohen, N.: "Wind Effects on the Normandy Cable-Stayed Bridge: Comparison between Full Aeroelastic Model Tests and Quasi-Steady Analytical Approach" in Proceedings of the IABSE/FIP International Conference on Cables-Stayed and Suspension Bridges, Deauville, 12–15 October, Vol. 2, 81–90, 1994
- [97] Saito, T., Ito, M., Yamaguchi, H. and Eya, S.: "Use of a Dynamic Damper for Aerodynamic Stability of its Support Tower" in Proceedings of 4th U.S.-Japan Workshop on Bridge Engineering, San Diego, 11–12 May, 1988

- [98] Kawahito, T., Tsuji, M., Kano, I. and Tsumura, N.: "Pendulum-Type Tuned Mass Damper to Suppress Wind-Induced Vibration of the Tower of Meiko-Nishi Bridge Under Construction" in Proceedings of the 8th National Symposium on Wind Engineering, Tokyo, Japan, 1984
- [99] Reed, D., Yeh, H., Yu, J. and Gardarsson, S.: "Tuned liquid Dampers Under Large Amplitude Excitation"; Journal of Wind Engineering and Industrial Aerodynamics, Vol. 74–76, 923–930, 1998
- [100] Bournand, Y.: "Development of New Stay Cable Dampers in Proceedings of the IABSE Conference Cable-stayed Bridges- Past, Present and Future". Malmö, Sweden, 1999
- [101] Ohashi, M.: Cables for Cable-Stayed Bridges, in Ito, M., Fujino, Y., Myiata, T. and Narita, N. (eds), "Cable-Stayed Bridges: Recent Developments and their Future"; Elsevier, 1991, 125–250
- [102] Main, J. and Jones, N.: "Influence of Rubber Bushings on Stay Cable Damper Effectiveness", in Fifth International Symposium on Cable Dynamics; AIM, Santa Margherita Ligure, 2003, 445–452
- [103] Ostenfeld, K.H. and Larsen, A.: Bridge Engineering and Aerodynamics, in Larsen, A. (ed), "Aerodynamics of Large Bridges", Proceedings of the First International Symposium on Aerodynamics of large Bridges, 19-21st February; Balkema, Copenhagen, 1992, 3–22
- [104] Wilde, K. and Fujino, Y.: "Aerodynamic Control of Bridge Deck Flutter by Active Surfaces"; Journal of Engineering Mechanics, Vol. 124, No. 7, 718–727, 1998
- [105] Yamazaki, S., Nagata, N. and Abiru, H.: "Tuned Active Dampers Installed in the Minato Mirai (MM) 21 Landmark Tower in Yokohama"; Journal of Wind Engineering and Industrial Aerodynamics, 1937–1948, 1992
- [106] Samali, B., Kwok, K. and Facioni, R.: "Wind Tunnel Comparison of Active and Passive Tuned mass Dampers", in Proceedings of the 17th International Modal Analysis Conference, 8–11February; SEM, Florida, 1999, 174–180
- [107] Fujino, Y. and Susumpow, T.: "An Experimental Study on Active Control of In-Plane Cable Vibration by Axial Support Motion"; in Earthquake Engineering and Structural Dynamics, Vol. 23, John Wiley & Sons, 1994, 1283–1297
- [108] Susumpow, T. and Fujino, Y.: "Active Control of Multimodal Cable Vibrations by Axial Support Motion"; Journal of Engineering Mechanics, Vol. 121, No. 9, 964–972, 1995, ASCE
- [109] Yamaguchi, H. and Dung, N.: "Active Wave Control of Sagged-Cable Vibration" in Proceedings of the 1st International Conference on Motion Vibration Control, Yokohama, Japan, 134–139, 1992
- [110] Johnson, E., Spencer, B. and Fujino, Y.: Semiaactive Damping of Stay Cables: a Preliminary Study, "Proceedings of the 17th International Modal Analysis Conference"; SEM, Florida, 8–11 February 1999, 417–423
- [111] Kovàcs, I.: "Zur Frage der Seilschwingungen und der Seildämpfung"; Die Bautechnik, Vol. 10, 325–332, 1982
- [112] Yoneda, M. and Maeda, K.: "A Study on Practical Estimation Method for Structural Damping of Stay Cable with Damper" in Canada-Japan Workshop on Bridge Aerodynamics, Ottawa, 25–27 September 1989, 119–128

- [113] Uno, K., Kitagawa, S., Tsutsumi, H., Inoue, A. and Nakaya, S.: "A Simple Method of Designing Cable Vibration Dampers of Cable-stayed Bridges"; Journal of Structural Engineering, 37A, 789–798, 1991
- [114] Pacheco, B., Fujino, Y. and Sulekh, A.: "Estimation Curve for Modal Damping in Stay Cables with Viscous Damper"; Journal of Structural Engineering, Vol. 119, No. 6, 1961–1979, 1993
- [115] Krenk, S.: "Vibrations of a Taut Cable with an External Damper"; Transactions of the ASME, Vol. 67, 772–776, December 2000
- [116] Crémona, C.: "Courbe Universelle pour le Dimensionnement d' Amortisseurs en Pied de Haubans"; Revue Française de Génie Civil, Vol. 1, No. 1, 137–159, 1997
- [117] Krenk, S. and Nielsen, S.: "Vibrations of a Shallow Cable with a Viscous Damper"; Proceedings of the Royal Society of London Series A, Vol. 458, 339–357, 2002
- [118] Tabatabai, H. and Mehrabi, A.: "Design of Mechanical Viscous Dampers for Stay Cables"; Journal of Bridge Engineering, Vol. 5, No. 2, 114–123, 2000
- [119] Hoang, N. and Fujino, Y.: "Analytical Study on Bending Effects in a Stay Cable With a Damper"; Journal of Engineering Mechanics, 2006 (submitted)
- [120] Fujino, Y. and Hoang, N.: "Design Formulas for Damping of a Stay Cable with a Damper"; Journal of Structural Engineering, 2006 (submitted)
- [121] Hoang, N. and Fujino, Y.: "Combined Damping Effect of Two Dampers on a Stay Cable"; Journal of Sound and Vibration, 2007 (submitted)
- [122] Krenk, S. and Hogsberg, J.: "Damping of Cables by a Transverse Force"; Journal of Engineering Mechanics, Vol. 131, No. 4, 340–348, 2005.
- [123] Main, J. and Jones, N.: "Free Vibrations of Taut Cable with Attached Damper. II: Nonlinear Damper"; Journal of Engineering Mechanics, Vol. 128, No. 10, 1072–1080, 2002
- [124] Sun, L., Shi, C., Zhou, H. and Zhou, Y.: "Vibration Mitigation of Long Stay Cable Using Dampers and Cross-Ties" in Proceddings of the Sixth International Symposium on Cable Dynamics, Charleston, 19–22 September 2005
- [125] Stubler, J., Ladret, P. and Domage, J.: "Vibration Control of Stay Cables", in Proceedings of the IABSE Conference on Cable-Stayed Bridges-Past, Present and Future, Malmö, Sweden, 1999
- [126] Øresund Konsortiet: "The Øresund Fixed Link: Design and Construction", 1998, ISBN-91-630-7268-4, Malmö
- [127] Irvine, H. M.: "Free Vibration of Inclined Cables"; Journal of the Structural Division, Proceedings of the American Society of Civil Engineers, Vol. 104, No. ST2, 343–347, 1977
- [128] Ernst, H.J.: "Der E-Modul von Seilen unter Berücksichtigung des Durchhangers"; Bauingenieur, Vol. 40, No. 2, 52–55, 1965
- [129] Liu, P.: "Static and Dynamic Behaviour of Cable Assisted Bridges"; Ph.D. Thesis, UMIST, 1982
- [130] Martins, J.C.: The International Guadiana Bridge at Castro Marim, in Almeida Fernandes J. and Oliveira Santos L. (eds), "Guadiana and Arade Cable-Stayed Bridges"; LNEC, 1992, 3–15
- [131] Irvine, H.M. and Caughey, T.K.: "The Linear Theory of Free Vibrations of a Suspended Cable"; Proceedings of the Royal Society of London Series A, Vol. 341, 299–315, 1974

- [132] Starossek, U.: "Boundary Induced Vibration and Dynamic Stiffness of a Sagging Cable", Internal Report; Universität Stuttgart. Institut für Statik und Dynamik der Luft- und Raumfahrtkonstruktionen; Professor Dr. Ing. Bernd H. Kröplin, 1990
- [133] Triantafyllou, M.S.: "The Dynamics of Taut Inclined Cables"; Quarterly Journal of Mechanics and Applied Mathematics, Vol. 37, Pt. 3, 421–440, 1984
- [134] Triantafyllou, M.S. and Grinfogel, L.: "Natural frequencies and modes of inclined cables"; J. Struct. Eng. 112, Vol. 1, 139–148, 1986, ASCE
- [135] Morse, P. and Ingard, K.: "Theoretical Acoustics"; Princeton University Press, Princeton, 1968
- [136] Yamagiwa, I., Utsuno, H., Endo, K., Sugii, K. and Morimoto, T.: "Application of the Identification of tension and flexural rigidity at once to the bridge cables"; Journal of Constructional Steel, Vol. 5, 15–22, 1997
- [137] Geier, R. and Wenzel, H.: "Field Testing of Ludwigshafen Cable-Stayed Bridge"; Deliverable D10, IMAC (Project n°. GRD1-2000-25654), 2003
- [138] Meharabi, A. and Tabatabai, H.: "Unified Finite Difference Formulation for Free Vibration of Cables"; Journal of Structural Engineering, Vol. 124, No.11, 1313–1322, 1998
- [139] Zui, H., Shinke, T. and Namita, Y.: "Practical Formulae For Estimation of Cable Tension by Vibration Method"; Journal of structural Engineering, Vol. 122, No. 6, 651–656, 1996
- [140] Mars, Ph. and Hardy, D.: "Meaure des efforts dans les structures a cables", Annales Travaux Publics Belgique, No. 6, 515–531, 1985
- [141] Robert, J., Bruhat, D. and Gervais, J-P.: "Mesure de la Tension des Câbles par Méthode Vibratoire"; Laboratoire des Ponts et Chausées, Vol. 173, Mai-Juin, Réf. 3572, 1991, 109–114
- [142] Reis, A., Pereira, A., Pedro, J. and Sousa, D.: "Cable-stayed Bridges for Urban Spaces" in Proceedings of the IABSE Conference on Cable-stayed Bridges-Past, Present and Future, Malmö, Sweden, 1999
- [143] Bloomstine, M. and Stoltzner, E.: "The Faroe Cable-Stayed Bridge-Maintenance Experience with Major Components", in Proceedings of the IABSE Conference on Cable-Stayed Bridges-Past, Present and Future, Malmö, Sweden, 1999
- [144] Andersen, H., Hommel, D. and Veje, E.: "Emergency Rehabilitation of the Zárate-Brazo Largo Bridges, Argentina", in Proceedings of the IABSE Conference on Cable-Stayed Bridges-Past, Present and Future, Malmö, Sweden, 1999

# Appendix A—Deformational Characteristics of Suspended Cables

## A.1 Objectives

The current Chapter discusses the most important formulae that are required for a description of the deformational characteristics of a suspended cable. These include the definition of cable profile under selfweight (e.g. sag and angle of deviation at the anchorages), the evaluation of undeformed and deformed cable length, and the estimation of the installed tension. Simplified formulae and numerical modelling are also discussed, as well as the levels of error attained for the approaches followed.

The intended application is the design and analysis of stays in cable-stayed bridges, although other types of structures whose cables fit the basic assumptions made here, such as suspension bridges and guyed masts, are also considered.

## A.2 Static Behaviour

Suspended cables are structural elements characterised by a significant non-linear behaviour. The relatively low level of stress attained by these elements (determined by fatigue considerations) makes this non-linearity predominantly geometric in nature.

A precise description of a cable suspended between two fixed points (*Fig. A.1*) should include the bending and axial deformation, marked by the mechanical stiffnesses  $EI_0$  and  $EA_0$ , respectively. It should also take into consideration the installed axial tension  $T_0$  and selfweight (the latter normally constant along the cable length, as long as the cross section remains constant), and finally the end conditions. Given the large displacements caused by the low flexural stiffness, second order effects should also be included.

The evident complexity of the above stated problem is further compounded by the difficulty in a rigorous assessment of the degree of restraint of rotations at the anchorages.

Some simplifications, which enable a more accurate and simple determination of the cable profile  $z(x)$  and tension  $T(x)$  are, however, possible.

### A.2.1 General assumption: Elastic catenary

The basic assumption adopted in the study of a suspended cable is that the cable acts as a perfectly flexible elastic structural element. Ignoring the cable bending stiffness is possible in view of its low value when compared with the axial stiffness  $EA_0$ . The bending effects can still be assessed locally for the static behaviour at the anchorages or integrated in the dynamic modelling in a simplified form (see Appendix B.4).

*Figure A.2* illustrates the flexible cable model resulting from the assumption of null bending stiffness. The equilibrium of a segment with undeformed length  $s$  measured from the support  $A$  (*Fig. A.2(b)*) allows for the determination of the parametric equations (A.1) and (A.2) of the cable profile, and of equation (A.3) for the evaluation of the tension  $T(s)$ , given by Irvine [127]

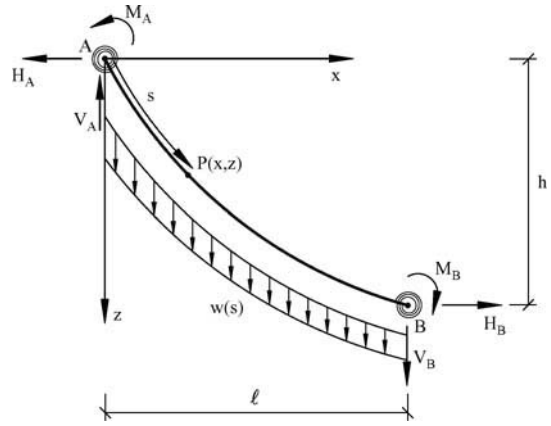


*Fig. A.1: Suspended cable subject to selfweight and axial tension*

$$x(s) = \frac{H_A s}{EA_0} + \frac{H_A L_0}{W} \cdot \left[ \sinh^{-1} \left( \frac{V_A}{H_A} \right) - \sinh^{-1} \left( \frac{V_A - Ws/L_0}{H_A} \right) \right] \quad (\text{A.1})$$

$$z(s) = \frac{Ws}{EA_0} \left( \frac{V_A}{W} - \frac{s}{2L_0} \right) + \frac{H_A L_0}{W} \left\{ \left[ 1 + \left( \frac{V_A}{H_A} \right)^2 \right]^{\frac{1}{2}} - \left[ 1 + \left( \frac{V_A - Ws/L_0}{H_A} \right)^2 \right]^{\frac{1}{2}} \right\} \quad (\text{A.2})$$

$$T(s) = \left[ H_A^2 + \left( V_A - \frac{Ws}{L_0} \right)^2 \right]^{\frac{1}{2}} \quad (\text{A.3})$$

In these equations, the Cartesian coordinates  $x$  and  $z$  of a generic point  $P$  are defined as a function of the unstrained length  $s$  associated with the cable segment  $AP$ , depending on the reactions at the end  $A$ ,  $V_A$  and  $H_A$ , on the cable weight  $W = mgL_0$ , on the unstrained length  $L_0$ , and on the axial stiffness  $EA_0$ ,  $A_0$  being the area of the undeformed cable cross section and  $E$  being the elasticity modulus of the cable.

The transcendental equations (A.1) and (A.2) of the cable profile define the so-called *elastic catenary*, and constitute the most precise description of the cable geometry under selfweight. The resolution of these equations requires the knowledge of the reactions  $H_A$  and  $V_A$ , which are obtained by the introduction of the boundary conditions, resulting in the numerical solution of

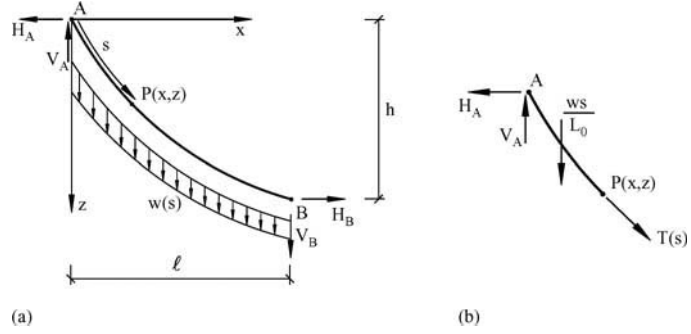


Fig. A.2: Suspended cable subject to selfweight and axial tension: (a) general simplified model; (b) equilibrium of the segment AP

$$\ell = \frac{H_A L_0}{E A_0} + \frac{H_A L_0}{W} \cdot \left[ \sinh^{-1} \left( \frac{V_A}{H_A} \right) - \sinh^{-1} \left( \frac{V_A - W}{H_A} \right) \right] \quad (\text{A.4})$$

$$h = \frac{W L_0}{E A_0} \left( \frac{V_A}{W} - \frac{1}{2} \right) + \frac{H_A L_0}{W} \cdot \left\{ \left[ 1 + \left( \frac{V_A}{H_A} \right)^2 \right]^{\frac{1}{2}} - \left[ 1 + \left( \frac{V_A - W}{H_A} \right)^2 \right]^{\frac{1}{2}} \right\} \quad (\text{A.5})$$

The knowledge of  $V_A$  and  $H_A$  allows also for the evaluation of the maximum tension along the cable,  $T_A$ , given by

$$T_A = [H_A^2 + V_A^2]^{\frac{1}{2}} \quad (\text{A.6})$$

and for the evaluation of the angle of deviation at the anchorages,  $\omega_A$  and  $\omega_B$  (Fig. A.3)

$$\omega_A = a \tan \left( \frac{V_A}{H_A} \right) - \alpha \quad (\text{A.7})$$

$$\omega_B = \alpha - a \tan \left( \frac{V_B}{H_B} \right) = \alpha - a \tan \left( \frac{V_A - W}{H_A} \right) \quad (\text{A.8})$$

The cable sag  $d$ , defined as the maximum vertical distance to the chord, can be assessed at the point  $S$  (Fig. A.3), characterised by the Lagrangian coordinate  $s_S$

$$s_S = \frac{L_0}{W} \left( V_A - h \frac{H_A}{\ell} \right) \quad (\text{A.9})$$

and is given by

$$d = z(s_S) - \frac{h}{\ell} x_S, \quad x_S = x(s_S) \quad (\text{A.10})$$

Finally the deformed cable length  $L_f$  can be obtained by

$$L_f = L_0 + \frac{H^2 L_0}{2 W E A_0} \cdot \left[ \frac{V_A}{H_A} \cdot \sqrt{1 + \left(\frac{V_A}{H_A}\right)^2} + \ln \left( \frac{V_A}{H_A} + \sqrt{1 + \left(\frac{V_A}{H_A}\right)^2} \right) \right. \\ \left. - \frac{V_A - W}{H_A} \cdot \sqrt{1 + \left(\frac{V_A - W}{H_A}\right)^2} - \ln \left( \frac{V_A - W}{H_A} + \sqrt{1 + \left(\frac{V_A - W}{H_A}\right)^2} \right) \right] \quad (\text{A.11})$$

*Table A.1* presents the geometric and mechanic characteristics of a series of cables from cable-stayed bridges, calculated on the basis of formulae (A.1) to (A.11). These will be used as reference for the next Section, where further simplifications will be introduced. Some useful conclusions can be inferred from the analysis of this table, which covers a wide range of cables:

- Cable-stayed bridge cables are subject to relatively low stresses  $\sigma_{\max}$ , no greater than 900 MPa. For these cables the variation of tension  $\Delta T$  along the length does not exceed 2% of the maximum tension;
- The values of the ratio  $\frac{mgL_0}{T_{\max}}$  attained for cable stays are also quite small and do not exceed typically 5% of the maximum component of cable tension  $T_{\max}$ . This ratio increases with cable length, as happens with the longest of the Normandy bridge cables.

An important parameter characteristic of a suspended cable has been introduced by Irvine [127], incorporating both the corresponding geometric and deformational characteristics. This parameter  $\lambda^2$  is defined as

$$\lambda^2 = \left( \frac{mgL}{T} \right)^2 \cdot \frac{L}{\frac{TL_e}{EA_0}} \quad (\text{A.12})$$

where  $L$  and  $T$  represent the chord length and the component of tension along the cable chord, respectively, and  $L_e$  is a virtual length of cable defined by

$$L_e = \int_0^L \left( \frac{ds}{dx} \right)^3 dx \approx L \cdot \left\{ 1 + 8 \left( \frac{d}{L} \right)^2 \right\} \quad (\text{A.13})$$

Typical values attained by stay cables vary in the range 0–1, while for suspension bridges  $\lambda^2$  is normally greater than 100. Very large stay cables can have a  $\lambda^2$  value greater than 1, as shown in *Table A.1* for the largest cable of the Normandy bridge. Small values of  $\lambda^2$  reflect relatively highly stressed and low sagging cables, whose deformation is achieved essentially by extensibility, while large values are typical of very low tensioned and higher sagging cables, whose deformation is mainly of geometric nature, exhibiting therefore a relative inextensibility.

These different characteristics imply different levels of simplification both for static and dynamic analyses.

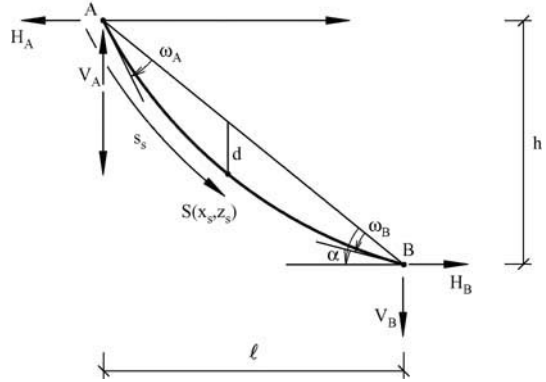


Fig. A.3: Elastic catenary

<b>Cable</b>	<b>Area (cm<sup>2</sup>)</b>	<b>EA (kN)</b>	<b>mass (kg/m)</b>	<b><math>\ell</math> (m)</b>	<b>h (m)</b>	<b><math>\alpha</math> (°)</b>	<b>L (m)</b>	<b><math>L_0</math> (m)</b>	<b><math>L_f</math> (m)</b>	<b>d (m)</b>	<b><math>\lambda^2</math></b>
V. Gamma											
HC01	46.5	906 750	42.9	1.81	34.65	87.0098	34.697	34.700	34.778	0.081	0.023
HC24	109.5	2 135 250	100.1	205.96	92.97	24.295	225.972	226.584	227.299	1.074	0.344
HC15	82.5	1 608 750	74.8	126.05	76.52	31.2596	147.457	147.752	148.145	0.569	0.241
Guadiana											
Central 1	77	1 501 500	72.9	152.42	71.94	25.2664	168.544	168.992	169.532	0.467	0.198
Central 16	27	518 700	21.0	18.64	45.84	67.8768	49.485	49.518	49.723	0.198	0.005
Normandy	153	2 907 000	133.0	420	134	17.6952	440.858	441.931	442.962	4.743	3.085
Ikuchi*	85.8	1 716 000	72.5	231.35	84.20	20	246.200	246.671	247.171	1.616	1.254

Table A.1: Geometric, mechanical and deformational characteristics of different cables

<b>Cable</b>	<b><math>\omega_A</math> (°)</b>	<b><math>\omega_B</math> (°)</b>	<b>Ss (m)</b>	<b>Ts (kN)</b>	<b>Tmin (kN)</b>	<b>Tmax (kN)</b>	<b><math>\Delta T</math> (%)</b>	<b><math>\sigma_{max}</math> (Mpa)</b>	<b><math>mgL_0/T_{max}</math> (%)</b>
V. Gamma									
HC01	0.0173	0.0389	28.048	2033.2	2030.4	2045	0.71	439.8	0.71
HC24	0.9234	2.6704	122.157	6738.8	6700.3	6785.5	1.26	619.7	3.28
HC15	0.6836	1.9411	81.924	4275.2	4251.4	4305.5	1.26	521.9	2.52
Guadiana									
Central 1	0.6114	1.9312	79.495	4793.6	4767.9	4817	1.02	625.6	2.51
Central 16	0.1329	0.2360	64.541	2141.7	2144.6	2154	0.44	809.8	0.47
Normandy	2.3281	7.0735	223.881	6778.9	6720.7	6850.5	1.89	447.7	8.42
Ikuchi*	1.3829	4.1450	126.468	3474.5	3450.2	3502.2	1.48	408.2	5.01
* $\alpha$ is estimated.									

Table A.1: Continued

### A.2.2 Elastic parabola

The use of the transcendental equations presented above to characterise the deformational characteristics of stay cables requires numerical manipulation. Although commercially available software can easily be employed, simplified practical formulae are of interest for a wide range of situations.

The elastic parabola approach applies to shallow cables, i.e. cables with a small sag to span  $d/L$  ratio, typically no greater than 1:8. This range covers stays from cable-stayed bridges and most of the cables from suspension bridges. The assumption of a unit ratio between the deformed and undeformed cable length yields the simple formulae for the cable profile defined in cartesian coordinates

$$z(x) = \frac{1}{2} \frac{mg}{H} \cdot \sec \alpha \cdot x \cdot (\ell - x) \cdot \left[ 1 + \frac{\varepsilon}{6} \cdot \left( 1 - 2\frac{x}{\ell} \right) \right] + \frac{h}{\ell} \cdot x \quad (\text{A.14})$$

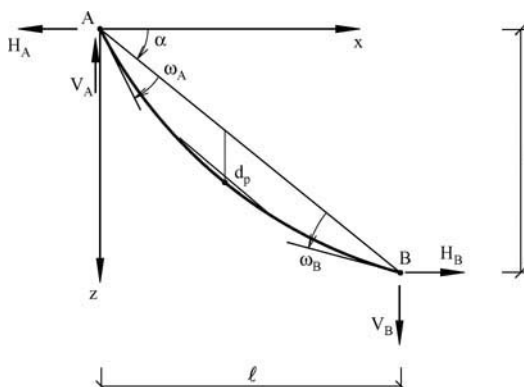


Fig. A.4: Elastic parabola

occurs at this same point and is given by

$$d_p = \frac{mgL^2}{8T} \quad (\text{A.16})$$

The angles of deviation at the anchorages  $A$  and  $B$ ,  $\omega_A$  and  $\omega_B$ , are

$$\omega_A = \omega_B = \alpha \tan \left( \frac{mgL}{2H} + \frac{h}{\ell} \right) - \alpha \quad (\text{A.17})$$

and the deformed cable length  $L_{fp}$  can be approximated by

$$L_{fp} = L \cdot \left[ 1 + \frac{8}{3} \cdot \left( \frac{d_p}{L} \right)^2 - \frac{32}{5} \cdot \left( \frac{d_p}{L} \right)^4 \right] \quad (\text{A.18})$$

Table A.2 presents the deformational characteristics of the above described stay cables based on the parabolic approach expressions (A.15) to (A.18).

Cable	$\omega_A (\circ) = \omega_B (\circ)$	T (kN)	$d_p$ (m)	$L_{fp}$ (m)	$\varepsilon_{dp}$ (%)	$\varepsilon_T$ (%)	$\varepsilon_{L_{fp}}$ (%)
V. Gama							
HC01	0.0173	2056.8	0.031	34.697	-61.8	1.2	-0.2
HC24	1.6239	6834.0	0.917	225.982	-14.6	1.4	-0.6
HC15	1.1278	4336.4	0.460	147.461	-19.2	1.4	-0.5
Guadiana							
Central 1	1.1365	4841.0	0.524	168.548	12.4	1.0	-0.6
Central 16	0.1401	2166.3	0.029	49.485	-85.3	1.1	-0.5
Normandy	4.3590	6933.6	4.572	440.985	-3.6	2.3	-0.4
Ikuchi*	2.5525	3531.9	1.526	246.225	5.6	1.7	-0.4

Table A.2: Deformational characteristics of cables resultant from parabolic approach

It can be observed from Table A.2 that the parabolic approach provides significant errors in the description of the static behaviour of the cable, in local quantities, like the angles of deviation to the chord at the anchorages and sag ( $\varepsilon_{dp}$ ). The error committed increases both with the angle of inclination of the cable to the horizontal and with the chord length. And even though the error in the deformed cable length ( $\varepsilon_{L_{fp}}$ ) is low, the fact is that a very small error in the initial cable length may result in a high error in the sag evaluation. Although very practical and useful for an approximate analysis during the design phase, the parabolic approach is not convenient whenever a precise description of the static behaviour of a stay cable is required, namely for installation purposes.

### A.2.3 Numerical modelling

The integration of the cable stay behaviour in the numerical description of a cable-stayed bridge requires further simplifications whose effects should be acknowledged.

#### A.2.3.1 Linear model: Truss element

The simplest and also most common approach employed in the numerical modelling of a stay cable is based on the idealisation of the so-called truss element.

The truss element is a two node elastic finite element characterised by null bending stiffness and an axial stiffness  $E A_0 / L$ , whose weight is concentrated at the nodes (Fig. A.5). These characteristics correspond actually to the treatment of the cable as a spring element, not accounting for geometric effects and providing

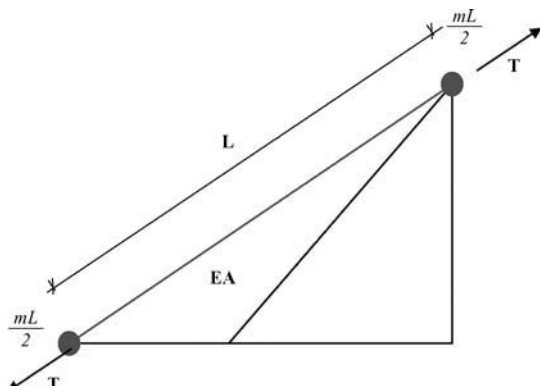


Fig. A.5: Truss element

naturally a poor description of the local deformational characteristics: both the sag and angles of deviation at anchorages are nil, the cable undeformed length is equal to the chord length, and the tension is assumed constant along the cable.

Despite the poor local characteristics, the linear model is of great interest for a global analysis of the bridge behaviour, allowing for a good estimation of the force distribution in the cable-stayed bridge, and providing therefore important information for the design of the stay cables. The major source of error associated with the linear model results from geometric effects. So, for taut stay cables, with a low  $\lambda^2$  value, small errors are expected, while for less tensioned or very long cables, with high values of  $\lambda^2$ , the errors may be significant.

#### A.2.3.2 Linear model refinement: Equivalent modulus of elasticity

It is still possible to introduce the non-linear geometric behaviour in a simplified form. This is achieved through the approximation of the cable profile by a parabola and determination of the axial stiffness as a function of both the cable tension and sag. An Equivalent Modulus of Elasticity  $E_{eq}$  is obtained which incorporates these quantities through the parameter  $\lambda^2$  and is given by

$$E_{eq} = \frac{E}{1 + \frac{\lambda^2}{12}} \quad (\text{A.19})$$

Another equivalent formula is given by Ernst [128]

$$E_{eq} = \frac{E}{1 + \frac{\gamma^2 L^2}{12 \sigma^3} E} \quad (\text{A.20})$$

where  $\gamma$  is the specific weight and  $\sigma$  is the tensile stress of the cable. The variation of  $E_{eq}$  with  $\lambda^2$  is represented in Fig. A.6, showing that for standard taut stay cables ( $\lambda^2 < 1$ ) the correction is actually very small ( $\lambda^2 = 1$ ,  $E_{eq} = 0.92 E$ ), while for very long stay cables the correction becomes significant (for the largest of the Normandy stay cables,  $\lambda^2 = 3.1$ ,  $E_{eq} = 0.79 E$ ). Figure A.7 shows the variation of the ratio  $E_{eq}/E$  with the cable chord length for different levels of stress. Using information from Table A.1, one can understand that this ratio is greater than 0.90 for all of the analysed stay cables, except the largest of Normandy bridge.

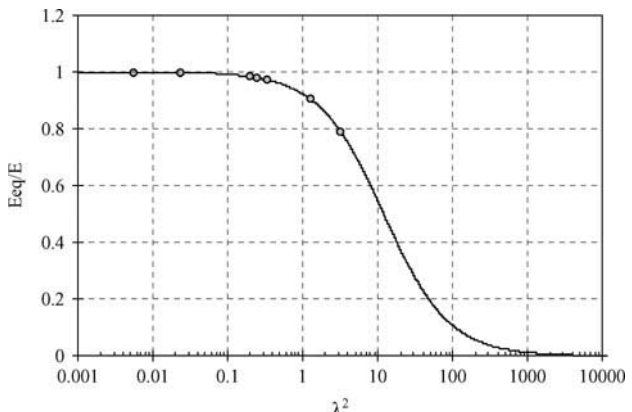


Fig. A.6: Variation of the ratio  $E_{eq}/E$  with  $\lambda^2$

The use of an Equivalent Modulus of Elasticity  $E_{eq}$  in the description of cable stay behaviour provides an improved distribution of forces throughout the bridge cables and a better approximation of the global cable deformability, and therefore an improved shape of the

bridge profile under permanent loads. It should be noted however that second order effects associated with other bridge elements, namely the deck and towers, which suffer significant compressions, may be more relevant in terms of the global bridge behaviour. This means that the use of a non-linear geometric formulation for global static analysis of the bridge may be more relevant than the introduction of corrections to sag/tension of individual cables.

#### A.2.3.3 Linear model refinement: Multi-link approach

A natural extension of the idealisation of the stay cable as a simple truss element to a series of truss elements (*Fig. A.8*) has been proposed in the past [129] as a computational improvement that allows for the accounting of geometric effects, as long as the discretisation is complemented with a geometric non-linear analysis. Owing to the resulting large dimension of numerical models, and to computational limitations, the implementation of this modelling technique has not been a current trend in the global modelling of a cable-stayed bridge. It should be noticed however that currently available commercial software and computer memory allow for reasonable computing times in the face of the advantages obtained: using an adequate number of elements to discretise a stay cable, the corresponding weight, applied at the nodes, approximates the distributed weight of the cable, and therefore the corresponding profile approximates the elastic catenary profile. As for the number of necessary elements to represent adequately the deformational behaviour of a stay cable, it is relevant to analyse the error associated with the discretisation for several physical quantities of interest. For this purpose, two stay cables from Vasco da Gama bridge were considered, the longest, HC024, and the shortest, HC01, with properties listed in *Table A.1*. The cables were discretised into a successively growing number of truss elements. Taking the 100 link discretisation as a basis, the relative errors obtained for various physical quantities were calculated and are plotted in *Fig. A.9*. The analysed quantities are: the minimum axial force,  $T_{min}$ ; the sag  $d$ ; the relative rotation to the chord at one end,  $\omega_B$ ; and also the first five natural frequencies,  $f_1$  to  $f_5$ . The relative errors, represented for each quantity in *Fig. A.9*, are designated respectively as  $ET_{min}$ ,  $Edv$ ,  $Ewb$ ,  $Efl$ , ...,  $Ef5$ .

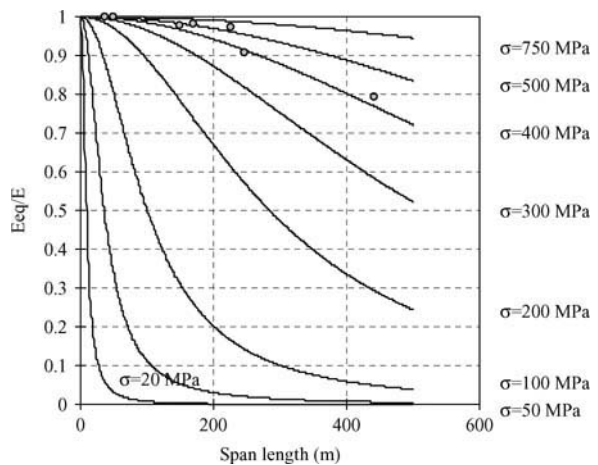


*Fig. A.7: Variation of the ratio  $E_{eq}/E$  with the cable span for different levels of cable stress*

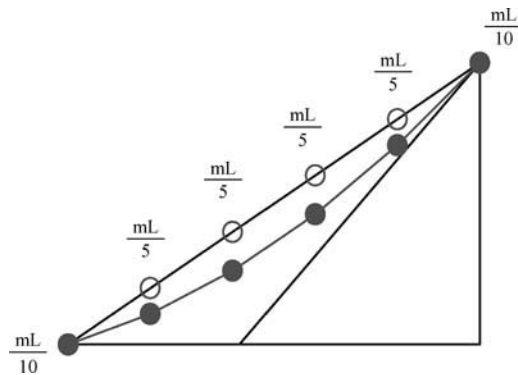


*Fig. A.8: Multi-link approach: undeformed and deformed mesh under selfweight*

The analysis of *Fig. A.9*: shows that a discretisation in 20 truss elements provides relative errors of less than 5% in all the mentioned quantities for the two cables. But if, for example, only the first three vibration modes of the cable are of interest and local effects, like the end rotations, are not relevant, then a discretisation into 9 elements is sufficient, both for the shortest and longest cables:

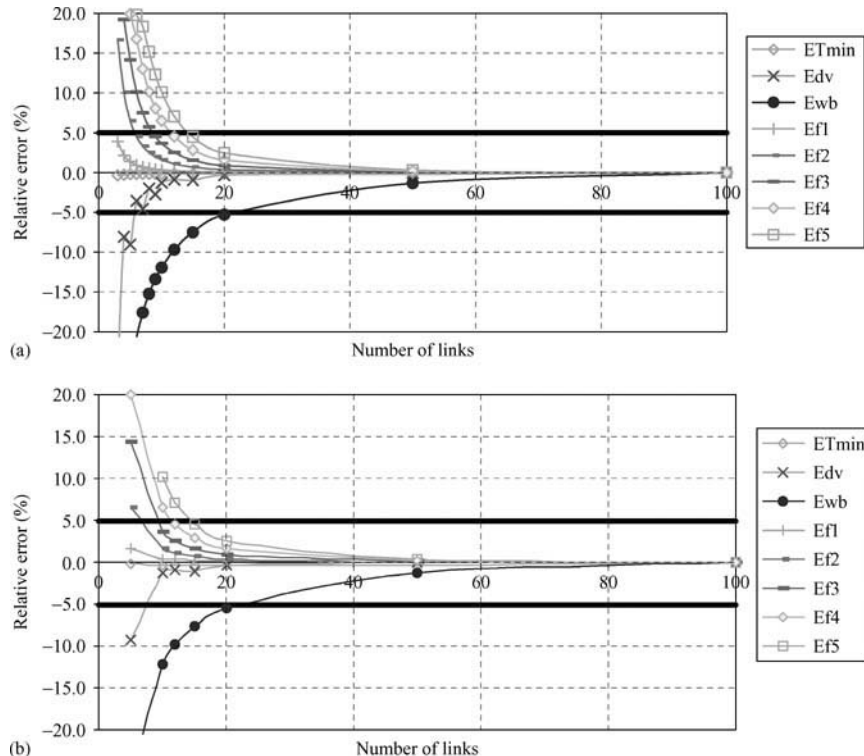


*Fig. A.9: Variation of relative error of discretisation with number of links for various physical quantities in two cables of Vasco da Gama bridge: (a) HC024; (b) HC 01*

#### A.2.3.4 Non-linear model: Cable element

The cable element is part of the element libraries of most commercial software packages and is based on the approximation of the displacement field inside the element by a parabola of  $(n-1)$ th order, where  $n$  is the number of nodes of the element. This description is of better quality than the linear two node element, although it must be remembered that it is still based on a linear elastic formulation. Therefore, only the division of the cable into various finite elements combined with a geometric non-linear formulation provides a good approximation of the corresponding static and dynamic behaviour.

#### A.2.3.5 Comparative analysis for global study of a cable-stayed bridge

In order to understand the relevance of the chosen numerical formulation of the stay cables in the global behaviour of a cable-stayed bridge, some results of a study developed on a conventional medium size bridge of this type are presented.

The bridge [130], represented in *Fig. A.10*, is composed of a central span of 324 m, two lateral spans of 135 m and two transition spans of 36 m, having a total length of 666 m. The 18 m wide deck has a prestressed concrete box section that is partially supported at the concrete 100 m high A-shaped towers and suspended by stay cables. These are arranged in a semi-fan, in a total of 32 pairs anchored at the top of each tower.



*Fig. A.10: General view of cable-stayed bridge under analysis*

The stay cables' chord length varies in the range of 49.5–170.2 m, and the stress measured on the site varies in the range of 340–680 MPa. The Irvine parameter  $\lambda^2$  varies, for the set of cables, in the range of 0.0162–0.4795, meaning that the Equivalent Modulus of Elasticity  $E_{eq}$ , defined by (A.19), is in the range of  $0.962 \cdot E_a$  to  $0.999 \cdot E_a$ ,  $E_a$  being the modulus of elasticity of steel. The fundamental natural frequency of the stay cables is in the interval between 0.78–2.97 Hz, while the first bridge natural frequencies of vertical, lateral and torsional modes were calculated as 0.38, 0.52 and 1.49 Hz, respectively.

The studies developed on this bridge consisted in the analysis of the static response to selfweight, followed by an evaluation of natural frequencies and modal shapes. This analysis was performed introducing the various degrees of simplification referred along this Chapter, i.e., (i) linear analysis based on idealisation of the cables as simple truss elements; (ii) linear analysis based on idealisation of the cables as truss elements with correction of the Modulus of Elasticity to take into account local effects (Equivalent Modulus of Elasticity approach); (iii) non-linear geometric analysis, based on idealisation of the cables as simple truss elements and (iv) non-linear geometric analysis based on the idealisation of each stay cable as a series of ten truss elements (multi-link approach).

It should be noted that for simplification purposes, the equivalent Modulus of Elasticity of stay cables was made uniform and equal to the average value of  $0.975 \cdot E_a$ .

*Table A.3* systematises some of the most important results obtained, expressed in terms of maximum displacement at the lateral span, midspan and top of one tower, maximum

Analysis	(i) Linear $E_a = 200 \text{ GPa}$	(ii) Linear $E_{eq} = 195 \text{ GPa}$	(iii) Non-linear geometric	(iv) Non-linear geometric (cable discretisation)
Displacement (mm):				
Lateral span	66.79	66.21	66.19	71.99
Mid-span	+25.35	17.35	17.38	+51.11
Right tower	+68.42	+58.32	+58.29	+44.04
Axial force (kN):				
Deck	55838	55656	55656	56703
Tower	71875	71848	71848	71225
Bending moment (kN·m):				
Deck	-45042	-45317	-45315	-47673
Tower	14485	14725	14724	18423
Natural frequencies (Hz):				
$f_1$	0.3804	0.3767	0.3767	0.3765
$f_2$	0.5077	0.5077	0.5077	0.5060
$f_3$	0.5246	0.5208	0.5208	0.5185
$f_4$	0.7833	0.7777	0.7777	0.78556*
$f_5$	0.8912	0.8843	0.8843	0.8854*
$f_6$	0.9706	0.9633	0.9633	0.9567*
$f_7$	1.1997	1.1932	1.1932	1.1948*
$f_8$	1.2221	1.2219	1.2219	*
$f_9$	1.3611	1.3597	1.3597	*
$f_{11}$	1.4993	1.4933	1.4933	*
$f_{13}$	1.6393	1.6390	1.6390	*

\* Multiple modes.

Table A.3: Comparison between various approaches on the static/dynamic analysis of cable-stayed bridge

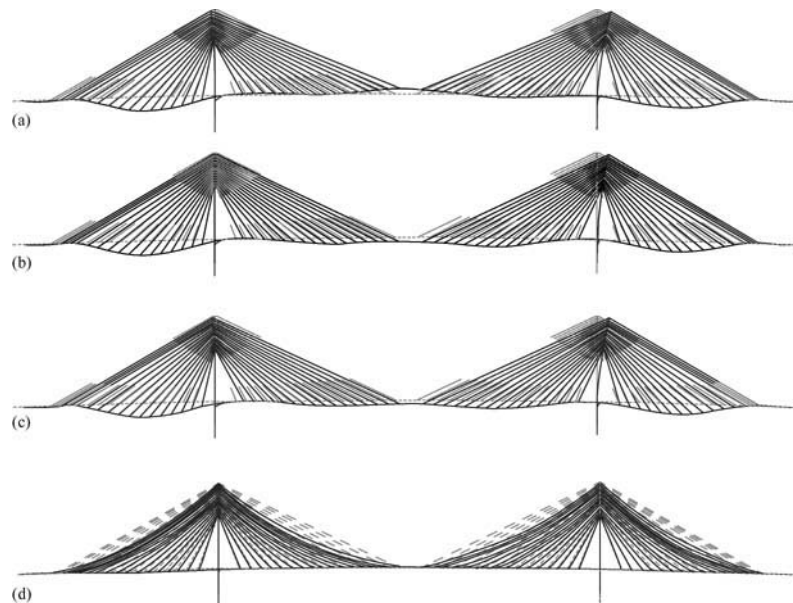
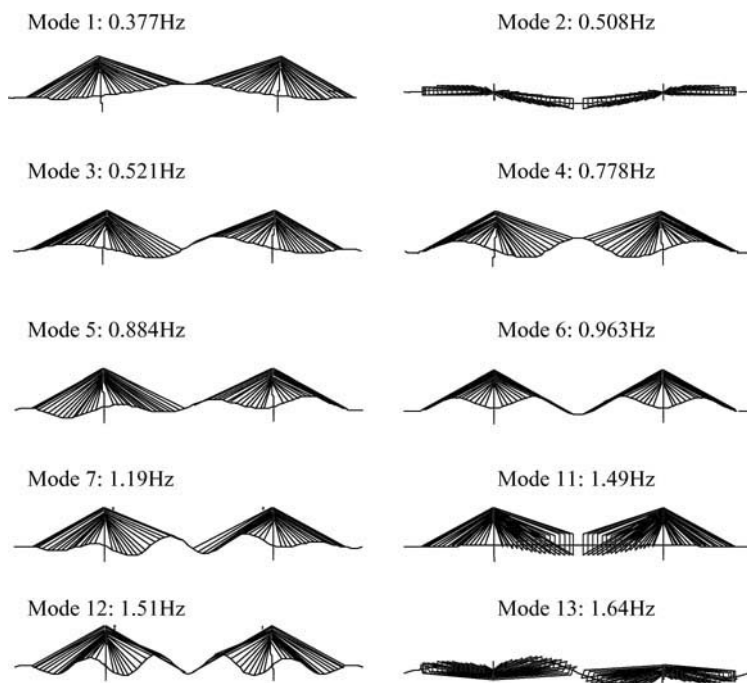


Fig. A.11: Dead load configuration of cable-stayed bridge for the analysis: (a) linear,  $E_a = 200 \text{ GPa}$ ; (ii) Linear,  $E_{eq} = 195 \text{ GPa}$ ; (c) geometric non-linear, one truss element per cable; (d) geometric non-linear, 10 truss elements per cable



compression force in the deck and towers, maximum bending moment in deck and tower, and most relevant natural frequencies.

The analysis of this table shows that, although not very significant in absolute value, the introduction of the equivalent modulus of elasticity leads to a substantial modification of the deformed structure under selfweight. *Figure A.11*, representing the undeformed and deformed finite element mesh obtained for each analysis, illustrates this aspect, showing that the reduction of cable stiffness leads to higher mid-span displacements. Note that the deformed configurations are represented at the same scale for the first three cases of analysis. The comparison between deformed configurations obtained under linear or geometric non-linear analyses shows very slight differences while the stay cables are idealised as single truss elements (model (iii)). However, the idealisation of each stay cable as a series of ten truss elements allows for the consideration of the cable geometric non-linearity, which significantly changes both deformations and internal forces.

With respect to the dynamic behaviour of the bridge, it can be noticed from *Table A.3* that the natural frequencies of the most relevant modes (modal configurations represented in *Fig. A.12*) have very slight variations for the various models, meaning that geometric non-linear effects have no significant influence in the global dynamic behaviour of the bridge. It is important however to notice that the multi-link model leads to the introduction of cable dynamics in the global bridge behaviour. As a consequence, significant coupling between cable and bridge vibration occurs, leading to numerous vibration modes, here called multiple modes, characterised by very close natural frequencies

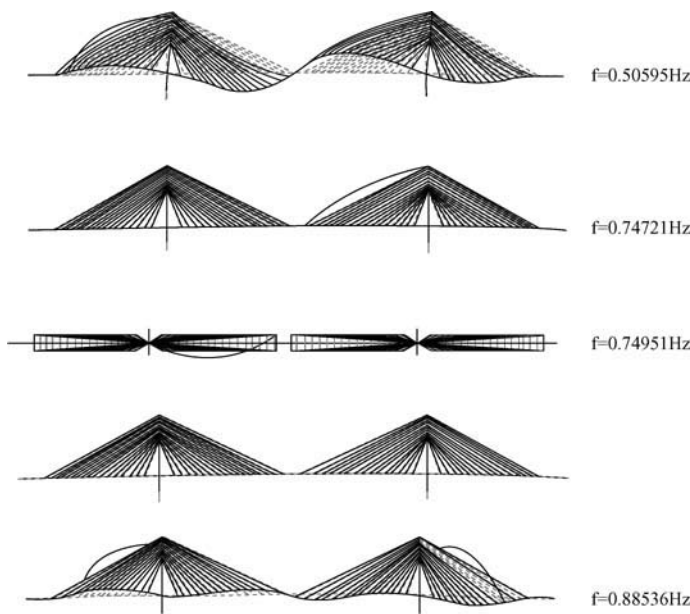


*Fig. A.13: Modal shapes associated with non-linear geometric model, idealising each stay cable as a series of ten truss elements*

and similar configurations of deck and towers, but involving the participation of different cables [85]. *Figure A.13* shows typical configurations of vibration modes involving the participation of cables with different degrees. It is thought that the parametric excitation phenomenon described in Chapter 5 is enhanced by this coupling effect.

# Appendix B—Fundamentals of Cable Dynamics

## B.1 Objectives

The basic aspects associated with the linear theory of cable vibration developed by Irvine and Caughey [131] for shallow cables are presented. These include formulae for the quantification of natural frequencies and modal shapes both for horizontal and inclined cables that are valid for almost all of the cable-stayed bridge vibration problems. An improved formulation developed by Triantafyllou is also presented. Finally the inclusion of bending effects in the dynamic description of a stay cable is discussed and simplified formulae for the evaluation of natural frequencies are presented.

## B.2 Linear Theory of Vibrations of Horizontal—Cables

### B.2.1 Basic assumptions and equilibrium equations

The linear theory of vibrations was derived for a rigidly supported cable with a small sag-to-span ratio  $d/L$  ( $0 \leq d/L \leq 1/8$ ) under the assumption of a quasi-static elastic deformation, i.e., of a constant dynamic component of cable tension  $\tau$  along the cable length.

Considering a horizontal cable of chord length  $L$  and mass per unit length  $m$  suspended between two supports at the same level (Fig. B.1), the application of a small displacement causes motion of a generic point  $P$  from dead load configuration position  $\bar{P}(x, 0, z)$  to  $\bar{P}'(x + u, v, z + w)$ , where  $u$ ,  $v$  and  $w$  represent the small components of motion along the horizontal (in-plane and out-of-plane) and vertical directions, respectively.

The study of the dynamic equilibrium of a segment of length  $ds$  cut at point  $P$  (Fig. B.2) leads to the following linearised equilibrium equations

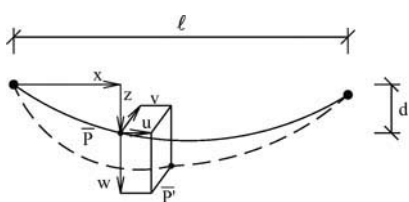


Fig. B.1: Components of displacement of a generic point  $P$  of a horizontal vibrating cable

$$H \frac{\partial^2 v}{\partial x^2} = m \cdot \frac{\partial^2 v}{\partial t^2} \quad (\text{B.1})$$

$$H \frac{\partial^2 w}{\partial x^2} + h_\tau \frac{d^2 z}{dx^2} = m \cdot \frac{\partial^2 w}{\partial t^2} \quad (\text{B.2})$$

$$\frac{h_\tau L_e}{EA_0} = \frac{mg}{H} \int_0^\ell w dx \quad (\text{B.3})$$

where  $H$  represents the horizontal component of tension at dead load configuration and  $h_\tau$  is defined as  $h_\tau = \tau dx / d\bar{s}$ . This quantity relates to the dynamic part  $h$  of the horizontal force on the cable through [132]

$$h = h_\tau - H \frac{dz}{dx} \cdot \frac{\partial w}{\partial x} \quad (\text{B.4})$$

The virtual length  $L_e$  is defined by equation (A.13) in Appendix A and has been derived based on the assumption of a parabolic profile of the cable.

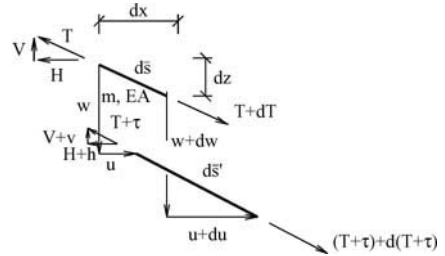


Fig. B.2: Dynamic equilibrium of a differential cable segment

## B.2.2 Natural frequencies and modal shapes

The most important consequence of the linearisation applied in the derivation of equation (B.3) is the uncoupling of in-plane and out-of-plane motion. This means that a disturbance applied in the plane of the cable produces no motion out-of-plane and vice-versa. Also, in contrast to in-plane motion, the vibration out-of-plane, characterised by equation (B.1), does not involve a variation of the cable tension.

This uncoupling, which is valid only for small levels of cable vibration, has the advantage of allowing for a separate derivation of the equations of motion presented above for in-plane and out-of-plane oscillation.

### B.2.2.1 Out-of-plane motion

The solution of the homogeneous equation (B.1) is obtained by separation of variables according to

$$v(x, t) = \tilde{v}(x) \cdot e^{i \omega t} \quad (\text{B.5})$$

where  $i^2 = -1$ . It is given by

$$\omega_n = \frac{n \pi}{\ell} \cdot \sqrt{\frac{H}{m}} \quad n = 1, 2, 3, \dots \quad (\text{B.6})$$

$$\tilde{v}_n(x) = A_n \cdot \sin\left(\frac{n \pi x}{\ell}\right) \quad n = 1, 2, 3, \dots$$

where  $\omega_n$  represents the  $n$ th frequency of vibration and  $\tilde{v}_n(x)$  is the corresponding modal shape, defined by an arbitrary constant  $A_n$ .

### B.2.2.2 In-plane motion

With regard to the in-plane motion, and with the assumption that the sag to span ratio ( $d/\ell \leq 1/8$ ) is small, the amplitude of the longitudinal component of motion is always substantially lower than the amplitude of the vertical component of motion. Consequently,

the characterisation of modal shapes as *symmetric* and *anti-symmetric* is made according to the profile of the vertical component of motion.

In the study of in-plane mode shapes, the separation into *symmetric* and *anti-symmetric* modes becomes relevant, as these two types of modes have distinct characteristics. In effect, the observation of equation (B.3) immediately shows that the *symmetric* motion involves a non-zero additional component of tension, while in the *anti-symmetric* case this component vanishes for this linear approach.

### (i) Anti-symmetric in-plane modes

With the in-plane vibration described by  $u(x, t)$  and  $w(x, t)$ , and using the separation of variables

$$\begin{aligned} u(x, t) &= \tilde{u}(x) \cdot e^{i\omega t} \\ w(x, t) &= \tilde{w}(x) \cdot e^{i\omega t} \end{aligned} \quad (\text{B.7})$$

the substitution into (B.2) and (B.3) and the solution of the equations yields, in the case of *anti-symmetric modes*

$$\begin{aligned} \omega_n &= \frac{2n\pi}{\ell} \cdot \sqrt{\frac{H}{m}} \quad n = 1, 2, 3, \dots \\ \tilde{u}_n(x) &= -\frac{1}{2} \left( \frac{mg\ell}{H} \right) A_n \left\{ \left( 1 - \frac{2x}{\ell} \right) \sin \left( \frac{2n\pi x}{\ell} \right) + \frac{1 - \cos(2n\pi x/\ell)}{n\pi} \right\} \\ \tilde{w}_n(x) &= A_n \cdot \sin \left( \frac{2n\pi x}{\ell} \right) \quad n = 1, 2, 3, \dots \end{aligned} \quad (\text{B.8})$$

where  $\omega_n$ ,  $\tilde{u}_n(x)$  and  $\tilde{w}_n(x)$  represent, respectively, the natural frequency for the  $n$ th order *anti-symmetric* in-plane mode, and the corresponding longitudinal and vertical components of the modal shape.

As can be observed from this expression, the amplitude of the longitudinal component of motion  $B_n = 1/2 \cdot mg\ell/H \cdot A_n$  is very small for a shallow cable, as the ratio  $mg\ell/H$  is small. It should also be observed that the maximum displacement is reached at the quarter spans for the first modal component. *Figure B.3* presents the longitudinal and vertical configurations for the first three anti-symmetric mode shapes of a shallow cable with a limiting sag to span ratio  $d/\ell = 1/8$ , where a maximum longitudinal amplitude of vibration equal to  $0.41 mg\ell/H$  of the vertical amplitude  $A_n$  is attained.

### (ii) Symmetric in-plane modes

In the case of *symmetric in-plane modes*, an additional cable tension is induced by the motion, which is assumed quasi-static and is characterised by the product

$$h_\tau(t) = \tilde{h}_\tau \cdot e^{i\omega t} \quad (\text{B.9})$$

Substituting the expressions in (B.7) and (B.9) into equations (B.2) and (B.3) and introducing the boundary conditions, the natural frequencies  $\omega$  of the cable for symmetric in-plane modes become the roots of

$$\tan \frac{\bar{\omega}}{2} = \frac{\bar{\omega}}{2} - \frac{4}{\lambda^2} \left( \frac{\bar{\omega}}{2} \right)^3 \quad (\text{B.10})$$

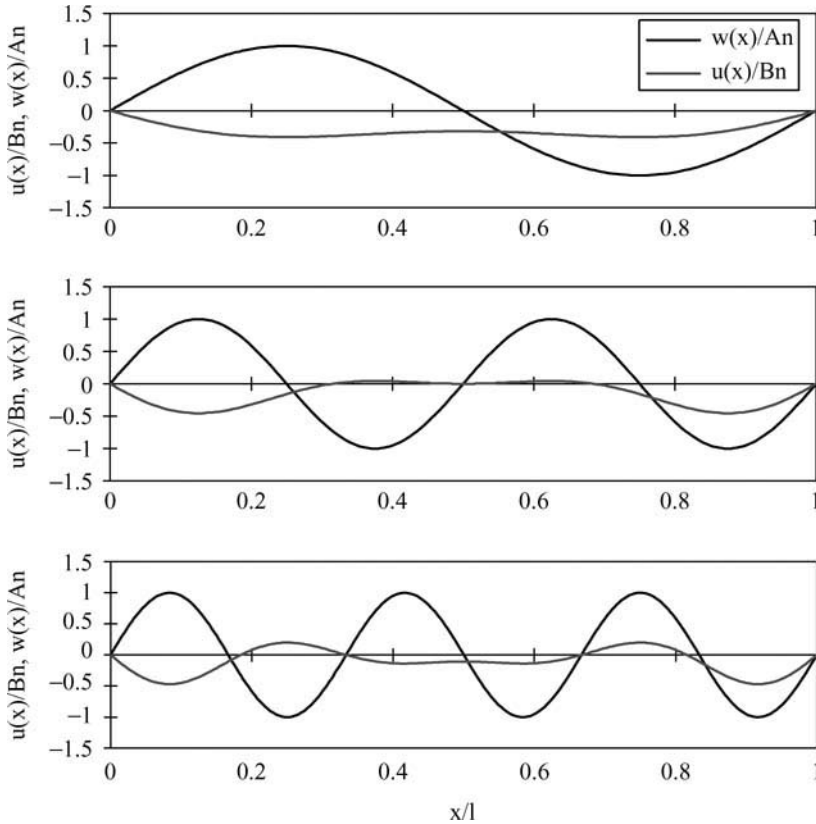


Fig. B.3: Vertical and longitudinal components of the first three anti-symmetric in-plane modes

where  $\bar{\omega}$  is the adimensional natural frequency given by  $\bar{\omega} = \omega\ell/(H/m)^{1/2}$ , and  $\lambda^2$  is the fundamental parameter of the cable system defined in Appendix A by expression (A.12). The modal shapes associated with these frequencies have then the following longitudinal  $\tilde{u}(x)$  and vertical  $\tilde{w}(x)$  components

$$\begin{aligned}\tilde{u}(x) &= \frac{mg\ell}{H} \cdot C_n \cdot \left[ \frac{\bar{\omega}^2}{\lambda^2} \cdot \frac{L_x}{L_e} - \frac{1}{2} \left( 1 - 2\frac{x}{\ell} \right) \cdot \left\{ 1 - \tan \frac{\bar{\omega}}{2} \cdot \sin \left( \frac{\bar{\omega}x}{\ell} \right) - \cos \left( \frac{\bar{\omega}x}{\ell} \right) \right\} \right. \\ &\quad \left. - \frac{1}{\bar{\omega}} \cdot \left\{ \frac{\bar{\omega}x}{\ell} - \tan \frac{\bar{\omega}}{2} \cdot \left( 1 - \cos \left( \frac{\bar{\omega}x}{\ell} \right) \right) - \sin \left( \frac{\bar{\omega}x}{\ell} \right) \right\} \right] \quad (\text{B.11}) \\ \tilde{w}(x) &= C_n \cdot \left( 1 - \tan \frac{\bar{\omega}}{2} \sin \frac{\bar{\omega}x}{\ell} - \cos \frac{\bar{\omega}x}{\ell} \right)\end{aligned}$$

Equation (B.10) is of utmost importance in the theory of cable vibration. The sole dependence of the natural frequencies of *in-plane symmetric modes* on the independent parameter  $\lambda^2$  also illustrates the importance of  $\lambda^2$  as an intrinsic characteristic of the cable system. Particular solutions for this equation can be obtained for the limiting cases of an *inextensible cable* and a *taut string*.

When the cable is *inextensible*,  $\lambda^2$  is very large and the deformations are essentially of a geometric nature. In this situation, the transcendental equation (B.10) reduces to

$$\tan \frac{\bar{\omega}}{2} = \frac{\bar{\omega}}{2} \quad (\text{B.12})$$

The roots of this equation are given by

$$\bar{\omega}_n = (2n + 1)\pi - \frac{4}{(2n + 1)\pi} \quad n = 1, 2, 3, \dots \quad (\text{B.13})$$

So, for large values of  $\lambda^2$ , the numeric solution of (B.10) can be replaced by (B.13).

On the contrary, when  $\lambda^2$  is very small, the roots of (B.10) approach the roots of the symmetric modes of a *taut string*

$$\bar{\omega}_n = (2n - 1)\pi \quad n = 1, 2, 3, \dots \quad (\text{B.14})$$

Comparing expressions (B.13) and (B.14), it becomes evident that the transition from the dynamics of a taut string ( $\lambda^2 = 0$ ) to the dynamics of an inextensible cable ( $\lambda^2 = \infty$ ) is marked by a shift of almost  $2\pi$  in the value of the adimensional frequency  $\bar{\omega}_n$  of symmetric modes. This fact can be observed in Fig. B.4, which represents the variation of the quantity  $\bar{\omega}_n/\pi$  with  $\lambda^2$ . An important aspect of this figure is the occurrence of the so-called *crossovers* in the transition regions, corresponding to values of  $\lambda^2$  beyond which the natural frequency of the *symmetric modes* becomes higher than the natural frequency of the same order *anti-symmetric modes*.

Generally, the values of  $\lambda^2$  associated with  $n$ th order *crossovers* can be obtained by

$$\lambda^2 = 4(n\pi)^2 \quad (\text{B.15})$$

This results from the substitution into (B.10) of the values  $\bar{\omega}_n = 2n\pi$  for the anti-symmetric modes of vibration. It can also be observed that the configuration associated with the vertical component of symmetric vibration modes varies according to the value of  $\lambda^2$ . Considering the *first* mode of vibration and the corresponding *crossover* value  $\lambda^2 = 4\pi^2$ , it is shown in Fig. B.5 that, for  $\lambda^2 < 4\pi^2$ , the vertical component of vibration has no internal nodes. For  $\lambda^2 = 4\pi^2$ , this component is tangential to the cable profile at the supports. Finally, for  $\lambda^2 > 4\pi^2$ , when the symmetric natural frequency becomes higher than the corresponding order anti-symmetric natural frequency, two internal nodes occur in the symmetric vertical component.

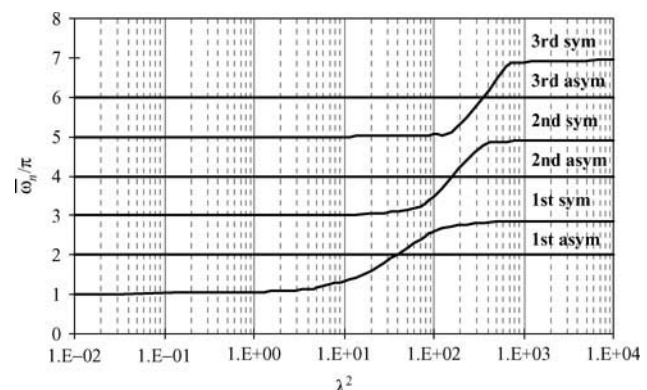
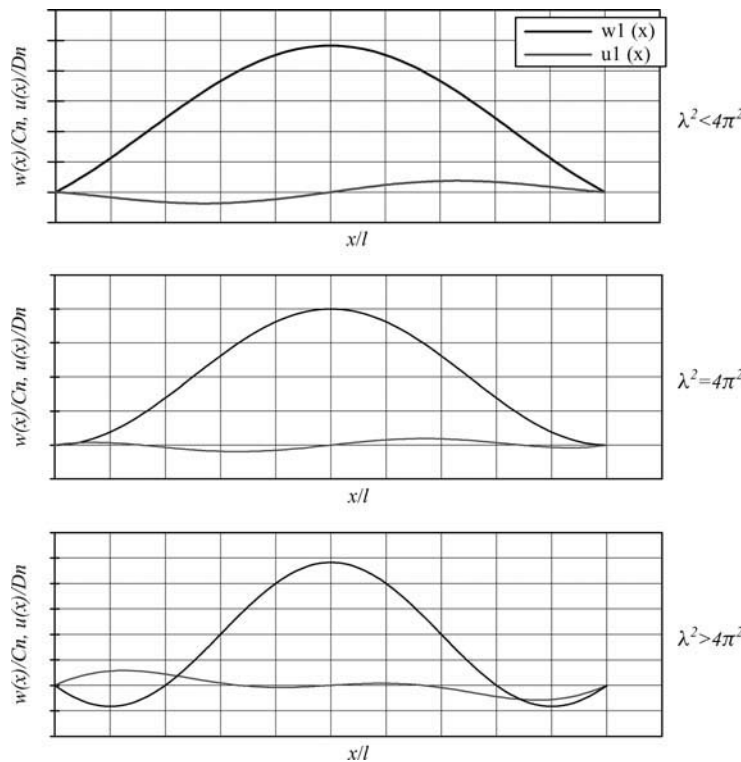


Fig. B.4: Variation of the natural frequencies of the first three symmetric and anti-symmetric modes of vibration with  $\lambda^2$



*Fig. B.5: Representation of the vertical and longitudinal modal components associated with the first vibration mode for different values of  $\lambda^2$  :  $\lambda^2 < 4\pi^2$ ,  $\lambda^2 = 4\pi^2$  and  $\lambda^2 > 4\pi^2$*

With respect to the longitudinal component of motion, and according to Fig. B.5, where this component has been represented in normalised form for the limiting situation  $d/\ell = 1/8$ ,  $\tilde{u}(x)$  is anti-symmetric, the number of internal nodes increasing from the situation where  $\lambda^2 < 4\pi^2$  to the case of  $\lambda^2 > 4\pi^2$ .

As a final consideration, it should be noted that the cables employed in cable-stayed bridges are tightly stretched, presenting in most cases small values of  $\lambda^2$  (typically inferior to 1, as already stated). Therefore, according to the representation in Fig. B.4, the corresponding natural frequencies lie outside the transition ranges and can be obtained using the formulae for taut strings. On the contrary, the cables from suspension bridges are generally in the transition range and, consequently, their vibration characteristics should consider both cable geometry and elasticity.

## B.3 Linear Theory of Vibrations of Inclined Cables

### B.3.1 Simplified approach

The theory of horizontal cable vibration was extended by Irvine [127] to inclined flat cables. The methodology employed consisted in performing a transformation of the horizontal/vertical

axes to inclined axes parallel/perpendicular to the cable chord with the basic assumption that the weight component parallel to the cable chord is negligible.

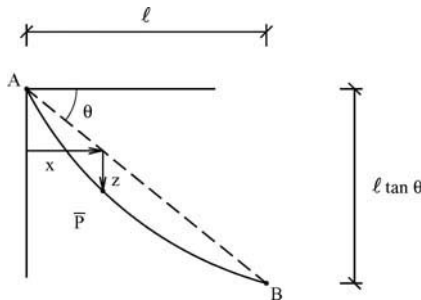


Fig. B.6: Definition of the profile of an inclined cable

natural frequency of an inclined cable and  $\bar{\omega}_{*n} = \omega_{*n} \ell_* \cdot \sqrt{m/H_*}$  as the corresponding adimensional natural frequency, with  $\ell_* = \ell \sec \theta$  and  $H_* = H \sec \theta$ , the out-of-plane modes of an inclined cable are now characterised by

$$\bar{\omega}_{*n} = n\pi \quad n = 1, 2, 3, \dots \quad (\text{B.17})$$

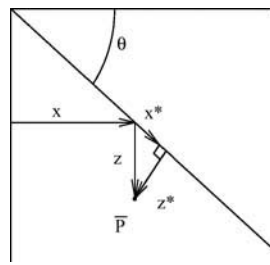


Fig. B.7: Transformation of axes for the definition of the cable profile

valid for all angles in the range  $[0, 90^\circ]$ . In fact, the precision of these equations decreases with the increase of the angle of inclination  $\theta$ . However, for the common case where  $\theta$  does not exceed  $60^\circ$ , validity of this theory can be assumed.

### B.3.2 Asymptotic approach

Triantafyllou [133] developed a more precise solution for the vibration problem of an inclined elastic cable with small sag by considering the spatial variability of the dynamic cable tension (Irvine had assumed only variation with time of this quantity) as well as the effect of the weight component parallel to the cable chord (Irvine had neglected this component).

By establishing the static and dynamic equilibrium of the inclined cable in Lagrangian coordinates and including the compatibility equations, Triantafyllou arrived at a set of four

Consider the inclined cable presented in Fig. B.6 and the transformation of axes represented in Fig. B.7, corresponding to a new set of coordinates  $(x_*, z_*)$  defined according to

$$\begin{aligned} x_* &= x \sec \theta + z \sin \theta \\ z_* &= z \cos \theta \end{aligned} \quad (\text{B.16})$$

As in the case of horizontal cables, the out-of-plane motion is, to first order, uncoupled from the in-plane motion. Also the in-plane longitudinal component of motion is much smaller than the in-plane transverse component and does not affect the calculation of natural frequencies. So, defining  $\omega_{*n}$  as the  $n$ th order

For in-plane anti-symmetric modes, the natural frequencies are obtained from

$$\bar{\omega}_{*n} = 2n\pi \quad n = 1, 2, 3, \dots \quad (\text{B.18})$$

while for symmetric in-plane modes,  $\bar{\omega}_{*n}$  are the roots of the transcendental equation

$$\tan\left(\frac{\bar{\omega}_{*n}}{2}\right) = \frac{\bar{\omega}_{*n}}{2} - \frac{4}{\lambda_*^2} \left(\frac{\bar{\omega}_{*n}}{2}\right)^3 \quad (\text{B.19})$$

Equations (B.17) to (B.19) are applicable in general and contain, as a particular case, the results corresponding to a horizontal suspended cable. Irvine states however that these equations are not

valid for all angles in the range  $[0, 90^\circ]$ . In fact, the precision of these equations decreases with the increase of the angle of inclination  $\theta$ . However, for the common case where  $\theta$  does not exceed  $60^\circ$ , validity of this theory can be assumed.

independent linearised first-order differential equations, whose asymptotic solutions were determined by considering two distinct physical mechanisms of cable vibration: (i) the transverse cable dynamics, in which the rate of spatial change of transverse displacement is large compared with the rate of change of the static solution and; (ii) the axial dynamics of the cable, that results in tangential and transversal vibrations with slow spatial variation. The first physical mechanism led to a so-called *fast solution*, while the latter led to a *slow solution*. The total solution is obtained from the sum of the independent solutions, giving the following coupled equations for the transverse and tangential displacements  $q$  and  $p$ , respectively, relative to the static solution [134].

$$q(s, t) = \left\{ \frac{1}{\sqrt[4]{T_0 \frac{s}{m}}} \cdot [c_1 \cdot \cos W(s) + c_2 \cdot \sin W(s)] + \frac{d\phi_0(s)}{ds} \right. \\ \left. \times [c_3 \cdot A_i(-z) + c_4 \cdot B_i(-z)] \right\} e^{i\omega t} \quad (\text{B.20a})$$

$$p(s, t) = \left\{ \frac{d\phi_0}{ds} \frac{\sqrt[4]{T_0 \frac{s}{m}}}{\omega} [c_1 \cdot \sin W(s) - c_2 \cdot \cos W(s)] - Q^{1/3} \right. \\ \left. \times [c_3 \cdot A'_i(-z) + c_4 \cdot B'_i(-z)] \right\} e^{i\omega t} \quad (\text{B.20b})$$

In these expressions,  $T_0$  represents the static tension,  $\phi_0(s)$  is the static angle at an arbitrary point defined by the Lagrangian coordinate  $s$  (Fig. B.8), the quantities  $W(s)$ ,  $Q$  and  $z$  being defined by

$$W(s) = \omega \int_0^s \frac{ds}{\sqrt{T_0 \frac{s}{m}}} \\ Q = \frac{4(mg)^3 \cos^2 \phi_\alpha \sin \phi_\alpha}{T_\alpha^3} \\ z = Q^{1/3} (s - s_0)$$

where  $\phi_\alpha$  represents the angle of inclination of the chord with respect to the horizontal (Fig. B.8), and  $T_\alpha$  is the tension at the point where the static angle of inclination is equal to  $\phi_\alpha$ , characterised by the Lagrangian coordinate  $s_\alpha$  given by

$$s_\alpha = \frac{-\left(\frac{mg \cos \phi_\alpha}{T_\alpha}\right)^2 + \frac{m \omega^2}{EA_0}}{Q}$$

The constants  $c_1$ ,  $c_2$ ,  $c_3$  and  $c_4$  are determined from the boundary conditions, and finally,  $A_i(z)$  and  $B_i(z)$  are the Airy functions of the first and second kind, respectively,  $A'_i(z)$  and  $B'_i(z)$  being the corresponding derivatives.

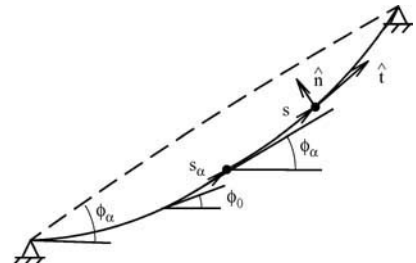


Fig. B.8: Inclined cable in static configuration

The first two terms in the second member of expressions (B.20a) and (B.20b) are associated with the *fast solution* referred to above and are of the same type as the solutions obtained previously by Irvine for the stretched cable. The last two terms are related with *slow solution* and can be of sinusoidal or exponential type, or a combination of the two.

A simplified approach can be used, if the cable inertia in the longitudinal direction is neglected. This corresponds to a quasi-static assumption for the stretching, leading to the following simplified equation for the determination of natural frequencies

$$\sin \theta \left[ \theta \left( \frac{4\theta^2}{\lambda^2} - 1 \right) \cos \theta + \sin \theta \right] - \frac{49}{64} \varepsilon^2 \cdot \sin^2 \phi_\alpha \cdot \cos 2\theta = 0 \quad (\text{B.21})$$

where

$$\varepsilon = \frac{mgL}{T_\alpha}$$

$$\theta = \frac{kL}{2}$$

$$k = \frac{\omega}{\sqrt{\frac{T_\alpha}{m}}}$$

$$\lambda^2 = \frac{EA_0}{T_\alpha} \left( \frac{mgL}{T_\alpha} \right)^2 \cos^2 \phi_\alpha$$

The transverse modes can be found from ref.[134]

$$\begin{aligned} q_n(s) = & C_n \left\{ \left\{ 2 \sin^2 \left( \frac{kL}{2} \right) \left[ \cos \left( \frac{kLs}{L} \right) - 1 \right] - \sin \left( \frac{kLs}{L} \right) \left[ \sin kL + kL \left( \frac{k^2 L^2}{\lambda^2} - 1 \right) \right] \right\} \right. \\ & + \frac{\varepsilon \sin \phi_\alpha}{4} \left\{ 2 \sin^2 \frac{kL}{2} \left[ \left( \frac{kLs}{L} \right) \left( \frac{s}{L} - 1 \right) \sin \left( \frac{kLs}{L} \right) - \left( \frac{s}{L} - \frac{1}{2} \right) \cos \left( \frac{kLs}{L} \right) \right] \right. \\ & + \frac{1}{2} \cos \left( \frac{kLs}{L} \right) \left( -\cos kL + 15 \right) + \left[ -\sin \left( \frac{kLs}{L} \right) \frac{1}{2} + \left( \frac{s}{L} - 1 \right) \left( \frac{kLs}{L} \right) \cos \left( \frac{kLs}{L} \right) \right. \\ & + \left. \left. \left( \frac{s}{L} - \frac{1}{2} \right) \sin \left( \frac{kLs}{L} \right) \right] \cdot \left[ \sin kL + kL \left( \frac{k^2 L^2}{\lambda^2} - 1 \right) \right] + 4 \left[ -1 - \frac{3}{4} \cos kL \right. \right. \\ & \left. \left. + 4 \sin^2 \left( \frac{kL}{2} \right) \left( \frac{s}{L} - \frac{1}{2} \right) \right] \right\} \\ & + \varepsilon^2 \sin^2 \phi_\alpha \left[ \frac{7}{2} \left( \frac{s}{L} - \frac{1}{2} \right) + \frac{7}{4} \cos \left( \frac{kLs}{L} \right) - \frac{7}{16} \left( \frac{s}{L} - \frac{1}{2} \right) \cos \left( \frac{kLs}{L} \right) - \frac{7}{32} \right. \\ & \left. + \frac{7}{16} \left( \frac{kLs}{L} \right) \left( \frac{s}{L} - 1 \right) \sin \left( \frac{kLs}{L} \right) \right] \} \end{aligned} \quad (\text{B.22})$$

in which  $C_n$  is an arbitrary amplitude. Finally, the dynamic tension is given by

$$T(s, t) = \frac{m\omega^2 L}{\varepsilon \cos \phi_\alpha} C_n \left( 2 \sin^2 \frac{kL}{2} + \frac{7}{4} \varepsilon \sin \phi_\alpha \right) \varepsilon^{i\omega t} \quad (\text{B.23})$$

Considering the analogy of the tension component  $T_\alpha$  with  $H_*$  defined by Irvine for inclined cables and assuming that the cable is flat, in which case the length  $L$  is very close to the cable chord  $\ell_*$  and the virtual length  $L_{e*}$  introduced by Irvine, i.e.,  $L \approx \ell_* \approx L_{e*}$ , the parameters  $\lambda^2$  and  $\lambda_{e*}^2$  defined by Triantafyllou and Irvine, respectively, become equivalent. Also it becomes evident that  $\theta \approx \bar{\omega}_{n*}/2$ . Replacing this value into equation (B.21), it can be seen that equations (B.19) and (B.22) differ only in the second order term  $-98/64 \cdot \varepsilon^2 \cdot \sin^2 \phi_\alpha \cdot 1/\tan 2\theta$  [134]. So, for the particular case of a horizontal cable,

equations (B.19) and (B.21) are identical. For inclined cables however, this second order term produces a modification in the solutions obtained by Irvine so that the *crossovers* never occur. From Fig. B.9, which represents the variation of the adimensional natural frequencies  $\bar{\omega}_{n*}/\pi$  associated with the first two modes of vibration with  $\lambda^2$  for different angles of inclination of the cables, the natural frequencies of consecutive modes of vibration come very close to each other in the regions previously defined for the crossovers, i.e., for  $\lambda^2 = 4(n\pi)^2$ , but never coincide. This phenomenon of noncrossing curves has no significant implication in terms of the values of the natural frequencies for inclined cables with a small sag, which differ only by a few percent from the corresponding frequencies obtained under the simplified approach of Irvine [134]. It has however a significant influence in the determination of the mode shapes, which are totally different from those obtained for horizontal cables over the transition regions. In effect, and according to the representation of Fig. B.10, near the so-called *avoided crossings*, the modes are hybrid, a mixture of symmetric and anti-symmetric forms. This results from the fact that the lower part of the cable is closer to an inextensible chain, while the upper part is closer to a taut string, which has major implications in the dynamic

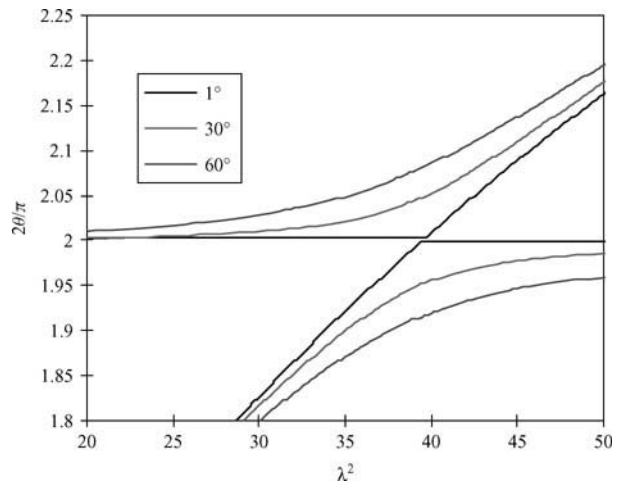


Fig. B.9: Variation of the natural frequency  $\bar{\omega}_{n*=2\theta}$  of the first two modes of vibration with  $\lambda^2$ , for different angles of inclination of the cable:  $\phi_\alpha = 1^\circ, 30^\circ, 60^\circ$  and  $\varepsilon = 0.3$

frequency obtained under the simplified approach of Irvine [134]. It has however a significant influence in the determination of the mode shapes, which are totally different from those obtained for horizontal cables over the transition regions. In effect, and according to the representation of Fig. B.10, near the so-called *avoided crossings*, the modes are hybrid, a mixture of symmetric and anti-symmetric forms. This results from the fact that the lower part of the cable is closer to an inextensible chain, while the upper part is closer to a taut string, which has major implications in the dynamic

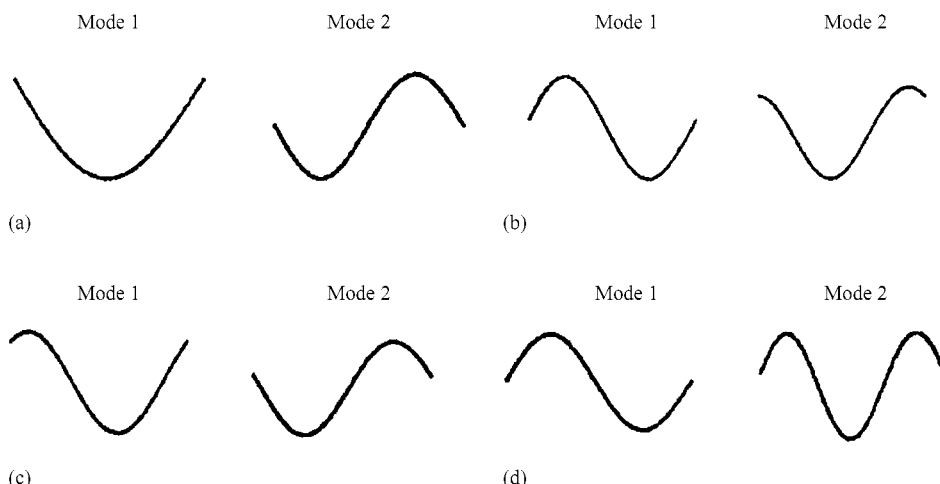


Fig. B.10: Transverse modal configuration of the first two modes of vibration of an inclined cable ( $\phi_\alpha = 30^\circ$ ) for different values of  $\lambda^2$  and  $\varepsilon = 0.3$ : (a)  $\lambda^2 = 0.01\pi^2$ ; (b)  $\lambda^2 = 3.61\pi^2$ ; (c)  $\lambda^2 = 5.29\pi^2$ ; (d)  $\lambda^2 = 64\pi^2$  [134]

cable tension. In fact, according to the theory of Irvine, the anti-symmetric modes do not develop, to first order, any dynamic tension. Consequently, for fatigue and strength analysis purposes, only the symmetric modes are of interest. With the present approach, all modes involve the development of a dynamic component of tension and are now of interest over the transition region.

Finally, it should be noted that for  $\lambda^2 < 1$ , the range of values of the parameter  $\lambda^2$  associated with cables from cable-stayed bridges, the theory of Irvine is still valid.

## B.4 Bending Stiffness Effects

### B.4.1 Taut string approach

Both the linear and asymptotic theories of cable vibration presented in the previous sections were based on the assumption that the cable is flexible. In practice the bending stiffness  $EI$  of a cable modifies its dynamic behaviour slightly. Considering that this effect is more pronounced for short cables, whose sag can be neglected, the simplified approach for the inclusion of the bending stiffness departs from the vibrating-chord theory applied to a taut string, for which the differential equilibrium equation in the lateral direction (*Fig. B.1*) is

$$H \frac{\partial^2 w}{\partial x^2} - \frac{\partial^2}{\partial x^2} \left( EI \frac{\partial^2 w}{\partial x^2} \right) = m \cdot \frac{\partial^2 w}{\partial t^2} \quad (\text{B.24})$$

A simplified solution to this equation for a cable clamped at both ends was derived by Morse and Ingard [135], giving the following expression for the  $n$ th order natural frequency  $\omega_n$

$$\omega_n = \frac{n \pi}{\ell} \cdot \sqrt{\frac{H}{m}} \cdot \left[ 1 + 2 \sqrt{\frac{EI}{H \ell^2}} + \left( 4 + \frac{n \pi^2}{2} \right) \cdot \frac{EI}{H \ell^2} \right] \quad (\text{B.25})$$

This expression is valid as long as the term  $EI/H \ell^2$  is small. The relative deviation,  $\varepsilon_{EI}^n$ , to the vibrating-chord theory of the natural frequencies of a taut cable characterised by a stiffness  $EI$  is then given by

$$\varepsilon_{EI}^n = \frac{2}{\zeta} + \frac{\left( 4 + \frac{n \pi^2}{2} \right)}{\zeta^2} \quad (\text{B.26})$$

where  $\zeta = \sqrt{H \ell^2/EI}$ . This deviation increases with the order of the mode shape. Considering the bending stiffness effect as negligible whenever  $\varepsilon_{EI}^n$  is less than 5% for the first five modes, it can be concluded that bending stiffness effects are negligible for stay cables with  $\zeta \geq 50$ .

The major difficulty in the application of expression (B.25) lies in the evaluation of the bending stiffness  $EI$ , which is not a function of only the modulus of elasticity of the cable and of the cross section characteristics. In effect,  $EI$  depends on the degree of constraint of the strands that form each stay cable, which itself depends on the type of cable and protection (locked coil, stranded, parallel wire, with/without grout), on the cable length and on the curvature. Therefore, although an estimation of  $EI$  can be obtained from laboratory tests, it is only from site measurements that an average  $EI$  can be assessed. According to

Yamagiwa *et al.* [136], typical values of  $EI$  are around 50% to 70% of the stiffness of a solid bar with the same diameter as that of the cable. Reported values on a cable-stayed bridge employing locked coil cables are of the order of 65% to 85% of that stiffness [137]. Considering a bending stiffness equal to 70% of the stiffness of the solid bar with diameter equivalent to the cross section, and applying it to cables 1 and 16 of the Guadiana bridge, the characteristics listed in *Table A.1*,  $\zeta$  values of 111 and 45 are obtained for cables 1 and 16, respectively, meaning that for the longest cable (chord length of 168.54 m) the natural frequencies of the fifth cable mode increase by 2% with the inclusion of the bending stiffness effect, while for the shortest cable (chord length of 49.48 m) the same frequency increases by 6%.

### B.4.2 Simplified sagged cable approach

Equation (B.25), which evaluates natural frequencies of a stay cable with inclusion of the bending stiffness effect, has been deduced based on the vibrating chord theory, ie., neglecting the effect of sag on the response. The simultaneous inclusion of the sag and bending stiffness effects in a unified finite difference formulation by Mehrabi and Tabatabai [138] led to a powerful tool for the dynamic analysis of stay cables. Some authors have also developed simplified formulae for the evaluation of a cable's natural frequency which includes both the bending stiffness effect and the sag effect. The simplified formulae provided by Zui *et al.* [139] apply to small sag-to-span cables. Designating by  $\eta_n$  and  $\varphi_n$  the ratios between the  $n$ th order natural frequency  $\omega_n$  and the  $n$ th order frequency of the equivalent taut string  $\omega_n^s$ , and

$\zeta$	$\eta_n$	$\varphi_n$
$0 \leq \zeta \leq 6$		$\varphi_1 = \sqrt{1 + \frac{\zeta^2}{42}}; \quad \varphi_2 = \sqrt{1 + \frac{\zeta^2}{85}}$
$6 \leq \zeta \leq 8$	$\eta_1 = 1.075 \cdot \sqrt{1 + \left(\frac{6.8}{\zeta}\right)^2}$	$\varphi_1 = \sqrt{1 + \frac{\zeta^2}{42}}; \quad \varphi_2 = \sqrt{1 + \frac{\zeta^2}{85}}$
$8 \leq \zeta \leq 17$	$\eta_1 = 1.075 \cdot \sqrt{1 + \left(\frac{6.8}{\zeta}\right)^2}$	$\varphi_2 = \sqrt{1 + \frac{\zeta^2}{85}}$
$17 \leq \zeta \leq 18$	$\eta_1 = \frac{\zeta}{\zeta-2.2}; \quad \eta_2 = 0.985 \cdot \frac{\zeta}{\zeta-3.1}$	$\varphi_2 = \sqrt{1 + \frac{\zeta^2}{85}}$
$18 \leq \zeta \leq 60$	$\eta_1 = \frac{\zeta}{\zeta-2.2}; \quad \eta_2 = 0.985 \cdot \frac{\zeta}{\zeta-3.1}$	
$60 \leq \zeta \leq 200$	$\eta_1 = \frac{\zeta}{\zeta-2.2}; \quad \eta_2 = \frac{\zeta}{\zeta-2.2}$	
$\zeta \geq 200$	$\eta_n = \frac{\zeta}{\zeta-2.2}$	

*Table B.1: Formulae for evaluation of cable frequency considering sag and bending stiffness effects [139]*

Cable	$\zeta$	Bending effect		Zui <i>et al.</i> [139]		Mehrabi and Tabatabai [138]	
		$\eta_1$	$\eta_2$	$\eta_1$	$\eta_2$	$\eta_1$	$\eta_2$
V. Gama							
HC01	23.99	1.0989	1.1075	1.1010	1.1312	1.0997	1.1075
HC24	116.56	1.0178	1.0182	1.0192	1.0192	1.0307	1.0182
HC15	94.67	1.0221	1.0227	1.0238	1.0238	1.0311	1.0227
Guadiana							
Central 1	129.53	1.0160	1.0163	1.0173	1.0173	1.0234	1.0163
Central 16	52.38	1.0414	1.0432	1.0438	1.0470	1.0416	1.0432
Normandy	182.15	1.0112	1.0114	1.0122	1.0122	1.1288	1.0114
Ikuchi*	161.34	1.0127	1.0129	1.0138	1.0138	1.0604	1.0129

Table B.2: Increase of first two cable natural frequencies associated with sag and bending stiffness effects (simplified formulae)

of the clamped beam  $\omega_n^b$ ,  $\eta_n = \omega_n / \omega_n^b$  and  $\varphi_n = \omega_n / \omega_n^b$ , respectively, where

$$\omega_n^s = \frac{\pi n}{\ell} \cdot \sqrt{\frac{H}{m}} \quad (\text{B.27})$$

$$\omega_n^b = \frac{\alpha_n^2}{\ell^2} \cdot \sqrt{\frac{EI}{m}}, \text{ with } \alpha_1 = 4.730 \text{ and } \alpha_2 = 7.853 \quad (\text{B.28})$$

the estimates summarised in Table B.1 are obtained.

The simplified formulae derived by Mehrabi and Tabatabai [138] considering the sag and bending stiffness effects are also of interest, although, according to the authors, the accuracy is higher for cables with a  $\zeta$  no less than 50 and with an Irvine parameter  $\lambda^2$  of less than 3.1. Mehrabi and Tabatabai, however, state that this situation is covered by 95% of the stay cables from cable-stayed bridges around the world. Accordingly, the  $n$ th order natural frequency of a cable  $\omega_n$  is given by

$$\omega_n = \frac{\pi n}{\ell} \cdot \sqrt{\frac{H}{m}} \cdot \left( \alpha \beta_n - 0.24 \frac{\mu}{\zeta} \right) \quad (\text{B.29})$$

with

$$\alpha = 1 + 0.039 \mu; \beta_n = 1 + \frac{2}{\zeta} + \frac{\left(4 + \frac{n\pi^2}{2}\right)}{\zeta^2}$$

$$\mu = \lambda^2, n = 1; \mu = 0, n > 1 \text{ (in-plane modes); } \mu = 0 \text{ (out-of-plane modes)}$$

Using the above definition for  $\eta_n$ , the formulae resulting from the three simplified approaches referred to above were applied to the stay cables with the characteristics listed in Table A.1.

The results are summarised in *Table B.2*. The formulae of Meharabi and Tabatabai seem to cover all eventualities: very long cables, like the Normandy Bridge longest cable, exhibit a significant increase of frequency due to sag effects, while short cables also exhibit a significant increase of frequency because of bending stiffness effects. This increase of frequency has consequences that should not be disregarded, particularly whenever the installed cable force is to be estimated through measurement of cable frequency.

# Appendix C—Assessment of Cable Force and Damping

## C.1 General

The assessment of cable force during the construction or service life of a bridge can be done by several methods based on (i) the direct measurement of the stress in the tensioning jacks; (ii) the application of ring load cells or strain gauges in the strands; (iii) the measured elongation close to an anchorage; (iv) a topographic survey and (v) the indirect measurement of vibrations. The advantages and drawbacks of the various techniques are discussed in the following section, focusing in particular on the technique of tension estimation through the measurement of vibrations. The assessment of damping based on the cable response is also discussed.

## C.2 Methods of Force Assessment

### C.2.1 Direct measurement of stress in tensioning jacks

This method is employed during the construction of the bridge and provides a direct measure of the installed tension. Mars and Hardy [140] found errors of 10% to 15% in the application of this technique. It is therefore of utmost importance to ensure that hydraulic jacks are properly calibrated. This technique is not adequate to estimate the tension after construction of the bridge as the installation of the jacks is a long process and can produce damage in the anchorages.

### C.2.2 Application of ring load cells or of strain gauges in strands

Ring load cells can be applied to either one or a few of the individual strands that form the cable, or to the set of strands. Therefore, either individual or average global measures of the installed tension are possible. Although the individual assessment of the strand tension would be of interest for the purpose of detection of cracks, the application to all strands of all cables would not be feasible. Therefore, the normal practice is to either select one or a few strands of a cable for installation of strain gauges or small load cells (see example in *Fig. C.1*), or to mount a ring load cell at one cable anchorage between two bearing plates. In any case the principle is the same, i.e., the measurement of deformation through strain gauge rosettes. The load ring cell is actually a spool of a heat-treated steel alloy with equally spaced bonded strain gauge rosettes. The number of rosettes is at least four, so that eccentricity effects are avoided. The rosettes are composed of two strain gauges, one for the axial and the other for tangential strain measurement. A strong aluminium housing filled with a high-density resin protects the strain gauges from moisture and impact damage. *Figure C.2* shows the installation of a ring load cell.

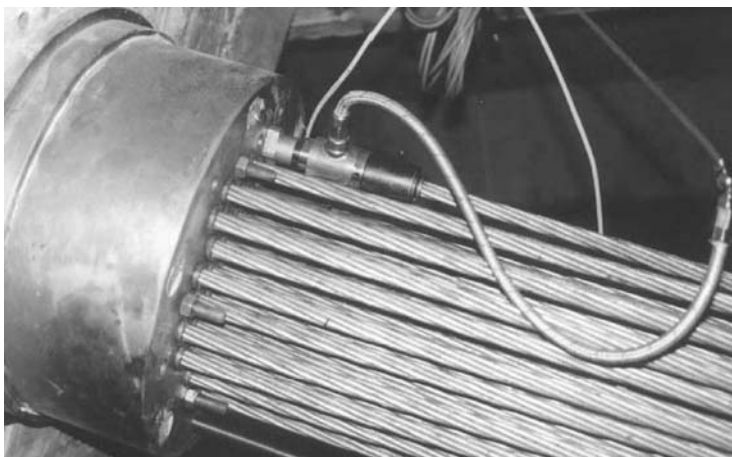


*Fig. C.1: Installation of a load cell on a strand of one stay cable*



*Fig. C.2: (a) Example of center-hole load cell (<http://www.slopeindicator.com/instruments/loadcell-bondedsg.html>) and; (b) Scheme of installation on laboratory application*

The major inconvenience in the use of load cells for assessment of cable force is the cost of the numerous sensors required, which have to remain installed in the structure and have to be adequately calibrated, given the time variation of strain gauge properties. The direct installation of strain gauge rosettes in particular strands of a cable is another possibility, the major inconvenience being the time required to properly mount the sensor.

### C.2.3 Measurement of cable elongation

The measure of the elongation of a segment of the cable close to the anchorage can be used to assess the corresponding deformation, providing a measure of the installed cable tension. Given the current deformations in stay cables of around  $10^{-3}$ , an elongation of about  $0.2 \text{ mm}$  is attained in a segment  $0.2 \text{ m}$  long. So, if a precision of 5% is required in the estimate, then

the measure should be made with an accuracy of 0.01 mm. This accuracy is not easy to obtain on site.

### C.2.4 Topographic survey

The assessment of cable tension based on topographical measurements is current practice during construction and provides particularly accurate results when the stay cable is only slightly tensioned.

### C.2.5 Vibration method

The indirect estimation of tension through the measurement of the cable's natural frequencies is based on the vibrating chord theory. This method will be described in the next section and is currently of great interest for the assessment of cable condition throughout its service life, given the ease of application. The major drawback is associated with the lesser accuracy whenever the free length of the cable is not accurately known.

## C.3 Force and Damping Assessment Based on the Vibration Method

### C.3.1 Vibrating chord theory

The method is based on the vibrating chord theory, a direct result of the theory of wave propagation [135] applied to a tensioned cable fixed at the two ends. Accordingly, a tensioned cable fixed at the two ends constitutes a non-dispersive medium, i.e. a medium where the velocity of wave propagation is independent of the frequency. A transverse perturbation applied at some point along the cable propagates till the end of the cable and reflects successively, leading to a system of transverse stationary waves with sinusoidal shape characterised by natural frequencies  $f_n$  given by

$$f_n = \frac{n}{2\ell} \cdot c = \frac{n}{2\ell} \cdot \sqrt{\frac{H}{m}} \quad (\text{C.1})$$

These frequencies are functions of the distance between the cable ends  $\ell$  (the chord length) and of the velocity of wave propagation  $c = \sqrt{H/m}$ , where  $H$  is the cable tension and  $m$  is the mass per unit length. So, if  $f_n$  is known, the installed tension  $H$  will be

$$H = 4m\ell^2 \cdot \frac{f_n^2}{n^2} \quad (\text{C.2})$$

The first reported applications of the vibrating chord theory to the estimation of cable tension in civil engineering structures are due to Mars and Hardy [140] and Robert *et al.* [141]. These authors have concluded that the application of the theory to the evaluation of the installed tension in stay cables is valid as long as the corresponding length is not too short. In effect, it was observed in Appendix B that, even though the bending stiffness  $EI$  is generally very small for stay cables, bending effects can be

important for small cable lengths, giving rise to a dispersive character of vibrations, the consequence being a change from the linear nature of the curve generated by the variation of the natural frequency with the order of mode. So, in order to guarantee the validity of application of the vibrating chord theory to a particular cable, one should measure first the harmonics of the cable and plot them against the mode order, in a graph of the type represented in *Fig. C.3*. If the deviation of the fitted curve to the tangent at the origin is very small, (Robert *et al.* [141] propose less than 0.6% for the seventh mode), then the estimate of the cable tension through the vibrating chord theory will be accurate.

Assuming the validity of expression (C.2), it is important to evaluate the level of accuracy provided by this technique. Designating by  $\varepsilon_H$ ,  $\varepsilon_{f_1}$ ,  $\varepsilon_\ell$  and  $\varepsilon_m$  the relative errors associated with the estimation of the tension and first cable frequency, and with the definition of the chord length and mass per unit length, respectively, the following relationship holds

$$\varepsilon_H = 2\varepsilon_{f_1} + 2\varepsilon_\ell + \varepsilon_m \quad (\text{C.3})$$

So, assuming errors of 1% in the measurement of the first natural frequency and in the definition of chord length and cable mass, an error of 5% is obtained in the estimate of cable tension. Furthermore, if the purpose of the measurement is to study the variation of tension between the two stages where measurements are performed, then the only error involved in the estimate of tension variation is due to the frequency measurement. Therefore the accuracy of tension variation estimates is enhanced.

### C.3.2 Bending and sag effects

The bending and sag effects in the dynamic behaviour of a stay cable have been described in Appendix B. Sag effects in particular were taken into account by Irvine, who developed an implicit equation (B.10) for the natural frequency as a function of the Irvine parameter  $\lambda^2$ . Simplified approaches also allowed for a simultaneous account of sag and bending effects, providing correction coefficients to the vibrating chord formula (C.1). Using the formula from Mehrabi and Tabatabai [138], the following corrected frequencies  $f'_n$  are obtained

$$\begin{aligned} f'_{1i} &= f_1 \cdot \left[ (1 + 0.039\lambda^2) \cdot \left( 1 + \frac{2}{\xi} + \frac{8.9348}{\xi^2} \right) - 0.24 \frac{\lambda^2}{\xi} \right] \text{(1st in-plane mode)} \\ f'_{1o} &= f_1 \cdot \left( 1 + \frac{2}{\xi} + \frac{8.9348}{\xi^2} \right) \text{(1st out-of-plane mode)} \\ f'_n &= f_n \cdot \left( 1 + \frac{2}{\xi} + \frac{4 + \frac{n\pi^2}{2}}{\xi^2} \right) \text{(n<sup>th</sup> mode, n > 1)} \end{aligned} \quad (\text{C.4})$$

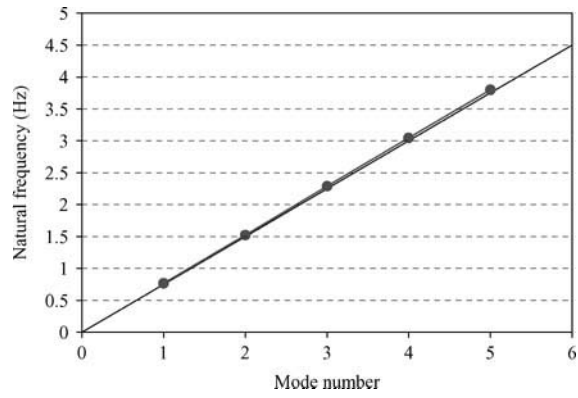


*Fig. C.3: Representation of the cable's natural frequencies with the mode number*

So, if  $\zeta = \sqrt{H \ell^2/EI}$  is known, the measured frequency  $f'_n$  can be easily used in the estimate of  $H$ . As normally only an approximation of  $\zeta$  is available, the best solution for an accurate estimate of the tension consists in the application of an algorithm for a simultaneous identification of  $H$  and  $\zeta$ , preferably based on higher order measured frequencies, in order to enhance bending effects.

It is important to notice that sag effects influence essentially the first in-plane mode of stay cables. Equation (C.4) reflects that aspect. Moreover, if the bending stiffness effects are neglected in this equation, the following linear function of  $\lambda^2$  yields

$$f'_{1i} = f_1 \cdot (1 + 0.039 \lambda^2) \quad (\text{C.5})$$

This expression provides a rather accurate approximation to the solution of the implicit equation (B.10) developed by Irvine, when applied to stay cables with  $\lambda^2$  values in the range of 0–5, typical of stay cables. In effect, the relative error associated with the increment of natural frequency calculated on the basis of this formula is no greater than 5% for this range of  $\lambda^2$  values. Figure C.4 shows a comparison between the correction to the fundamental frequency calculated on the basis of equation (B.10) and given by (C.5), as well as the relative errors given by the second with respect to the correction proposed by Irvine.

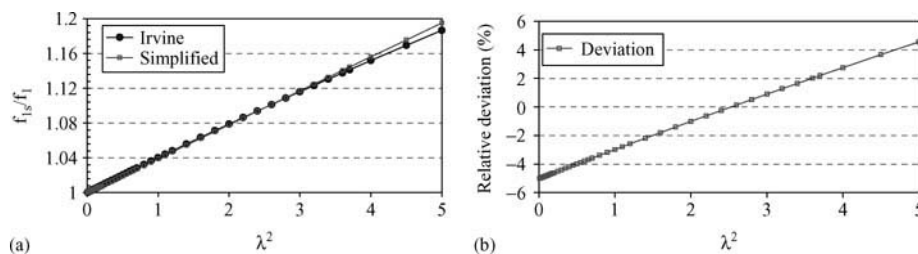


*Fig. C.4: (a) Correction to fundamental vibrating chord frequency associated with sag effects, Irvine and simplified solutions; (b) Relative error to Irvine solution*

### C.3.3 Measurement of cable frequencies

The measurement of the cable's natural frequencies is performed normally using an accelerometer connected to the stay cable at some point close to the deck anchorage (*Fig. C.5*). This accelerometer is connected to a data acquisition system that records the time response to some external excitation, as the one produced by an impact hammer, or simply the ambient excitation. Piezoelectric accelerometers with a low limit frequency range of almost DC and a sensitivity of at least 10 mV/g are an interesting option, given that they do not require power supply, but only a combination with a signal pre-amplifier. For the acquisition system, although many solutions are currently available in the market, a requirement of ease of application and portability should be made. The solution represented in *Fig. C.5*, composed by a 2-channel portable Fourier Analyzer materialised by a PCMCIA card installed in a conventional laptop, is one of the simplest and also most portable solutions.

With respect to the measurement parameters, namely the length of the recorded time series and frequency range of sampling, a good practice is to measure the cable response in a frequency range corresponding to the first 10 natural frequencies of the cable. Given the usual range of



*Fig. C.5: Measurement of acceleration close to the cable anchorage: accelerometer, conditioning unit and Fourier Analyzer. Excitation using impact hammer*

0.2–2 Hz for the first mode, this means a frequency range of 0 to 2–20 Hz. The time resolution should consider the maximum accepted measurement error and the fundamental frequency of the cable. If an error  $\varepsilon_f$  of 1% is expected in the frequency, then for a cable characterised by a fundamental frequency  $f_1$ , the frequency resolution  $\Delta f$  should be less than  $0.01 \cdot f_1$ . This means that the time record associated with one measurement should have a length of  $T_1 = 100/f_1$ . Assuming that the frequency content of the recorded signals is obtained from an average of the frequency content of  $n$  time records for the purpose of reducing the noise present in the measurements and given an overlap of 50%, combined with a Hanning time window (for records of response to ambient excitation), then the length  $T$  of the necessary time records is

$$T = \frac{50 + 50n}{f_1} \quad (\text{C.6})$$

So, for a cable with a fundamental frequency of 1 Hz, an average spectral estimate of the frequency content based on six records will require a sampling time of 350 s to guarantee a frequency measurement error no greater than 1%.

### C.3.4 Estimation of cable damping

The most accurate form of estimating the damping of a stay cable consists in measuring the corresponding free vibration response after inducing resonance in the mode of interest. This task is relatively easy to achieve prior to installation of the damper by the manual pulling of a rope attached to the cable in the vicinity of the deck anchorage till resonance, or else by manually pulling the cable from a height of 10–15 m from an elevated platform. The interruption

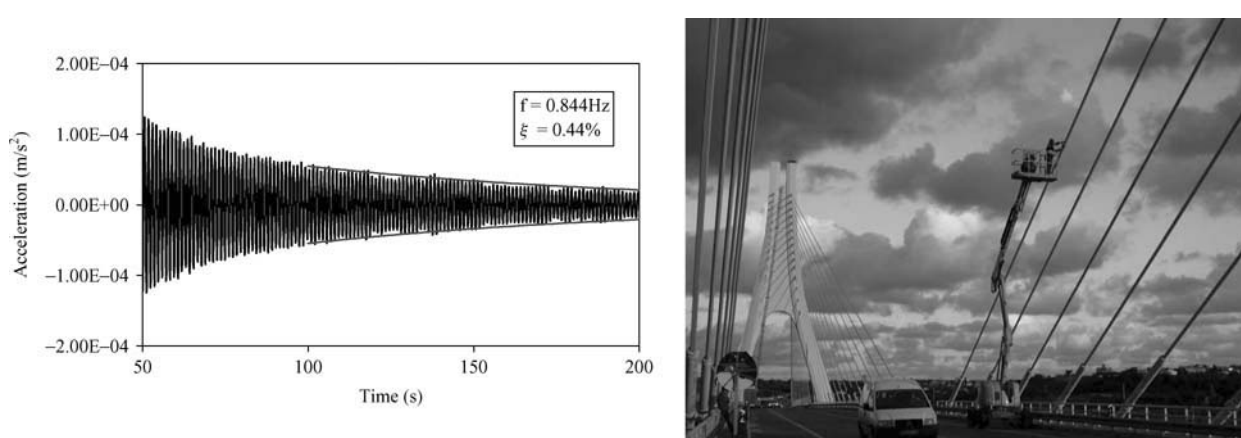


Fig. C.6: Free vibration response of stay cable, time response and fitted envelope. Manual excitation from elevated platform

of the excitation and the measurement of the free vibration response allow for an estimate of the logarithmic decrement, by fitting a single degree exponential to the envelope of the response (*Fig. C.6*).

After installation or activation of the dampers, it may be difficult to induce a measurable level of response from excitation of the cable in the vicinity of the anchorage. In that circumstance and in case an elevating platform is not available, the use of an impact hammer constitutes an interesting alternative: the hit of the cable close to the anchorage with an impulse hammer incorporating a force sensor at the tip and the simultaneous measurement of the applied force and cable response allow for the estimation of frequency response functions. The damping coefficients associated with the various induced modes can be identified by an appropriate fitting algorithm, or simply by application of the half-power bandwidth method.

A less accurate estimate of damping coefficients can still be obtained whenever a force sensor is not available at the hammer tip, or even when no hammer is available. In this case, spectral estimates of the ambient response of the cable close to the anchorage can be obtained. Assuming stationarity and a constant frequency content of the excitation, damping coefficients can be extracted from system identification applied to power spectral estimates.

The application of frequency domain techniques to the identification of damping coefficients may lead to considerable errors when these coefficients are very low, e.g. less than 0.5%. In that case a high frequency resolution is required for a limitation of those errors.

### C.3.5 Practical application

In this section a practical application is presented which refers to the following problem: for a cable-stayed bridge under construction it is the purpose of the designer to have an accurate estimate of the installed tension in the stay cables for three phases during construction. The bridge is formed by two spans of 120 and 69 m, and has a concrete deck box section 18 m wide, as represented in *Fig. C.7* [142]. The larger span is suspended by a central plane composed of ten stay cables. Three pairs of backstays are anchored at each side of the other span, as shown in *Figures C.7* and *C.8*.

The tensions were estimated at the following stages: (i) first, after the installation and initial tensioning of the first suspension cable and the first pair of backstays; (ii) second, after the end of construction, prior to the introduction of the asphalt layer and activation of cable dampers and (iii) third, after completion of the bridge, at the commissioning stage (loaded and unloaded). *Figure C.9* illustrates the three phases referred to here.

The estimation of tension was based on the vibration method described above, in which the ambient response of the cables was measured using a piezoelectric accelerometer and the average power spectral densities were calculated. *Figure C.10* shows an example of the average power spectral density estimate that was obtained at the third test stage, for the unloaded bridge, at the shortest suspension stay S1 (length of 55.1 m). This estimate was obtained with a frequency resolution of 0.02414 Hz for the range of 0–19.53 Hz, based on the average of 10 time records. This led to a frequency resolution of  $0.014 \cdot f_1$ , which is a little higher than advised. However each measurement was carried out in less than 5 min, which was relevant as subsequent loading operations on the bridge were programmed. The analysis of *Fig. C.10* shows that, due to the low level of ambient excitation, only the first four modes of vibration are clearly induced. So the verification of the applicability of the vibrating chord

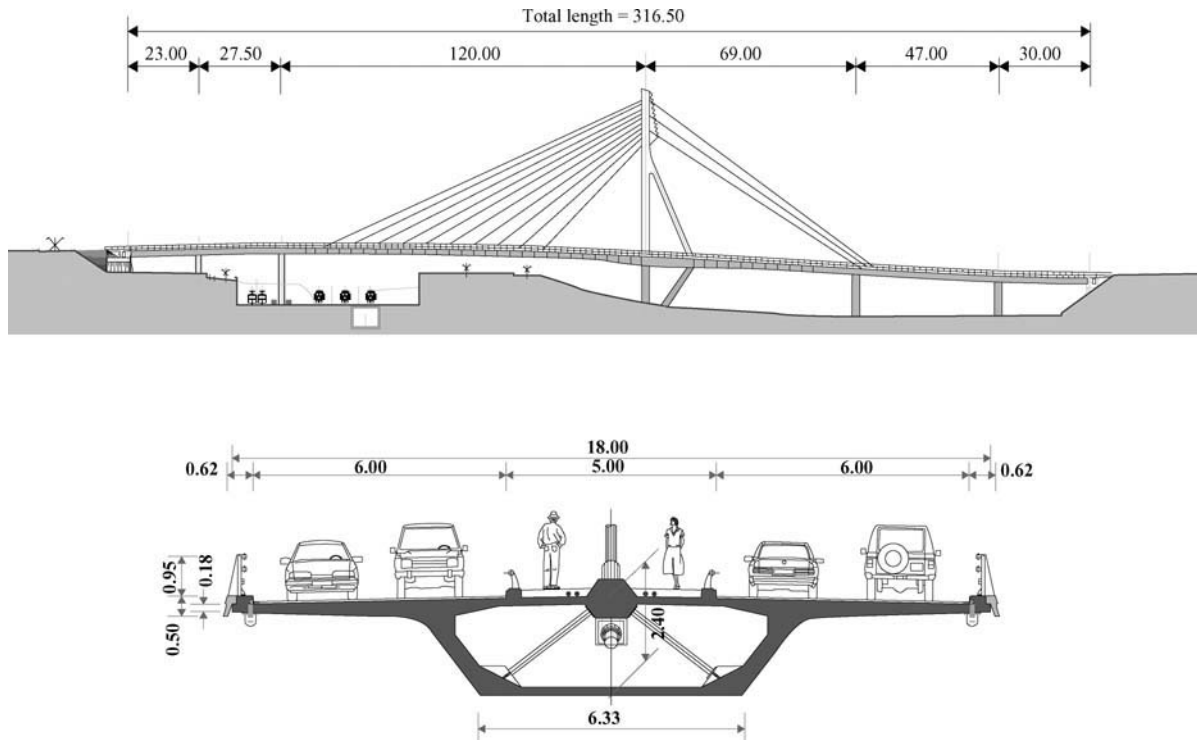


Fig. C.7: Schematic elevation and deck cross-section of cable-stayed bridge [142]



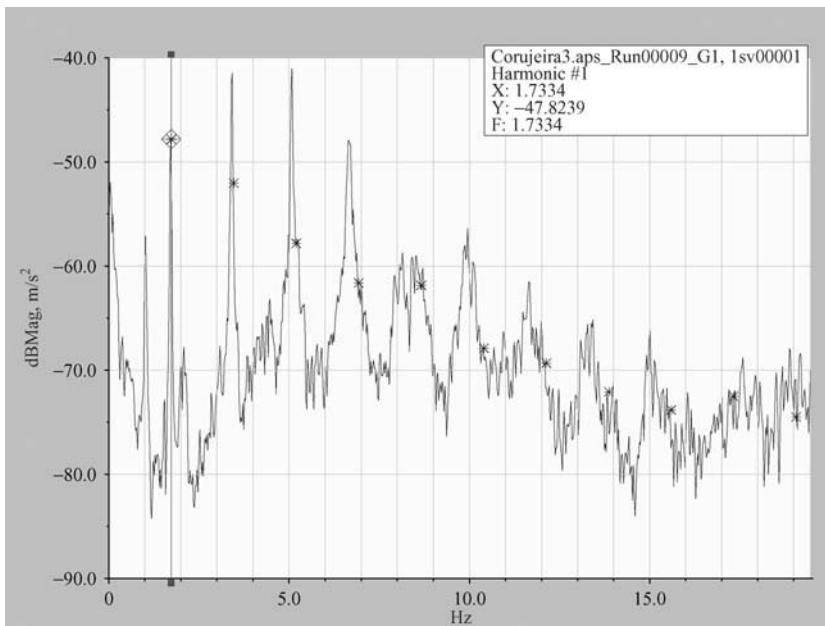
Fig. C.8: General view of cable-stayed bridge



Fig. C.9: Phases of construction of bridge during which installed tension was estimated:  
(a) first; (b) second; (c) third

<b>Test</b>		<b>FIRST</b>	<b>SECOND</b>	<b>THIRD</b>	<b>FIRST</b>	<b>SECOND</b>	<b>THIRD</b>
Corujeira Bridge	<b>Stay</b>	<b>S1</b>	<b>S1</b>	<b>S1</b>	<b>1RN</b>	<b>1RN</b>	<b>1RN</b>
Chord length	L (m) =	55.148	55.148	55.148	82.212	82.212	82.212
Distributed mass	m (kg/m) =	59.25	59.25	59.25	92.32	92.32	92.32
	$\lambda^2$	0.1075	0.5706	0.1233	1.6810	0.0354	0.0354
	Lc (m)	55.149	55.152	55.150	82.229	82.213	82.213
	EA (N)	1.219E + 09	1.219E + 09	1.219E + 09	1 899 450 000	1 899 450 000	1 899 450 000
	$\zeta$ (estimate)	60	45	59	65	124	124
Tension estimate (Vibration chord theory)		2267	1300	2166	1843	6678	6678
Tension estimate (Sag effect correction)		<b>2248</b>	<b>1244</b>	<b>2145</b>	<b>1623</b>	<b>6660</b>	<b>6660</b>
Tension estimate (Sag and bending correction)		<b>2095</b>	<b>1132</b>	<b>1996</b>	<b>1522</b>	<b>6442</b>	<b>6442</b>
Relative error to sag corrected estimate (%)		0.8	4.5	1.0	13.5	0.3	0.3
Relative error to sag and bend.corrected est. (%)		8.2	14.9	8.5	21.1	3.7	3.7
1st measured natural frequency	1	1.7734	1.3428	1.7334	0.8594	1.6357	1.6357
2nd measured natural frequency	2	3.4766	2.6367	3.4424	1.6211	3.2471	3.2715
3rd measured natural frequency	3	5.1953	3.8818	5.1514	2.4219	4.8340	4.8828
4th measured natural frequency	4	5.2002	6.7627		6.4209	6.4453	
1st natural frequency corrected to sag effect		1.7660	1.3135	1.7251	0.8065	1.6335	1.6335
1st nat. Freq. corrected to sag and bend. effect		1.7049	1.2530	1.6640	0.7808	1.6066	1.6066

Table C.1: Mechanical characteristics and natural frequencies of two stay cables for estimation of installed tension



*Fig. C.10: Average power spectral density of ambient response at stay S1, at the third test stage*

theory is not possible. It is also important to notice the presence of global bridge frequencies mixed with cable frequencies, which is typical of this type of measurements and requires particular attention whenever a bridge frequency is very close to a cable's natural frequency. In that case, the analysis of successive harmonics plays a relevant role in the identification of cable modes.

*Table C.1* presents the mechanical characteristics of two selected cables, one suspension cable, S1, and one backstay, 1RN, as well as the first natural frequencies that were identified from the analysis of average power spectral densities. The identification of tensions was formerly based on the vibration chord theory. The calculation of  $\lambda^2$  then allowed for a correction of the estimate introducing sag effects, through simplified formula (C.5). The estimate of the bending parameter  $\zeta$  allowed a second correction of the tension, using the simplified formula (C.4). *Table C.1* presents the estimates obtained, as well as the relative error of vibration chord estimates to sag or sag and bending corrected estimates.

It can be concluded from the analysis of this Table that the vibration chord theory provides good tension estimates while the Irvine parameter is no greater than one. Sag effects, evaluated on the basis of the simplified formula (C.5), are of significance for the first tension level of backstay 1RN, where  $\lambda^2 = 1.6810$ . The vibration chord theory leads in this case to an error of 13.5% in the estimate of tension. As for bending effects, more than 5% error is found for stay cables with  $\zeta < 100$ . It should be noted however that the finite element modelling of bending effects for the stay cables listed above, considering the estimated bending parameters, leads to much smaller differences to the sagged cable model than the ones resulting from the formulae employed.